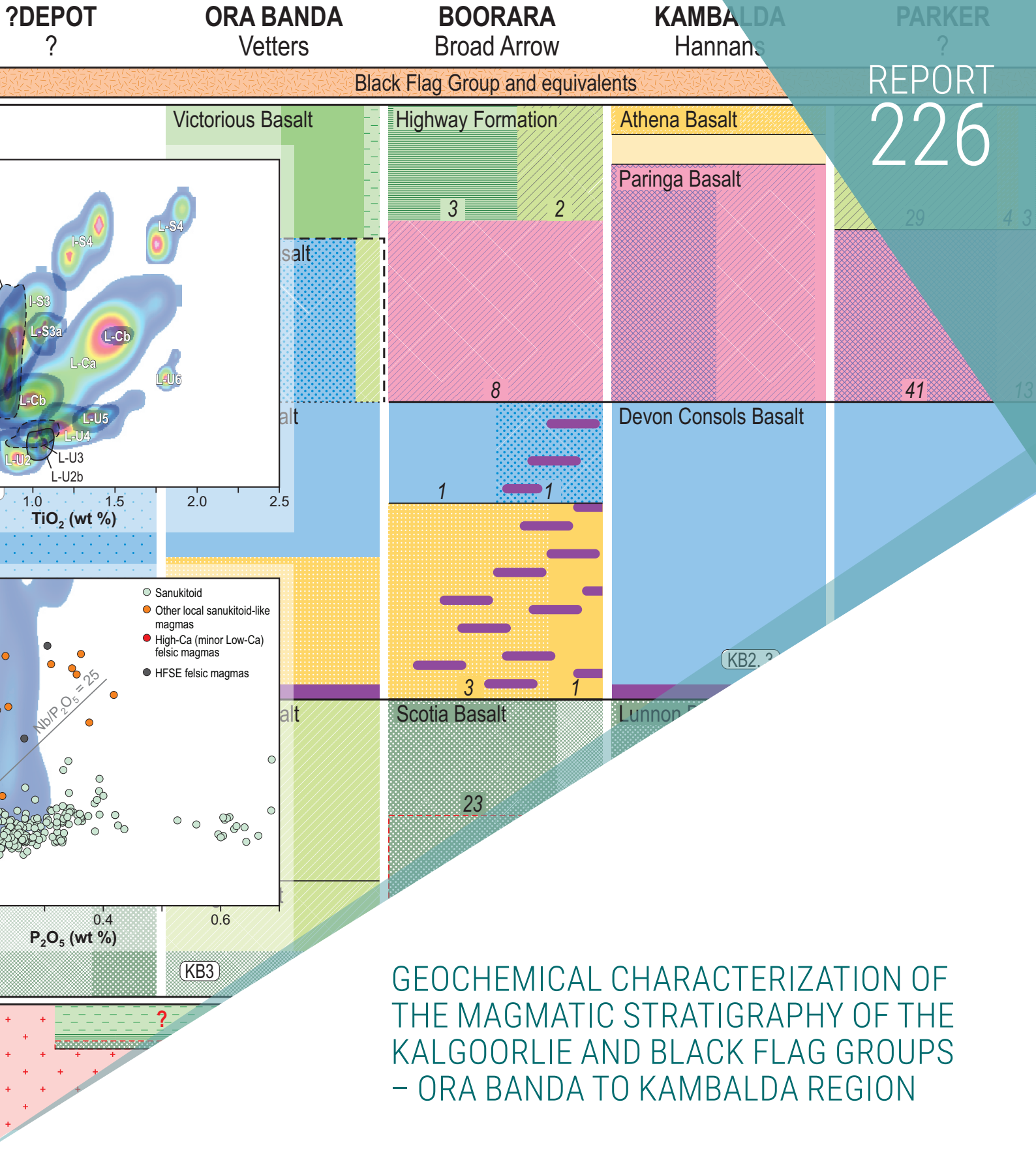

REPORT 226

GEOCHEMICAL CHARACTERIZATION OF THE MAGMATIC STRATIGRAPHY OF THE KALGOORLIE AND BLACK FLAG GROUPS – ORA BANDA TO KAMBALDA REGION

RH Smithies, JR Lowrey, J Sapkota, MC De Paoli, P Hayman, SJ Barnes, DC Champion, Q Masurel, N Thébaud, LL Grech, M Drummond and R Maas

Government of Western Australia
Department of Mines, Industry Regulation and Safety

Geological Survey of Western Australia

Government of **Western Australia**
Department of **Mines, Industry Regulation and Safety**

REPORT 226

GEOCHEMICAL CHARACTERIZATION OF THE MAGMATIC STRATIGRAPHY OF THE KALGOORLIE AND BLACK FLAG GROUPS – ORA BANDA TO KAMBALDA REGION

RH Smithies, JR Lowrey, J Sapkota, MC De Paoli, P Hayman[1], SJ Barnes[2], DC Champion[3], Q Masurel[4], N Thébaud[4], LL Grech, M Drummond and R Maas[5]

1 School of Earth and Atmospheric Sciences, Queensland University of Technology, Brisbane QLD 4000
2 CSIRO, Mineral Resources, Perth WA 6155
3 Geoscience Australia, GPO Box 378, Canberra ACT 2601
4 Centre for Exploration Targeting, The University of Western Australia, 35 Stirling Highway, Crawley WA 6009
5 School of Geography, Earth and Atmospheric Sciences, University of Melbourne, Parkville VIC 3010

PERTH 2022

Geological Survey of Western Australia

MINISTER FOR MINES AND PETROLEUM
Hon Bill Johnston MLA

DIRECTOR GENERAL, DEPARTMENT OF MINES, INDUSTRY REGULATION AND SAFETY
Richard Sellers

EXECUTIVE DIRECTOR, GEOLOGICAL SURVEY AND RESOURCE STRATEGY
Jeff Haworth

REFERENCE
The recommended reference for this publication is:
Smithies, RH, Lowrey, JR, Sapkota, J, De Paoli, MC, Hayman, P, Barnes, SJ, Champion, DC, Masurel, Q, Thébaud, N, Grech, LL, Drummond, M and Maas, R 2022, Geochemical characterization of the magmatic stratigraphy of the Kalgoorlie and Black Flag Groups — Ora Banda to Kambalda region: Geological Survey of Western Australia, Report 226, 100p.

ISBN 978-1-74168-957-0
ISSN 1834-2280

A catalogue record for this book is available from the National Library of Australia

Grid references in this publication refer to the Geocentric Datum of Australia 1994 (GDA94). Locations mentioned in the text are referenced using Map Grid Australia (MGA) coordinates, Zone 50. All locations are quoted to at least the nearest 100 m.

Published 2022 by the Geological Survey of Western Australia
This Report is published in digital format (PDF) and is available online at <www.dmirs.wa.gov.au/GSWApublications>.

Further details of geoscience publications are available from:
First Floor Counter
Department of Mines, Industry Regulation and Safety
100 Plain Street
EAST PERTH WESTERN AUSTRALIA 6004
Telephone: +61 8 9222 3459 Email: publications@dmirs.wa.gov.au
www.dmirs.wa.gov.au/GSWApublications

Contents

Appendices

Figures

Tables

Geochemical characterization of the magmatic stratigraphy of the Kalgoorlie and Black Flag Groups – Ora Banda to Kambalda region

RH Smithies, JR Lowrey, J Sapkota, MC De Paoli, P Hayman[1], SJ Barnes[2], DC Champion[3], Q Masurel[4], N Thébaud[4], LL Grech, M Drummond and R Maas[5]

Summary

A new dataset of ~2800 high-quality whole-rock geochemical analyses of subvolcanic, volcanic, and volcaniclastic rocks from the Kalgoorlie Group is used to construct chemostratigraphic barcodes within the broader Ora Banda – Kambalda region, encompassing most of the previously defined domains of the Kalgoorlie Terrane as well as the Bulong complex area of the Kurnalpi Terrane. Twenty-six distinct mafic compositional units are identified based on combinations of major and trace element variation diagrams, and in particular, on bivariate plots utilizing strongly incompatible trace elements. These distinctions highlight the controls that various fundamental igneous processes and source compositional variations exerted on evolving magma compositions. There are broad trends in compositional change common to the chemostratigraphy in most areas throughout the region. As described in numerous previous studies, the three commonly identified regional stratigraphic levels (basaltic lower, komatiitic/basaltic middle, and basaltic upper) correspond to changes in tectonomagmatic processes, and in particular, a general increase in the degree of mantle partial melting, an increase in the amount and/or effect of crustal contamination, and an increase in overall magmatic compositional diversity.

According to the new barcode data, individual established lithostratigraphic units, typically of formation level, seldom comprise a single geochemical unit. Most stratigraphic formations comprise at least two distinct geochemical units. Most of these units occur at multiple stratigraphic levels, and in most regional stratigraphic columns. Thus, the individual greenstone stratigraphic formations comprise overlapping flow fields, each representing the products of a discrete eruptive event and/or eruptive centres that tapped genetically unrelated magma sources. This potentially makes some stratigraphic formation boundaries somewhat arbitrary reflections of changing source eruptions. Although complex, this diversity ensures that, in most cases, the position of stratigraphically unknown geochemical samples can be uniquely established as long as enough samples are taken over a continuous stratigraphic interval that also incorporates the overlying and underlying units.

However, there are rare cases where local mafic geochemical associations appear anomalous with respect to the surrounding associations. For example, in the Kundana region to the west of the Zuleika Shear Zone and in an area close to Londonderry Siding, a stratigraphy characteristic of the Ora Banda Domain, rather than of the Coolgardie Domain, is intersected in drillcore and in outcrop. The reasons for this remain elusive.

Because of the greater continuity of low-viscosity flows that characterize its basalt-dominated stratigraphy, the application of chemostratigraphic barcoding is more reliable or appropriate for the Kalgoorlie Group than for the overlying Black Flag Group. Geochemical characteristics and relationships within the felsic-dominated Black Flag Group, nevertheless, provide broad stratigraphic information and significant insight into crustal architecture and regional geological evolution.

The regional distribution of the mafic chemostratigraphic associations is distinctly asymmetric, in many cases ignoring previously established domain boundaries. However, a broadly north-trending structure incorporating segments of (from south to north) the Zuleika Shear Zone, Abattoir Fault, and the Bardoc Shear Zone (ZAB) does appear to separate the 'western domains' (Coolgardie and Ora Banda) from the 'eastern domains' (Kambalda, Boorara, Parker, and the Bulong complex). These domain groups have distinctive chemostratigraphic variations that probably reflect a fundamental crustal architectural control and potentially provide some basis for reassessing the present domain boundaries. In particular, the mafic units in the western domains probably reflect melting of a more depleted source in thicker lithosphere. The Ora Banda Domain is clearly a part of the western domains throughout evolution of the lower and middle greenstone stratigraphy, but it also appears transitional to the eastern domains in terms of its diversity of fractionated layered sill-derived magmatism in its upper stratigraphy. The chemostratigraphic differences between the western and eastern domains extend to the felsic units of the Black Flag Group. The subvolcanic, volcanic, and volcaniclastic rocks of the Black Flag Group have the composition of sanukitoids, which are likely derived from a metasomatically enriched lithospheric mantle source. They show a wide range in La/Th ratios, which broadly correlates with crystallization age, source composition, and location. Low La/Th sanukitoid is typically older (>c. 2678 Ma), derived from a source with less radiogenic Nd (i.e. is more crustal) and is more common west of the ZAB, whereas high La/Th sanukitoid is typically younger (<c. 2675 Ma), has more mantle-like isotopic compositions and is virtually restricted to east of the ZAB. The simplest explanation for the regional compositional variations in the mafic and felsic rocks is that the ZAB is the exposed trace of a structure separating compositionally contrasting translithospheric domains. Northern and southern extensions of that trace should be entirely identifiable based on geochemical and isotopic data.

Keywords: Crustal evolution, geochemistry, greenstone, Neoarchean, stratigraphy, Yilgarn Craton

1 School of Earth and Atmospheric Sciences, Queensland University of Technology, Brisbane QLD 4000

2 CSIRO, Mineral Resources, Perth WA 6155

3 Geoscience Australia, GPO Box 378, Canberra ACT 2601

4 Centre for Exploration Targeting, The University of Western Australia, 35 Stirling Highway, Crawley WA 6009

5 School of Geography, Earth and Atmospheric Sciences, University of Melbourne, Parkville VIC 3010

Introduction

This Report discusses the use of a large amount of new, high-quality, geochemical data from drillcore and outcrop samples collected from the Eastern Goldfields Superterrane in the Archean Yilgarn Craton of Western Australia, to establish unique lithogeochemical characteristics (barcodes) applicable to local- to regional-scale greenstone stratigraphy. Although large regional lithogeochemical datasets can be extremely useful in identifying petrogenetic processes (e.g. Barnes et al., 2021; Halley, 2021), they typically include analyses of a range of individual lithological units that have no geological reasons to be genetically related. Inferring stratigraphic or lithological correlations between such geochemical data without significant additional geological constraints is fraught with danger. However, by generating a substantial amount of data on specific rock units within a more geologically and geographically constrained area, and taking into account their stratigraphic context, chemically distinctive groups that relate to lithostratigraphy can be identified.

There are numerous benefits in employing a geochemical approach to stratigraphy within an established geological context. This is particularly the case in many Archean greenstone sequences, where the typically basalt-dominated stratigraphy offers very few mineralogical or textural clues that can be used to uniquely identify a specific unit. This problem is significantly compounded in regions such as the Yilgarn Craton, where typically poor outcrop and locally high structural complexity severely limit the geological context required to confidently assign stratigraphy.

The barcodes we produced, are based on the better-known and sampled stratigraphic sections and provide templates against which geochemical data sourced from other parts of a specific greenstone belt can be evaluated for possible lithostratigraphic or chemostratigraphic equivalence. Some of the established stratigraphic units we examined are geochemically unique. In these cases, inferring the stratigraphic position of geochemically similar 'unknowns' within that general region can be done with a high degree of confidence. More typically, individual lithostratigraphic units have a composition or compositional range similar to several other units from the same or other stratigraphic intervals, resulting in non-unique stratigraphic allocation options. In these cases, a single or low number of analyses will not uniquely identify a lithostratigraphic position. However, more comprehensive sampling, particularly if it incorporates the underlying and overlying stratigraphic units, almost certainly will.

The geochemical barcoding approach is particularly applicable to basalt-dominated stratigraphy, since low-viscosity mafic (and ultramafic) lavas can travel long distances and blanket the underlying surface. This may particularly be the case where magmas rapidly erupted on to subdued topography, as suggested for mafic flows of at least the lower parts of the stratigraphy in the region between Ora Banda and Kambalda (Morris, 1993). However, the approach is less effective in the case of felsic volcanic and volcaniclastic accumulations, although broad but significant compositional variations can still be observed and utilized.

It is hoped that the geochemical barcodes that we have constructed will provide a useful stratigraphic tool from the mine site to the regional scale. An additional, substantial benefit is perhaps the most comprehensive, regional, high-quality, and (analytically) internally consistent, major and trace element geochemical dataset from any Archean greenstone terrane globally.

The Ora Banda – Kambalda region (Fig. 1) provides the ideal choice for an initial attempt at establishing a greenstone chemostratigraphy. This region is extremely well-studied geologically and the focus of many geochemical studies. Perhaps the most detailed study is by Morris (1993), and many of its conclusions are confirmed and repeated here. The study region lies mainly within the Kalgoorlie Terrane but crosses the boundary with the Kurnalpi Terrane to the east (Fig. 1). The present stratigraphic interpretations show that each domain of the Kalgoorlie Terrane has its own, slightly different, greenstone lithostratigraphic variation (Fig. 2) within a broadly similar framework based on the classic Kalgoorlie–Kambalda stratigraphy of the Kambalda Domain. The latter comprises basalt (Lunnon Basalt)-komatiite (Kambalda Komatiite)-basalt (Devon Consols Basalt)-basalt (Paringa Basalt) magmatic stratigraphy of the 2720–2690 Ma Hannans Subgroup overlain by the 2690–2665 Ma felsic volcaniclastic-dominated Black Flag Group.

Within the study region, the geochemical barcoding project has so far produced ~2300 new high-quality geochemical samples of greenstones from drillcore and outcrop, to supplement the ~500 existing, publicly available high-quality analyses. We largely restrict our analysis to data from volcanic rocks covering the mafic to felsic compositional range (SiO_2 from ~45–77 wt% anhydrous) and MgO up to 18 wt% (except for some partial cumulate and cumulate layers that have MgO up to 25 wt%). We have omitted any interpretation of komatiite compositional variation, although our data sampling regime has routinely included ultramafic rocks; those data are presented in Appendix 1. Likewise, we have routinely sampled mafic dykes and mineralogically layered sills within the stratigraphy (data presented in Appendix 1); however, we only refer to these data where appropriate, in terms of comparisons with basaltic stratigraphy. A detailed account of these mafic intrusions is given by Hayman et al., (2021).

We compare our chemostratigraphy against the current lithostratigraphic interpretations and assess our results in the light of existing domain boundaries, and more recent studies suggesting alternative geographical arrangements of lithostratigraphically coherent blocks (e.g. Hayman et al., 2015). We also discuss compositional changes within and between regional stratigraphic successions that could add to our understanding of greenstone-sequence evolution. In addition, we assess what mafic and felsic magma evolutionary trends might indicate in terms of lithospheric architectural evolution and the identification of those transcrustal to translithospheric structures that played the most fundamental roles in fluid and melt transfer.

A short summary of the more functional aspects of the chemostratigraphy and its potential field application, without the accompanying geochemical, petrological or geodynamic discussions or implications, is provided as Appendix 6.

Regional geological introduction

The Yilgarn Craton has been subdivided into seven terranes based on distinct stratigraphic characteristics, geochemistry, and age (Fig. 1). The western part includes the Narryer, Youanmi and South West Terranes. The eastern part of the craton includes the Kalgoorlie, Kurnalpi, Burtville and Yamarna Terranes, which together comprise the Eastern Goldfields Superterrane (Cassidy et al., 2006; Pawley et al., 2012). The terrane boundaries in the eastern half of the craton are widely believed to correlate with large-scale shear zones active during late Archean tectonic events. Geophysical data show at least some of them to be east-dipping listric structures that penetrate the deep crust (Drummond et al., 2000; Goleby et al., 2006; Blewett et al., 2010).

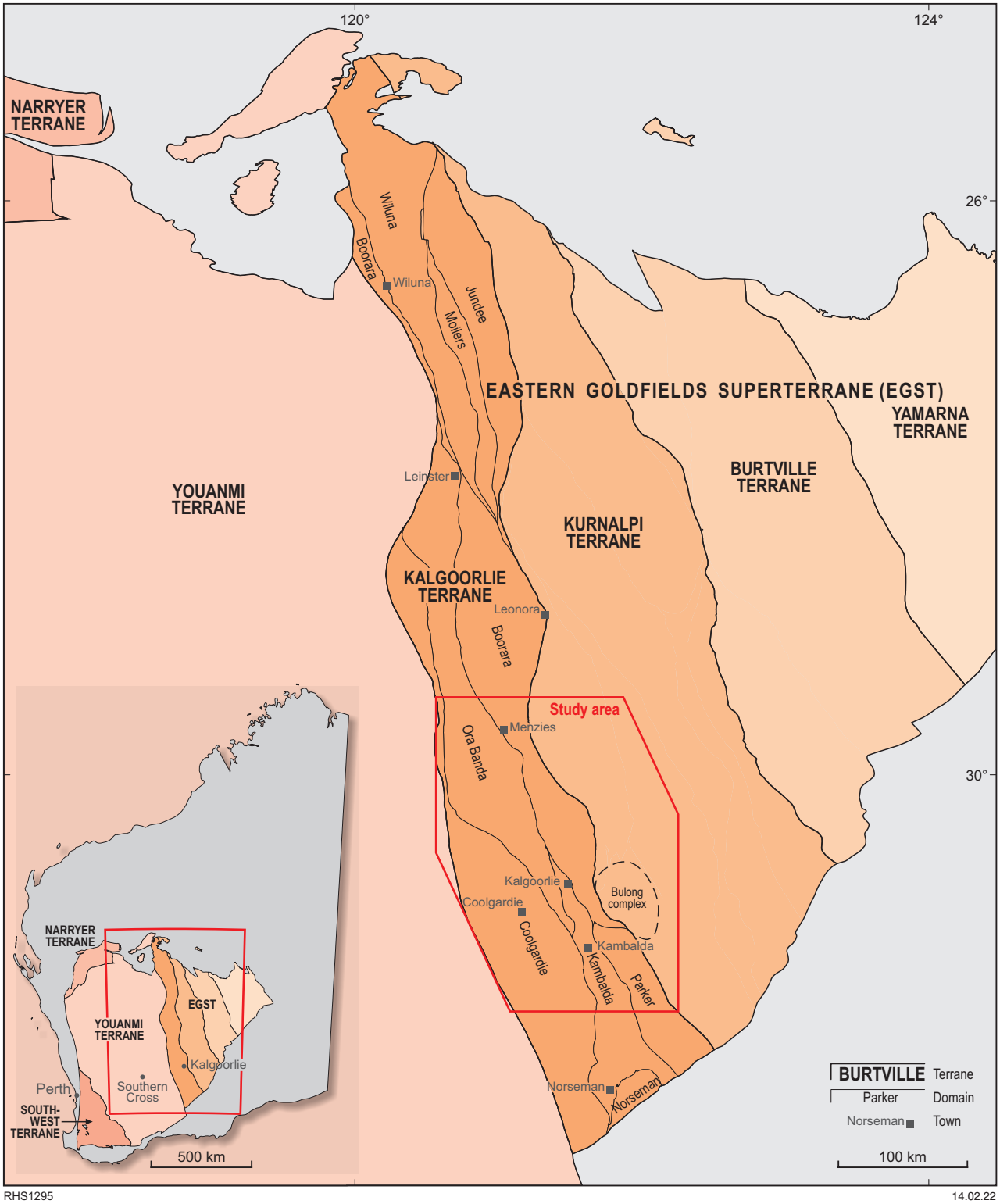

Figure 1. Regional map of the Eastern Goldfields region of the Yilgarn Craton showing the outline of the various proposed terrane and domain boundaries (from Cassidy et al., 2006), and the location of the study area, mainly within the Kalgoorlie Terrane

The Kalgoorlie Terrane includes several domains (Fig. 1) representing structurally bound regions each showing unique variations within an otherwise broadly common stratigraphic succession and structural history (Swager et al., 1990). These include the Coolgardie, Bullabulling, Kambalda, Parker, Ora Banda and Boorara Domains. Cassidy et al., (2006) subdivide the Coolgardie Domain into the Depot Domain, separating the remainder of the Coolgardie Domain, to the west, from the Kambalda and Ora Banda Domains to the southeast and northeast, respectively. The study region incorporates parts of all domains of the Kalgoorlie Terrane, except Bullabulling Domain. To the east, the Kalgoorlie Terrane is separated from the Kurnalpi Terrane by the Mount Monger Fault. Within the Kurnalpi Terrane, the western part of the Bulong Domain, comprising the Bulong complex, is also included within the study region. In general, although the Bulong Domain shows significant stratigraphic, structural, and geochronological differences with the Kalgoorlie Terrane, it has been suggested that the area around the Bulong Anticline (i.e. the Bulong complex) shows closer similarities with the Kalgoorlie Terrane (e.g. Nelson, 1997; Hollis et al., 2017).

The Kambalda Domain contains the classic Kalgoorlie–Kambalda stratigraphy developed and modified by Woodall (1965), Gresham and Loftus-Hills (1981), and Roberts (1988), which was subsequently used as the template for greenstone stratigraphy throughout the eastern Yilgarn Craton. Current GSWA nomenclature includes the lower (2720–2690 Ma) mafic–ultramafic package of this model stratigraphy in the Hannans Subgroup (Kalgoorlie Group) (Fig. 2), with the basal Lunnon Basalt overlying unknown basement. In turn, this is overlain by the Kambalda Komatiite, Devon Consols Basalt, Kapai Slate, and the Paringa Basalt (Fig. 2). A detailed description of the magmatic stratigraphy, its lithological variations, physical volcanological features, and geochemical variations has previously been provided by Morris (1993). The Hannans Subgroup is conformably to locally unconformably overlain by the Black Flag Group (2690–2665 Ma), which mainly comprises felsic volcanic and volcaniclastic rocks. These felsic rocks and their stratigraphy have been studied in detail by Tripp (2013, 2019). All parts of this stratigraphy have been extensively intruded by mafic- or mafic–ultramafic sills and granitic rocks.

Variations in detailed stratigraphy across major structures and between greenstone belts has formed a basis for the recognition of domains. However, the significance of the various domains, at least as presently defined – if not, the concept in general – is increasingly questioned (e.g. Hayman et al., 2015) as our understanding of the stratigraphy and structural evolution increases. The recent GSWA Eastern Goldfields Superterrane seamless geological mapping program attempted to avoid domain-based lithostratigraphic nomenclature altogether. According to the current GSWA nomenclature (Sapkota, 2020), the Kalgoorlie Group comprises most of the mafic–ultramafic package in greenstone belts between Norseman and Leinster (Figs 1 and 2) and is overlain by the felsic volcanosedimentary succession of the Black Flag Group or its regional equivalent. The various rock successions that form the Kalgoorlie Group, although linked in terms of broadly similar stratigraphy and age range, are not physically continuous throughout the Kalgoorlie Terrane. However, it is probable that they are products of the same geological events and at least some successions were originally deposited in distinct depocentres.

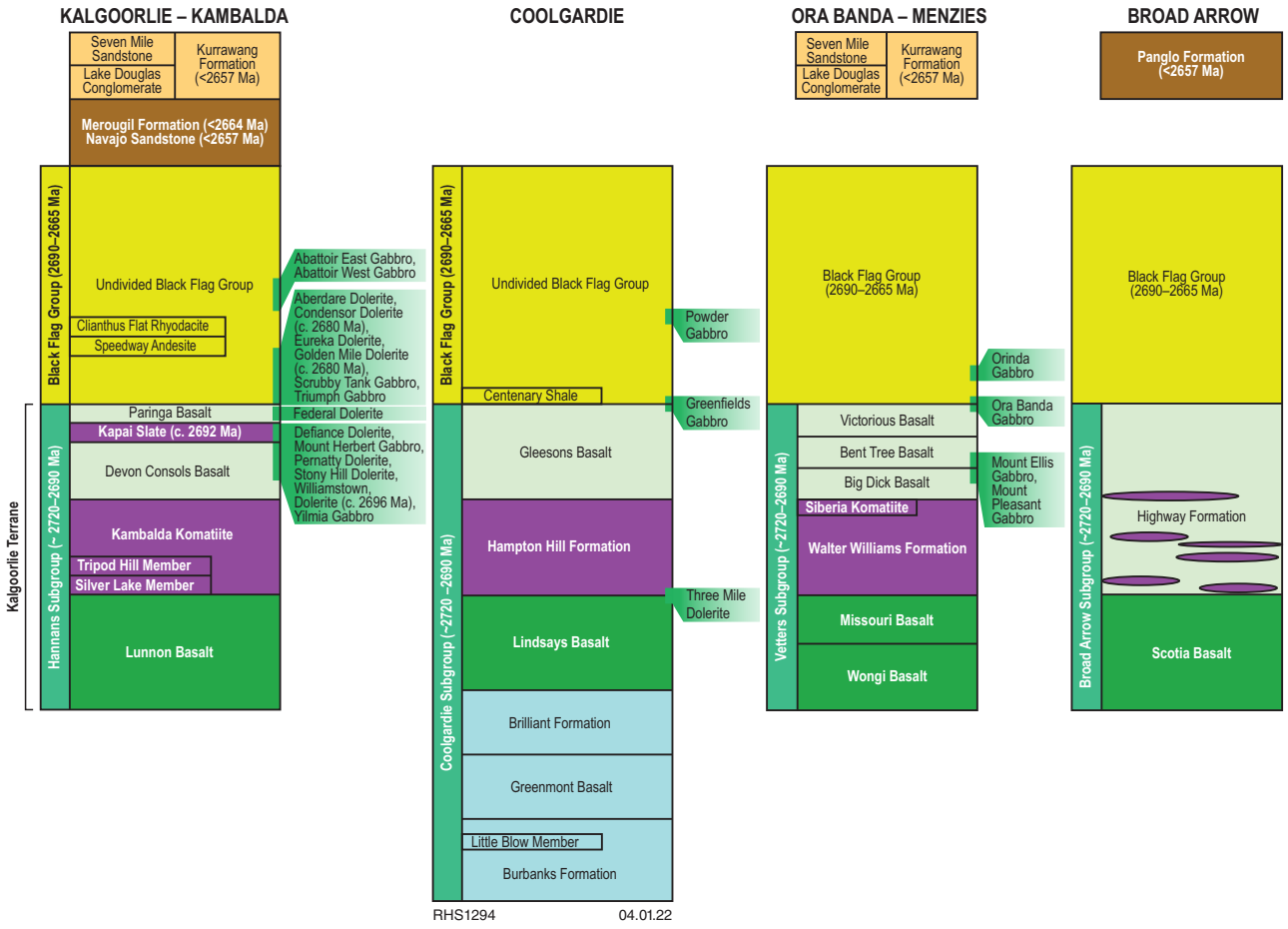

Figure 2. Present stratigraphic interpretations of the central part of the Kalgoorlie Terrane (Sapkota, 2020)

Where these structurally or geographically isolated sequences form stratigraphically continuous successions of the Kalgoorlie Group, they have each been distinguished as a distinct subgroup (Sapkota, 2020; Fig. 2). However, this new interpretation uses much the same dataset used to establish the original domains and the spatial distribution of the subgroups does not differ markedly from that of the original domains. Hence:

- In the Kalgoorlie–Kambalda region, this part of the stratigraphy is assigned to the Hannans Subgroup, and lies entirely within the Kambalda Domain
- Greenstone successions around and to the north and west of Coolgardie are placed in the Coolgardie Subgroup, which is entirely within the Coolgardie Domain. However, isolated greenstone outcrops between the Coolgardie Subgroup and the Hannans Subgroup are currently placed within the Coolgardie or the Hannans Subgroups or have been left stratigraphically unassigned
- Greenstones in the Ora Banda region and those to the north, in the area west of Menzies, are placed in the Vetters Subgroup, which lies entirely within the Ora Banda Domain
- Greenstones in the area immediately east of Broad Arrow and Menzies are placed in the Broad Arrow Subgroup, which lies entirely within the Boorara Domain.

Hayman et al., (2015) integrated detailed stratigraphic logging with previously available and new whole-rock geochemistry and suggested modifications to the structural arrangement apparently separating stratigraphically coherent blocks throughout much the same region studied in this Report. This interpretation identifies an enriched basaltic component contributing to the lower basaltic units in the Coolgardie and Ora Banda Domains that appears absent from domains further east (Kambalda, Boorara, Parker). If valid, this interpretation has significant implications in terms of regional stratigraphic correlations at least as far north as the Agnew region.

Additionally, basement greenstone stratigraphy older than 2730 Ma and in some cases, older than 2750 Ma, has been confirmed stratigraphically or structurally beneath several successions of the Kalgoorlie Group (e.g. Hill et al., 1992; Hayman et al., 2015; Jones et al., 2020). These include greenstone sequences and felsic units with close geochronological similarities with units of the Youanmi Terrane to the west and the Burtville Terrane to the east. This has led to the suggestion that the Eastern Goldfields Superterrane was continuously underlain by basement of that age, and formed an incomplete rift of the Youanmi Terrane crust at c. 2710 Ma (Pawley et al., 2012, Smithies et al., 2018a, Mole et al., 2019).

There has been debate about whether the complex basalt-komatiite stratigraphy underlying the Lindsays Basalt in the Coolgardie Subgroup (Fig. 2) is a thrust repetition of the Lindsays Basalt and overlying Hampton Hill Formation or an older (lower) and hitherto undated sequence (perhaps one of the >2730 Ma basement remnants). This lower basaltic sequence is portrayed in most existing stratigraphic columns to include a lower basaltic Burbanks Formation overlain by the Greenmont Basalt and capped by ultramafic flows and sills of the Brilliant Formation, and is currently assigned to the Coolgardie Subgroup.

In this study, we use domain names as convenient, familiar, regional geographic markers, and subgroup names in reference to the regional stratigraphy. Our sampling of the Coolgardie Subgroup included units from below, within, and above the Lindsays Basalt and does not support the suggestion of major stratigraphic repetition (see later). Where a distinction is required, the terms 'lower Coolgardie succession' and 'upper Coolgardie succession' are used to denote the stratigraphy below and above the boundary between the Brilliant Formation and Lindsays Basalt, respectively.

Sample selection and analytical techniques

Dataset content

From an initial dataset of 2843 whole-rock major and trace element analyses, we used a subset of ~2100 analyses covering nearly all the supracrustal igneous (or meta-igneous) lithologies, including volcaniclastic rocks [omitting komatiites (n = 279), dolerites (n = 243), and altered felsic rocks (n = 184); analyses of altered mafic rocks are not reported]. The initial dataset incorporates 2272 new analyses (see analytical techniques below) performed specifically for this project, of which 1733 are from diamond drillcores (Appendix 2) and the remainder from outcrop samples. For samples that were not specifically analysed (or re-analysed in the case of many samples from Morris, 1993) for this project, only analyses that incorporated a wide range of trace element determinations by ICP-MS [including the full suite of rare earth elements (REE), Nb and Th], were included in our dataset. New GSWA data, and older ICP-MS data from GSWA and Geoscience Australia are presented in Appendix 1 and their distribution is shown in Figure 3. Appendix 1 includes suitable ICP-MS data from literature sources but does not include company data or other otherwise unpublished data. Table 1 shows the number of samples collected within each domain. Relatively low sample numbers from the Boorara Domain (n = 219), Parker Domain (178), and the Bulong complex (n = 244) mean chemostratigraphic interpretations from these regions are significantly less robust than those from the regions to the west. Sampling in the Parker Domain was mainly limited to several drillholes to the west of Logans Find on the northeast edge of Lake Lefroy, hence, the regional stratigraphic context was limited. In the case of the Boorara Domain, the majority of the samples are from the stratigraphically lower regions of the Broad Arrow Group (Scotia Basalt) and should reflect a reasonable representation of that part of the stratigraphy.

Analytical procedure for new GSWA samples

All samples specifically collected for the greenstone geochemical barcoding project were analysed at BV Minerals, Canning Vale, Perth. The drillcore and surface samples were visibly inspected and any weathering or excessive vein material was removed. Each sample was crushed in-house or by BV Minerals in a plate jaw crusher and low-Cr steel mill to produce a pulp with a nominal particle size of 90% <75 µm. A representative pulp aliquot was analysed for 13 elements as major components, ignition loss, and 54 elements as trace elements (ppm or ppb). The major elements were determined by X-ray fluorescence spectrometry on a fused glass disc. A fragment of each disc was then laser ablated and analysed by ICP-MS for 51 of the 54 minor elements. Gold, Pd, and Pt were analysed on a separate pulp aliquot by lead-collection fire assay and ICP-MS. Data quality was monitored by blind insertion of sample duplicates (a second pulp aliquot), GSWA internal reference materials, and the certified reference material OREAS 24b (www.ore.com.au). BV Minerals also included duplicate samples (including OREAS 24b), variably certified reference materials, and blanks. The accuracy and precision was assessed using data from 17 analyses of OREAS 24b, determined during the analysis of greenstones.

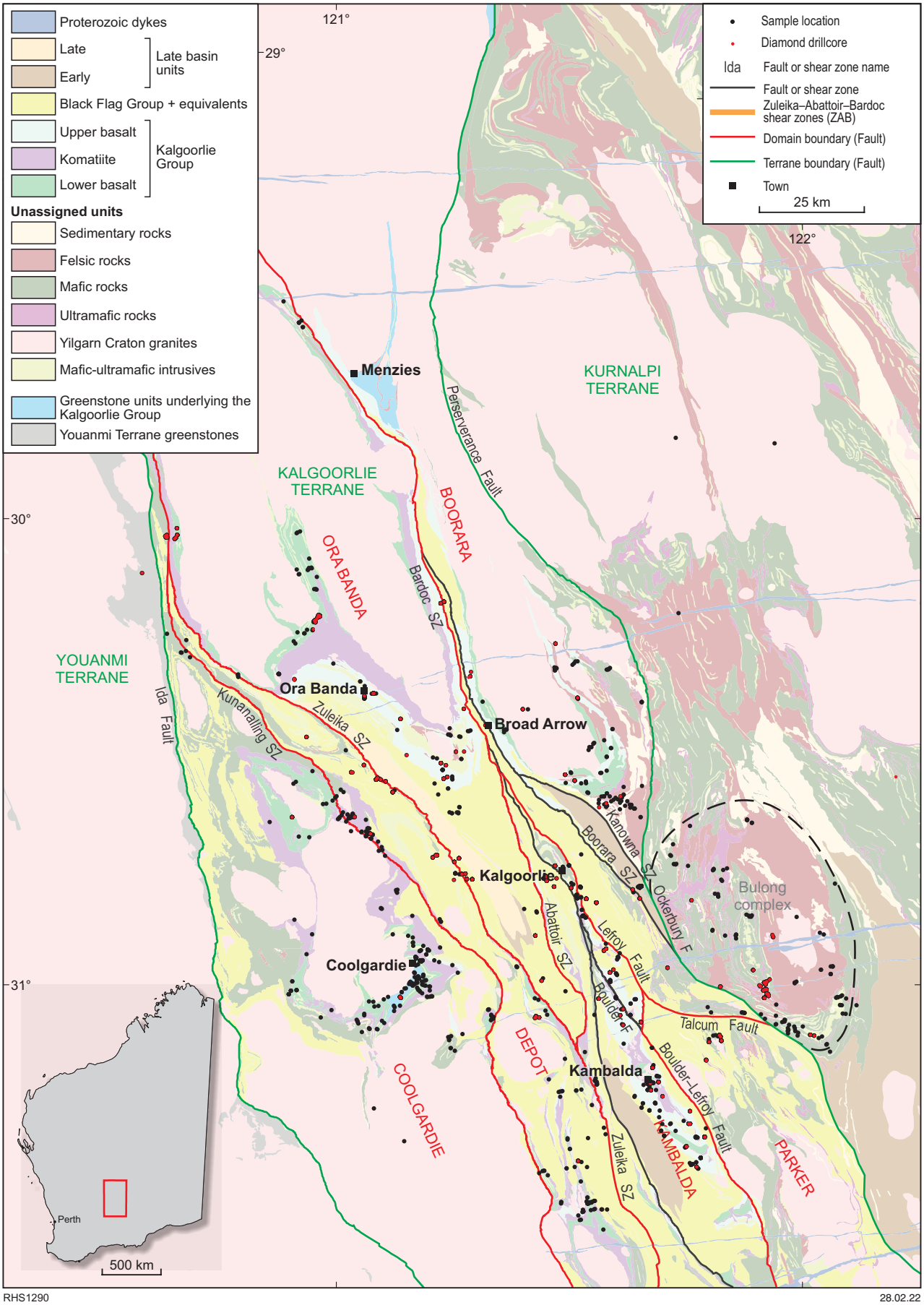

Figure 3. Geological map of the study area within the Kalgoorlie Terrane, showing a simplified version of the current interpreted bedrock geology, including the major faults and shear zones. Also shown is the distribution of sites where greenstones have been sampled for whole-rock geochemical data, including the locations for diamond drillcore. Diamond drillcore locations are typically the sites of multiple (up to 55) individual samples

Table 1. Number of samples from various regions

Domain	*Coolgardie*	*Depot*	*Coolgardie + Depot*	*Ora Banda*	*Boorara*	*Kambalda*	*Parker*	*Bulong (complex)*	*Totals*
Mafic volcanic samples									
Core	137	88	225	263	41	406	105	27	1067
Outcrop	127	110	237	69	57	28	12	63	466
Dolerite	19	41	60	25		143	1	27	256
Komatiite	35	71	106	18	11	114	16	41	306
Felsic samples									
Core	12	77	89	121	59	114	60	139	582
Outcrop	6	12	18	28	62	42	1	15	166
Total samples	336	399	735	524	230	847	195	312	2843

For analytes where the concentration is at least ten times the lower level of detection, a measure of accuracy is provided by the agreement between the average determined value and the certified value (Stanley and Lawie, 2007), which is <0.05 for all analytes, except Be and Cu. In terms of precision, the percent relative standard deviation or covariance for the analysis of OREAS 24b is <10 for all analytes, except As, Cu, Ni, Sc, and Zn. Similar levels of agreement were found for parent-duplicate pairs. All blank values were <3 times the lower level of detection.

Primary lithological classification and sample screening

For the classification and screening of rocks with broadly mafic to ultramafic compositions, we slightly modified the approach by Barnes et al. (2012). In particular, the maximum SiO_2 content used to identify rocks of broadly basaltic composition has been raised from 56 wt% to 57 wt%. This modification recognizes that even diamond drillcore samples from the Eastern Goldfields Superterrane, particularly in regions close to known mineralization, are commonly hydrothermally altered, often with significant effects on the concentrations of important major elements, such as SiO_2, CaO, Na_2O, and K_2O. Often, this alteration is not obvious during visual inspection of samples prior to selection for analyses. All samples taken as part of the greenstone geochemical barcoding project represent the visually least-altered examples of lithologically, texturally, and mineralogically homogeneous intervals of core. Nevertheless, it is not uncommon that one or more of a group of samples taken from within a lithologically uniform segment of drillcore has anomalous concentrations of SiO_2 (e.g. above the 56 wt% maximum value of Barnes et al., 2012) or other major elements, despite being visually indistinguishable from the associated samples. The approach used by Barnes et al. (2012) allows for the expansion of such parameters for classification of various basaltic rock types, as it primarily uses variations in ratios of incompatible trace elements (Ti, Th, La, Nb, Zr) that are relatively immobile during hydrothermal alteration and low- to medium-grade metamorphism, and are insensitive to small variations in major elements related to common igneous processes (e.g. fractional crystallization).

Since classification of the mafic rocks was based primarily on variations in ratios of fluid immobile trace elements, high loss on ignition (LOI) values were not used as a filter for strongly altered rocks. Nevertheless, >80% of our samples had LOI values <5 wt%.

All major element concentrations used and quoted throughout this Report have been recalculated on a volatile-free basis, although the differences with non-normalized data are typically insignificant.

The following screens and caveats were applied to the data:

- Intrusive rocks with SiO_2 <57 wt% and MgO <18 wt% were classified as dolerite or gabbro, depending upon their grain size. Those samples with MgO >18 wt% were classified as peridotite
- Non-intrusive rocks with SiO_2 <57 wt% were classified as basaltic, if MgO was <18 wt% and >3 wt% and komatiite, where MgO >18 wt%
- Many samples with MgO between 16 wt% and 18 wt% (and a few with MgO <16 wt%) have Al_2O_3/TiO_2 ratios ~20 (Al/Ti of ~1.0), a criteria Barnes et al. (2012) used to identify komatiitic basalts (KB). In nearly every case, these were directly associated, in drillcore, with true komatiites (olivine spinifex-textured rocks or rocks intimately associated with olivine spinifex-textured rocks) and have been classified as komatiitic basalt. In some cases, these formed a compositionally distinct series that extended to much lower MgO contents
- Intrusive rocks with SiO_2 >57 wt% were almost invariably plagioclase-porphyritic and were simply classified as felsic dykes [andesitic/dioritic (SiO_2 up to 63 wt%), dacitic/granodioritic (SiO_2 between 63 wt% and 68 wt%) or rhyolitic/granitic (SiO_2 between 68 wt% and 77 wt%)
- Rocks with SiO_2 >57 wt% and strong evidence for a volcanic and volcaniclastic origin were classified as felsic volcanic or volcaniclastic (andesitic, dacitic or rhyolitic) rocks
- Rocks with SiO_2 >57 wt% and no clear evidence for a volcanic and volcaniclastic origin were classified simply as felsic (andesitic, dacitic or rhyolitic) rocks
- Rocks with SiO_2 >57 wt% were initially excluded from the dataset if:
  - The aluminium saturation index [ASI = molar $Al_2O_3/(CaO+Na_2O+K_2O)$] exceeded 1.1 (i.e. the sample was peraluminous in many cases indicative of feldspar-destructive alteration)
  - SiO_2 exceeded 77.5 wt% (silica concentrations higher than values achievable through normal igneous processes; i.e. silicified)
  - Na_2O was <1 wt% or Na_2O+K_2O <3.5 wt% (values suggestive of alkali loss).

Mafic rocks

Identifying primary mafic geochemical groups

Having applied the screens described above, samples identified as basaltic were further divided into primary lithochemical groups, including low-Th basalt [LTB, a proxy for any light rare earth element (LREE)-, high field strength element (HFSE)-, and Th-poor basalts], intermediate-Th basalt (ITB), and high-Th siliceous basalt (HTSB) groups, as defined by Barnes et al. (2012) (Fig. 4). LTB, ITB, and HTSB groups, by definition, are typically distinguished on a plot of Th vs TiO_2. Although Th concentrations are generally more sensitive to contamination and fractionation, the fluid immobile and only slightly less incompatible elements, Zr, Nb, and La, can also be used to discriminate broadly similar low, intermediate, and high groups. Instances where the variation in one or more of these elements is slightly decoupled from the others provide potential means of further subdivision. Hence, some LTB groups identified because of their low Th, Nb, and La concentrations can have slightly high Zr concentrations that result in Zr/TiO_2 ratios within the range typical of ITB, rather than LTB. These would be separated as a Zr-enriched LTB group. Similarly, if anomalism is identified with Th, the result might be a Th-enriched LTB. If this is a persistent characteristic within a specific geographical region and/or at a specific stratigraphic level, then we define a LTB group with high-Th. Similar arguments apply for the identification of ITB. HTSB should be identified based on Th and La vs TiO_2 alone. We used all four trace elements (each plotted against TiO_2) to identify our primary mafic LTB and ITB groups. In cases where a sample plots in one field based on two elements and in another based on the other two elements, geological judgement is required to classify the sample. For example, the degree of alteration (visually or inferred from high LOI) compared to that of closely associated but less ambiguously classifiable samples might need to be considered. Likewise, whether a feature was an unusual or a persistent feature within a spatially or stratigraphically related series of samples might need to be considered. Although it is clearly feasible that a group of related samples could truly have perfectly transitional characteristics between LTB and ITB or ITB and HTSB, we have not yet identified any such cases.

Some samples classified earlier as komatiite based on having MgO >18 wt%, fall into the HTSB field in plots of TiO_2 vs Th, Nb, La, and Zr. These are clearly not komatiites based on their trace element patterns. Some could be fine-grained sills, although many show clear pillow structures, are closely associated in core with HTSB, and are interpreted here to reflect primitive HTSB lavas containing variably high proportions of olivine phenocrysts.

Some basalts with MgO generally between 10 wt% and 18 wt% and $Mg^{\#}$ [molar ratio of Mg/(Mg+Fe) where all Fe is calculated as Fe^{2+}] from 60 to 78 (higher than typical LTB), have Al_2O_3/TiO_2 ratios of ~20 but have concentrations of Th, Zr, Nb, and La considerably lower than that of HTSB (and mostly lower than LTB). These are typically directly associated with komatiites and are classified as komatiitic basalt.

Further subdivision of mafic geochemical groups

Primary mafic geochemical groups were further manually subdivided into smaller geologically plausible geochemical groups. This was an iterative process undertaken by simultaneously viewing the position of data points with respect to natural data clusters on plots of:

- TiO_2 vs Th, Nb, Zr, and La
- Th vs Nb and Zr
- Nb/Yb vs Th/Yb (Pearce, 2014)
- Al_2O_3/TiO_2 vs Th/Nb
- Mantle-normalized incompatible trace element diagrams
- $Mg^{\#}$ vs all major elements, Cr, Ni, and Al_2O_3/TiO_2
- Longitude vs latitude vs position in drillcore (a map).

Given the need to draw comparisons between numerous individually large data populations, many of the geochemical variation diagrams shown in this Report appear extremely cluttered (data rich), particularly at the presented scale. For this reason, most geochemical variation diagrams are also reproduced in Appendix 3 in a layered PDF format, which allows a user to enlarge the figure on screen and select specific geochemical unit(s) (each as separate layers) they wish to display.

Compositional variations in the plots listed (above) highlight the controls that various fundamental igneous processes and source compositional variations might have exerted on an evolving magma, and in the case of TiO_2, P_2O_5, and most of the selected trace elements, are not strongly influenced by post-magmatic alteration. Throughout this process, there is continuous consideration of critical factors, including whether:

- an observed geochemical trend or cluster plausibly reflects a rational geochemical/igneous process
- the identified trend- or cluster-related groups make sense in terms of spatial relationships (map patterns), clear and established geological features (textural, mineralogical, structural characteristics), and currently understood stratigraphic relationships. This does not mean that all members must be restricted to a single stratigraphic horizon in a single region. A geochemical grouping simply reflects a specific set of petrogenetic conditions, which might be reproduced at several stages in time and at several localities.

Mafic rock trends and units

The groups or units defined in this way, commonly show a degree of compositional overlap with other groups or units on one or many of the compositional variation diagrams, although each has either a compositional feature or a geographical distribution (or both) that allows it to be uniquely distinguished. A total of 26 units were identified (Table 2) and most of these were either LTB or ITB. These cannot be given stratigraphic names because in most cases they occur at several stratigraphic positions, even within a single subgroup stratigraphy. They also commonly form one of several distinct geochemical units that together form an established stratigraphic unit. For example, the Big Dick Basalt in the Vetters Subgroup comprises at least two distinct geochemical units and the Lindsays Basalt in the upper Coolgardie succession comprises at least three units.

Most of the basalt units were named primarily using plots of Th against TiO_2 and Th against Zr. The naming convention was constructed to emphasize the magmatic or petrogenetic history of the unit without any necessary implications in terms of direct

genetic relationships to other units. It is clear from the systematic data spread in bivariate plots utilizing incompatible trace elements that varying degrees of crustal contamination probably exerted the greatest control over compositional differences between the units identified here. The primary classification itself is based on increasing amounts of crustal contamination from LTB to ITB to HTSB; however, we added a secondary code that reflects the relative degrees of contamination of a specific unit within a given primary classification (Fig. 5). An additional code is added to indicate the relative extent of fractionation of a specific unit. Thus:

- For the primary classification descriptor:
  - LTB is denoted as 'L'
  - ITB is denoted as 'I'
  - HTSB is denoted as 'H'.
- The secondary measure of the amount of crustal material a mafic parental magma had incorporated was based broadly on the position of a unit in plots of Th vs TiO_2 and Th vs Zr, (with Th/TiO_2 and Th/Zr ratios increasing with increasing contamination) relative to the other units of the same primary classification, such that:
  - U = uncontaminated or nearly uncontaminated
  - C = contaminated
  - S = strongly contaminated
  - VS = very strongly contaminated.
- The degree of fractionation was a qualitative measure within each primary classification group for each specific secondary measure of contamination (e.g. L-S for strongly contaminated LTB) and was based on the concentration range of Th and Nb in each unit. For example, L-S1 had lower Th concentrations (was less fractionated) than L-S2, which was less fractionated than L-S3, and so on.

Hence, L-U5 would be an uncontaminated but strongly fractionated LTB whereas I-S2 would be a strongly contaminated but weakly fractionated ITB.

It is important to note that 10 of the 26 identified units could be combined to produce three distinct geochemical trends, each characterized by relatively constant incompatible trace element ratios. Variation between these various trends ranges from ratios between normal mid-oceanic ridge basalt (N-MORB) and primitive mantle values, reflecting very little or no crustal contamination, to ratios reflecting significant amounts of crustal contamination of the parental magmas. However, if we assume that the consistency of the ratios defining each of the three distinct geochemical trends is not fortuitous, then variation along the trends (element concentration) reflects closed-system fractionation.

Mafic groups, units and trends identified using the procedure outlined above (Figs 6–8) include:

- LTB
  - L-U1 and L-U2: two units of uncontaminated (or nearly uncontaminated) and relatively unfractionated primitive LTB, including one minor variant (L-U2*)
  - L-U3–7: five units of uncontaminated (or nearly uncontaminated) but moderately to strongly fractionated LTB, forming the L-U3–7 trend
  - L-Ca: a coherent unit of contaminated LTB showing a continuous fractionation trend that [except for a possible Zr-enriched variant (L-Cb)], cannot plausibly be divided into discrete units. L-Ca also forms the L-C* trend

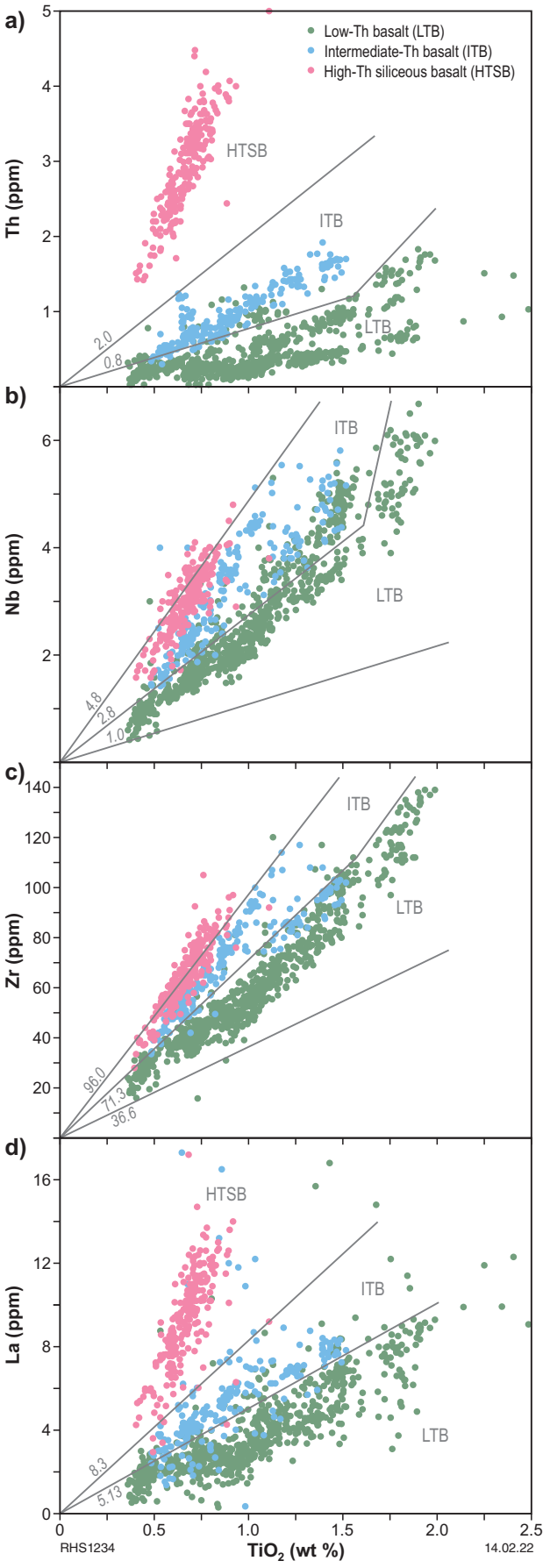

Figure 4. Variation in Th, Nb, Zr, and La with TiO_2 used for the primary classification of basalts into LTB, ITB, and HTSB (after Barnes et al., 2012). Numbers indicate the x/TiO_2 ratio of the lines chosen here to separate the various groups

  - L-S1 and L-S2: two units of strongly contaminated but relatively unfractionated LTB
  - L-S3a, L-S3b, and L-S4: three groups of strongly contaminated and strongly fractionated LTB.
- ITB
  - I-S1–3: three units of strongly contaminated and weakly to moderately fractionated ITB, forming the I-S1–3 trend
  - I-S4: a strongly contaminated and strongly fractionated ITB, but compositionally distinct from units of the I-S1–3 trend
  - I-VS: a very strongly contaminated but relatively weakly fractionated ITB.
- HTSB: By definition, all HTSB are strongly contaminated with crustal material. Three groups are recognized:
  - H-HMg#: HTSB with high Mg#
  - H-LMg#: HTSB with lower Mg#
  - H-LTh: HTSB with lower Th concentration compared with other HTSB.
- KB (Not shown in Figs 6–8)
  - Three units: KB1–3.

Table 2. List of mafic geochemical units identified and the corresponding symbols used in this Report

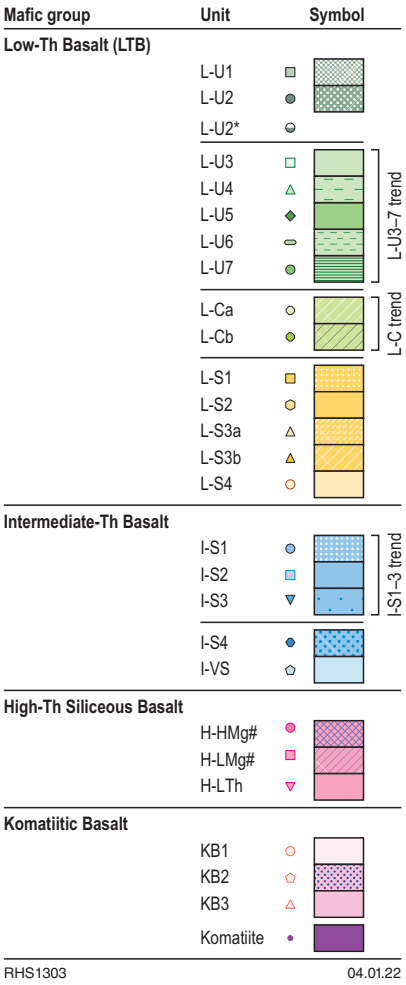

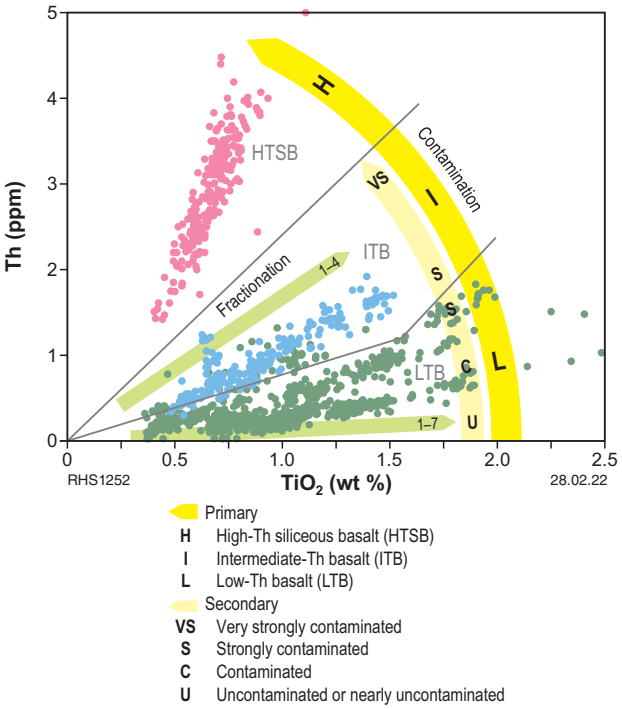

Figure 5. Variation in Th with TiO_2 used for classification of basalts (after Barnes et al., 2012) showing the rationale behind the system used to give unique codes to each specific mafic geochemical unit (see text for details)

A degree of caution should be exercised regarding discrimination procedures, such as the one outlined above, which utilizes trace elements typically present at concentrations approaching analytical detection limits. This is particularly the case for Th. Under these circumstances, it can be difficult to be certain that some of the typically more incompatible trace element-depleted groups are not simply artefacts of variation within the limits of analytical precision. In Figure 6, we show the estimated precision of analyses for Th, Nb, Zr, and La at very low concentrations, based on historical analytical results from BV Minerals (Champion et al., 2021). These uncertainties are generally small but clearly, at least in the case of Th, do potentially provide a plausible explanation for some of the compositional groups. However, we are confident that these groups are geologically meaningful for several reasons:

- The precision estimates are (only) indicative values based on analysis of a wide range of rock types and standards mostly with significantly higher concentrations of Th and Nb (for example). These estimates would almost certainly be improved, if calculated based only on samples and standards with very low concentrations.
- Mantle normalized incompatible trace element patterns (see later) are typically smooth between Th, which has a relatively high analytical uncertainty, and La and other LREE, which have a significantly lower analytical uncertainty; strongly suggesting that the analytical precision for Th is much better than the estimated values.
- The same groups are consistently identified and often well defined and on a wide range of compositional variation diagrams, including those using major element data at concentrations not subject to the same limitation in precision.
- Most of the groupings make geological sense in terms of their geographic and/or stratigraphic distribution.
- The compositional groups typically comprise samples from several different analytical batches.

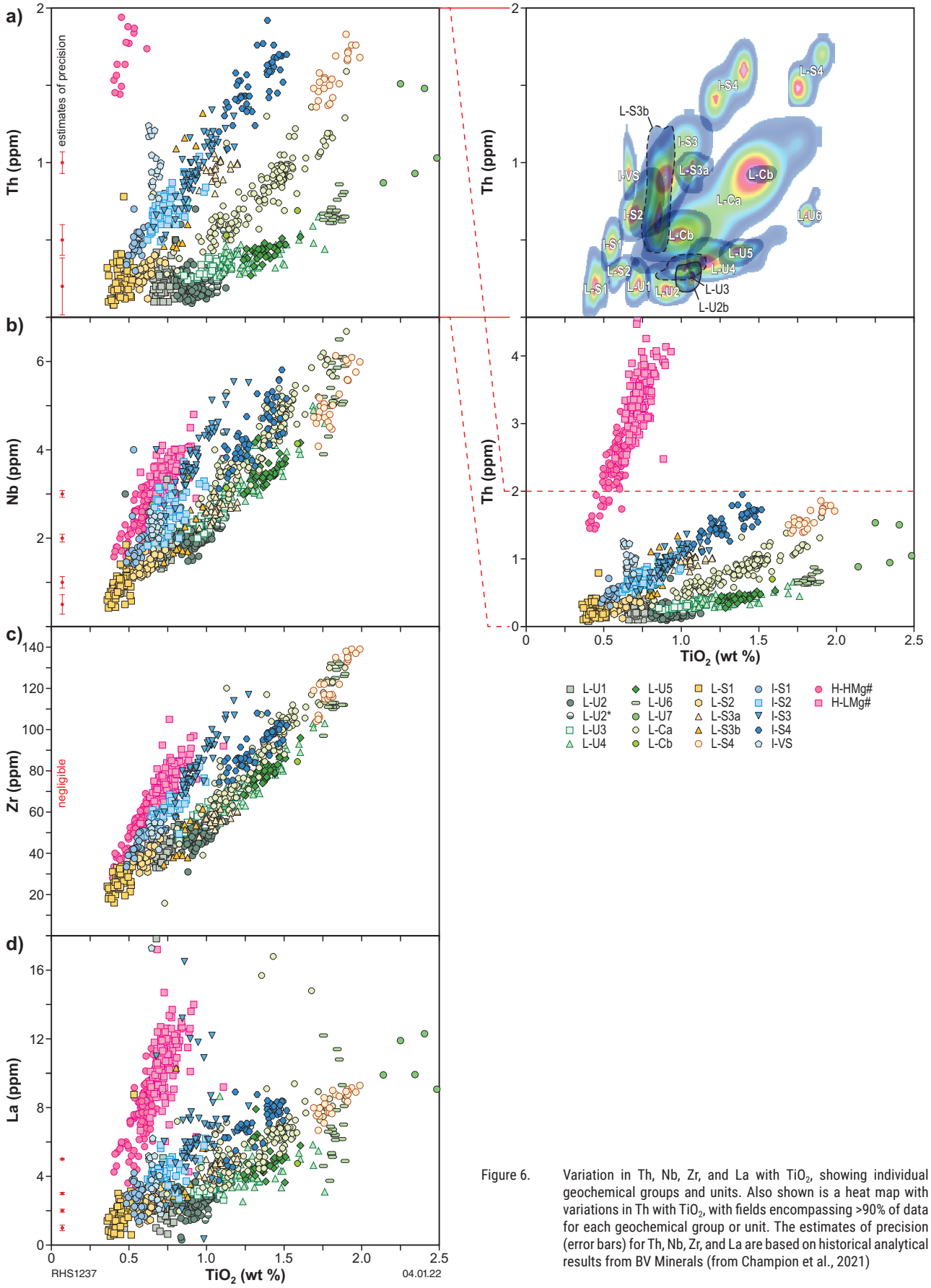

Figure 6. Variation in Th, Nb, Zr, and La with TiO_2, showing individual geochemical groups and units. Also shown is a heat map with variations in Th with TiO_2, with fields encompassing >90% of data for each geochemical group or unit. The estimates of precision (error bars) for Th, Nb, Zr, and La are based on historical analytical results from BV Minerals (from Champion et al., 2021)

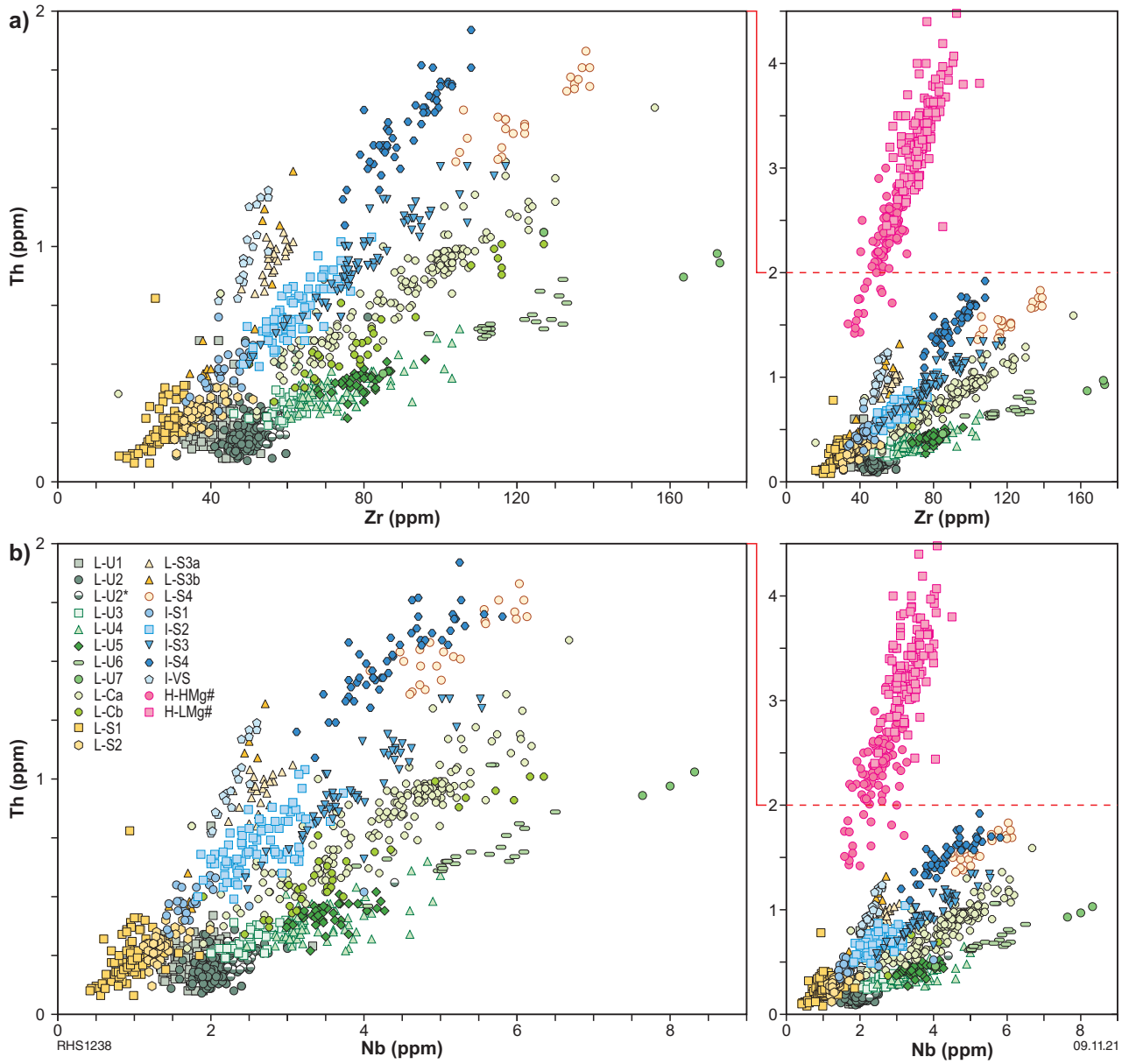

Figure 7. Variation in Th with Zr and Nb showing individual geochemical groups and units (right-hand panels are expanded to include data for the HTSB)

There is an additional problem, unrelated to the analytical issues outlined above, inherent in initially grouping basaltic magmas using the TiO_2 vs Th, Nb, Zr, and La diagrams. This is that for primitive (high $Mg^{\#}$, high MgO) magmas with very low concentrations of incompatible trace elements, the fields for LTB and ITB converge to the point where the classification becomes difficult to apply. Such compositions typically represent high degrees of mantle partial melting and are probably transitional to komatiitic basalts, if not actually komatiitic basalt. Two such groups encountered in this study are designated as L-S1 and L-S2 (Fig. 6).

Using the available stratigraphic information, we identified various geochemical components comprising the basaltic formations of the stratigraphic columns for regions broadly corresponding to each of the domains within the study region (Fig. 9). Within some of these regions, in particular, those corresponding with the Depot Domain, several areas show a local stratigraphy significantly different to the wider domain stratigraphy. These stratigraphic segments are discussed further in a following section. In general, however, the regional stratigraphies are divided into three levels (lower, middle, and upper) according to previous lithostratigraphic interpretations (e.g. Swager et al., 1990; Morris, 1993), which clearly correspond to broad but significant changes in the composition and style of magmatism (see later). Komatiite provides a convenient marker at the base of the middle level. We provide no information on the relative stratigraphic thicknesses of levels within each column. The dashed line shown in the upper part of the Coolgardie, Depot, and Ora Banda columns (Fig. 9) indicates that an upper stratigraphic level does not appear to have been developed or preserved (e.g. in the case of the Coolgardie Domain: e.g. Swager et al., 1990) or that the boundary between the middle and upper levels is unclear (e.g. for the Ora Banda Domain). Relatively low sample numbers mean that the chemostratigraphy for some parts of the Boorara and Parker Domains and the Bulong complex is less robust than for the regions to the west. For units where this might be of concern, the actual number of samples collected is indicated in Figure 9.

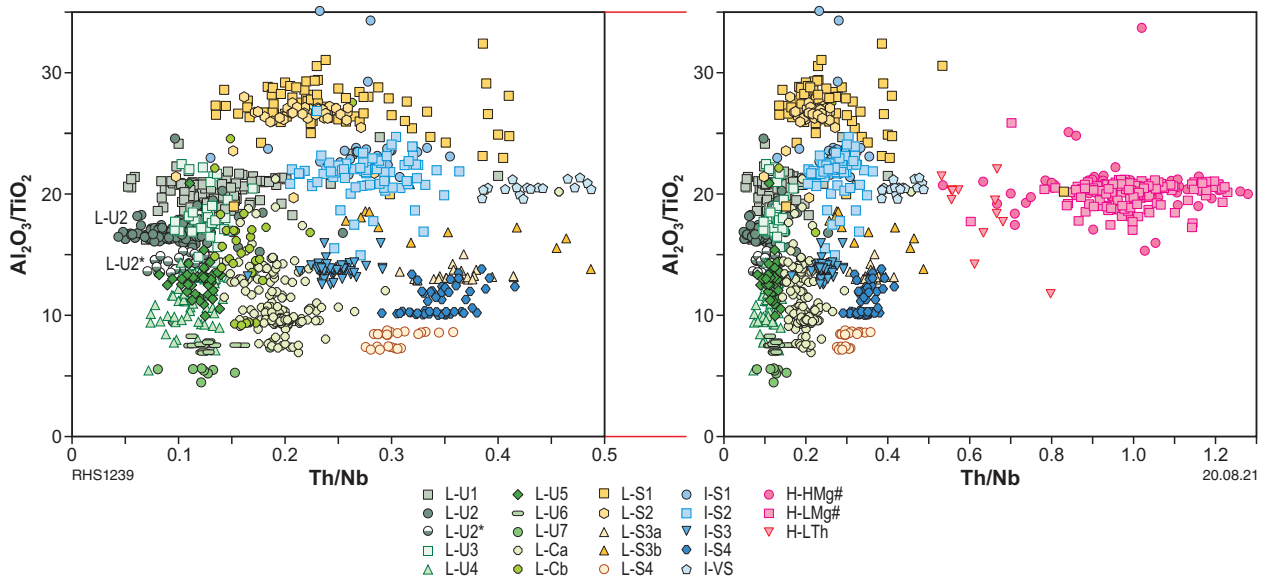

Figure 8. Variation in Al_2O_3/TiO_2 with Th/Nb showing individual geochemical groups and units (right-hand panel is expanded to include data for the HTSB)

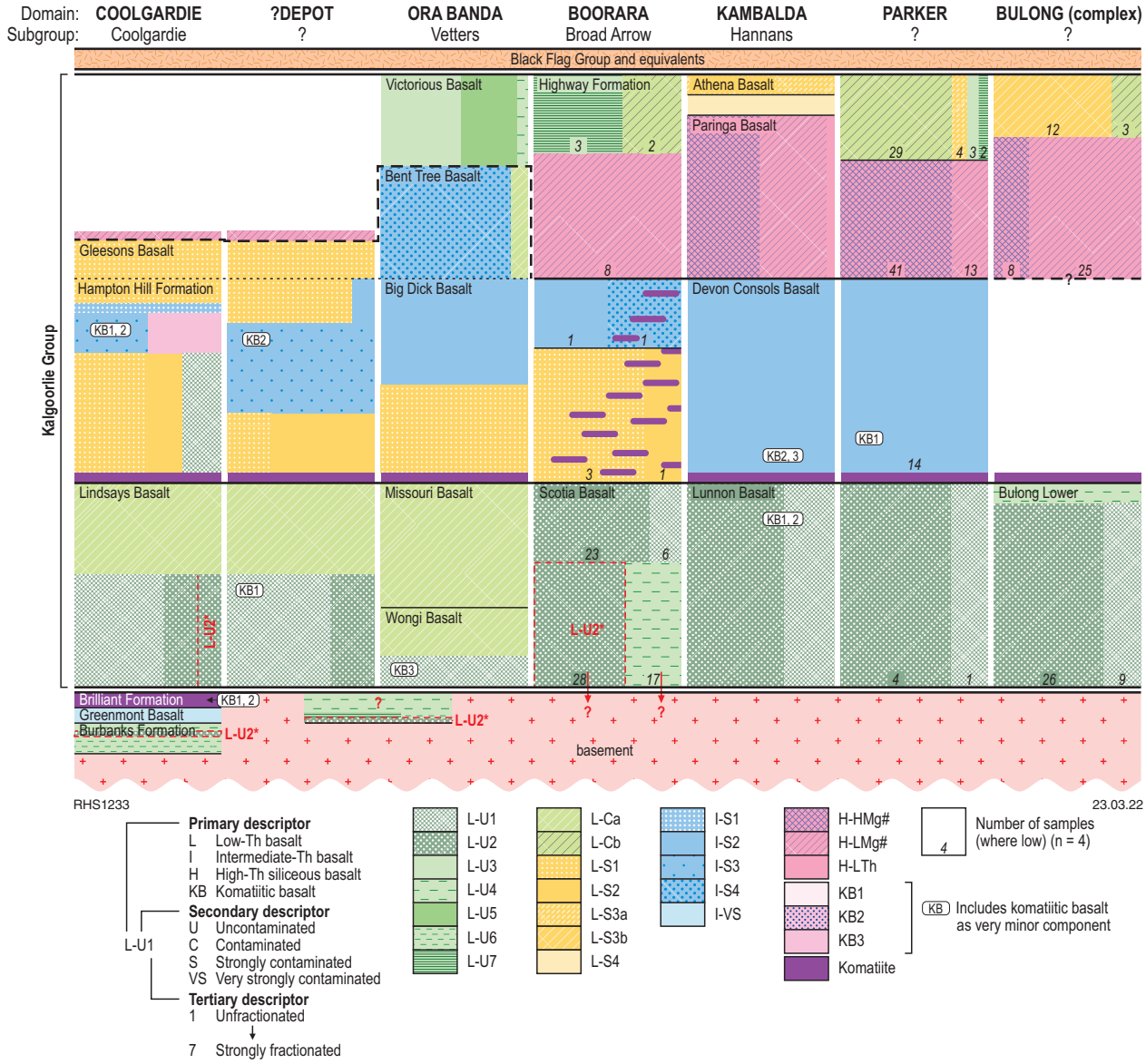

Figure 9. Chemostratigraphic columns representing each of the domain regions within the area studied. Also included is a brief graphical explanation of the coding system used. See text for further details and explanation

Otherwise, for each stratigraphic formation, the volume of each specific geochemical unit is proportional to the number of samples analysed. Whilst this might be broadly representative of true relative abundances in most cases, it is clearly open to sample bias. Where the relative position of geochemical units within a stratigraphic formation is known or reasonably inferred, those units are organized vertically. Otherwise, geochemical units within the stratigraphic formations are organized horizontally.

Low-Th basalts (LTB)

By definition, most of the LTB units have undergone relatively little contamination by compositionally evolved crustal material. Therefore, most have Th/Nb and La/Nb ratios close to primitive mantle values (Fig. 10). Even the most strongly contaminated LTB are typically less contaminated than most ITB units. The LTBs are tholeiitic basalts and the more primitive examples (less contaminated and less fractionated) represent the most common class of Archean mafic rock globally (Barnes et al., 2021). They can occur at all levels within a typical greenstone stratigraphy but in general, more contaminated and fractionated units occur at higher stratigraphic levels, dominantly as intrusions rather than volcanic rocks. Although they are classified based mainly on where they lie on plots of Th, Nb, Zr, and La against TiO_2, we found that the individual LTB units and trends are also well discriminated based on their Th/Zr ratios (Fig. 7a).

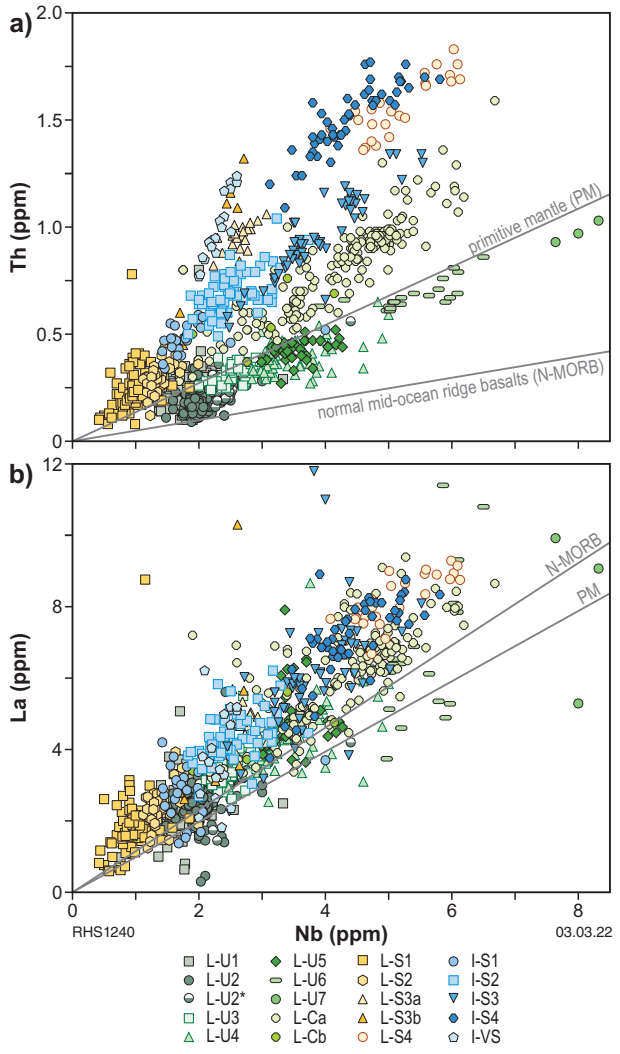

Figure 10. Variation in Th and La with Nb for individual LTB and ITB geochemical groups and units. Ratios for primitive mantle and mid-oceanic basalt (N-MORB) are from Sun and McDonough (1989)

An important finding from this work is that there are at least 12 major geochemically discrete LTB units within the study area. This represents a significant problem or source of serious misinterpretation when LTB compositions are erroneously regarded as synonymous with the Lunnon Basalt (the stratigraphic unit) or more broadly referred to as Lunnon-like. Similar problems arise regarding the Devon Consols Basalt and the ITB groups. Of the 12 LTB units, seven are L-U units but only two (L-U1 and L-U2) occur within the Lunnon Basalt. Hence:

- **LTB is not synonymous with Lunnon Basalt:** Only a basalt pile within the region between Kalgoorlie and Kambalda, comprising combinations of primitive L-U1 < L-U2 alone, overlain by komatiite and then by I-S2 (i.e. the Devon Consols Basalt), is Lunnon Basalt. Likewise, ITB is not synonymous with Devon Consols Basalt.

Primitive LTB (L-U1 and L-U2)

Primitive L-U1 and L-U2 typically include a large proportion of samples with higher $Mg^{\#}$ (>50) and correspondingly high MgO contents and Cr concentrations (>200 ppm) than other LTB units (Fig. 11). They typically show very restricted ranges in incompatible trace element concentrations and at a given $Mg^{\#}$, have lower incompatible trace element concentrations than all other magmas, except for the L-S1 and L-S2 units. As with the other L-U units, they have low Th/TiO_2 and high Zr/Th ratios reflecting least-contaminated compositions. Some examples have compositions consistent with derivation from a mantle source slightly more depleted than primitive mantle, approaching that of modern N-MORB source. Many samples also show only a minimal or no perceptible mantle-normalized Nb anomaly. L-U2 have slightly lower $Mg^{\#}$ and slightly lower Th/Nb, Th/La, and Th/Zr ratios than L-U1 (Figs 7, 11; Appendix 4), indicating that neither fractional crystallization nor crustal contamination (alone or together) can directly genetically relate the two units.

Discriminating primitive L-U1 and L-U2

On most compositional variation diagrams, L-U1 shows significant compositional overlap only with L-U2 but can be uniquely identified by its lower TiO_2 (<0.8 wt%) (Fig. 11) and unique position with respect to all other LTB units on a plot of Al_2O_3/TiO_2 vs Al_2O_3 (L-U1 = 18.3–22.5) (Fig. 12). L-U2 can be separated on a plot of Al_2O_3/TiO_2 vs Al_2O_3 (L-U2 mostly 13–18) from other LTB units except L-Ca and L-S3 (a and b), which show a minor overlap but can all be uniquely separated from L-U2 on a plot of Th vs TiO_2. (Fig. 6a).

L-U2 can be subdivided based on slight differences in Al_2O_3/TiO_2 ratio (Figs 8, 12a). A main group has Al_2O_3/TiO_2 ratios from 16 to ~18, whilst a minor group (denoted L-U2* where a distinction is required) has ratios from 13 to 16. No other systematic difference is noted between the two populations, although L-U2* has a specific geographical coverage (see below).

Like L-U1 and L-U2, L-S1 and L-S2 have very low incompatible trace element concentrations but can be clearly identified by their unusually high Al_2O_3/TiO_2 (mainly >25) (Fig. 8).

Distribution of primitive L-U1 and L-U2

Primitive L-U1 and L-U2 are geochemically distinctive and widespread, forming a significant component of the basalt stratigraphy (Figs 9, 13). They appear mainly restricted to the basal basalt units of each stratigraphic sequence, including the lower and upper Coolgardie successions, lying immediately below the main komatiite layer. Exceptions are L-U1 samples taken from the lower

levels of the komatiitic Hampton Hill Formation, although these could be from tectonic slices of Lindsays Basalt. The subsidiary L-U2* population includes all L-U2 samples from the Burbanks Formation in the lower Coolgardie succession. It also includes >50% of L-U2 sample of the Scotia Basalt at the base of the Broad Arrow Subgroup, forming what appears to be the stratigraphically lowest samples around the southern flank of the Nine Mile Monzogranite in the Scotia–Kanowna Anticline. Samples of L-U2* form scattered occurrences in the Ora Banda Domain near Davyhurst, immediately east of the Zuleika Shear Zone, and these are potentially age equivalents of the Burbanks Formation.

Fine-grained L-U2 also occurs stratigraphy above (Bent Tree Basalt) and below (Big Dick Basalt) the Mount Pleasant Gabbro (sill) in the Vetters Subgroup, but in these cases are almost certainly quenched marginal intrusions related to the Mount Pleasant Gabbro itself, which comprises 76% L-U2 compositions (Table 3). L-U2 forms a significant component of other major mafic sills (e.g. Condenser and Golden Mile Dolerites) (Table 3) emplaced at the end of or immediately after mafic greenstone deposition.

While both L-U1 and L-U2 occur throughout the study region, there is a clear tendency for L-U1 to be the dominant primitive L-U unit in the western domains (Coolgardie/Depot and Ora Banda Domains) while L-U2 is slightly more common to the east. L-U2 is almost twice as common as L-U1 in the Lunnon Basalt (Hannans Subgroup), locally forming the entire formation. However, where accompanied by L-U1, neither is confined to any specific stratigraphic interval within the formation (L-U1 and L-U2 can be interlayered). Similarly, L-U1 is twice as abundant as L-U2 in the Lindsays Basalt at the base of the upper Coolgardie succession.

L-U3–L-U7 and L-U3–7 trend

L-U3–L-U7 are more evolved (fractionated) than L-U1 and L-U2, although they show a similar, negligible, degree of crustal contamination. Near-constant incompatible trace element ratios (Th/Zr, Th/Nb, Nb/Zr, La/Sm; Fig. 14) that extrapolate to or close to the origin (x=0, y=0) in compositional variation diagrams, define a common bulk parental composition with most trace element ratios around or slightly lower than primitive mantle values. The constant incompatible trace element ratios also indicate that all subsequent compositional evolution of these magmas was essentially by crystal fractionation alone, in a system closed to further contamination. The concentrations of most strongly incompatible trace elements overlap between many of the units forming the L-U3–7 trend. However, the degree of enrichment in incompatible trace elements broadly follows the order L-U3 to L-U7, reflecting a general increase in the degree of crystal fractionation. On bivariate plots employing TiO_2, the straight incompatible trace element trends break down at TiO_2 concentrations above ~1.7 wt% (Figs 4, 6), as FeTi oxides become saturated and join the fractionating mineral assemblages. Only L-U6 and L-U7 reach such high TiO_2 contents.

It is important to note that the consistent incompatible trace element ratios shared by units of the L-U3–7 trend only indicate that each individual unit was derived from a compositionally similar source and suffered no later crustal contamination, not that they were necessarily directly genetically related to each other or to a common magma batch. The wide overlap in $Mg^{\#}$ between the units combined with significant variations in Al_2O_3 and Al_2O_3/TiO_2 (Figs 11, 12) suggests that plagioclase fractionation (removal or accumulation) was a major control on trace element enrichment or depletion. Commonly, the upper volcanic L-U3–L-U5 units contain conspicuous plagioclase phenocrysts, megacrysts, and glomerophenocrysts.

Discriminating units of the L-U3–7 trend

There are significant compositional overlaps between the various units forming the L-U3–7 trend, although combinations of various plots uniquely distinguish each unit. All of the units are completely distinct from all ITB units in a plot of Th vs TiO_2 (Fig. 6a).

L-U3 has low incompatible trace element concentrations that overlap those of L-U2 on most plots. However, L-U3 has a higher Al_2O_3 content (>17.5 wt%, e.g. Fig. 12). In any case, primitive L-U2 has not been found within the same stratigraphy as L-U3. Higher Al_2O_3 and lower TiO_2 (hence higher Al_2O_3/TiO_2) also distinguishes L-U3 from other units in the L-U3–7 trend (Fig. 12).

L-U4 has the broadest range of incompatible trace element concentrations within the L-U3–7 trend, with extensive overlap with L-U5 but occupies a unique field from all other L-U units on plots of Al_2O_3/TiO_2 vs Al_2O_3 or TiO_2 (Fig. 12). An exception includes very minor overlap with L-U2*, although the latter can be separated based on its slightly lower Nb concentrations (L-U2* <2.75 ppm <L-U4).

L-U5 shows extensive overlap only with L-U4 in terms of incompatible trace element concentrations, but also occupies a unique field on plots of Al_2O_3/TiO_2 vs Al_2O_3 or TiO_2 (Fig. 12).

L-U6 and L-U7 are effectively discriminated from the other units of the L-U3–7 trend units by their high (L-U6 = 1.75–1.9 wt%) and very high (L-U7 = >2.0 wt%) TiO_2 contents (e.g. Fig. 12).

Distribution of units of the L-U3–7 trend

Samples from various units of the L-U3–7 trend are considerably less abundant overall than those of the primitive L-U1 and L-U2 units (Fig. 15). They are not found within the upper Coolgardie succession or the Hannans Subgroup, although quenched intrusive equivalents of L-U4 and L-U5 related to the intrusion of the Golden Mile Dolerite form a minor component of the Black Flag Group overlying the Hannans Subgroup.

Units of the L-U3–7 trend occur in the Burbanks Formation of the lower Coolgardie succession (L-U4 and L-U6) and, more commonly, in the uppermost part of the basalt-dominated greenstone stratigraphy of the Vetters Subgroup (Victorious Basalt: L-U3, 4, and 5) and the Highway Formation (L-U7).

The more incompatible trace element-enriched and plagioclase-poor (lower Al_2O_3) L-U6 unit occurs only in the Burbanks Formation of the lower Coolgardie succession. However, strongly fractionated L-U7 occurs in several major mafic sills (Condenser Dolerite, Golden Mile Dolerite, Mount Pleasant Gabbro; Table 3) emplaced at the end of mafic greenstone deposition. The less incompatible trace element-enriched but plagioclase-rich (higher Al_2O_3) units (L-U3–5) mostly lie in the upper parts of the stratigraphy and form a significant component of late gabbro sills. However, L-U4 is associated with L-U6 in the Burbanks Formation and is found in the Scotia Basalt at the base of the Broad Arrow Subgroup (Fig. 9).

Contaminated LTB–L-C

This contaminated LTB unit covers a broadly similar major and compatible trace element compositional range to the units forming the L-U3–7 trend (Fig. 11), although it is characterized by higher values of incompatible trace element ratios such as Th/Nb, Th/Zr, La/Sm, and La/Yb (Fig. 16). As inferred from a plot of Th vs TiO_2 (Fig. 6a), ranges in these ratios reflect the significant effect of crustal contamination (assimilation) on the composition of primitive L-C basalts.

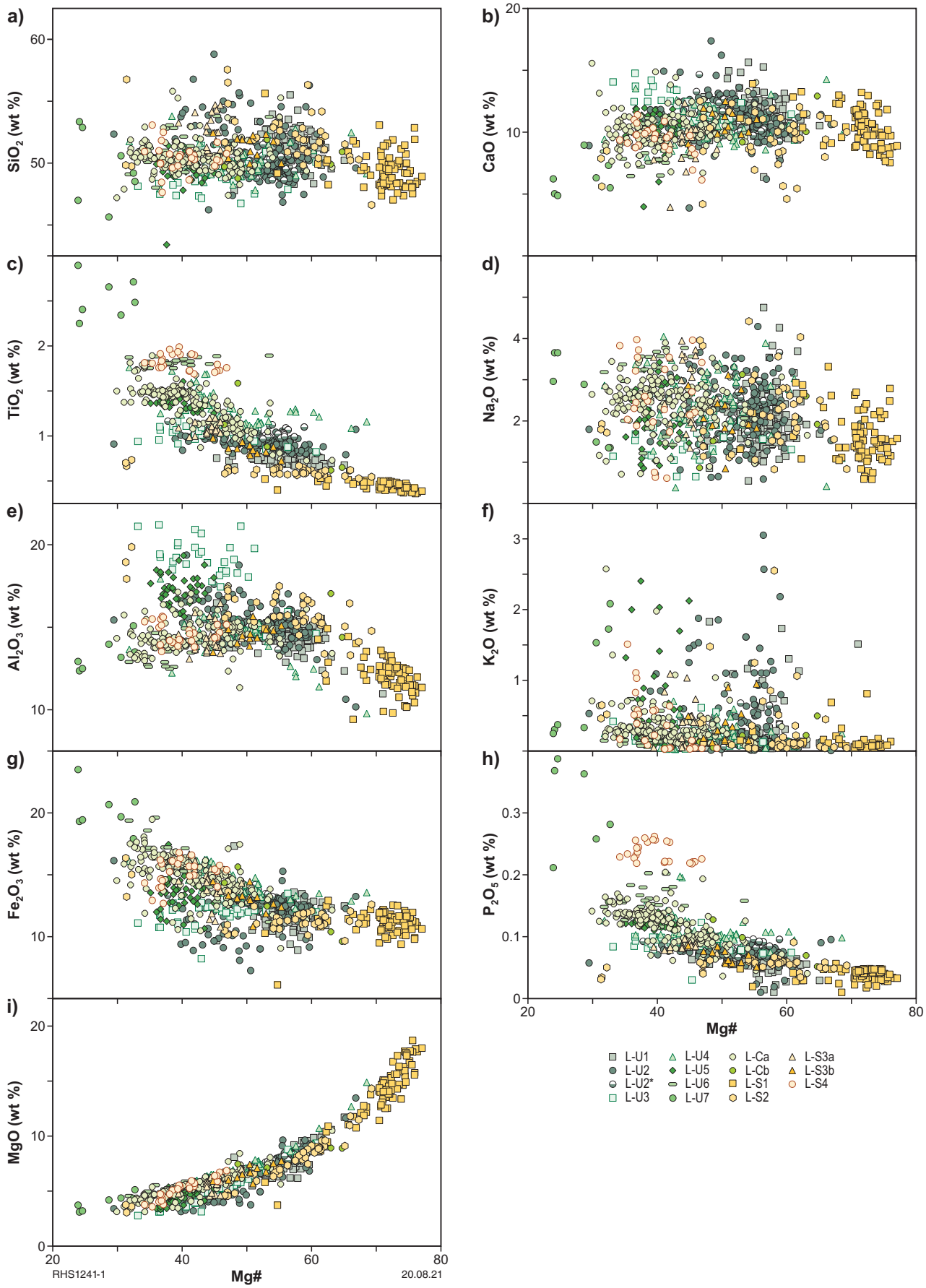

Figure 11. Variation in major and selected trace elements with Mg# for individual LTB geochemical groups and units

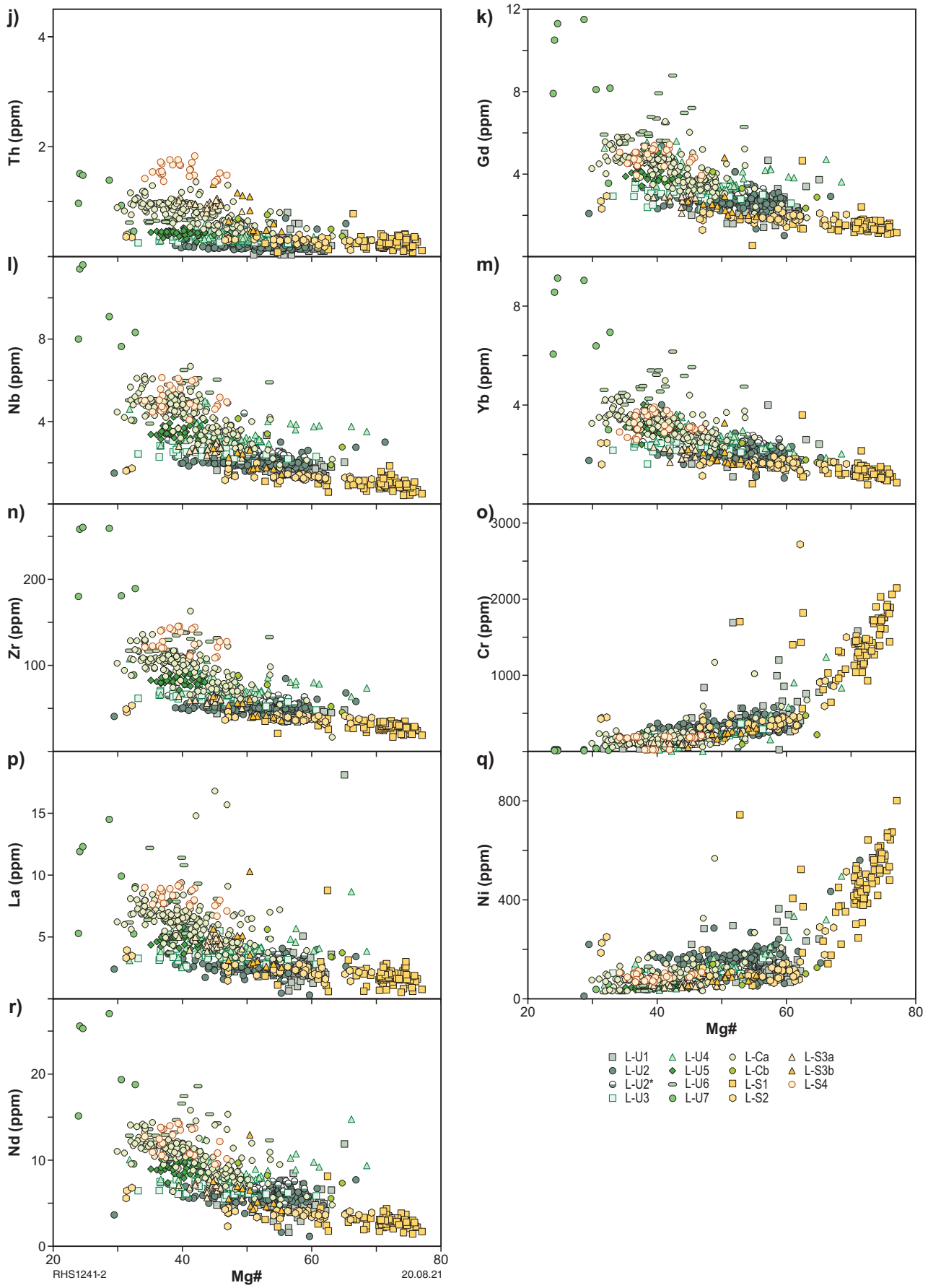

Figure 11. continued

A potential subset of the main unit (L-Cb) is identified based on low Th concentrations and consequently low Th/Nb and Th/Zr ratios, consistently within (or below) the lowest end of the range for L-Ca. L-Cb also has La/Sm ratios that scatter at higher values than those of L-Ca and shows a much wider and correlated range to lower $Mg^{\#}$ (65 to 21) and higher SiO_2 (49.6 to 57.2 wt%) (Fig. 11).

Discriminating L-C

Most diagrams plotting co-variation of two strongly incompatible trace elements effectively discriminate L-C units from other LTB units (Fig. 16). Plots of Th vs TiO_2, Nb, and Zr appear most effective. L-Ca and L-Cb are probably best distinguished from each other on a plot of SiO_2 vs $Mg^{\#}$ or La vs Sm.

Distribution of L-C

Although L-C is common and widespread throughout much of the western part of the study region, it does not occur within the Kambalda Domain (Hannans Subgroup) (Fig. 17). L-Ca broadly corresponds to an enriched basalt unit first identified by Hayman et al. (2015), who noted that it was primarily restricted to the region to the west and north of the Kambalda Domain. There seems to be a strong association with primitive L-U1 and together, these units dominate the lower part of the upper Coolgardie succession and the lower Vetters Subgroup (Wongi and Missouri Basalts) (Fig. 9). Although less common, L-Ca also forms a component in the upper part of the Vetters Subgroup (Bent Tree Basalt). L-Cb forms a minor component in the upper parts of the Broad Arrow Subgroup and in the upper parts of the Bulong complex and Parker Domain stratigraphy. It is restricted to the regions east of the Coolgardie/Depot and Ora Banda Domains (referred here as the 'eastern domains').

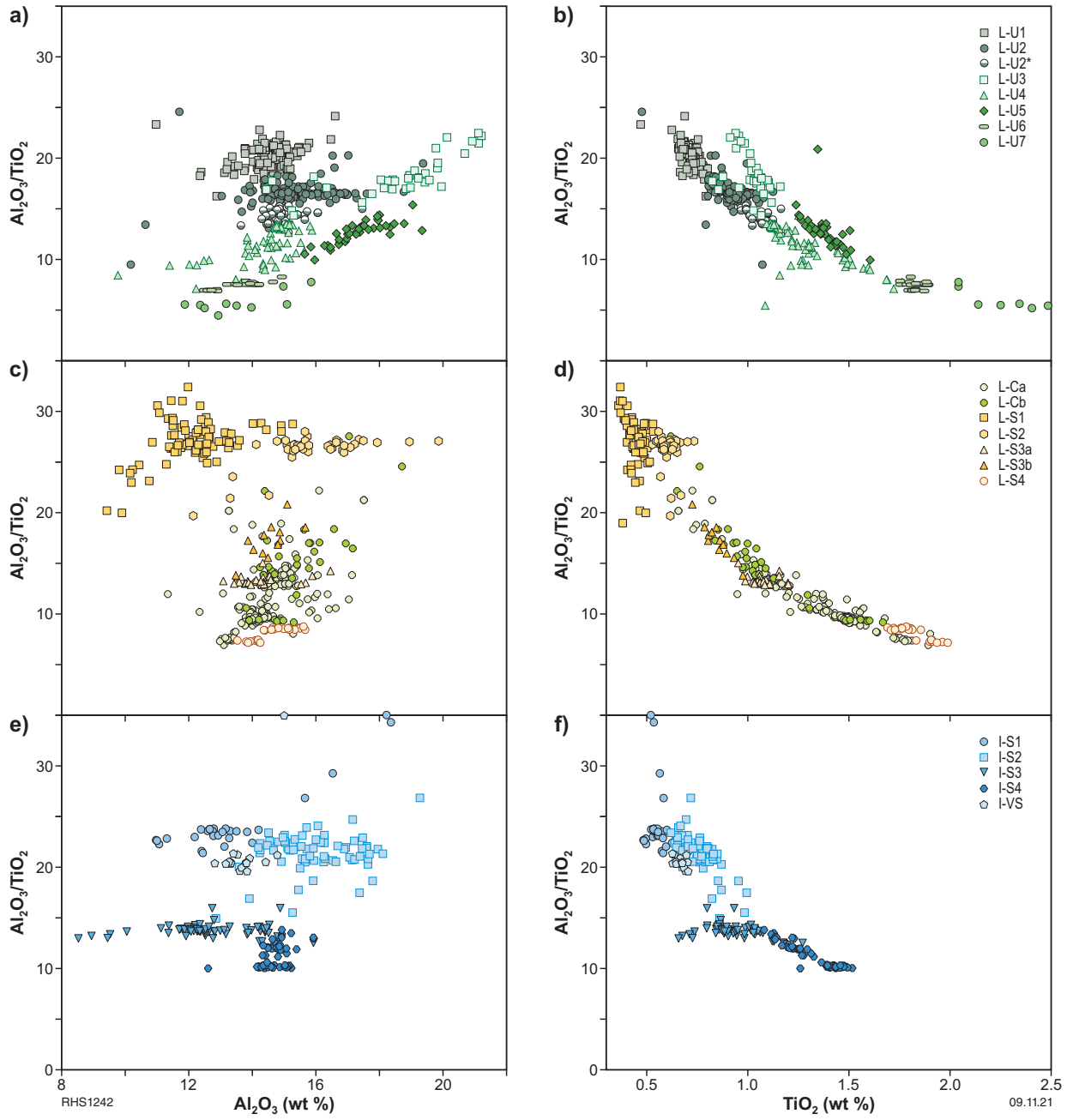

Figure 12. Variation in Al_2O_3/TiO_2 with Al_2O_3 (left-hand column) and Al_2O_3/TiO_2 with TiO_2 (right-hand column) for individual LTB and ITB geochemical groups and units

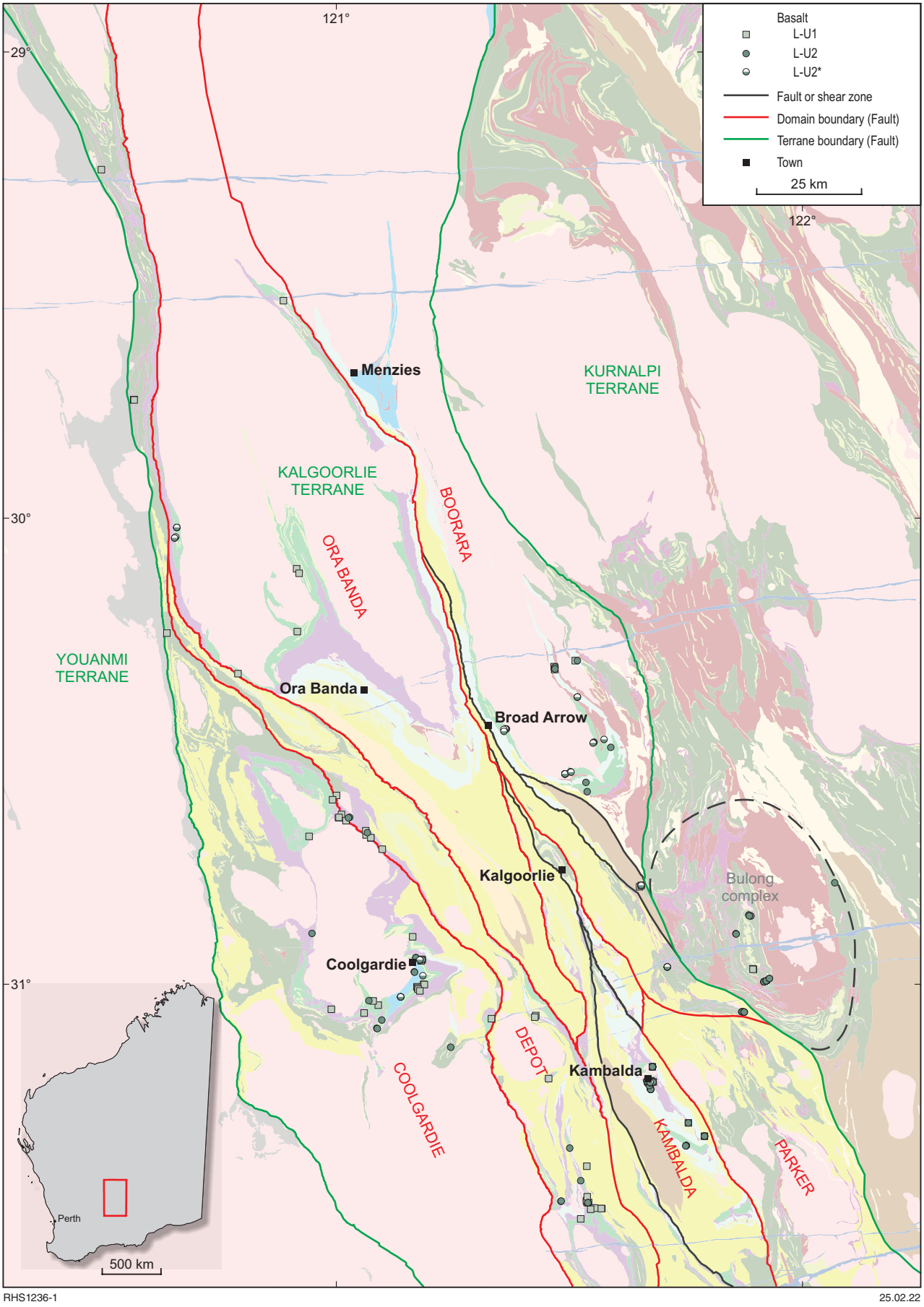

Figure 13. Geological map of the study area within the Kalgoorlie Terrane, showing a simplified version of the current interpreted bedrock geology and the distribution of primitive L-U geochemical units (see Figure 3 for fault names)

Table 3. Geochemical units and relative abundance within selected major mafic intrusions

Intrusion		*L-U1*	*L-U2*	*L-U4*	*L-U5*	*L-U7*	*L-C*	*L-S3*	*L-S4*	*H-HMg#*	*H-LMg#*
Condenser Dolerite	(n=28)	7%	11%	57%		21%	4%				
Golden Mile Dolerite (GMD)	(n=100)		32%	26%	37%	2%	2%		2%		
Gabbroic GMD	(n=85)		31%	27%	40%	2%					
Basaltic GMD in the Black Flag Group	(n=21)		42%	29%	29%						
Mount Pleasant Gabbro	(n=40)	3%	71%	5%	18%		3%				
Oak Hill Gabbro	(n=17)									41%	59%
Powder Gabbro	(n=23)									43%	57%
Stony Hill Dolerite	(n=19)	16%	52%	5%	11%			16%			
Three Mile Dolerite	(n=17)						100%				
Triumph Gabbro	(n=6)			33%	17%	50%					

Strongly contaminated LTB–L-S

L-S units are tentatively grouped as LTB magmas, but compared with other LTB magmas, show higher Th/TiO_2, Th/Nb, and Th/Zr ratios (Figs 6a, 16), interpreted to reflect very high degrees of crustal contamination. As discussed earlier, L-S1 and L-S2 are so depleted in incompatible trace elements that it is difficult to determine, if they relate to either LTB or ITB bulk sources. Although the most primitive members do appear to originate in the LTB field, they extend to higher $Mg^{\#}$ (77 and 69 respectively) and Ni and Cr concentrations than all other LTB (Fig. 11) and most ITB, with I-S1 being the only ITB unit having similarly primitive compositions. In most bivariate incompatible trace element diagrams, L-S1 appears to lie at the primitive extension of the ITB I-S1–3 trend and the L-C trend (Figs 6, 16), suggesting it might be a primitive member of either trend, and in this respect possibly an ITB. The common stratigraphic association of L-S1 and L-S2 with ITB units and L-Ca (Fig. 9) supports either relationship. Plots of various incompatible trace elements against $Mg^{\#}$ (Fig. 18) show trends suggesting that L-S2 is simply fractionated L-S1 magma.

L-S3 (a and b) and L-S4 are minor units that are also transitional to ITB in terms of Th/TiO_2 ratio but are more clearly LTB in terms of TiO_2 vs Zr and Nb (Figs 6a, 16). They are all restricted to the upper basaltic parts of the stratigraphy, although there is no indication that they are petrogenetically related to each other, and probably derive their high Th/Zr character through different processes. L-S4 shows very strong enrichments in P_2O_5, TiO_2, Fe_2O_3, and in all incompatible trace elements (Fig. 11) and has compositional features resembling strongly fractionated tholeiitic magmas that locally form granophyric portions of intrusions. It is possible that this unit represents the local eruption of highly evolved magmas from a fractionating subvolcanic mafic sill similar to, for example, the Golden Mile Dolerite, although the extreme enrichments in Th are difficult to explain without an additional process. Such a process might include the assimilation of high-Th country rock or mixing with high-Th magmas.

L-S3a, which is entirely equivalent to the Athena Basalt, is less evolved than L-S4 and shows closer similarities with L-U and L-Ca units on all plots that do not involve Th. L-S3b shares very similar compositions with L-S3a but also shows considerably greater scatter in data.

Discriminating L-S

A plot of Al_2O_3/TiO_2 vs Th/Nb (Fig. 8) collectively distinguishes L-S1 and L-S2 from all other basaltic units, with L-S1 and L-S2 effectively separated from each other based on TiO_2 concentration (L-S1 <0.54 wt% TiO_2 <L-S2). The Al_2O_3/TiO_2 vs Th/Nb plot also uniquely identifies L-S3a, L-S3b, and L-S4 (based on Al_2O_3/TiO_2 range) from all basalt units except for I-S4, which can be uniquely separated from the L-S units on a plot of Th vs Zr (Fig. 16b).

Distribution of L-S

L-S1 forms the main component of the lower part of the Big Dick Basalt in the Vetters Subgroup. However, the main concentration of L-S1 and L-S2 is in the Coolgardie and Depot Domains. L-S2 is almost exclusively restricted to a small area in the eastern Depot Domain (A in Fig. 17), where it appears to be part of the lower basaltic component interleaved with komatiite (e.g. in BDDD0017). In the Coolgardie Domain (upper Coolgardie succession), L-S1 forms part of the upper basaltic section of the Hampton Hill Formation and is the sole component of the Gleesons Basalt, and appears to occupy a similar stratigraphic position in the Depot Domain (Fig. 9).

L-S3 (a and b) and L-S4 are minor units found only in the eastern part of the studied region in the Hannans Subgroup (L-S3a and L-S4) and Bulong complex stratigraphy (L-S3b) (Figs 9, 17), where they occur in the uppermost parts of the basalt-dominated stratigraphy. In the Hannans Subgroup, L-S3a overlies L-S4 and both are localized between the Paringa Basalt and the Black Flag Group.

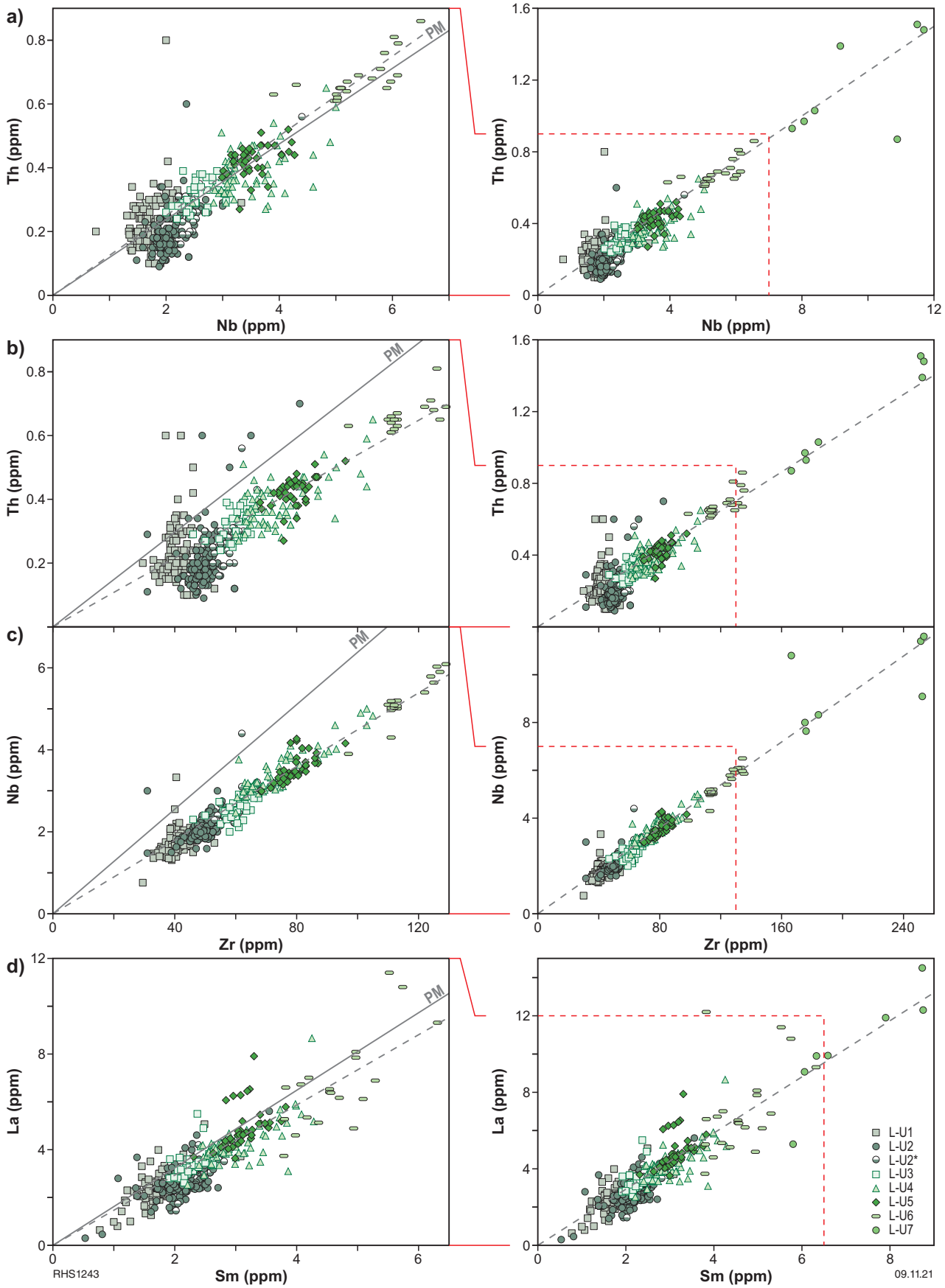

Figure 14. Variation in Th with Nb, Th and Nb with Zr and La with Sm for individual LTB geochemical groups and units (left-hand columns are expanded views)

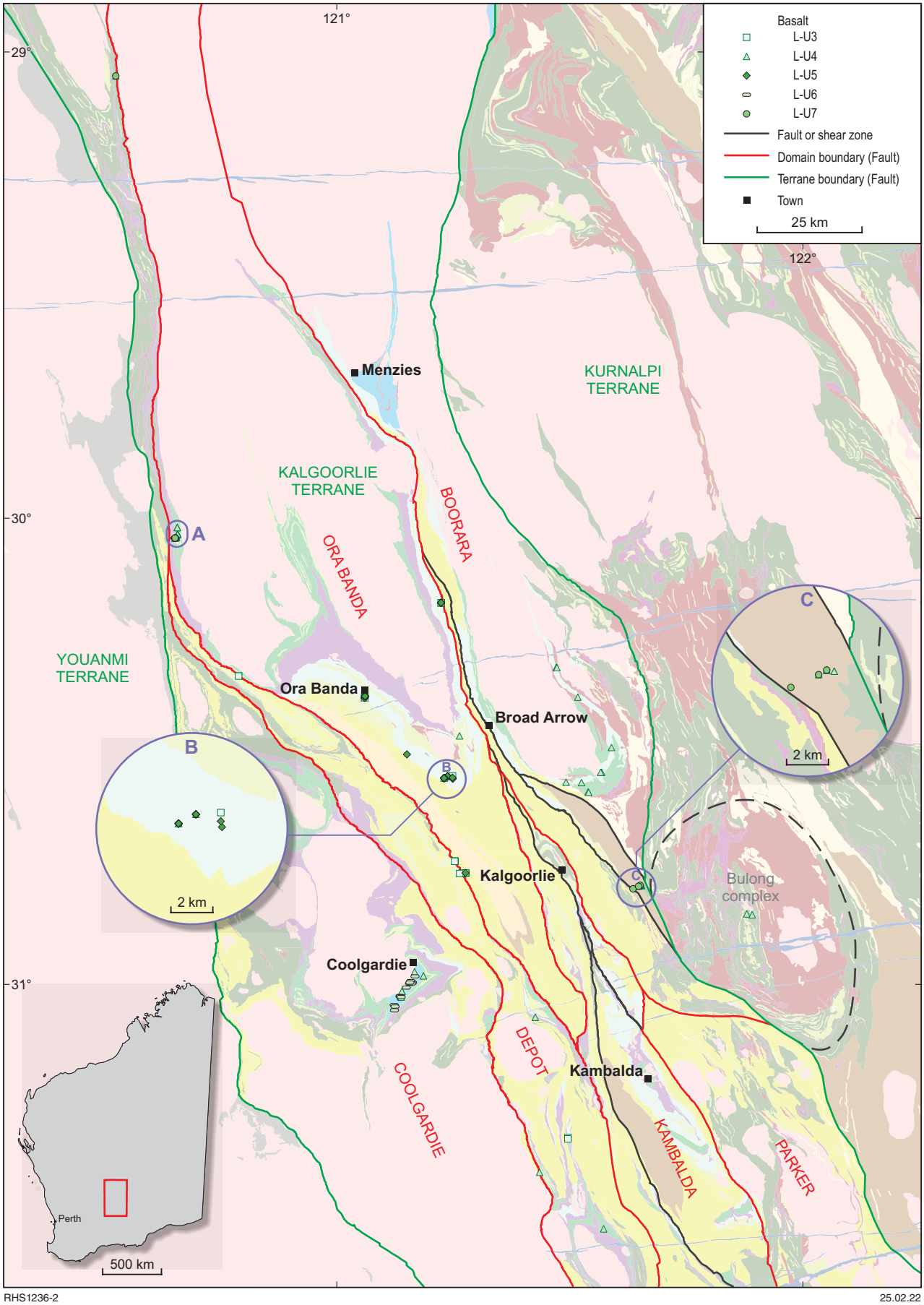

Figure 15. Geological map of the study area within the Kalgoorlie Terrane, showing a simplified version of the current interpreted bedrock geology and the distribution of L-U3 to L-U7 geochemical units (see Figure 3 for fault names)

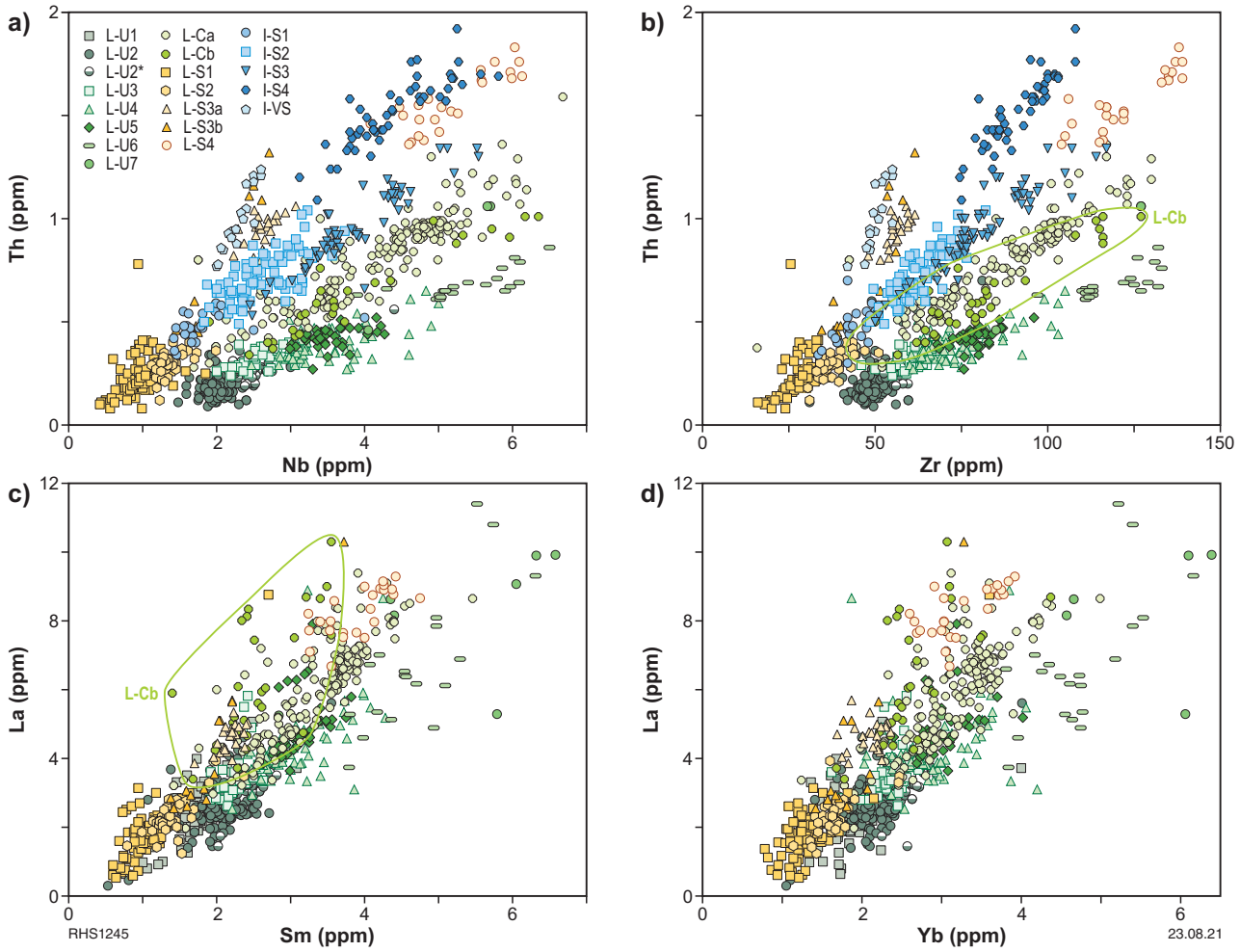

Figure 16. Variation in Th with Nb, Th with Zr, La with Sm, and La with Yb for individual LTB and ITB geochemical groups and units. Green line in b) and c) outlines the fields for L-Cb

Intermediate-Th basalts (ITB)

ITB cover a broadly similar major element compositional range as LTB, except in the case of P_2O_5, which at a given $Mg^{\#}$ is generally higher in abundance in ITB than in most LTB (Fig. 19). However, ITB groups seldom include samples with $Mg^{\#}$ <45, whereas several LTB units are dominated by such evolved samples. Conversely, samples of LTB with $Mg^{\#}$ >~62 (and MgO >10 wt%) are very rare, whereas the range for ITB extends to high-Mg basalts with $Mg^{\#}$ ~71 (MgO ~14.7 wt%). L-S1 has $Mg^{\#}$ as high as 77 (MgO to 17.9 wt% although some of these are probably partial olivine cumulates), although it is unclear whether these are LTB or ITB. Nevertheless, this highlights the possibility that some or most ITB might be derived through the fractionation of ultramafic (komatiitic) magmas (i.e. are really komatiitic basalts) rather than being direct basaltic melts of the mantle.

ITB by definition are typically significantly more enriched in incompatible trace elements, and have higher Th/Nb, La/Nb, and La/Sm ratios than most LTB at a given $Mg^{\#}$ (Fig. 20), suggesting the ITB magmas have incorporated a slightly greater amount of crustal material. As with the LTB, although the concentrations of incompatible trace elements increases with decreasing $Mg^{\#}$ (Fig. 19), the range in incompatible trace element ratios (La/Sm, La/Yb, Th/Nb, La/Nb) remains relatively constant (Fig. 20). This indicates that the addition of any crustal material to parental magmas has occurred before significant magmatic differentiation, which itself is controlled by minerals with very low incompatible trace element concentrations (e.g. olivine, pyroxenes, and plagioclase). Incompatible trace element plots show that the ITB form trends that extrapolate to primitive compositions more depleted in incompatible trace elements than the most primitive LTB units (L-U1 and L-U2), and similar to L-S1 (Fig. 7).

Discriminating ITB units

ITB units occur in the middle parts of all well-characterized stratigraphies (Fig. 9), although they have compositionally unique characteristics in each case. A plot of Th vs TiO_2 (Fig. 6a) serves to discriminate ITB units from LTB units and a plot of Al_2O_3/TiO_2 vs Th/Nb (Fig. 8) discriminates between most of the individual ITB units. However, I-S1, I-S2, and I-S3 consistently form continuous incompatible trace element trends (I-S1–3 trend). As with the L-U3–7 trend, it is possible that these relationships reflect the varying degrees of fractionation (I-S1 least fractionated, I-S3 most fractionated) of magmas sharing very similar bulk source compositions. They can be broadly separated based on their increasingly enriched character. However, I-S1 has a lower TiO_2 content (<0.6 wt%) than I-S2 (0.6–1.0 wt%), whereas I-S3 has a distinctly lower Al_2O_3/TiO_2 (<15 cf. >20) than both I-S1 and I-S2, as a result of plagioclase fractionation (Fig. 12).

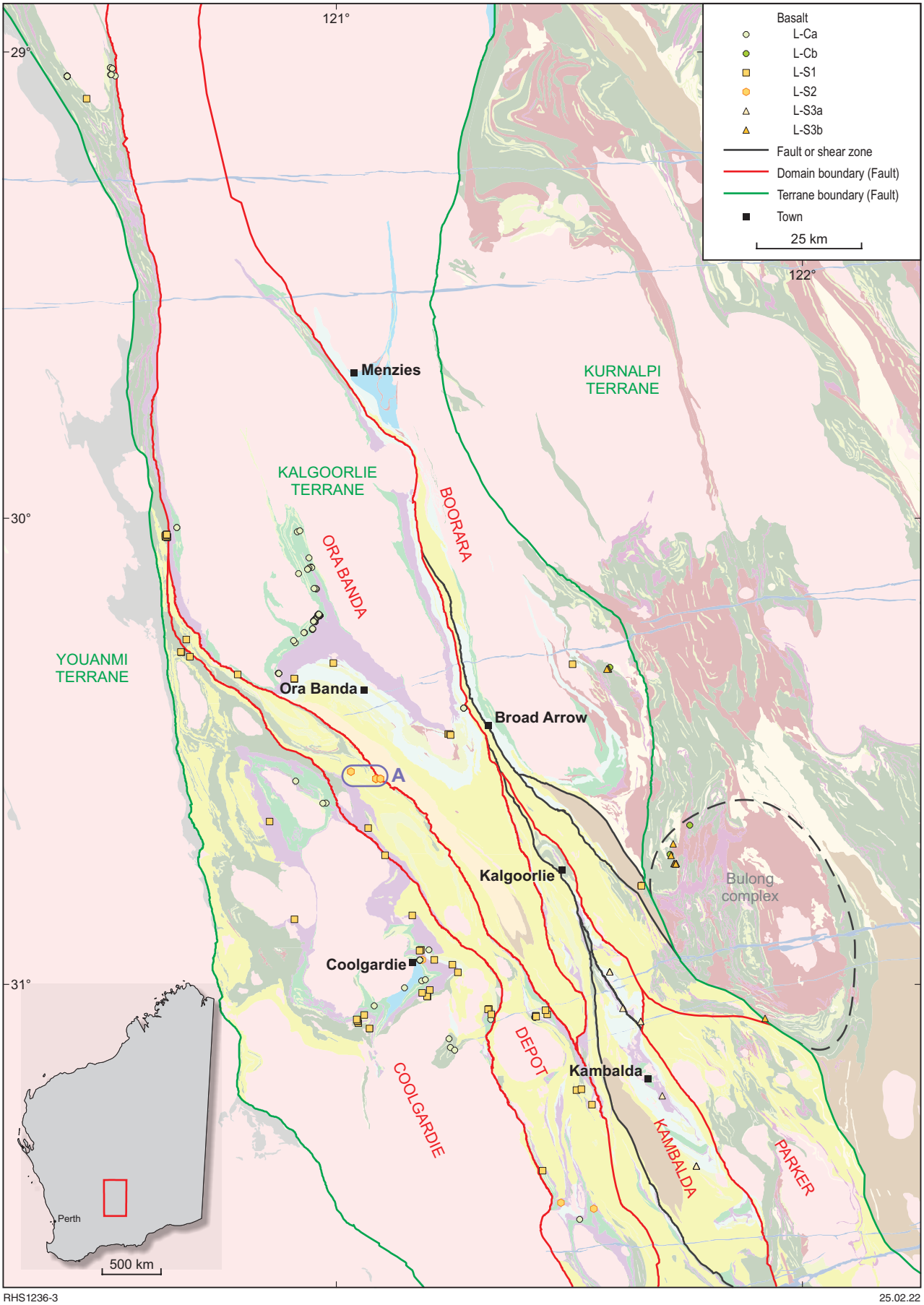

Figure 17. Geological map of the study area within the Kalgoorlie Terrane, showing a simplified version of the current interpreted bedrock geology and the distribution of L-C and L-S geochemical units (see Figure 3 for fault names)

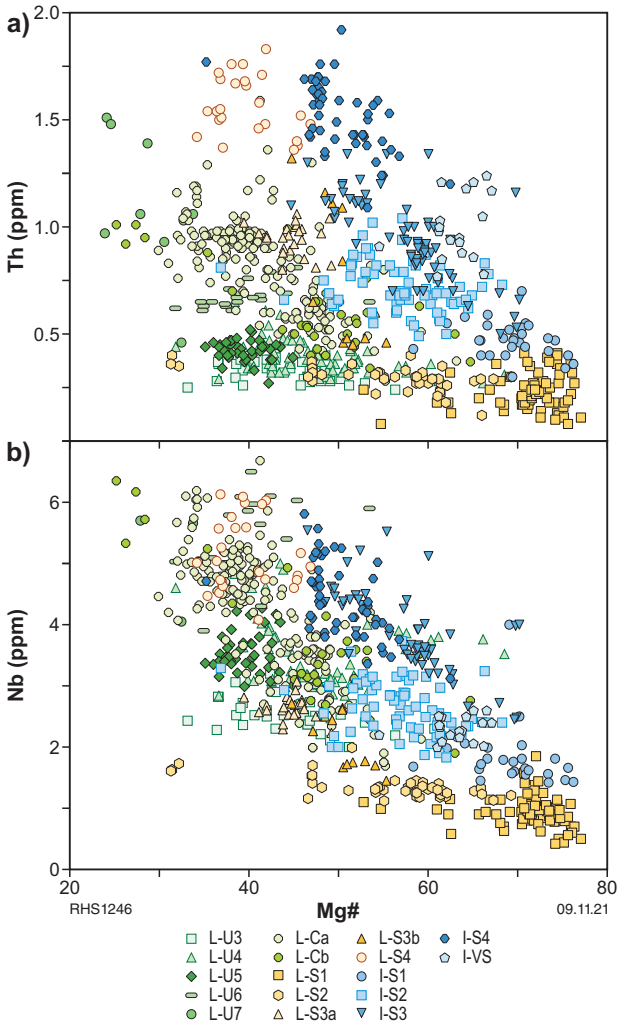

Figure 18. Variation in Th and Nb with Mg# for individual LTB and ITB geochemical groups and units

I-S4 falls at the enriched end of the I-S1–3 trend for some incompatible trace elements, but is a TiO_2-enriched (TiO_2 >1.13 wt%) unit readily distinguishable from other ITB and LTB by its combination of high Th concentration (>1 ppm) and moderately low Zr/Th ratio (median 0.017) (Figs 6a, 7). Like contaminated LTB units, such as L-S4, and uncontaminated units, such as L-U6 and L-U7, I-S4 shows many of the strongly fractionated tholeiitic compositional attributes typical of granophyre.

On many trace element variation diagrams, particularly those involving Th and La, I-VS shows trends towards low-Th outliers of HTSB (i.e. the H-LTh unit) and the komatiitic basalt unit KB3 (Fig. 21). Likewise, it has an MgO-rich composition (MgO 8.5–12.0 wt%; Mg# 67–61). The enrichment patterns that clearly distinguish I-VS reflect a scale of crustal contaminant similar to that required within HTSB. I-VS is best discriminated geochemically from H-LTh and KB3 by its unique position in plots of Zr or Y vs Th (slightly lower Th/Zr and Y/Th ratios). It is not known to be stratigraphically associated with these units or with any HTSB units.

Distribution of ITB units

The ITB are widely distributed throughout most of the study area (Fig. 22), although less commonly in the Boorara Domain and Bulong complex. Most commonly, they occur in the middle basaltic portions of the stratigraphy, overlying or in the upper portions of the komatiite-dominated stratigraphic levels (Fig. 9). I-S1 and I-S3 together dominate the basaltic component of the Hampton Hill Formation in the upper Coolgardie succession and in the stratigraphy of the Depot Domain. I-S2 is the dominant component of the Devon Consols Basalt in the Hannans Subgroup and in the upper part of the Big Dick Basalt in the Vetters Subgroup. I-S4 is the main component of the Bent Tree Basalt in the upper part of the Vetters Subgroup and is unique to that formation. Similarly, I-VS is unique to the Greenmont Basalt in the lower Coolgardie succession and the sole component of that formation.

High-Th siliceous basalts (HTSB)

The HTSB are perhaps the most geochemically distinctive mafic unit within the study region. Compared with LTB and ITB, the HTSB are characterized by higher Th/TiO_2 and La/TiO_2 ratios in particular, slightly higher Nb/TiO_2 and Zr/TiO_2 ratios (Fig. 6), and higher concentrations of Th and LREE at a given Mg# (but similar concentrations of Nb and Zr) (Fig. 23). They also show higher (and constant) ratios of Th and La against Nb and Zr (i.e. larger negative Nb anomalies) (Fig. 21), and higher SiO_2 contents at a given Mg# (Fig. 23). Such features reflect significant early contamination by particularly Th- and LREE-enriched crust. The other notable feature of HTSB is their generally very primitive composition with Mg# as high as ~77 (MgO ~21.7 wt%), likely reflecting derivation from an ultramafic parental magma. In both respects, these are similar to I-VS.

We have used an apparent gap in the Mg# range to subdivide HTSBs into:

1. A unit with Mg# between 63 and 78 (H-HMg#)
2. A unit with Mg# between 43 and 62 (H-LMg#)
3. A unit with low Mg# and consistently lower concentrations of Th (H-LTh).

Both H-HMg# and H-LMg# include examples of pillowed lavas. Therefore, the apparent break in the range of Mg# clearly does not simply reflect the distinction between lavas (lower Mg#) and cumulate intrusions (higher Mg#). However, the range to high Mg# (i.e. >70) and MgO >18 wt% in H-HMg# requires those lavas to include a significant cargo of olivine phenocrysts. It is also possible that many samples of H-HMg# that do not show clear indications of an extrusive origin are indeed cumulate or partial cumulate intrusions.

The petrogenesis of HTSB is less understood than that of LTB- and ITB-type basalts, probably reflecting the range of processes that can potentially achieve such enriched primitive compositions (e.g. Barnes et al., 2021), and also because the distinction between HTSB, KB, and primitive LTB and ITB can be very difficult. Barnes and Arndt (2018) and Barnes et al. (2021) use a plot of Al/Ti vs Mg# (Fig. 24) to distinguish komatiitic basalts derived through high-pressure fractionation (not involving plagioclase) of komatiitic magmas, from typical tholeiitic basalts. The tholeiites are believed to have been generated directly in the mantle as primary high-Mg basaltic partial melts that subsequently undergo low-pressure fractionation involving plagioclase. Most HTSB suites show high, mantle-like, Al_2O_3/TiO_2 ratios (~20), signifying little or no plagioclase fractionation) over much of their range in Mg#. Hence, their enriched compositions have been attributed to early contamination of komatiitic magmas in deep crustal chambers where pressures were too high to stabilize plagioclase. HTSB taken from the study area likewise show a remarkably constant Al_2O_3/TiO_2 ratio ~20.3 across a wide range of Mg# (from 77 to 54). Subsequent decreases in Al_2O_3/TiO_2 ratio to values as low as 17 at Mg# around 45 can be related to plagioclase fractionation and scattered values higher than 20 probably reflect plagioclase accumulation.

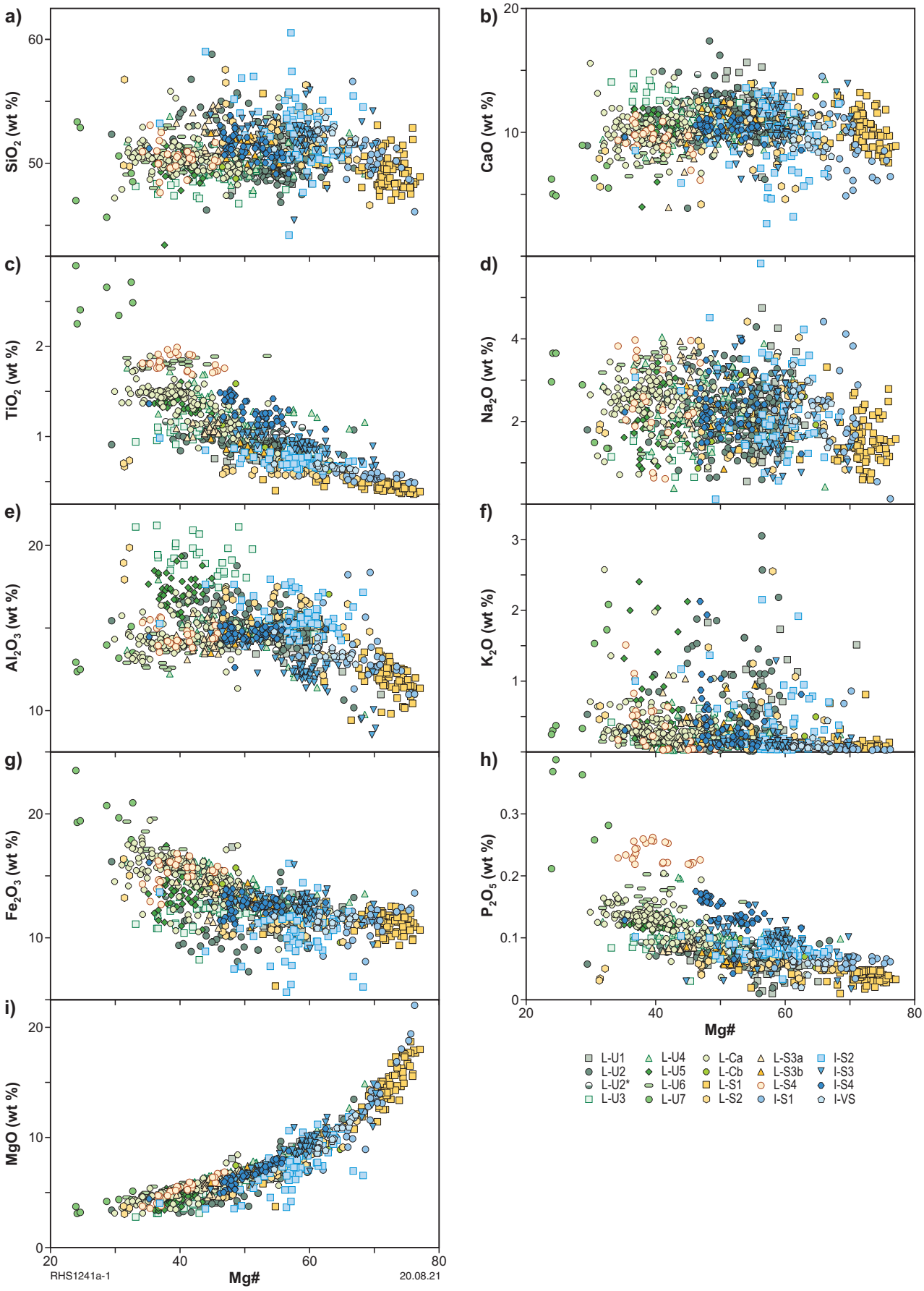

Figure 19. Variation in major and selected trace elements with Mg# for individual LTB and ITB geochemical groups and units

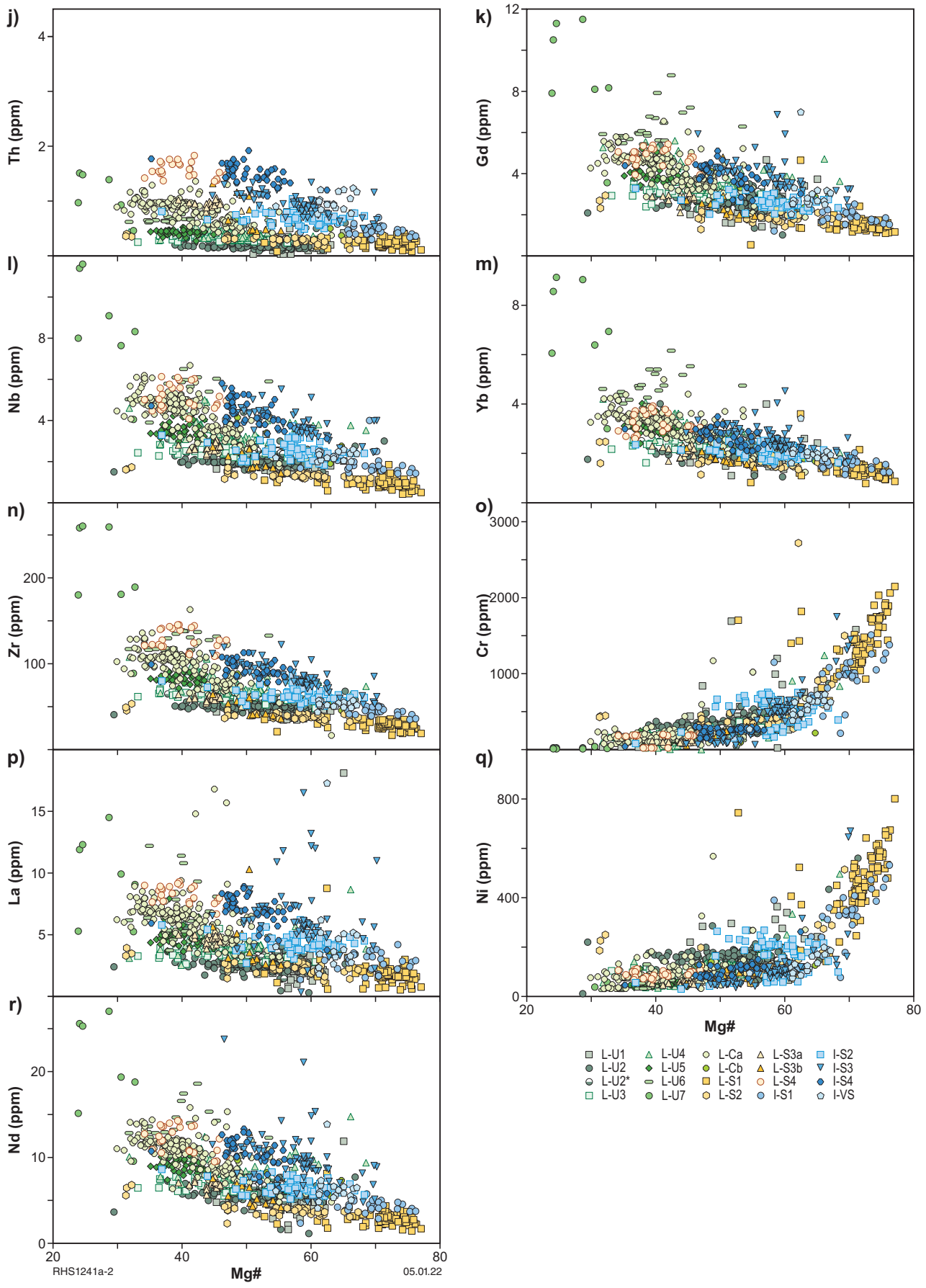

Figure 19. continued

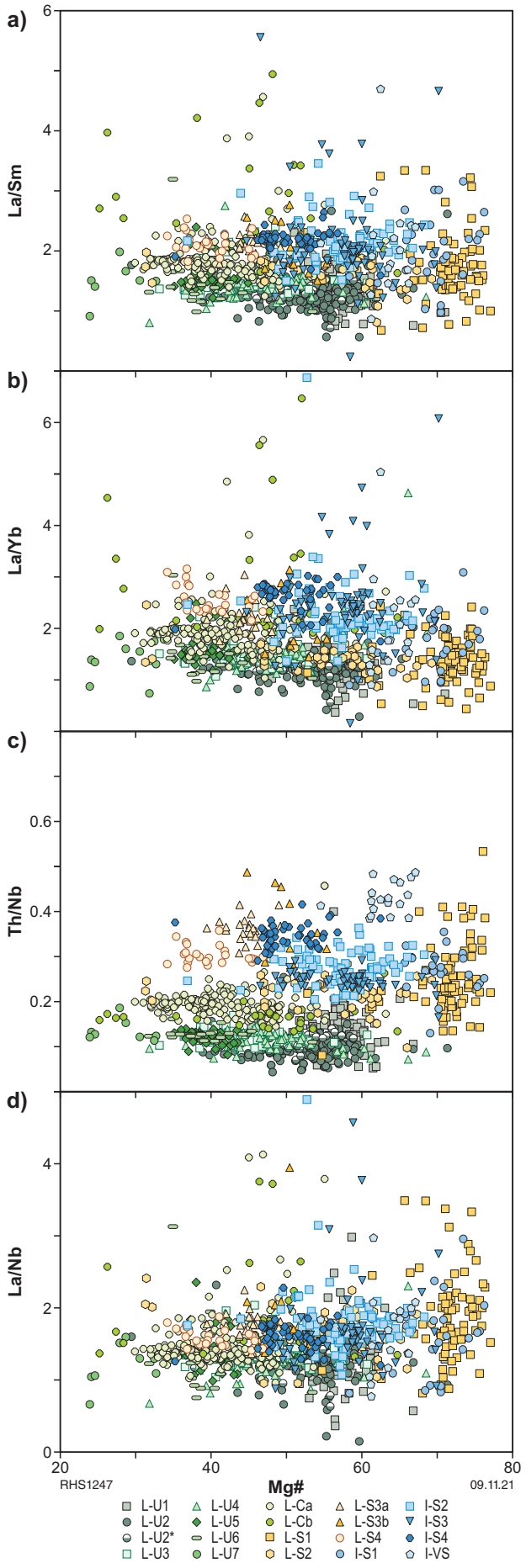

Figure 20. Variation in various trace element ratios with Mg# for individual LTB and ITB geochemical groups and units

Discrimination of H-HMg# and H-LMg#

These two groups of HTSB are discriminated from each solely based on Mg#. HTSB are completely discriminated from all LTB and ITB units based on their extremely high Th (e.g. Figs 4, 5, 23). Although >65% of all HTSB belong to the Paringa Basalt (Hannans Subgroup), there is no clear compositional distinction between these and samples found in the neighbouring domains.

Distribution of H-HMg# and H-LMg#

Most (>65%) of the HTSB samples presented here are from the Paringa Basalt, forming the upper part of the Hannans Subgroup (Fig. 9). This is a relatively unbiased reflection of the typically low abundance of such magmas within that part of the study area outside the Kambalda Domain. Nearly all the remaining HTSB samples lie to the north, in the Broad Arrow Subgroup or east, in the Parker Domain and Bulong complex (Fig. 25). HTSB do not appear to be common to the west of the Kambalda Domain, within the upper Coolgardie succession or the Vetters Subgroup. Outside of the Kambalda Domain, the stratigraphic position of the HTSB is difficult to constrain with the available data. It appears to relate to the upper parts of the stratigraphy at least within the Bulong complex. Within the Paringa Basalt, the relationship between H-HMg# and H-LMg# is clearly constrained within only one drillhole intersection examined (SE18), where H-LMg# broadly overlies H-HMg#.

Discriminating H-LTh

H-LTh has a very similar major and trace element concentration range to H-LMg#, including a similar range of Mg#, but has Th concentrations that lie between H-LMg# and ITB units (Figs 21, 23). One unit of komatiitic basalt (KB3) is notably more enriched in Th than the others (see below) and has major and trace element concentrations and ratios similar to those of H-LTh, but at higher Mg#.

Distribution of H-LTh

Although relatively rare, H-LTh shows a similar distribution to H-LMg#. Of the 16 H-LTh samples identified, five are found in the upper part of the Hannans Subgroup, and in cases where lithostratigraphic relationships can be inferred (e.g. in core from CD339W3), lie in the lower part of the Paringa Basalt, possibly mixed with or contaminated by the underlying Devon Consols Basalt.

Komatiitic basalts (KB) other than HTSB

As discussed above, in addition to the HTSB, which likely represent strongly contaminated komatiite, many ITB units, and LTB units such as L-S1 and L-S2, and possibly primitive L-U1, also combine high MgO contents, high Mg#, and Al_2O_3/TiO_2 ratios ~20 that possibly suggest a link to komatiitic parental magmas. There are several other groups (KB1, KB2, and KB3) that show similar characteristics but have probably remained strongly under sampled in our dataset because they typically occurred directly associated with komatiite-dominated horizons, which were generally sampled specifically for komatiites. Generally, these komatiitic basalts are primitive (Mg# >60, many >70), typically with MgO between 10 wt% and 18 wt% and Al_2O_3/TiO_2 close to 20 (17.5–22.5) (Figs 23, 24).

KB1 appears to bridge the compositional gap between the primitive LTB and L-Ca groups and komatiite. This does not necessarily imply a genetic relationship, as the trend simply reflects minimal contamination, although it clearly indicates a very similar mantle source composition. Similarly, KB2 potentially

bridges the compositional gap between komatiite and the IBT magmas forming the I-S1–3 trend. KB3 has incompatible trace element characteristics very similar to H-LTh and shares a similar geographical distribution, although unlike the latter, the concentrations of incompatible trace elements increase at constant, rather than decreasing, Al_2O_3/TiO_2.

The various identified komatiitic basalts are generally not difficult to distinguish geochemically from other mafic units (see below), and in particular from the HTSB. However, it is difficult to make a petrogenetic distinction between these units, other than the lack, in the case of the HTSB, of any clear and direct association with komatiite. KB and HTSB almost certainly are derived from ultramafic parental melts (in the case of KB, associated with those forming komatiites) and have undergone minor but variable (KB) or significant (HTSB) crustal contamination. It might be that differences between these units simply reflect aspects of the melt/crust-mixing process or the composition of the crustal component incorporated into the mantle-derived melts.

Distribution of KB units

One or more of the KB units occur throughout all the regional stratigraphies, although they are rarely sampled (Figs 9, 25). By definition, they are directly associated with komatiite or fine-grained peridotite and hence, are typically found around the middle komatiite-bearing parts of most stratigraphies.

Domain chemostratigraphic columns–Building the barcode

A significant finding of this study is that individual lithostratigraphic units, typically of formation level, seldom comprise a single geochemical unit (Fig. 9). Those that do, include the Greenmont Basalt (I-VS– lower Coolgardie succession), Gleesons Basalt (L-S1– upper Coolgardie succession), Paringa Basalt (HTSB– upper Hannans Subgroup), and Athena Basalt (L-S3a– upper Hannans Subgroup). Most stratigraphic formations comprise at least two distinct geochemical units, and in most cases, these units cannot be related back to a common parental magma composition. Thus, individual greenstone formations combine overlapping flow fields, each representing the products of a discrete eruptive event and/or eruptive centres supplied by genetically unrelated magma sources. This potentially makes some formation boundaries arbitrary reflections of changing source eruptions. Nevertheless, the subdivision of the regional (domain) stratigraphy into three levels (lower, middle, and upper basalts) reflects broader changes in magma compositions (see below) and provides useful markers of relative stratigraphic level.

Because textural or mineralogical features often cannot effectively discriminate between compositionally distinct basaltic units, mapping the discrete units at a stratigraphic 'Member' level might not be possible without a level of geochemical sampling density even greater than employed here.

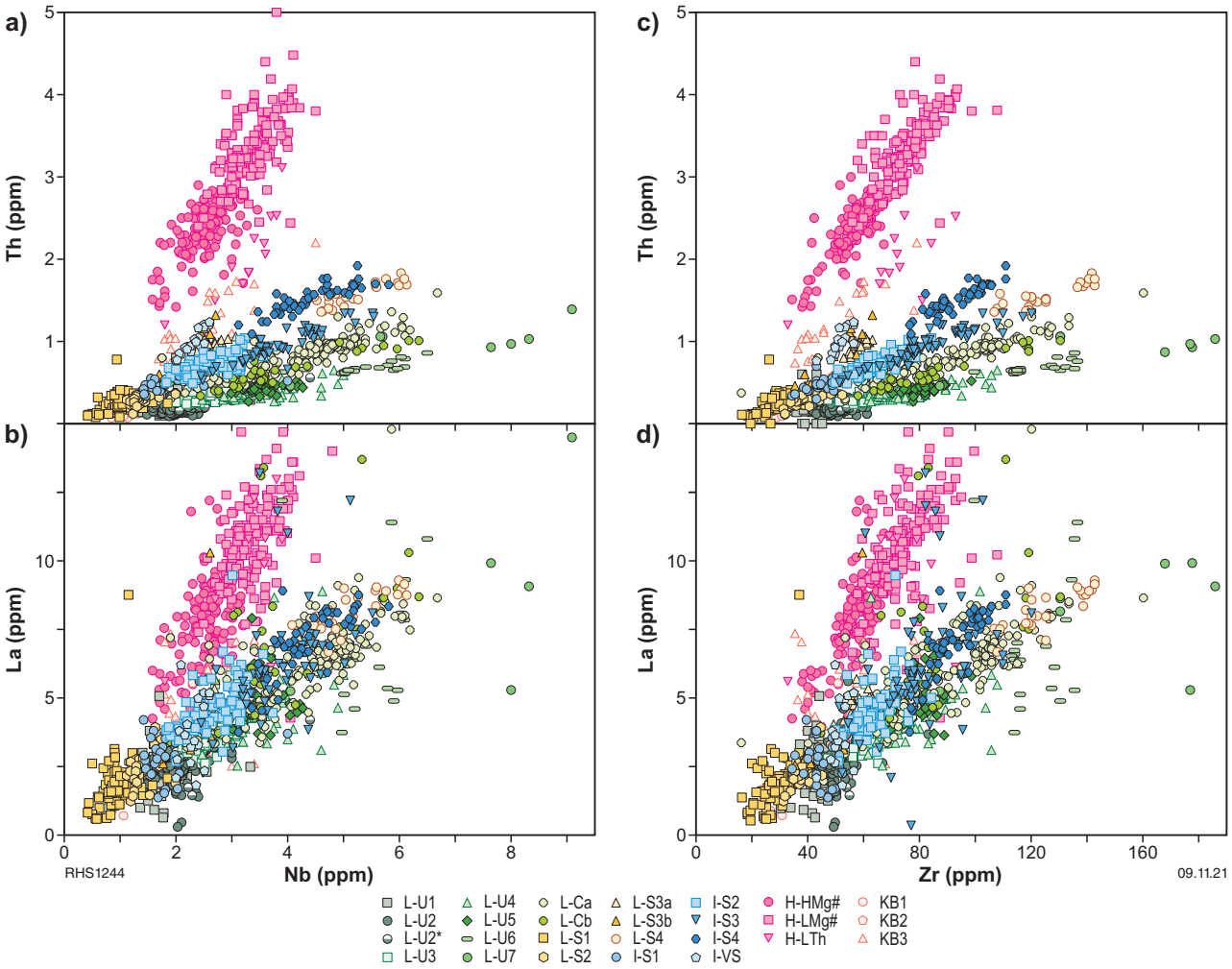

Figure 21. Variation in Th and La with Nb and Zr, for individual LTB, ITB, HTSB and KB geochemical groups and units

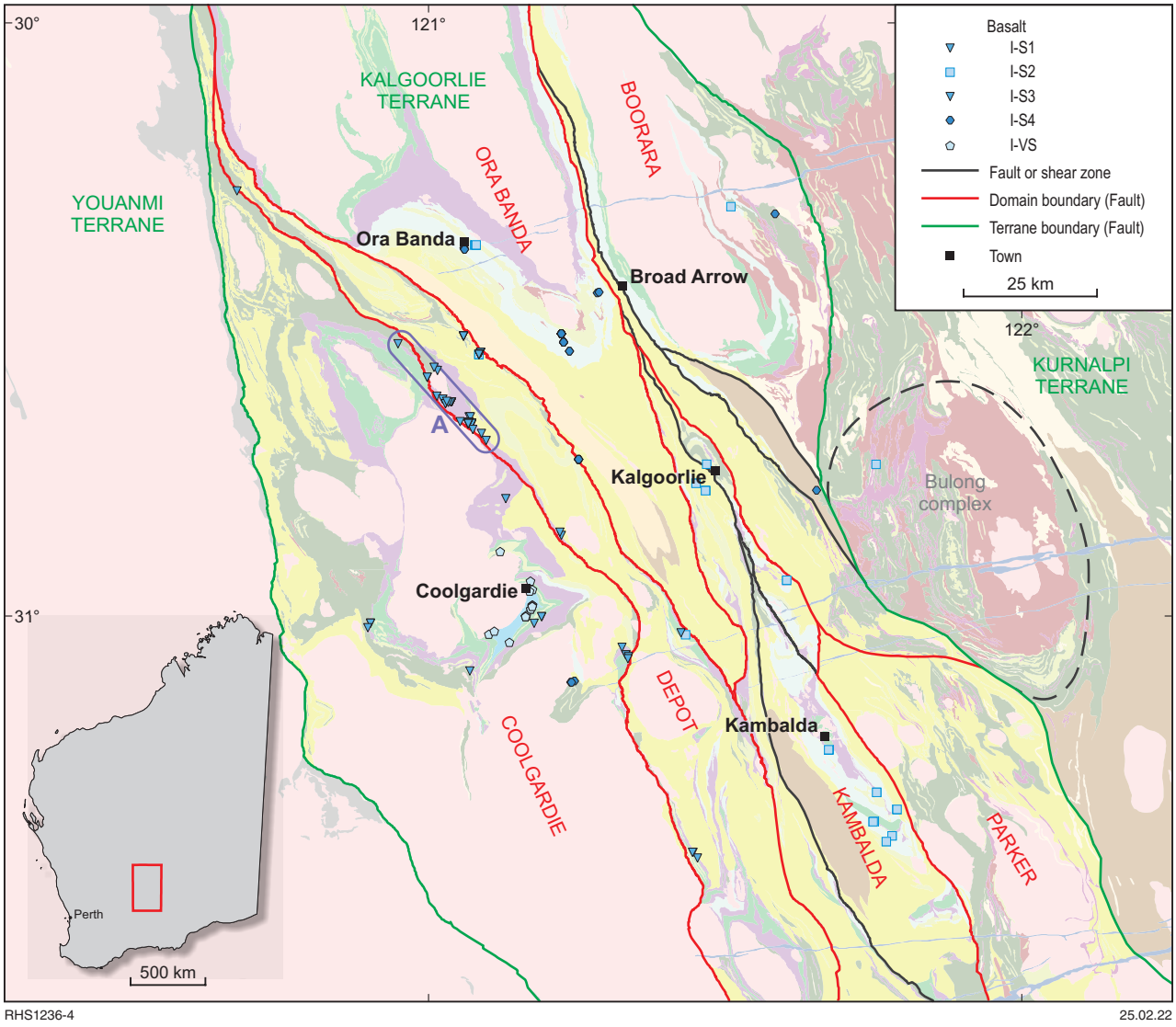

Figure 22. Geological map of the study area within the Kalgoorlie Terrane, showing a simplified version of the current interpreted bedrock geology and the distribution of I-S and I-VS geochemical units (see Figure 3 for fault names)

This would almost certainly not add any clarity to the potential ambiguities involved in identifying higher-order lithostratigraphic boundaries. This has implications for using geochemistry to infer stratigraphic position because, except in very rare cases, a single or low number of analyses will not be sufficient to uniquely identify a lithostratigraphic position. However, more comprehensive sampling, particularly if it incorporates the underlying and overlying stratigraphic units almost certainly will identify a unique lithostratigraphic position. Here, we describe the range of basaltic geochemical types forming various evolutionary stages of the regional stratigraphies.

Coolgardie Domain

Immediately apparent is that there are significant geochemical differences between the lower and upper stratigraphic successions of the Coolgardie Domain (Fig. 9). Here, the lithogeochemistry provides a clear indication that the upper and lower successions do not represent a structural repetition, although it remains plausible that they might be in thrust contact. The lower Coolgardie succession almost certainly should not be considered part of the Coolgardie Subgroup, as is presently the case.

Lower Coolgardie succession

The lower Coolgardie succession is presently limited to outcrops around the eastern and southern margins of the Calooli Monzogranite (Fig. 26). As currently mapped, the Burbanks Formation, forming the lowest exposed unit, comprises approximately:

- 56% L-U6
- 26% L-U4
- 18% primitive L-U2*.

The strongly TiO_2-enriched L-U6 unit is virtually unique to the Burbanks Formation. L-U6 is found at only one other locality within the study region, near Davyhurst in the Ora Banda Domain to the north-northwest, immediately east of the Zuleika Shear Zone (A in Figs 15, 27). There, it is also associated with interlayered L-U2* and L-U4, as well as another Ti-rich LTB unit, L-U7. It seems quite plausible that this exposure also belongs to a lower greenstone succession, possibly correlated with the Burbanks Formation.

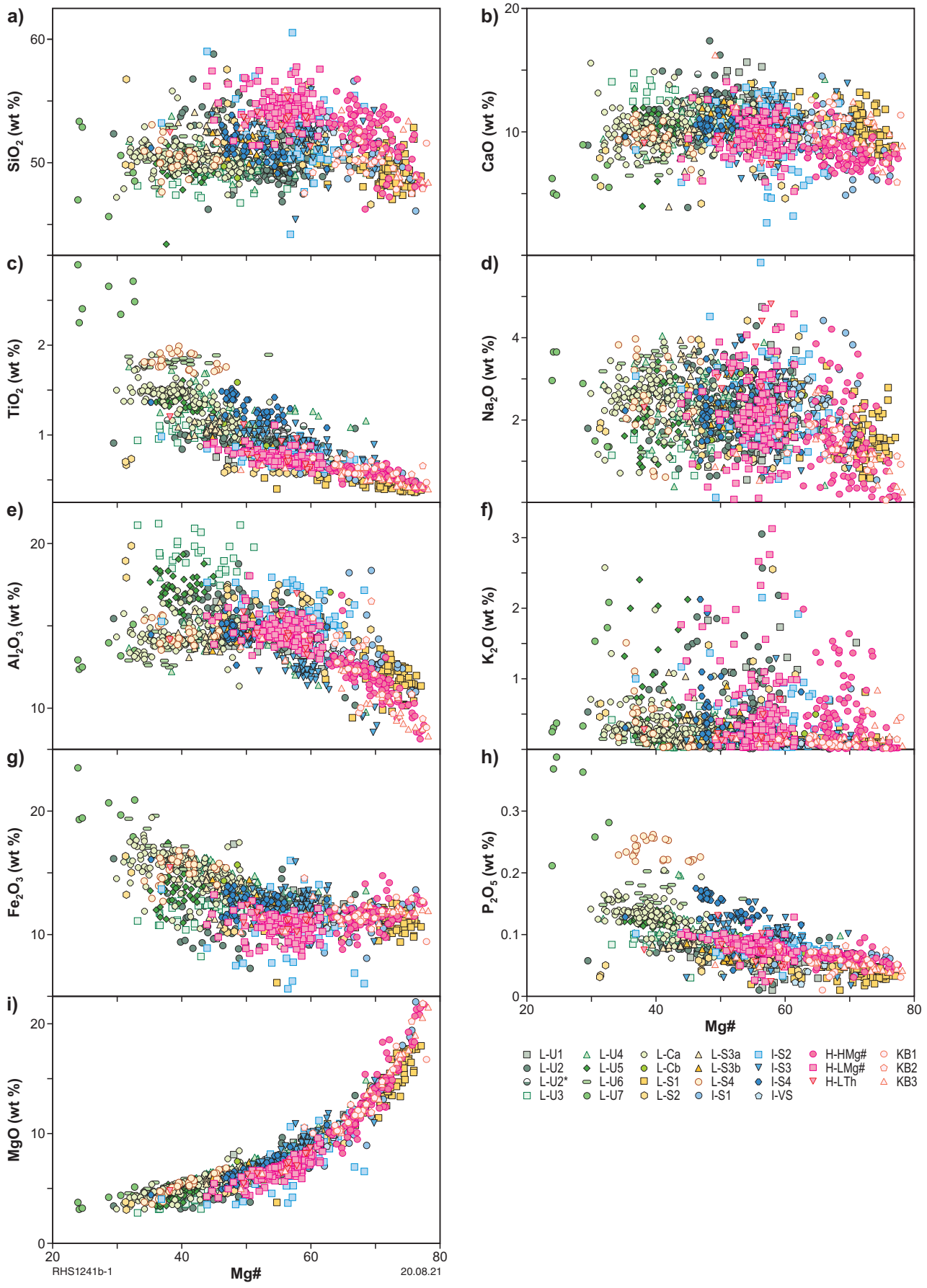

Figure 23. Variation in major and selected trace elements with Mg# for individual LTB, ITB, HTSB and KB geochemical groups and units

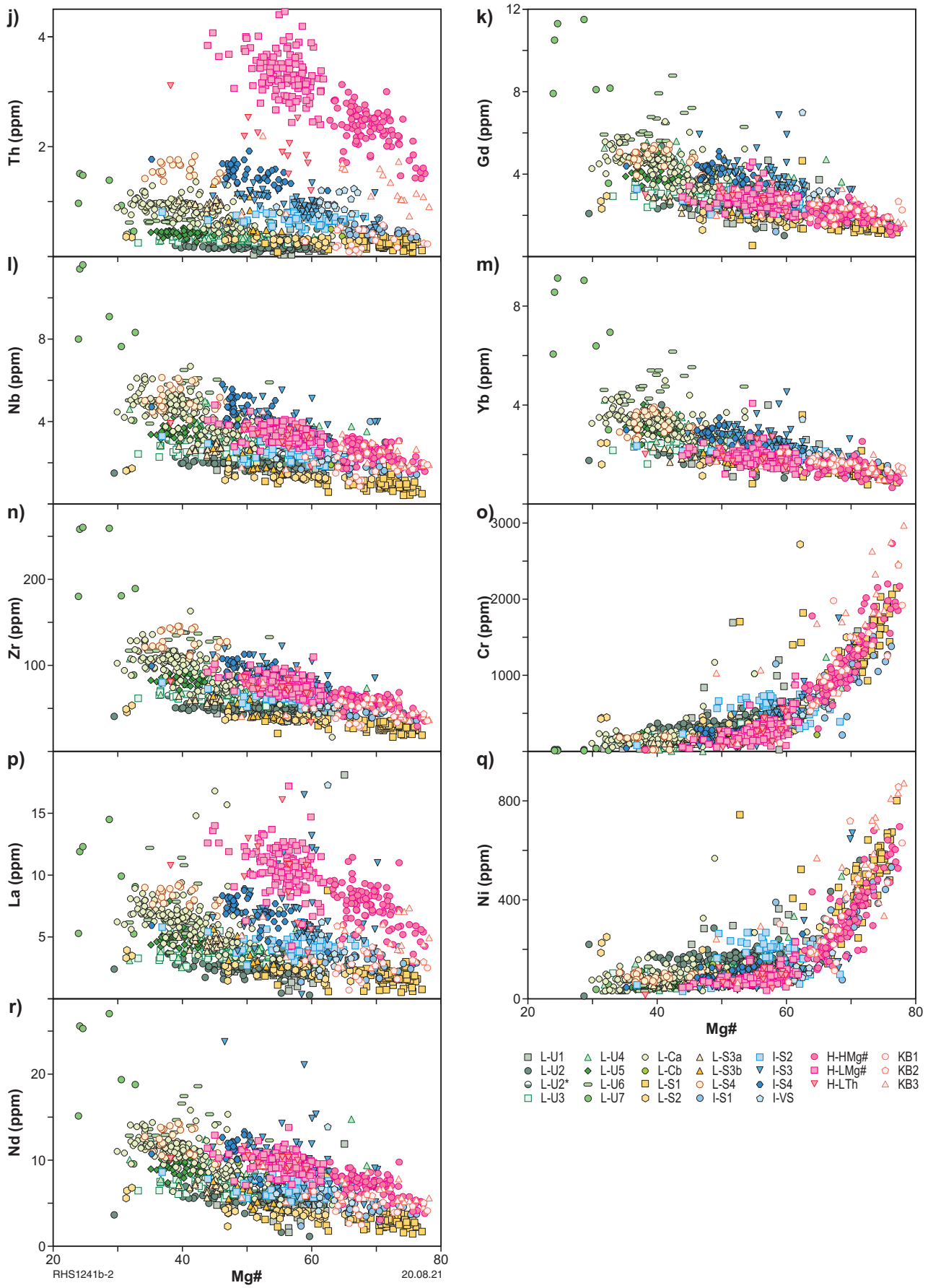

Figure 23. continued

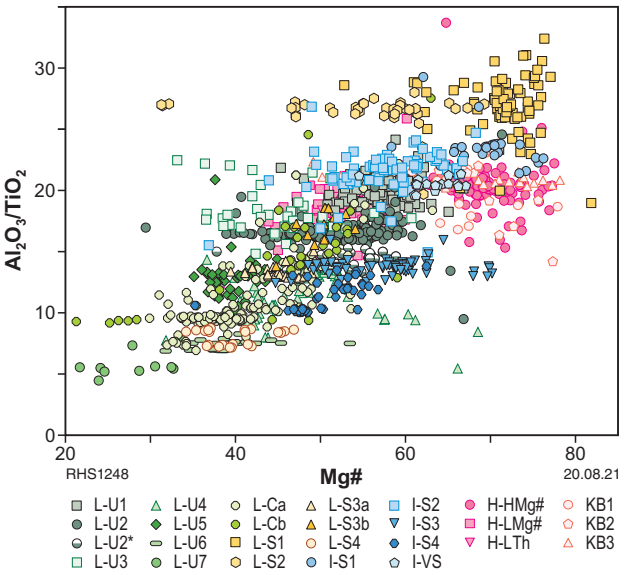

Figure 24. Variation in Al_2O_3/TiO_2 with $Mg^{\#}$ for individual LTB, ITB, HTSB and KB geochemical groups and units

The Little Blow Member of the Burbanks Formation, within the limits of the presently available data (3 samples only), consists of primitive L-U2* (2 samples) and L-U4 (one sample).

The Greenmont Basalt (possibly a sill) overlies the Burbanks Formation and is entirely composed of I-VS, which is unique to this stratigraphic unit.

Our dataset contains only three samples of the basaltic component of the typically ultramafic Brilliant Formation, including two samples of KB1 and a single sample of KB2.

Upper Coolgardie succession (Coolgardie Subgroup)

The Lindsays Basalt at the base of the upper Coolgardie succession comprises approximately:

- 42% L-Ca
- 36% primitive L-U1
- 13% primitive L-U2
- 9% primitive L-U2*.

Where stratigraphic relationships can be inferred within the Lindsays Basalt, it appears that primitive basalts L-U1, L-U2, including minor L-U2*, occur mainly in the lower stratigraphic regions, underlying a sequence dominated by L-Ca. Clear identification of Lindsays Basalt in the field, and in particular, distinguishing it from basaltic units of the overlying mafic–ultramafic Hampton Hill Formation, is hampered by poor outcrop and is potentially problematic. Current GSWA mapping shows vast areas in the Coolgardie region surrounding the Bali–Calooli Monzogranite (including regions of the Depot Domain) as comprising either 1) interleaved Lindsays Basalt and Hampton Hill Formation or 2) Hampton Hill Formation ranging from basalt to komatiite. Where Lindsays Basalt can be confidently identified, including where basalt directly overlies the lower Coolgardie sequence, it is volumetrically dominated by L-Ca. Since L-Ca has not been found in sequences clearly belonging to the Hampton Hill Formation, it can be regarded as a reliable geochemical signature of Lindsays Basalt when identified in the Coolgardie region. The Three Mile Dolerite, which intrudes Lindsays Basalt, is likewise almost entirely formed of L-Ca (Table 3). It is unclear, if minor L-U2* found in the lower Lindsays Basalt truly belongs to that formation or represents isolated (tectonically interleaved?) samples of the underlying Burbanks Formation.

The Hampton Hill Formation, as presently defined on GSWA mapping, is very complicated structurally and lithologically, and consequently geochemically. Overall, it is dominated by komatiite, but locally contains abundant basaltic geochemical components that also characterize the overlying Gleesons Basalt (L-S1), suggesting the stratigraphic boundaries are either tectonically or magmatically interleaved, or both. In addition, there are regions along the northeastern part of the Bali Monzogranite and the eastern side of the Calooli Monzogranite, where intercalated Lindsays Basalt and Hampton Hill Formation (undivided) (GSWA terminology) underlies the intercalated mafic and ultramafic components of the Hampton Hill Formation. This in turn, underlies the Gleesons Basalt, representing the upper part of the upper Coolgardie sequence. The basalt components of the intercalated mafic and ultramafic Hampton Hill Formation in these regions are very distinctive ITB units (I-S1 and I-S3, with interleaved KB1-3) (A in Figs 22, 26). It seems very likely that these represent a previously unrecognized ITB formation that at least locally separated the Hampton Hill Formation from Gleesons Basalt, and is now tectonically interleaved with the underlying Hampton Hill Formation.

Nevertheless, taking the Hampton Hill Formation as presently mapped, our data indicate a range of possible basaltic geochemical components including:

- 42% L-S1 – 25% of which, in the upper section is probably Gleesons
- 16% primitive L-U1
- 15% L-S2
- 11% I-S3 – all of which might constitute an upper ITB unit
- 11% KB3 – all of which might constitute an upper ITB unit
- 5% I-S1 – all of which might constitute an upper ITB unit.

Where inferred to lie in the upper part of the Hampton Hill Formation, L-S1 is possibly a tectonic slice of, or is magmatically transitional to, the overlying Gleesons Basalt. Where inferred to lie in the lower portions of the formation, L-S1 is often associated with L-S2 and more clearly forms true basaltic components of the Hampton Hill Formation.

L-S1 is also the sole geochemical unit within the stratigraphically overlying Gleesons Basalt, and elsewhere only occurs at the top of the Depot Domain stratigraphy.

Depot Domain (superseded)

Current GSWA mapping no longer recognizes the Depot Domain, which has been re-incorporated into the Coolgardie Domain. However, there remains significant confusion in this region as lithostratigraphic codes (GSWA mapping) appear to have been arbitrarily extrapolated from either the Coolgardie or Kambalda Domain or are generic Eastern Goldfields Superterrane codes. The former Depot Domain restricted the Coolgardie Domain to the area west of the Kunanalling Shear Zone. The limited outcrops in the Depot region do not allow the same degree of confidence in the broad stratigraphic context of the various geochemical components as it does in many of the other domains. However, from the previous discussion, it is quite clear that the upper Coolgardie succession and the superseded Depot Domain stratigraphy show very close lithogeochemical similarities (Fig. 9).

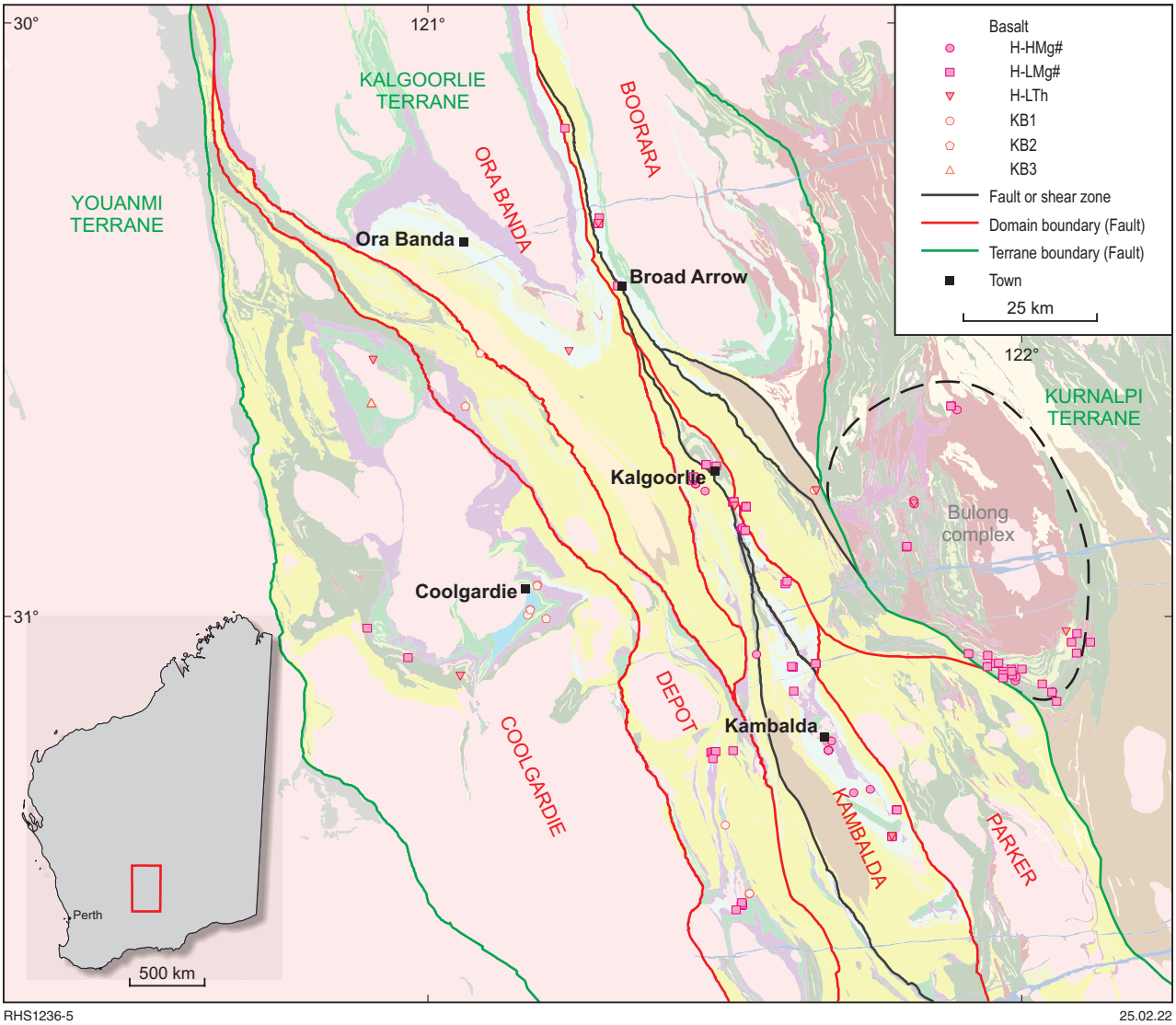

Figure 25. Geological map of the study area within the Kalgoorlie Terrane showing a simplified version of the current interpreted bedrock geology and the distribution of HTSB and KB geochemical units (see Figure 3 for fault names)

For example, the available data from the superseded Depot Domain indicate:

- A lower basaltic stratigraphy dominated by LTB with a high L-U1/L-U2 ratio (2.4) similar to that of Lindsays Basalt (1.6), locally containing L-Ca (12% of the lower basalt), and including L-S1 in some areas
- Apart from minor occurrences in the upper Coolgardie succession, L-S2 is unique to the eastern part of the former Depot Domain, with a concentration of 28 samples from three separate drillholes (BDDD0017, BDDD0002, and PXGD0089), in one hole apparently interleaved with komatiite (B in Fig. 26)
- A middle stratigraphy with a basaltic component almost exclusively of I-S3, either magmatically or tectonically interleaved with komatiite. This is overlain by a unit dominated, at least in one drillcore (BDDD0006: Fig. 26), by I-S1 (85%) and locally interleaved with I-S2 (15%), overlain by a discrete unit with L-S1 compositions identical to Gleesons Basalt of the upper Coolgardie succession.

These very close chemostratigraphic similarities with the upper Coolgardie succession strongly support re-incorporation of the Depot Domain into the Coolgardie Domain. However, there are a few anomalies. For example, I-S2 overlies I-S1 in drillcore (BDDD0017) immediately west of the Zuleika Shear Zone (approximately 10 km to the north of the Powder Gabbro) (C in Fig. 26), in what is inferred here to be the middle to upper part of the stratigraphy, and is otherwise unique within the Coolgardie Domain. I-S2 is a significant component of the stratigraphy of the Ora Banda and Hannans Subgroups and forms part of the I-S1–3 trend. We cannot determine whether its presence in this area reflects a stratigraphic transition or is simply part of a fractionation sequence from L-S1 to L-S2, although the latter process cannot be demonstrated in any other regional stratigraphy. In addition, in the Kundana region near Bullock Hole (D in Fig. 26), immediately west of the Zuleika Shear Zone that marks the boundary between the Coolgardie Domain and the Ora Banda Domain (in the north) or Kambalda Domain (in the south), stratigraphy identical to the upper part of the Vetters Subgroup is intersected in drillcores (PGDD15001, MEDD148, MEDD144, and FLRD04) and outcrop. Presumably, either the (GSWA) trace of the

Zuleika Shear Zone in the region is incorrectly located or the Ora Banda and Coolgardie stratigraphies impinge. Likewise, between the Connolly Gneiss and the Maloneys Dam Granite, approximately 13 km southeast of Londonderry Siding (E in Fig. 26), the greenstone stratigraphy is dominated by an I-S4–L-Ca association that is reminiscent of the upper part of the Vetters Subgroup and otherwise unique within the upper Coolgardie succession. However, this observation is based on limited data (7 analyses).

Ora Banda Domain

The Wongi Basalt is the basal formation of the Vetters Subgroup and comprises 61% L-Ca and 39% primitive L-U1. The relationships between the two geochemical components cannot be confidently assessed based on the current data (no mutual contacts are observed), although outcrop distribution suggests that L-Ca lies near the top of the sequence. The overlying Missouri Basalt is comprised entirely of L-Ca (Fig. 9) and it is plausible that the L-Ca component of the Wongi Basalt actually belongs to the Missouri Basalt or represents very fine-grained feeder dykes or sills related to the Missouri Basalt.

The Big Dick Basalt overlies the ultramafic component of the Vetters Subgroup (the Walter Williams Formation) that separates it from the Missouri Basalt and appears to comprise two geochemically distinct units:

- 55% I-S2
- 45% L-S1.

The I-S2 unit that forms the upper part of the Big Dick Basalt also forms a small component of the upper Coolgardie succession, potentially indicating close chemostratigraphic similarities between the lower and middle parts of the Vetters Subgroup and upper Coolgardie succession.

Overlying the Big Dick Basalt, the Bent Tree Basalt is overwhelmingly dominated (89%) by I-S4, which appears regionally unique to this formation. Six samples (11%) of fine-grained L-Ca from drillcore KND15001, collared within the Bent Tree Basalt, are tentatively assigned to this formation.

At the top of the Vetters Subgroup, the Victorious Basalt comprises three geochemically distinct units:

- 54% L-U5
- 39% L-U3
- 7% L-U4.

At least two of these geochemical units appear interlayered in several drillcores (e.g. L-U5 and L-U4 in the case of PMPD0080) (B in Fig. 27). L-U3 and L-U5, in particular, are strongly enriched in Al_2O_3 and this is locally expressed in a distinctive plagioclase megacrystic or even glomeroporphyritic texture in outcrop.

Kambalda Domain

The basal unit of what has traditionally been defined as the Hannans Subgroup is the Lunnon Basalt, which is almost entirely composed of primitive L-U1 (~43%) and L-U2 (~65%) (Fig. 9), with rare (<2%) samples of komatiitic basalts (KB1 and 2), particularly in the higher stratigraphic levels close to the onset of komatiitic magmatism. The Lunnon Basalt appears restricted to the southern half of the Kambalda Domain (Fig. 28), not having been found in outcrop or drillcore in the Kalgoorlie region. Where L-U1 and L-U2 are found in the same drillcore (e.g. in DDH KD1029), each typically dominates specific intervals (a flow or sequence of flows) but no consistent stratigraphic relationship was noted; hence, L-U1 and L-U2 magmatism is considered to be synchronous.

Apart from the notable absence of L-Ca from the Hannans Subgroup, a clear difference between the Lunnon Basalt and the primitive L-U rich portions of the Lindsays Basalt (and Wongi Basalt in the Vetters Subgroup) is the much lower L-U1/L-U2 ratio (0.49) in the Lunnon Basalt (cf. 1.6 to 2.4 for the Lindsays Basalt), although this ratio varies widely between locations within the Kambalda Domain (Fig. 28).

The basaltic components of the Kambalda Komatiite (not shown) appear to be limited to samples of komatiitic basalt (KB2>KB1) and this distinguishes the formation from the Hampton Hill Formation of the upper Coolgardie sequence, which appears to include locally voluminous ITB (I-S) and L-S LTB components. However, this might reflect a better understanding of the stratigraphy of the Kambalda Domain.

Overlying the Kambalda Komatiite, the Devon Consols Basalt is almost entirely composed of I-S2 (84%), with ~16% komatiitic basalt (KB2>KB3) mainly found stratigraphically close to the lower contacts with the Kambalda Komatiite.

The Paringa Basalt is the only clearly stratigraphically defined occurrence of HTSB within the study region, although H-LMg# forms a significant component of the upper Highway Formation of the Broad Arrow Subgroup and both H-HMg# and H-LMg# are significant components of the stratigraphy of the Parker Domain and Bulong complex. H-HMg# and H-LMg# are equally abundant components (49% each) of the Paringa Basalt. Relationships established in drillhole SE18 (Fig. 28) suggest that H-LMg# broadly overlies H-HMg# and similar observations were made by Morris (1993). Close to the contact with the Devon Consols Basalt, H-LTh also forms a component of the Paringa Basalt, possibly reflecting either tectonic or magmatic mixing with I-S2 of the underlying unit.

Strongly contaminated units overlying the Paringa Basalt – i.e. L-S4 and Athena Basalt (L-S3a) – are a relatively minor but widespread component of the Kambalda Domain (Fig. 28). Both units overlie (apparently conformably) the Paringa Basalt, separating it from the Black Flag Group (Fig. 9), with the Athena Basalt (L-S3a) locally present throughout the southern part of the Kambalda Domain and L-S4 restricted to its northern part. In a narrow region of overlap, drillhole intersections (MSC27310-1) indicate that L-S4 is overlain by the Athena Basalt (Fig. 28).

Although younger than the Hannans Subgroup, fine-grained mafic rocks occur within the overlying Black Flag Group. Locally, they show peperitic contacts with volcaniclastic rocks of the Black Flag Group and have been interpreted as lavas or synvolcanosedimentary sills (McMann, 2018; Cas et al., 2019). Six samples were taken during the current study and a further 10 samples were taken during a more detailed analysis of the Golden Mile Dolerite (McMann, 2018). These samples are dominantly of L-U2 with other major components comprising L-U4 and L-U5. These three units also overwhelmingly dominate the Golden Mile Dolerite itself (Table 3), which has been interpreted as a major synvolcanosedimentary sill (McMann, 2018; Cas et al., 2019). The fine-grained and peperitic rocks are interpreted as marginal facies associated with the Golden Mile Dolerite. Similar fine-grained quenched intrusions are associated with other high-level layered mafic–ultramafic sills emplaced within the upper basaltic units of many of the domain subgroups and into the overlying Black Flag Group or stratigraphically equivalent volcanosedimentary units.

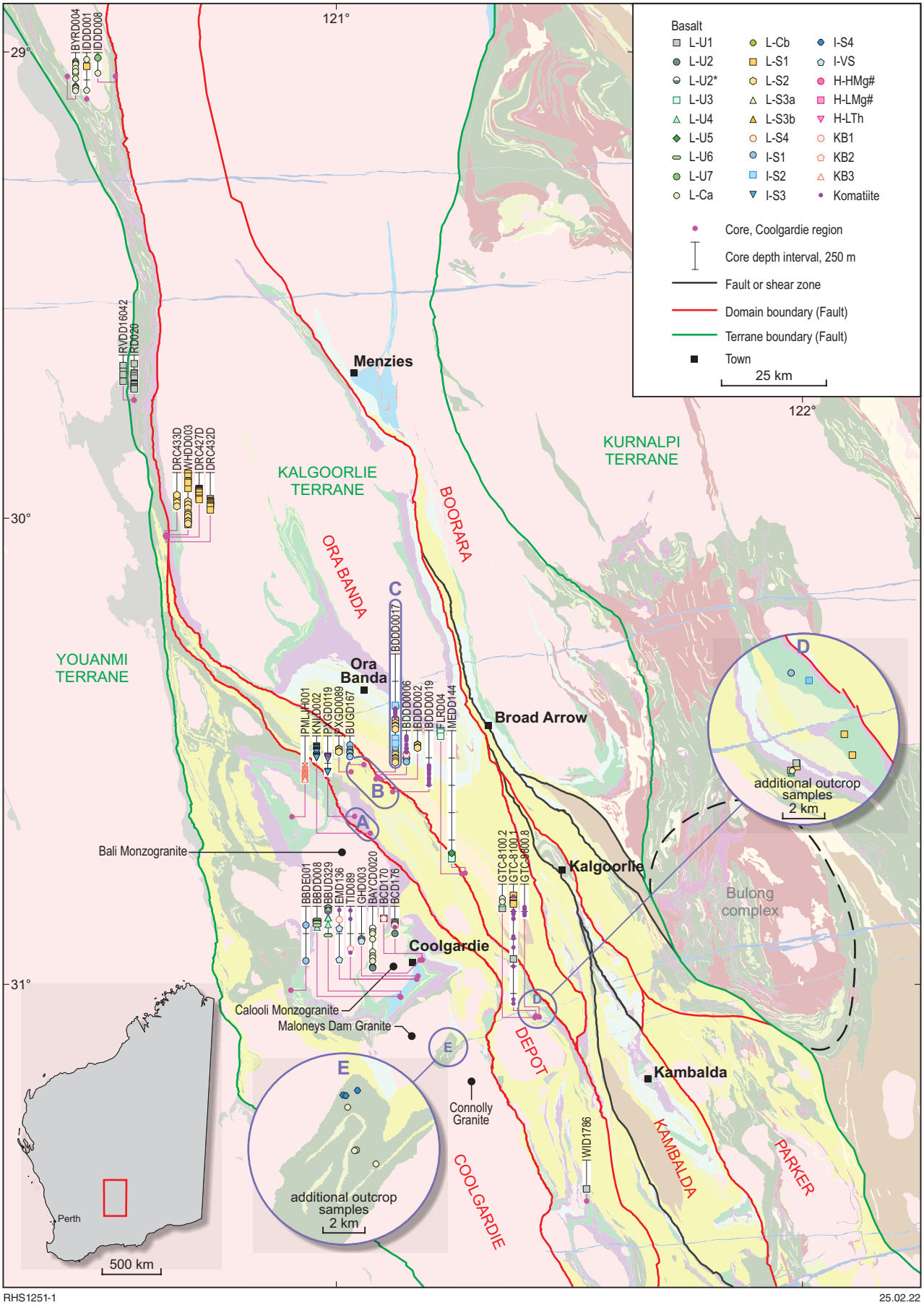

Figure 26. Geological map of the study area within the Kalgoorlie Terrane, showing a simplified version of the current interpreted bedrock geology and the distribution of diamond drillcore sample sites within the Coolgardie (and Depot) Domain (see Figure 3 for fault names)

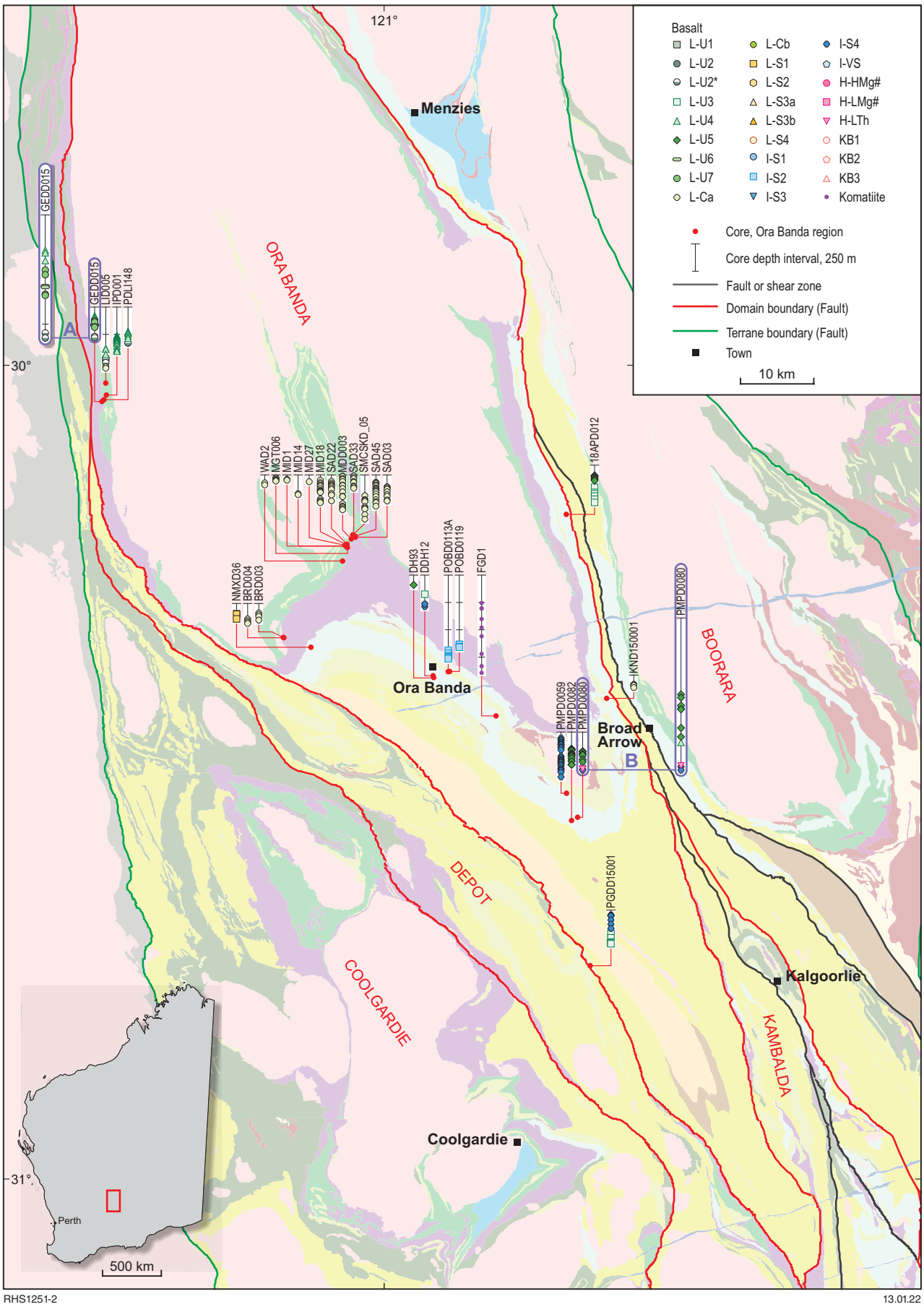

Figure 27. Geological map of part of the study area within the Kalgoorlie Terrane, showing a simplified version of the current interpreted bedrock geology and the distribution of diamond drillcore sample sites within the Ora Banda Domain (see Figure 3 for fault names)

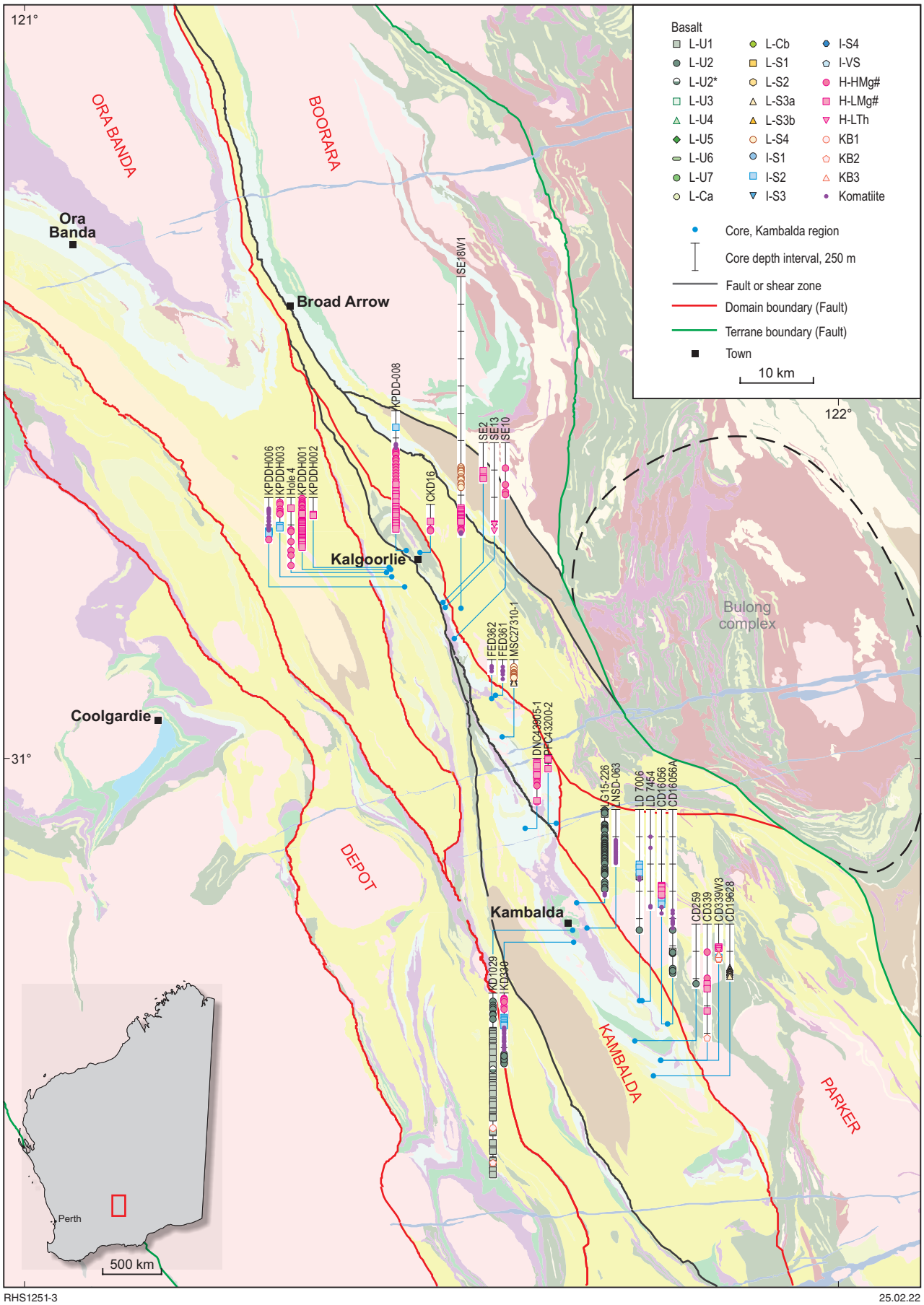

Figure 28. Geological map of part of the study area within the Kalgoorlie Terrane, showing a simplified version of the current interpreted bedrock geology and the distribution of diamond drillcore sample sites within the Kambalda Domain (see Figure 3 for fault names)

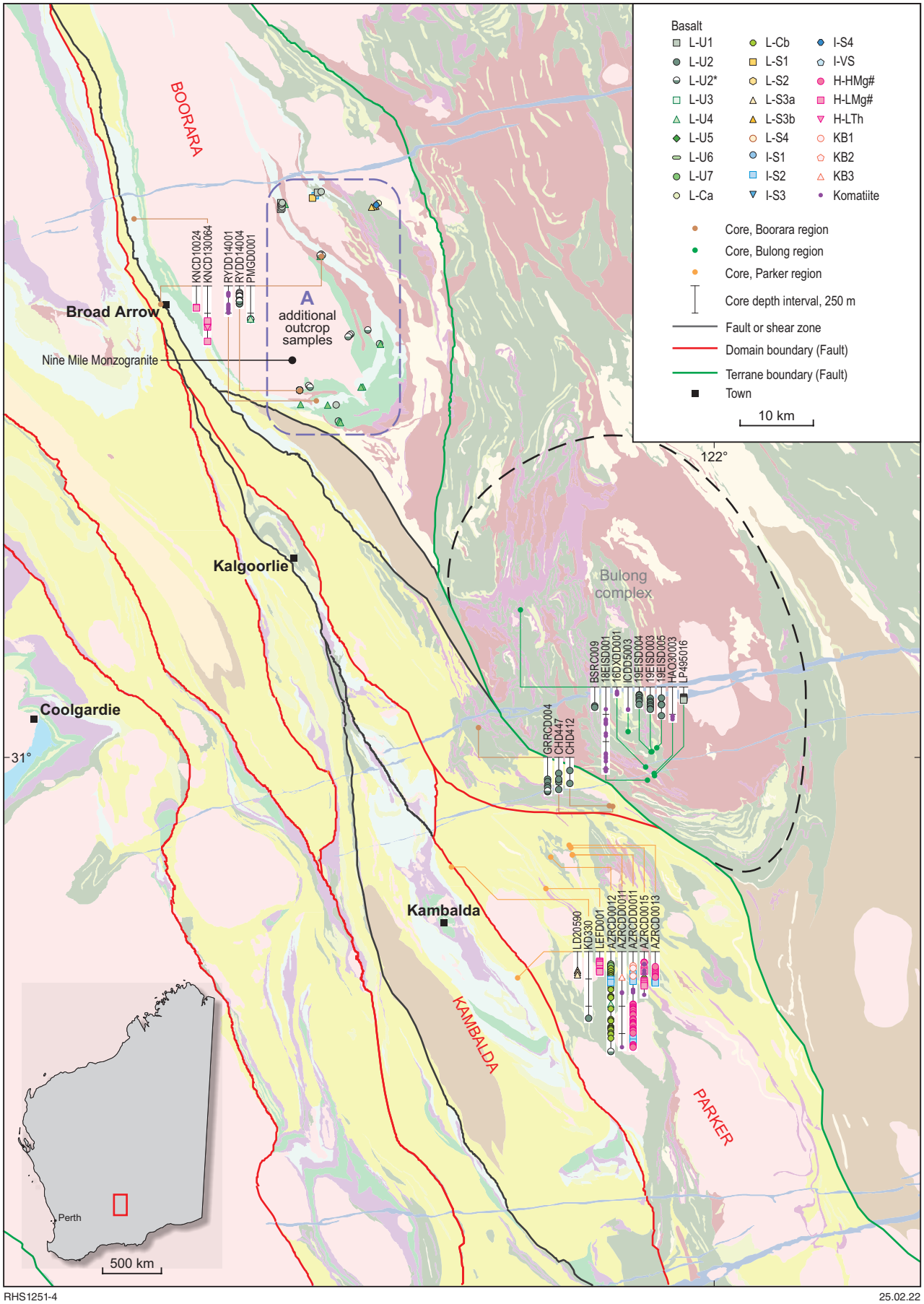

Figure 29. Geological map of the study area within the Kalgoorlie Terrane, showing a simplified version of the current interpreted bedrock geology and the distribution of diamond drillcore sample sites within the eastern domains (see Figure 3 for fault names)

Most of the sills for which we presently have significant data, comprise L-U2 >L-U1 parental compositions but are dominated by more differentiated compositions typical of the L-U3–7 trend. The presence of the sills and their dominant L-U3–7 fill is consistent with some lavas that form the upper levels of the regional mafic stratigraphies reflecting eruptions from evolved upper crustal chambers.

Domains to the east of the Kambalda and Ora Banda Domains (eastern Domains)

We currently have significantly fewer basalt data (~380) from the Boorara and Parker Domains and Bulong complex than for the regions to the west; nevertheless, these data provide valuable insight into the compositional variations in basaltic rocks within these regions. We have attempted to place these data into a stratigraphic context using available relationships in drillcores and current field mapping, and hence, produce a broad chemostratigraphy to compare with the regions to the west. Of all of these regions or stratigraphic levels, the basal portion of the Broad Arrow Subgroup, the Scotia Basalt (Fig. 9), is probably best characterized. However, the overlying Highway Formation comprising a basaltic stratigraphy with interleaved ultramafic rocks, including komatiite, remains poorly constrained.

A notable feature of all of these areas is an L-U dominated lower basalt sequence with L-U2 >>L-U1, similar to the Hannans Subgroup (Fig. 9). The Scotia Basalt contains some additional complexity with a lowest sequence, including L-U2* and L-U4, an association only seen elsewhere within the Burbanks Formation of the lower Coolgardie succession and suspected equivalents in the Ora Banda Domain near Davyhurst. This raises the possibility that a basaltic basement to the Broad Arrow Subgroup, possibly equivalent to the lower Coolgardie succession, is exposed on the southern flank of the Nine Mile Monzogranite, south of the Scotia–Kanowna Anticline (A in Fig. 29).

The Bulong complex stratigraphy apparently has none (or we have not yet sampled any) of the ITB that characterizes the komatiite-rich central portions of the domain stratigraphies (Figs 9, 28). However, I-S2 and I-S4 (one sample each) accompany L-S1 and L-S2 (4 samples) to form what might reflect a very poorly sampled equivalent of the middle stratigraphy in the Broad Arrow Subgroup, and I-S2 occupies possibly the same stratigraphic position in the Parker Domain. Also in common with the Hannans Subgroup, is an upper basalt stratigraphy dominated by HTSB and fractionated LTB, including L-S3b and L-Cb (Bulong complex) or L-U3, L-U7, L-S3a, and L-Cb (Parker Domain). Overall, this stratigraphic pattern appears to show considerably greater similarities with the Hannans Subgroup than with the upper Coolgardie succession or the Vetters Subgroup.

Discussion

Our geochemical analysis of local greenstone stratigraphy uncovers a surprisingly complex, but largely systematic, geochemical variation within and between established local and more regional lithostratigraphies. The chemostratigraphic variations, packages, and sequences presented here, particularly when accompanied by additional geological context, should provide a relatively reliable means of establishing the lithostratigraphic position of poorly constrained geochemical samples. The reliability of this approach will increase as more data are added. However, these data also provide potentially significant insights into the evolution of the greenstone belts within the region, including the evolution of lithospheric architecture. In addition to viewing the regional basaltic sequences lithostratigraphically, we can also examine the ways that factors such as source composition, degree of contamination, crustal level of fractionation, and emplacement mechanism (direct ascent or stalled ascent) changed throughout accumulation of the total magmatic greenstone sequences, i.e. the tectonomagmatic evolution.

Potential geochemical relationships between various units and trends

As previously discussed, it is common that during early fractionation of a mantle-derived magma and/or low to moderate degree partial melting of mantle sources, there are no mineralogical changes in the crystal assemblages that might significantly affect mineral/melt partitioning of strongly incompatible trace elements. In such situations, all magmas derived from a given mantle composition should plot on straight lines (in plots of incompatible elements, for example, Th vs Nb or Zr) that extrapolate to the origin (i.e. x, y both = 0 ppm). The slope of these lines gives the ratio of those elements in the source. The L-U units form a relatively consistent trend (well defined in the case of the L-U3–7 trend) that extrapolates to the origin and has the lowest Th/TiO_2, Th/Nb, and Th/Zr ratios of all magmas examined here (Figs 6, 7, 10). The source for these L-U units can be considered broadly similar in composition, although not identical as indicated by minor variations in, for example, Th/Nb ratios between L-U1 and L-U2 (Fig. 10). This mantle source is broadly representative of the ambient southeastern Eastern Goldfields Superterrane mantle at c. 2700 Ma and has compositions lying between those of primitive mantle and N-MORB (Fig. 10), like most Archean primitive basaltic rocks (Barnes et al 2021). The observation that komatiites plot close to the primitive part of the L-U trend, between L-U2 and the origin (Fig. 30), shows that komatiitic sources and non-komatiitic sources had broadly similar mantle compositions, although komatiitic sources range to slightly more depleted compositions (e.g. Barnes et al., 2021).

Although varying degrees of partial melting and fractional crystallization can result in similar straight-line trends in bivariate plots of strongly incompatible trace elements, we attribute the L-U3–7 trend primarily to fractional crystallization. The main reasons are that the trend is dominated by samples with low $Mg^{\#}$ (<50), significantly out of equilibrium with peridotite at realistic mantle pressures and temperatures. In addition, there is no clear difference in composition (including $Mg^{\#}$ and Nb/Yb ratios, which are both sensitive to changes in melt fraction) between primitive members of the stratigraphically lowest L-U2 units (e.g. Lunnon Basalt) and L-U2 magmas parental to sills that intrude the upper levels of the greenstone stratigraphy, although associated L-U samples within the sills (L-U3–7) vary widely in composition through fractionation.

We do, however, see evidence for considerable variation in the degree of mantle melting throughout the evolution of the greenstone sequences (i.e. Kalgoorlie Group). The occurrence of komatiitic magmatism and the dominance of ITB suggests that the middle basaltic sequences of the Kalgoorlie Group generally reflect a higher degree of partial melting than magmatism forming the lower basaltic sequences. ITB typically have slightly higher incompatible trace element concentrations and Th/Nb, Th/Zr, and Th/La ratios than LTB, despite ITB clearly reflecting the products of higher degree mantle melting based on typically higher MgO contents and $Mg^{\#}$ of primitive end members. This indicates that the parental magmas for ITB were also contaminated (enriched) at an earlier stage than the parental magmas for L-U compositions.

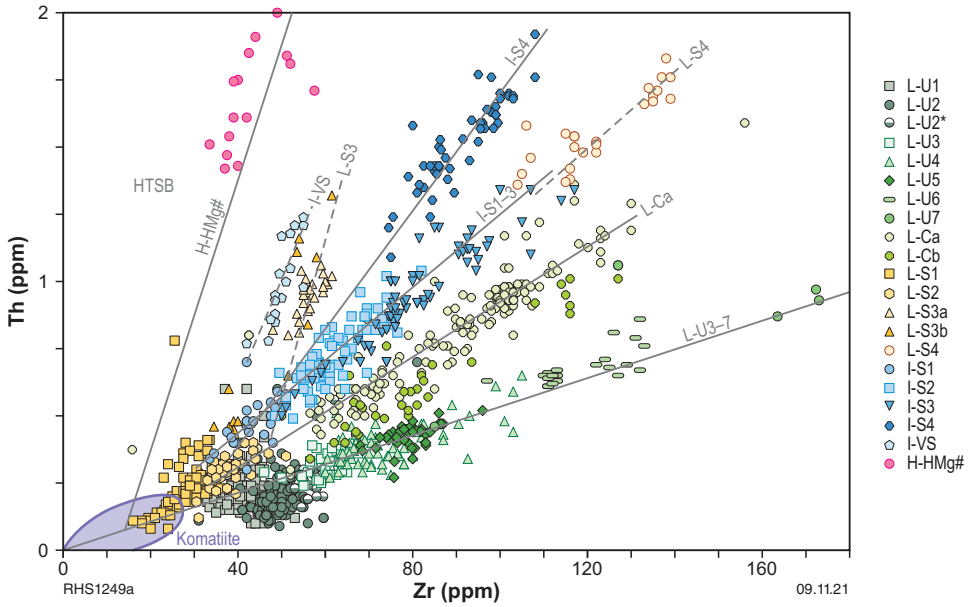

Figure 30. Variation in Th with Zr for individual LTB, ITB and HTSB geochemical groups and units. Also shown is the field for komatiites sampled during this project and the geochemical trends defined by many of the specific units

Most ITB are derived from ultramafic or komatiitic basaltic parental compositions with a higher thermal capacity to assimilate crustal material and at a stage when the base of the crust had already been considerably thermally weakened. The HTSB in the upper greenstone sequences represents an even more extreme case of this (e.g. Arndt and Jenner, 1986; Barnes and Arndt, 2018; Barnes et al, 2021).

Units of the L-U3–7 trend were not only derived from a compositionally similar and broadly primitive mantle source, but they all evolved via the same range of fractionation processes without significant additional contamination from the crust. Most other units or trends of LTB, ITB, and HTSB plot on lines that do not extrapolate to the origin, although many intersect the L-U or komatiite trend at various points (Fig. 30). A plausible interpretation of these relationships is that these mafic magmas reflect episodes when primitive L-U or komatiite magmas (if there was a significant difference) became contaminated by crustal material and subsequently evolved along different trace element trends, each reflecting the composition and proportion of the crust that was incorporated. Most of these subsequent trends are also linear, suggesting that once contaminated by crustal material, subsequent evolution (fractionation) is simple and involves no further crustal contamination. Hence, it is plausible that all ITB units and L-C units were derived through contamination of L-U or parental komatiite magmas more primitive than L-U1 and L-U2. Rare cases, including I-VS, I-S4, L-S3, and L-S4, show evidence of representing a second stage of either contamination, magma mixing or a major change in the mineralogy of the fractionating assemblage. We see no clear evidence with any unit or trend, for continuous contamination. With the exception of L-S1 and L-S2, we also see no clear evidence requiring melting of a mantle source already contaminated with crust, consistent with the findings of Smithies et al. (2018a). This means that contamination primarily occurred in or at the base of the crust through assimilation into mantle-derived melts. It remains plausible that prior crustal contamination of mantle sources did occur, but if this is the case, it was so minor and/or inhomogeneous that the compositional affects were swamped by subsequent crustal assimilation.

However, L-S1 and L-S2 potentially provide an exception in that their compositions might reflect a slightly more depleted bulk mantle source than that of most of the other magmas. Within the limits of the present data, it is difficult to assess the relationship between the L-S1 and L-S2 magmas and the other LTB units. Many incompatible trace elements trends are consistent with either L-S1 or L-U1 being a potential parental magma to L-Ca, although based simply on when these compositional variants appear in the regional stratigraphies, a relationship between L-U1 and L-Ca seems more likely and equally consistent with spatial relationships.

For HTSB and most ITB, trends away from the main L-U trend happen at a relatively primitive stage along that trend (Fig. 30). This indicates contamination of a high MgO, possibly komatiitic magma that was considerably less evolved than L-U1 or L-U2, probably at or just above the mantle-lower crust interface. In the case of more evolved HTSB and ITB magmas (e.g. I-S3 and I-S4), Al_2O_3/TiO_2 ratios below mantle values (~20) reflect subsequent plagioclase fractionation (without further contamination) at mid- to upper crustal levels.

We do see some deviation or scatter from straight-line trends at high TiO_2 contents in the L-U3–7 trend, with Th/TiO_2 ratios increasing in L-U6 and scattering in L-U7 (Fig. 6), as a result of magnetite saturation and fractionation, although this is unrelated to contamination of L-U composition magmas since trends for Zr/Th and Nb/Th (Fig. 7) remain relatively constant.

Individual units of the L-U3–7 and I-S1–3 trends have mantle-normalized trace element plots that broadly parallel each other (L-U3 parallels L-U4 and L-U5 etc.) at different element concentrations (Fig. 31); i.e. they show very limited ranges in incompatible trace element ratios and wide ranges in concentrations. For both trends, ~three-fold increases in Th concentrations indicate a ~70% reduction in magma volume, assuming a closed system. This reflects the role that fractionation of minerals (such as plagioclase, olivine and orthopyroxene), with exceptionally low (and similar) abilities to concentrate REE and HFSE, can have during cooling of mafic magmas.

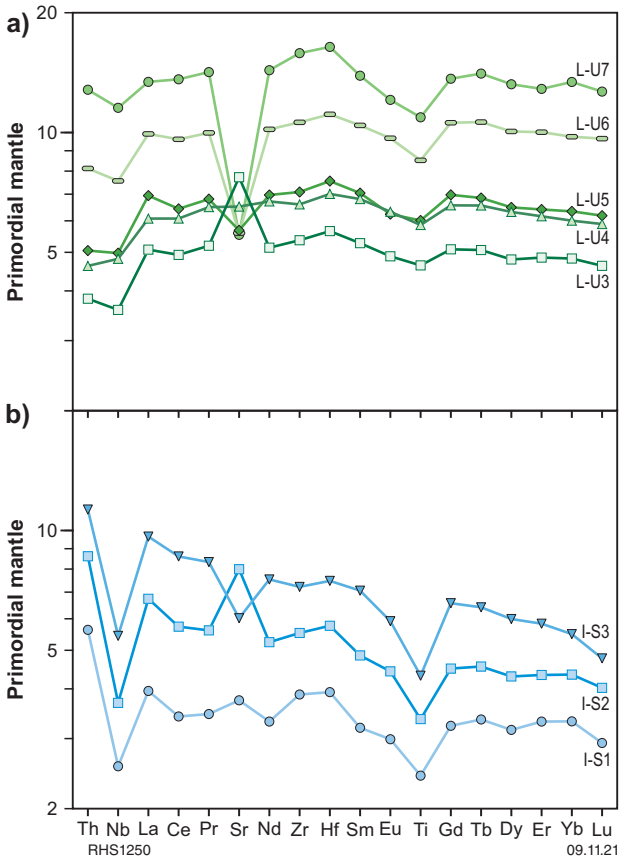

Figure 31. Average mantle-normalized trace element patterns for various LTB and ITB geochemical groups and units (normalizing values from Sun and McDonough, 1989)

Wide ranges in Al_2O_3/TiO_2 and in mantle-normalized Sr-anomalies (positive to negative) (Figs 24, 31) indicate the significant role of plagioclase fractionation (accumulation or removal); however, variations in Al_2O_3 and $Mg^{\#}$ vs Al_2O_3/TiO_2 (Figs 12, 24) are not systematic. Hence, although different units within each trend have similar incompatible trace element ratios, they have evolved through fractionation of different combinations of incompatible trace element-poor minerals. This emphasizes the dominant control that initial source composition and early contamination have on mafic magma composition. The evidence for extensive closed-system crystal fractionation trends suggests evolution in, and eruption from, standing crustal magma chambers at mid- to upper crustal levels.

Regional stratigraphic and geographic relationships and implications for greenstone evolution

The range of mantle-derived parental magmas feeding the mafic greenstone stratigraphies in the study area is limited mainly to L-U and komatiitic compositions (themselves not clearly distinguishable in source composition). We also infer that a range of conditions and processes operating at various crustal levels has resulted in significant compositional diversity in the erupted products. This includes changes in the regional deformation regime or in crustal thickness that favoured the rapid transfer of only weakly fractionated and uncontaminated magmas (L-U1 and L-U2) from the source to the deposition site. A crustal shortening regime and/or the presence of thicker crust would have favoured ponding in mid- to upper crustal chambers, prior to eruption of variably fractionated L-U3–7 magmas. In addition, we can infer a broad but non-systematic increase in the extent of magma contamination by crust, despite the occurrence of L-U3–7 magmas in the upper stratigraphies. Viewing these variations in stratigraphic and geographic contexts allows a generalized sequence of regional greenstone evolution to be inferred, and potentially identifies crustal architectural control on magma compositional distribution.

Lower basaltic stratigraphy

Primitive L-U magmas, L-U1 and L-U2 are the most sampled mafic units and form the basal component of all stratigraphies. As well as a stratigraphic pattern, there is a broad geographic pattern in their distribution. Both occur throughout the region but L-U1 greatly dominates the lower stratigraphy in the western domains (Coolgardie and Ora Banda), although it does not occur in the lower Coolgardie sequence. Conversely, L-U2 (main population) is more common and dominates the lower stratigraphy of the eastern domains (i.e. Kambalda, Boorara, and Parker Domains and the Bulong complex). With $Mg^{\#}$ typically <65, the parental magmas for L-U1 and L-U2 almost certainly fractionated to some extent before and during emplacement in the crust, but were not contaminated to any significant degree. In the case of L-U1, mantle-like Al_2O_3/TiO_2 ratios ~20 (Fig. 12) suggest that plagioclase was probably not stable during early fractionation, which probably occurred within the spinel stability field at or beneath lower crustal depths (broadly below ~35km). In the case of the main population of L-U2, a slightly lower Al_2O_3/TiO_2 (~16–17) ratio probably does reflect limited early plagioclase fractionation, perhaps as a result of thinner lithosphere. Slightly higher Th/Nb and Th/Zr ratios also suggest that L-U1 (Fig. 7) incorporated a slightly greater (although still very minimal) proportion of a crustal component. Thus, there is a broad but weak variation between eastern and western domains, in terms of the early history of the primitive L-U unit that dominates the lower basaltic stratigraphy. These small differences are consistent with L-U1 magmas ponding and fractionating at deeper levels than L-U2 magmas, in an environment that permitted slightly greater crustal contamination (i.e. within thicker crust) (Fig. 32). The relatively narrow compositional range for the primitive L-U1 and L-U2 magmas of the lower stratigraphy suggests a regional crustal deformation regime that permitted ascent through the full crustal column at rates rapid enough to avoid further significant compositional evolution.

However, the upper portion of the lower basalt succession in the western domains (the upper part of the Lindsays Basalt in the upper Coolgardie sequence and the upper part of the Wongi Basalt as well as the overlying Missouri Basalt in the Vetters Subgroup) is dominated by L-Ca. In contrast, with the primitive L-U units, L-Ca requires significant early contamination and homogenization of primitive magmas, prior to undergoing significant fractionation at low to mid-crustal levels, where plagioclase was stable (as indicated by positive correlations between $Mg^{\#}$ and Al_2O_3 with Al_2O_3/TiO_2 and by Al_2O_3/TiO_2 <20) (Figs 12, 24). This unit is unique to the western domains and clearly requires a change in the early ascent history of these magmas to conditions that have not affected the eastern domains at that time. Relaxing extension as the axis of rifting migrated eastwards is potentially one cause for ascending primitive magmas to stall and pond in the mid to lower crust (Fig. 32).

Middle basaltic stratigraphy

In all the regional stratigraphies, the lower basalt sequence is overlain by a sequence of komatiite and komatiitic basalt. Although not examined in this study, this c. 2705 Ma komatiite-dominated magmatism is traditionally attributed to melting in the tail of a

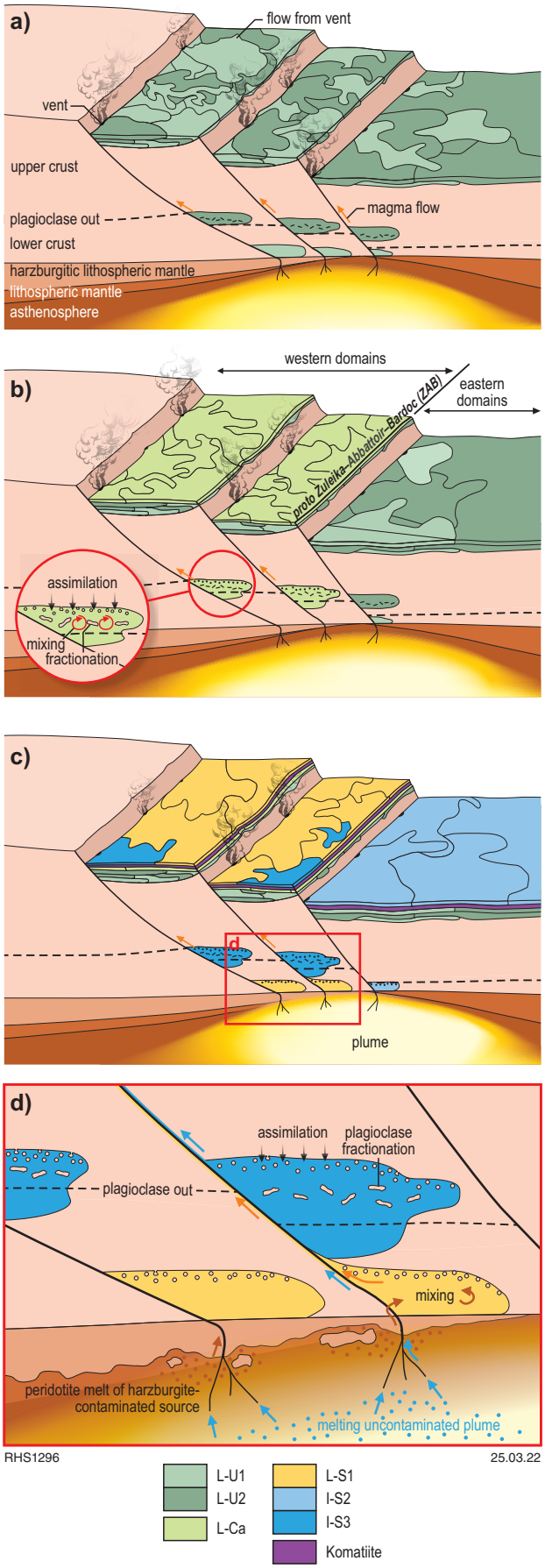

mantle plume (e.g. Campbell et al., 1989; Begg et al., 2010; Barnes et al., 2012; Mole et al., 2019) in an active magmatic rift setting. In the well-studied Hannans Subgroup of the Kambalda Domain, the stratigraphy is thought to be relatively simple, with the Kambalda Komatiite conformably overlying primitive L-U magmatism of the Lunnon Basalt (in places with an intervening shale unit) and in turn being conformably overlain by ITB of the Devon Consols Basalt. Tectonic interleaving locally complicates this stratigraphy, although in many other areas, structural complexity or magmatic interleaving typically causes significantly more complicated stratigraphy, particularly near the contacts with lower and upper basaltic sequences. It is clear, for example, that the komatiite-bearing parts of the upper Coolgardie sequence (Hampton Hill Formation), Vetters Subgroup (Walter Williams Formation and lower Big Dick Basalt), and Broad Arrow Subgroup (Highway Formation), include a much greater proportion of basalt than the Kambalda Komatiite. In the lower parts of the Hampton Hill Formation, it is not clear if L-U1 intercalated with komatiite is part of that formation or a component of the underlying Lindsays Basalt. In no other regional stratigraphy is extrusive L-U1 found above the lower basalt succession, although intrusive L-U1 forms a very minor component of major mafic sills emplaced at the end of mafic greenstone deposition.

Figure 32. Schematic block interpretation of the magmatic evolution of lower and middle parts of the mafic stratigraphy within the study region, showing the possible position of the ZAB shear zone (see text) and the contrasting magmatic evolution of the western and eastern domains. Earliest evolution of the mafic assemblages (a) involves L-U1 and L-U2 magmatism throughout the region in response to crustal extension and mantle upwelling (cause/response?) with the relative proportions of L-U1 and L-U2 decreasing eastwards as the proportion of primitive magma coming from lower crustal staging chambers, lying at pressures too high to crystallize plagioclase, decreases with crustal thinning. Eastwards migration of the point of maximum upwelling and possibly minor incorporation into L-U magmas of material from harzburgitic lithosphere lying only under the western region (b) resulted in less transient lower to mid-crustal chambers open to assimilation (i.e. L-Ca). L-U1 and L-U2 magmatism continues in the eastern domains. With arrival of an upwelling/plume head (c), regional komatiite magmatism blanketed the region. In the western domains, komatiite was preceded and followed by L-S lavas derived from ultramafic magmas formed as the outer plume margin assimilated harzburgitic lithosphere (d). Melting of slightly deeper, uncontaminated outer plume mantle, formed komatiitic to komatiitic basalt magmas that ponded in the now thermally weakened middle-crust where they fractionated plagioclase as well as assimilated surrounding country rock to produce predominately I-S3 magmas. To the east of the ZAB, beneath the eastern domains, the absence of a harzburgitic lithospheric layer meant that L-S magmas were not produced and the more extensional environment directly overlying the plume prevented crustal magma chambers forming at levels above the crust/mantle interface. Here, assimilation of thermally weakened low crust still occurred but was at pressures too high to be accompanied by plagioclase fractionation and resulted in I-S2 compositions. Dashed line approximates the position of the plagioclase-out phase boundary. Note the interpreted progressive easterly migration of the mantle-upwelling zone, which evolves into a distinct plume-like body. Harzburgitic lithosphere is interpreted to only lie west of the ZAB, based on the compositional features consistent with an influence of such a source component on specific magmas only in that region. The ZAB is, therefore, interpreted as a potential trace of a lithospheric domain boundary (see later text)

A middle basaltic succession distinctly dominated by ITB (and the I-S1–3 trend) is found in all regional stratigraphies (other than in the Bulong complex), either clearly overlying or intercalated within the upper parts of the komatiite-dominated stratigraphy. In the case of the western domains, the onset of ITB magmatism is immediately preceded by L-S magmatism, L-S1 in the case of the lower Big Dick Basalt and L-S1 and L-S2 in the case of the Hampton Hill Formation. Although constrained by only four samples, there is also a hint that minor L-S magmatism occurs at the same stratigraphic level in the Broad Arrow Subgroup.

As suggested earlier, L-S1 and L-S2 can probably be related through fractional crystallization. Like L-U1, they have high Al_2O_3/TiO_2 ratios that remain relatively constant over large decreases in $Mg^{\#}$ (>75 to <50) (Fig. 24), suggesting minimal fractionation at crustal pressures low enough to crystallize plagioclase. However, in the case of L-S1 and L-S2, Al_2O_3/TiO_2 ratios are unusually high (L-S1 ~27, L-S2 ~26), and where L-S magmas overlap in $Mg^{\#}$ with L-U magmas (other than L-U1), they typically range to slightly higher concentrations of SiO_2 and lower Ni (Fig. 33). This potentially points to a slightly more refractory harzburgitic mantle source component (possibly a modified lithospheric mantle component) than for other magmas studied here. Hence, a plausible interpretation of this magmatism involves extraction from a bulk mantle source that was mineralogically slightly discrete from that of all the other magmas (Fig. 32). L-S1 was contaminated either directly from that source (i.e. a metasomatized source) or immediately upon emplacement into the lowest crust but subsequent fractionation to L-S2 compositions was at pressures too high for plagioclase crystallization.

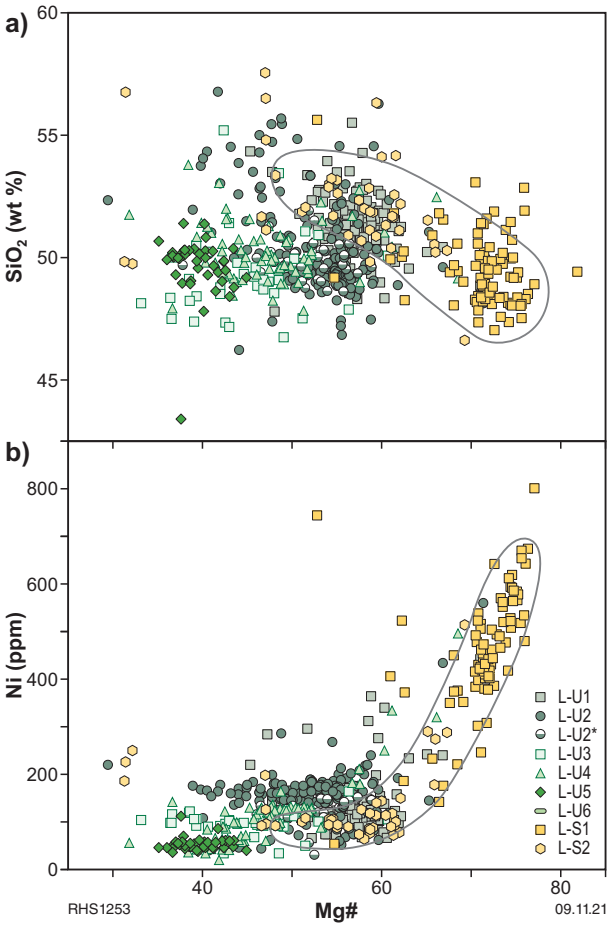

Figure 33. Variation of SiO_2 and Ni with $Mg^{\#}$ for individual LTB geochemical groups and units

The virtual absence of L-S1, L-S2, and L-Ca from the eastern domains also highlights a clear lithostratigraphic difference between the western and eastern domains. It is likely that L-U1 forms part of this association, showing some of the same geochemical attributes (e.g. higher SiO_2, lower Ni) and geographical and stratigraphic distribution as the L-S and L-Ca magmas. Because these differences between the western and eastern domains likely relate to variations in mantle source compositions and the depths at which various magmas are either contaminated or fractionated, they almost certainly reflect a variation in crustal architecture, possibly including lithospheric thickness. Hayman et al. (2015) suggested that a zone of enriched lower basalts (broadly equivalent to L-Ca) was restricted to the eastern domains and this is clearly corroborated here. Our eastern boundary to this zone is a north-northeast line comprising segments of (from south to north) the Zuleika, Abattoir and Bardoc shear zones (ZAB) (Fig. 34). Furthermore, the observation that the lower basalt (Never Can Tell Basalt) of the <c. 2720 Ma greenstone succession in the Agnew region, in the far north of the Ora Banda Domain, comprises the same enriched (L-Ca) component permits the intriguing possibility that the same lithospheric architectural controls on early basalt compositions existed in that region. It also suggests that such regional chemostratigraphic correlations may indeed be valid (Hayman et al., 2015).

Overlying komatiite in the Hannans Subgroup, or interleaved komatiites and L-S1 and L-S2 in the western domains, is a prominent succession comprising units of the I-S1–3 trend. Like the komatiite unit and the underlying L-U succession, the I-S1–3 magmas represent a reliable regional first-order stratigraphic marker, reflecting a certain stage in a process common to the greenstone stratigraphic evolution in all areas studied here. The relevance of this to greenstone evolution in other areas or of a significantly different age is unclear. The lower Coolgardie sequence, for example, contains no I-S1–3 magmas. It contains a strong crustally contaminated high-Mg ITB unit (I-VS) with compositional features transitional with HTSB and this underlies rather than overlies ultramafic units of the Brilliant Formation.

The compositional differences between the ITB in each of the stratigraphies examined here is relatively small. I-S2 represents the overwhelmingly dominant component of the Devon Consols Basalt. It is also the sole component in the upper part of the Big Dick Basalt and a major component of the lower part of the basaltic sequence overlying komatiites in the domains to the east of the Kambalda and Ora Banda Domains (although few data are available here). It forms only a very minor component of the ITB succession in the upper part of the Hampton Hill Formation, but is accompanied there by the more (I-S3) and less (I-S1) fractionated equivalents within the I-S1–3 trend. This diversity of ITB magmas is diagnostic of the upper-middle basaltic stratigraphy of the upper Coolgardie sequence. So too is an additional phase of L-S1 magmatism, forming the sole component of the overlying and regionally extensive Gleesons Basalt.

All ITB magmas of the I-S1–3 trend are derived from either L-U magmas or, more likely, komatiitic to komatiitic basalt parental magmas that were significantly more primitive (i.e. MgO rich and with a higher $Mg^{\#}$) than L-U1 or L-U2 when they underwent crustal contamination. Together, I-S1–3 magmas reflect a broad increase in the degree of crust interaction with mantle-derived magmas (e.g. Arndt and Jenner, 1986; Morris, 1993). This probably reflects their formation in the waning thermal wake of komatiite magmatism, where very primitive magmas reflecting relatively high-degree partial melts of the mantle were more readily contaminated at the base of the crust by material that was already close to solidus conditions.

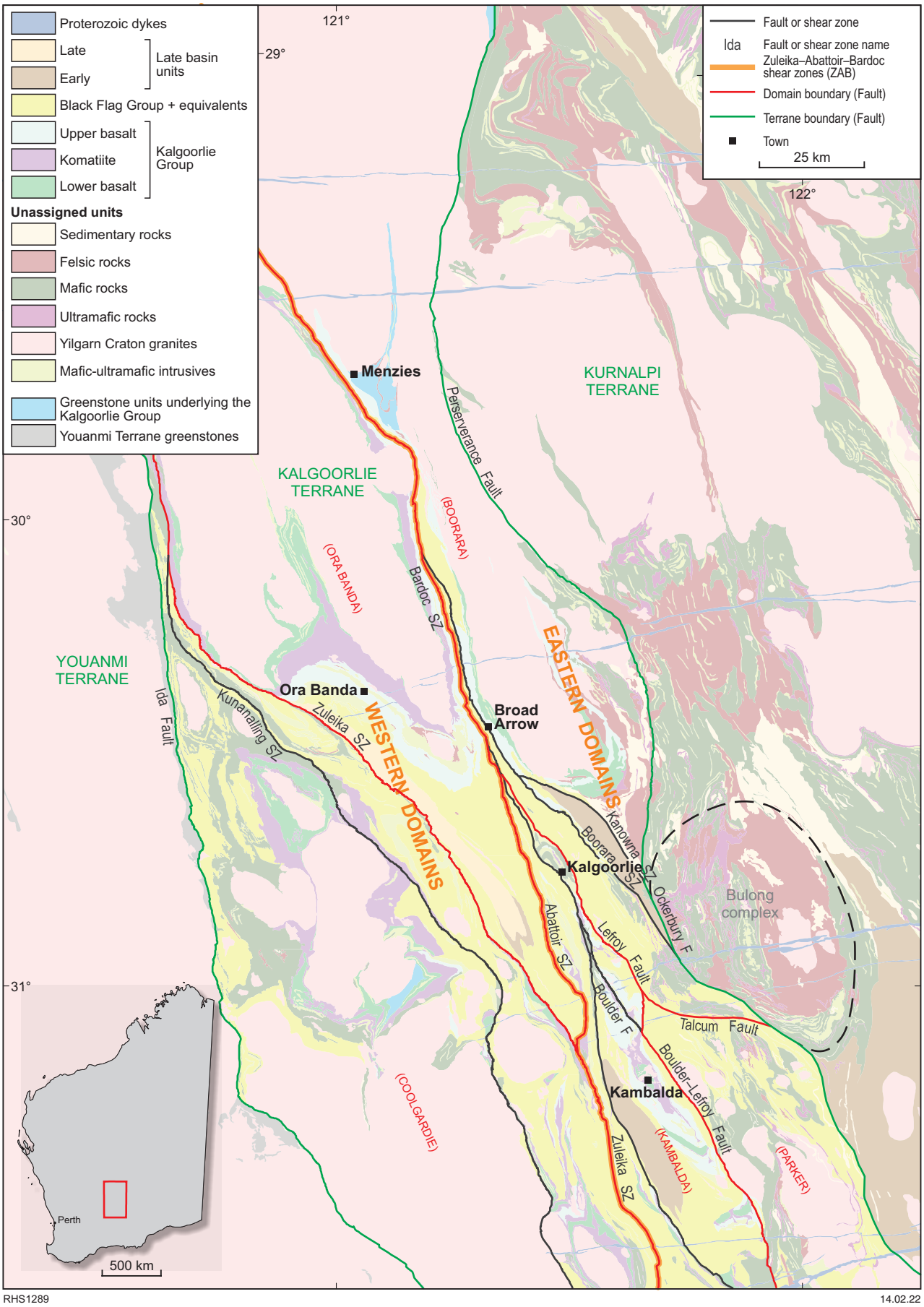

Figure 34. Geological map of the study area within the Kalgoorlie Terrane, showing a simplified version of the current interpreted bedrock geology. Also shown are the major faults and shear zones, including those forming proposed domain and/or terrane boundaries (from Cassidy et al., 2006). The trace of the combined ZAB shear zones forming a potential alternative boundary between areas of common chemostratigraphic evolution is highlighted

Upper basaltic stratigraphy

The upper basaltic stratigraphy is dominated either by HTSB or strongly fractionated LTB (LTB>>ITB) or both. A clear and important exception is the upper Coolgardie sequence, where the basaltic stratigraphy overlying the Gleesons Basalt is very poorly developed or absent. The scarcity or absence of this upper stratigraphy was noted by Swager et al. (1997) and appears to be the only significant chemostratigraphic difference between the upper Coolgardie sequence and the Vetters Subgroup.

Overall, magma diversity is perhaps greatest within the upper basaltic units of the regional stratigraphies and much of this diversity reflects processes that occurred within the upper crust. In contrast with the lower basaltic stratigraphies, where most of the extruded LTB magmas underwent relatively little compositional change since leaving the mantle, lavas in the upper basaltic stratigraphies erupted from mid- to upper crustal chambers large enough for parental compositions to fractionate to a range of evolved compositions.

Where HTSB magmatism is present, it typically forms the earliest component of the upper basaltic stratigraphy, with the Paringa Basalt of the Hannans Subgroup deposited at or after c. 2690 Ma (Carey, 1994). Although stratigraphic relationships are not as well established throughout the domains to the east of the Kambalda and Ora Banda Domains, HTSB clearly forms a dominant component within parts of these regions. HTSB is rare or absent (either does not occur or is in such low abundances that it was overlooked) in the Ora Banda and Coolgardie Domains, although rare intrusive equivalents, including notable (but younger) examples (such as Powder Gabbro) occur high in the stratigraphic sequence, close to the Zuleika Shear Zone, possibly suggesting the volcanic equivalents have been removed (eroded).

While most HTSB magmatism pre-dates deposition of the volcanosedimentary Black Flag Group (Powder Gabbro being an obvious exception), the fractionated LTB>>ITB magmatism overlying the HTSB arguably pre-dates and is syndepositional with respect to the Black Flag Group. We see no geochemical differences between the various compositions sampled from large mafic intrusions, such as the Golden Mile Dolerite and the Mount Pleasant Gabbro, emplaced within or immediately overlying the basaltic greenstone sequences, and the evolved LTB lavas forming the uppermost stratigraphic levels of the Vetters Subgroup and Highway Formation. Nor are we aware of any geochronological data that disallows such a potential genetic link. Tripp (2013, 2019) interprets the volcanosedimentary sequence of the Black Flag Group to conformably overlie the Victorious Basalt.

The LTB-dominated (LTB>>ITB) magmatism in the upper part of the upper basaltic stratigraphy forms two broad compositional groups. A group of significantly Th-enriched basalts directly overlies the Paringa Basalt in the Hannans Subgroup [L-S3a (Athena Basalt) and L-S4], overlies HTSB in the upper part of the Bulong complex (L-S3b), and forms the Bent Tree Basalt (I-S4) in the Vetters Subgroup. L-S3 (a and b) is a weakly to moderately fractionated LTB magma with major element similarities to compositions lying between L-U2 and L-U3. L-S4 is a strongly fractionated magma with compositions typical of granophyre-like magmas reflecting late-stage evolution in a high-level mafic magma chamber. Enrichments in, and ratios between, Zr, Nb, and La, in L-S3 (a and b) and L-S4 (e.g. Fig. 6) suggest evolution within an L-U3–7 chamber. However, if this were true then the distinctive and extreme enrichments in Th (>>La>Nb, Zr; Fig. 6) in these units can only be explained, if this chamber became contaminated or mixed, and homogenized prior to eruption with minor amounts of a component similar in composition to HTSB. Given their stratigraphic position in the upper part of the Hannans Subgroup (or upper Highway Formation in the case of L-S3b), this is a clear possibility. Similarly, I-S4 compositionally resembles L-S4 in many respects and can be broadly modelled through mixing and homogenizing a relatively small amount (~20%) of HTSB into an L-Ca chamber.

The second broad compositional group of LTB>>ITB magmas in the upper part of the upper basaltic stratigraphies belongs to the L-U3–7 trend. These form the lavas of the Victorious Basalt at the top of the Vetters Subgroup, and lavas contributing to the upper mafic stratigraphy of the Boorara and Parker Domains. They derive from upper crustal chambers large enough for parental L-U2 (>>L-U1) compositions to fractionate to a range of evolved compositions. Large mafic intrusions, such as the Golden Mile Dolerite and the Mount Pleasant Gabbro, emplaced within or immediately overlying the basaltic greenstone sequences between 2690 Ma and 2680 Ma are the youngest and uppermost crustal level expressions of these chambers. Their compositional range essentially mimics that of the L-U2 and L-U3–7 lavas (Table 3). These intrusions include fine-grained, quenched, L-U2 marginal facies material. In the case of the Golden Mile Dolerite, L-U2 forms peperitic contacts with the host sedimentary rocks of the Black Flag Group (McMann, 2018; Cas et al., 2019).

Thus, during deposition of the upper basaltic stratigraphic levels, conditions favourable for the establishment and maintenance of mid- to upper crustal magma chambers prevailed, perhaps for the first time, at least in the evolution of the greenstones of the eastern domains. However, evidence that mixing and homogenizing between HTSB and already-ponded L-U3–7 chambers produced a range of unusual hybrid compositions, also reflects a dynamic mid- to upper crustal environment that apparently did not exist in the Coolgardie region, west of the Zuleika Shear Zone.

Hence, in broad terms, the three commonly identified regional stratigraphic levels (lower, middle and upper, e.g. Swager et al., 1990) correspond to changes in tectonomagmatic processes. However, the distribution of the subgroups, processes, and products is distinctly asymmetric, producing regional-scale chemostratigraphic differences (e.g. Hayman et al., 2015) between the western and eastern domains that probably reflect a fundamental crustal architectural control and potentially provide some basis for reassessing present domain boundaries. The boundary between the two regions – the ZAB (Fig. 34) – separates a region to the west characterized by slightly thicker crust (no plagioclase fractionation in L-U1), earlier crustal contamination of primitive magmas, a broadly more refractory bulk mantle source, and a mafic magmatic history missing a significant upper stratigraphy, from the eastern domains (Kambalda, Boorara and Parker Domains and possibly also the Bulong complex). The Ora Banda Domain is clearly a part of the western domains throughout evolution of the lower and middle greenstone stratigraphic evolution, but also appears transitional to the eastern domains in terms of its upper stratigraphy characterized by the diversity of fractionated L-U3–7 magmatism formed in and erupted from layered sills.

Felsic rocks

Introduction

Felsic rock samples (andesite to rhyolite; i.e. intermediate and acid) taken during this study are mainly from plagioclase (±hornblende or quartz) porphyritic dykes or sills, representing subvolcanic intrusions and from the volcanic or volcaniclastic rocks, including probably poorly sorted and very immature proximal turbidite units. The majority of these samples are from the Black Flag Group, which is interpreted to have been deposited between 2690 and 2665 Ma across all of the domains of the Kalgoorlie Terrain within the study area. However, the presence of older felsic volcanic rocks is speculated within the lower Coolgardie sequence, and demonstrated at numerous localities within the study area. For example, felsic tuff and andesite-derived sandstone interleaved with ultramafic rocks have been dated at 2705 ± 4 Ma (Nelson, 1995a) and 2708 ± 5 Ma (Barley et. al., 2002) respectively, from the Bulong complex. Similarly, dacite interbedded with komatiite from the Highway Formation (Boorara Domain) has been dated at 2708 ± 7 Ma (Nelson, 1995b).

It is important to note there is no clear difference in the composition or compositional range of the intrusive, volcanic, and volcaniclastic rock populations; i.e. no evidence that a specific depositional process has significantly modified the primary magmatic compositions. Of the original set of 845 samples, filtering for alteration eliminated a total of 213 (~25%) samples. Approximately 50% of these were excluded based on a high ASI [molar $Al_2O_3/(CaO+Na_2O+K_2O)$] up to 2.2, reflecting a secondary alteration or significant sedimentary reworking or both. After filtering, the remaining samples were grouped based on distinct compositional trends reflecting igneous processes. At this stage, the samples initially removed from the dataset based on alteration screens were compared with the various geochemically classified groups. Considering only fluid immobile geochemical components, 113 of the altered samples could be confidently matched to a geochemically classified group. These altered samples were not considered for any petrogenetic interpretations but were used to examine the spatial distribution of the geochemically classified groups.

The majority of subvolcanic intrusions and associated volcanic or volcaniclastic deposits forming the Black Flag Group have been shown to have the composition of sanukitoids and comprise one of the first recognized examples of Archean sanukitoid volcanic rocks, and one of the most voluminous intrusive/extrusive Archean sanukitoid systems globally (Smithies et al 2018b). Sanukitoids are relatively rare hornblende-bearing rocks, typically in the monzonitic to dioritic and granodioritic (andesitic to dacitic but reaching rhyolitic) compositional range. They have been attributed to direct extraction as low-degree felsic partial melts from a hydrated mantle source (Shirey and Hanson, 1984; Smithies and Champion, 2000). However, more recently they have been interpreted to be (or include examples that are) fractionated from mafic to ultramafic parental magmas (including calc-alkaline lamprophyres), themselves partial melts of metasomatically hydrated and enriched mantle lithosphere (Smithies et al., 2018b, 2019). Sanukitoids are amongst the most hydrated and oxidized Archean magmas and their presence implicitly defines a translithospheric plumbing system that transferred fertile mantle material to upper crustal levels (Smithies, 2019; Smithies et al., 2019). In the Yilgarn Craton and other Archean regions, sanukitoids have a clear spatial and temporal association with gold mineralization (Champion and Cassidy, 1998; Witt et al., 2013, 2015; Fayol and Jébrak, 2017). In the Eastern Goldfields, many of the structures used as magma pathways by sanukitoids are faults that also played a primary role in the structural evolution of the 2664–2657 Ma sedimentary basins (Late Basins – Fig. 2) that overlie the Black Flag Group. Smithies et al. (2018b) and Smithies (2019) suggest Black Flag Group magmatism represents a long-lived, multiphased, crustal-scale magma system that along with the associated hydrothermal systems fueled by exsolved magmatic water and water entrained from intrusion-related country-rock fluid convection had the capacity to transfer large amounts of Au from the mantle source and crustal pathways, into the upper crust (Fig. 35). These systems are envisaged to resemble modern porphyry copper systems in many respects, including their distinctive high Sr/Y primary magmatic composition. As suggested in the case of many Archean gold deposits in the Abitibi Subprovince of the Canadian Superior Province (Fayol and Jébrak, 2017), the apparent orogenic characteristics of many gold deposits in the Eastern Goldfields, may reflect the upgrading of pre-existing magma-related concentrations during post-c. 2680 Ma orogenic-style deformation (Smithies et al., 2018b; Smithies, 2019). This is supported by sulfur isotope studies on Eastern Goldfields gold deposits that have shown early mineralizing fluids with mantle-like isotopic compositions overprinted by late-stage mineralizing fluids with crust-derived sulfur (e.g. Thébaud et al., 2018; Sugiono et al., 2021).

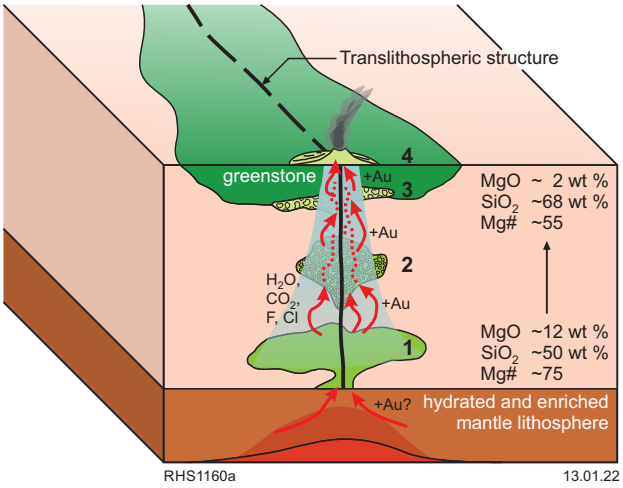

Figure 35. Schematic diagram showing the potential relationship between sanukitoid magmatism (e.g. Black Flag Group), translithospheric structures and gold mineralization (Smithies, 2019). We suggest that sanukitoids can form long-lived, multiphased, crustal-scale magma systems involving multiple staging chambers, where magmas undergo variable degrees of hornblende-dominated fractionation and frequent recharge events that typically incorporate a cargo of partially to largely crystallized material from earlier sanukitoid magma batches (i.e. 'cognate' xenoliths). Composite lower crustal chambers are filled with primitive, mantle-derived lamprophyric to high-Mg dioritic magmas (1 in Fig. 35), with subsequent higher-level chambers (2–3 in Fig. 35) having sequentially more evolved bulk compositions. In rare cases, such as the Black Flag Group, eruption of sanukitoid material occurs (4 in Fig. 35). Significant hornblende fractionation results in early and ongoing exsolution of strongly oxidized magmatic fluids. The associated hydrothermal systems (red arrows and blue screen) fuelled by this exsolved magmatic water, and by country-rock fluid convection, have the capacity to transfer large amounts of Au and other metals originating from magmatic (enriched mantle) and country-rock sources into the upper crust. In this respect, it might be irrelevant whether the primary lamprophyre/sanukitoid magmas and their mantle source regions were intrinsically Au rich, since the sanukitoid-related crustal-scale magmatic/hydrothermal system had the capacity to sequester metals over the entire crustal column. The volcanic environment exposed by the Black Flag Group also offers the opportunity for epithermal type processes to further enrich the country rock systems in Au, prior to any late upgrading caused by orogenic processes (e.g. Fayol and Jébrak, 2017)

Classification of felsic rocks

A workflow for classifying felsic rocks is provided in Appendix 5. Figure 36 attempts to graphically show aspects of this workflow. Although this classification is based primarily on geochemical data, the geographical and lithological association of the samples and mineralogy remain extremely important considerations. Sanukitoids typically have quite specific field appearances and mineralogy, particularly at the lower silica end of their compositional range, where they are invariably hornblende-rich and often contain cognate (hornblende-plagioclase±pyroxene) xenoliths. However, at silica contents higher than ~68 wt%, sanukitoids and High-Ca granites can be virtually impossible to distinguish from geochemistry alone; field association or relationships, and mineralogy become critical factors in classification. Similarly, High-Ca granites are typically plagioclase-rich and K-feldspar-poor, but can fractionate to K-feldspar-bearing examples that geochemically resemble Low-Ca granites.

The granite classification scheme of Champion and Sheraton (1997) and Cassidy et al. (2002) was initially applied to the felsic rocks within the study area. This classification divides Archean granites into five broad groups including:

- High-Ca granites, typically with SiO_2 >68 wt% and a compositional range broadly consistent with the Archean tonalite–trondhjemite–granodiorite (TTG) suites, reflecting deep crustal melting of dominantly mafic source regions
- Low-Ca granites, typically also with SiO_2 >68 wt% but generally more potassic in composition (broadly equivalent to Archean K-rich granite series) and more enriched in incompatible trace elements, reflecting higher temperature melting of dryer, more heterogeneous and slightly more refractory sources, including mafic crust and earlier-formed TTG crust
- HFSE granites, that are generally very silica rich (SiO_2 >70 wt%), Fe rich, and strongly enriched in Nb, Zr, and REE, and commonly showing characteristics consistent with the involvement of tholeiitic parental magmas or sources
- Syenites, typically very alkali rich, quartz-poor, and Fe-rich rocks, also enriched in Nb, Zr, and REE, and in large ion lithophile elements (LILE) such as Sr and Ba. They are thought to be derived through melting of a metasomatically enriched deep lithospheric source (Smithies and Champion, 1999)
- Mafic granites, typically hornblende-bearing rocks showing a wide range of silica concentrations upwards of ~57 wt% with a significant proportion of samples with SiO_2 <68 wt%. Sanukitoids form a large component (>50%) of this group. The remainder includes suites that have $Mg^{\#}$, and/or Cr, Ni, and/or Sr or Ba concentrations lower than expected for sanukitoids, but generally slightly higher than is typical of modern calc-alkaline magmas, possibly as a result of a hotter Archean mantle (e.g. Barnes and Van Kranendonk, 2014).

Since sampling was primarily directed at greenstone successions, the emphasis was on volcanic, volcaniclastic rocks or subvolcanic intrusions. For the most part, sampling of large plutonic bodies was avoided. Nevertheless, it is somewhat surprising that very few clear examples of felsic rocks with compositions similar to Low-Ca granites were identified despite these being the regionally dominant felsic magma type and mainly formed in the period immediately post-dating the evolution of the Black Flag Group.

The entire felsic dataset (Fig. 37) was divided between samples with compositions equivalent to:

- Mafic granites 87% – of which 66% are true sanukitoid and 34% are sanukitoid-like High-Ca granites (10%)
- HFSE granites (3%)
- Low-Ca granites (<<1%).

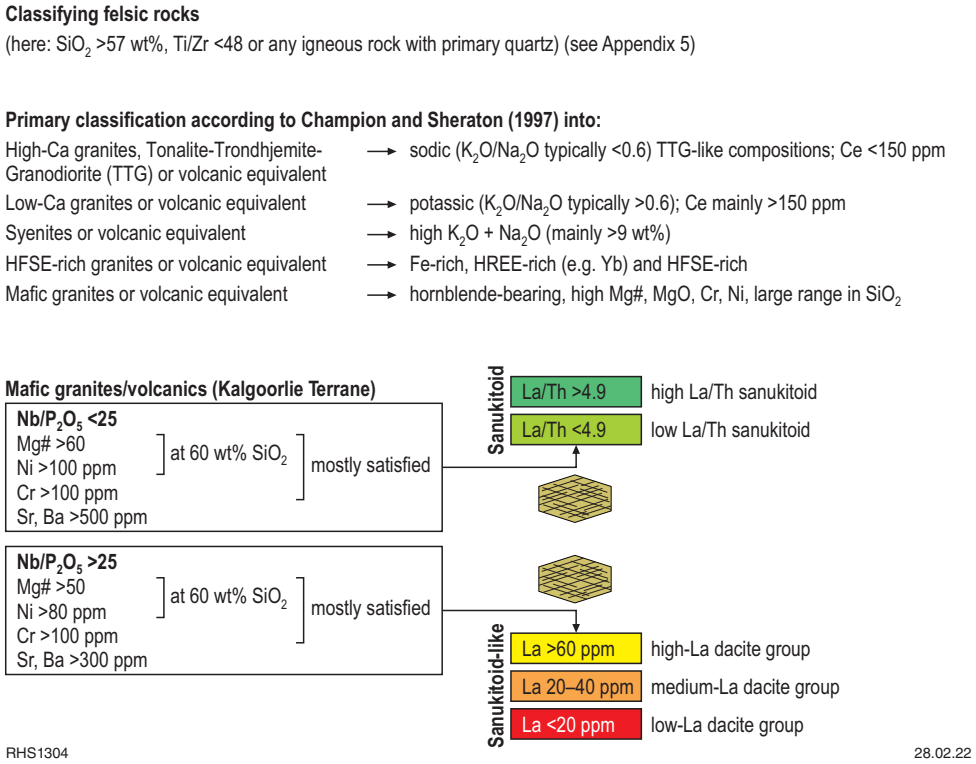

Figure 36. Flow sheet explaining the methodology used here to classify felsic units

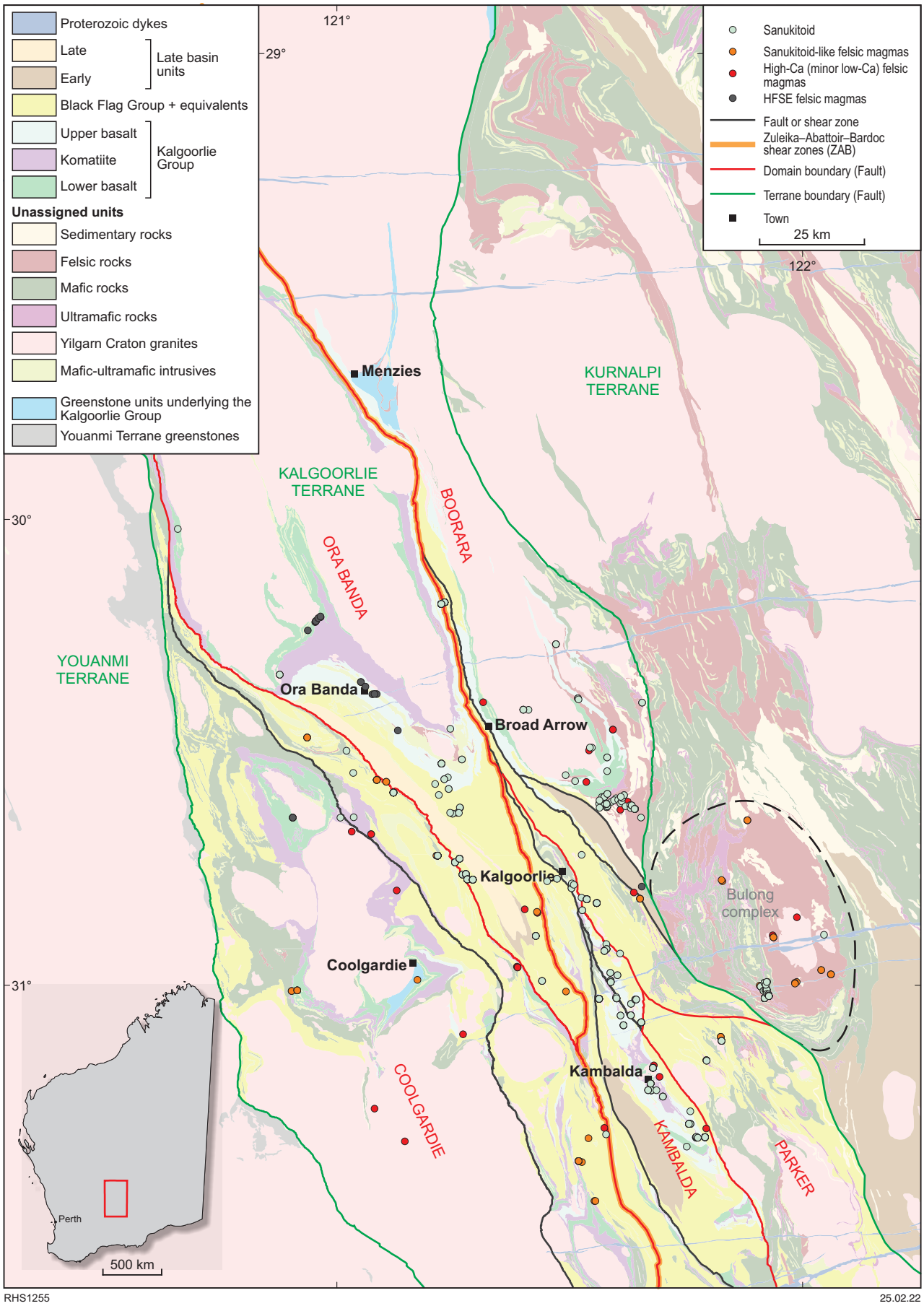

Figure 37. Geological map of the study area within the Kalgoorlie Terrane, showing the distribution of samples of various felsic volcanic and subvolcanic rock studied here (see Figure 34 for fault names)

Rocks compositionally equivalent to Mafic granites

Sanukitoids

Geochemical identification of sanukitoids is not always straightforward and is particularly problematic in populations that contain few samples with silica contents below ~65 wt%. Felsic rocks with low silica contents are relatively uncommon in Archean terrains. They are, however, unusually common in the Kalgoorlie–Kambalda region, particularly in the Black Flag Group. Strictly, a sanukitoid suite should be a geochemically coherent (genetically related) group of relatively sodic (K_2O/Na_2O <1.0) rocks, which at low silica values (at 60 wt% SiO_2 or reasonably extrapolated to that value), are dominated by members with $Mg^{\#}$ ≥60, Cr and Ni concentrations ≥100 ppm, Sr and Ba concentrations ≥500 ppm, and La concentrations ≥25 ppm. Concentrations of HFSE, including Nb and Zr, largely depend on the extent and nature of metasomatic enrichment of the mantle source, i.e. either fluid mediated (low HFSE) or melt mediated (higher HFSE) (Smithies and Champion 2000). At silica content >68 wt% sanukitoid is very difficult to geochemically distinguish from High-Ca granites or rocks of TTG suites. Smithies et al. (2019) suggest some High-Ca granites or TTGs, particularly those showing flat mantle-normalized HREE patterns that reflect hornblende fractionation, are probably fractionated sanukitoids. Nevertheless, at least at silica contents approaching 68 wt%, most sanukitoid suites (and Mafic granites, and volcanic equivalents) should still range to a higher $Mg^{\#}$ and higher Ni and Cr concentrations.

From a more practical point of view, the important aspects of a sanukitoid petrogenesis emphasize derivation from a highly MgO-rich hydrated source. Therefore, any magmatic series that includes low silica (<~65 wt%) members containing abundant primary hornblende, and characterized by anomalously high $Mg^{\#}$, and Cr and Ni concentrations, might also be considered sanukitoid-like (Fig. 36).

Most of the felsic magma series in the Kalgoorlie–Kambalda region that satisfies all or most aspects of the sanukitoid definition (Fig. 38) has a Nb/P_2O_5 ratio <25, whereas most of the other felsic magma types have higher ratios (Fig. 39). Whilst this discrimination appears to be useful for the Kalgoorlie–Kambalda region, even here it fails to identify all relatively hydrated sanukitoid-like magmas (see low-La dacites below). The concentrations of both Nb and P are likely to be strongly related to lithospheric mantle-enrichment processes. We do not recommend the application of this discrimination plot to other regions without further testing.

Nevertheless, considering only the sanukitoids from the Kalgoorlie–Kambalda region (Nb/P_2O_5 ratio <25 where P_2O_5 >0.1 wt%), two main groups – high La/Th sanukitoid (La/Th ≥ 4.9) and low La/Th sanukitoid (La/Th <4.9) – can be distinguished using a plot of La vs Th (Figs 40, 41). These groups are broadly equivalent to the high- and low-LILE subgroups of Mafic granites described by Champion and Cassidy (1998). Both high- and low-La/Th sanukitoid groups span the full silica range from <8 to >75 wt% (Fig. 42). A third, smaller, group has La/Th <4.9, but is restricted to high silica values between 70 wt% and 74 wt%. It has incompatible trace element patterns similar to those of high La/Th sanukitoid, but which are also transitional with silica-rich examples of low La/Th sanukitoids. We referred to this third group as evolved low La/Th sanukitoid (Fig. 40). It shows an extensive overlap with rocks that have compositions equivalent to High-Ca granites (Figs 42–44) (see below) but typically has higher Th and LREE concentrations and lower HREE concentrations. Hence, they have higher La/Yb and Th/Yb ratios as well as higher La/Nb and Sr/Y ratios (Figs 43, 44).

The low La/Th sanukitoid group can be further subdivided. A small subgroup of samples, the P-rich low La/Th sanukitoid subgroup, forms a distinct high-Th (U)-LREE trend. It is characterized by typically higher P_2O_5 concentrations (generally >0.24 wt%) (Fig. 42), although all other major element variations are within those of the main low La/Th sanukitoid group. This subgroup also has distinctly high La/Nb, Th/Nb, and Nd/Zr ratios reflected in mantle-normalized trace element patterns showing more steeply fractionated profiles with a distinct negative Zr (Hf) anomaly (Fig. 45).

The high La/Th sanukitoid group can be further subdivided based on distinctive trends in plots of Ni (and Cr) against SiO_2, which identify a low-Ni subgroup (low-Ni group referred to only where a distinction is required) (Fig. 43). The low-Ni sanukitoid has Ni values lower than those of typical sanukitoids but clearly meets all other requirements of the classification. There is a considerable overlap in Cr, Ni, MgO, and $Mg^{\#}$ between these two subgroups at high silica content, and other than for Cr, Ni, MgO, and $Mg^{\#}$, they are compositionally indistinguishable across the entire silica range (Figs 42, 43).

High La/Th sanukitoids have distinctly more radiogenic Nd-isotope compositions (Table 4), with initial $\varepsilon_{Nd\ (2690\ Ma)}$ values between 1.5 and 2.7 (a single outlier with a value of −3.28 almost certainly reflects an analytical problem and is not considered further), compared with a range for all types of low La/Th sanukitoids between 0 and 0.8 (Fig. 46).

Non-sanukitoid samples compositionally equivalent to Mafic granites

A large population of subvolcanic, volcanic, and volcaniclastic rocks with Mafic granite compositions has La/Th ratios overlapping those of the high and low La/Th sanukitoid groups, but has Nb/P_2O_5 ratios >25 (see 'Other local sanukitoid-like magmas' in Fig. 39). Three groups can be recognized based on distinctive mantle-normalized trace element patterns (Fig. 45d) and are reasonably well distinguished based on their La concentrations (Fig. 43). These will be referred to here as low-, medium- and high-La dacites, noting that the low-La dacite group also includes abundant andesite and the medium- and high-La dacite groups also include rhyolite.

Low-La dacites (La <20 ppm) have relatively flat mantle-normalized trace element patterns with La/Yb ratios <20 and clear positive normalized Zr (Hf) anomalies (Nd/Zr <0.15). Medium-La dacites (La = 20–60 ppm) have more steeply inclined mantle-normalized trace element patterns (La/Yb = 15–70) with only very subtle positive or negative mantle-normalized Zr (Hf) anomalies (Nd/Zr = 0.125 – 0.25). High-La dacites (La>70 ppm) have steeply inclined mantle-normalized trace element patterns (La/Yb >60) and clear negative mantle-normalized Zr (Hf) anomalies (Nd/Zr >0.275). All three types have a range of initial $\varepsilon_{Nd\ (2690\ Ma)}$ values between 0.25 and 2.1, overlapping the range for the high La/Th and low La/Th sanukitoids (Fig. 46).

Apart from generally lower LREE concentrations, the low-La dacites have compositions that closely approach those of sanukitoids, with relatively high $Mg^{\#}$ (mainly 50–55 at 60 wt% SiO_2), Ni (75–100 ppm at 60 wt% SiO_2), and Sr and Ba (both mainly ~300 ppm at 60 wt% SiO_2) concentrations. The concentrations of Cr (at 60 wt% SiO_2) are typical of sanukitoids and the low $Mg^{\#}$ can be attributed to high FeO rather than low MgO, with MgO concentrations within the range for true sanukitoids at a given silica value. We consider these rocks to be sanukitoid-like.

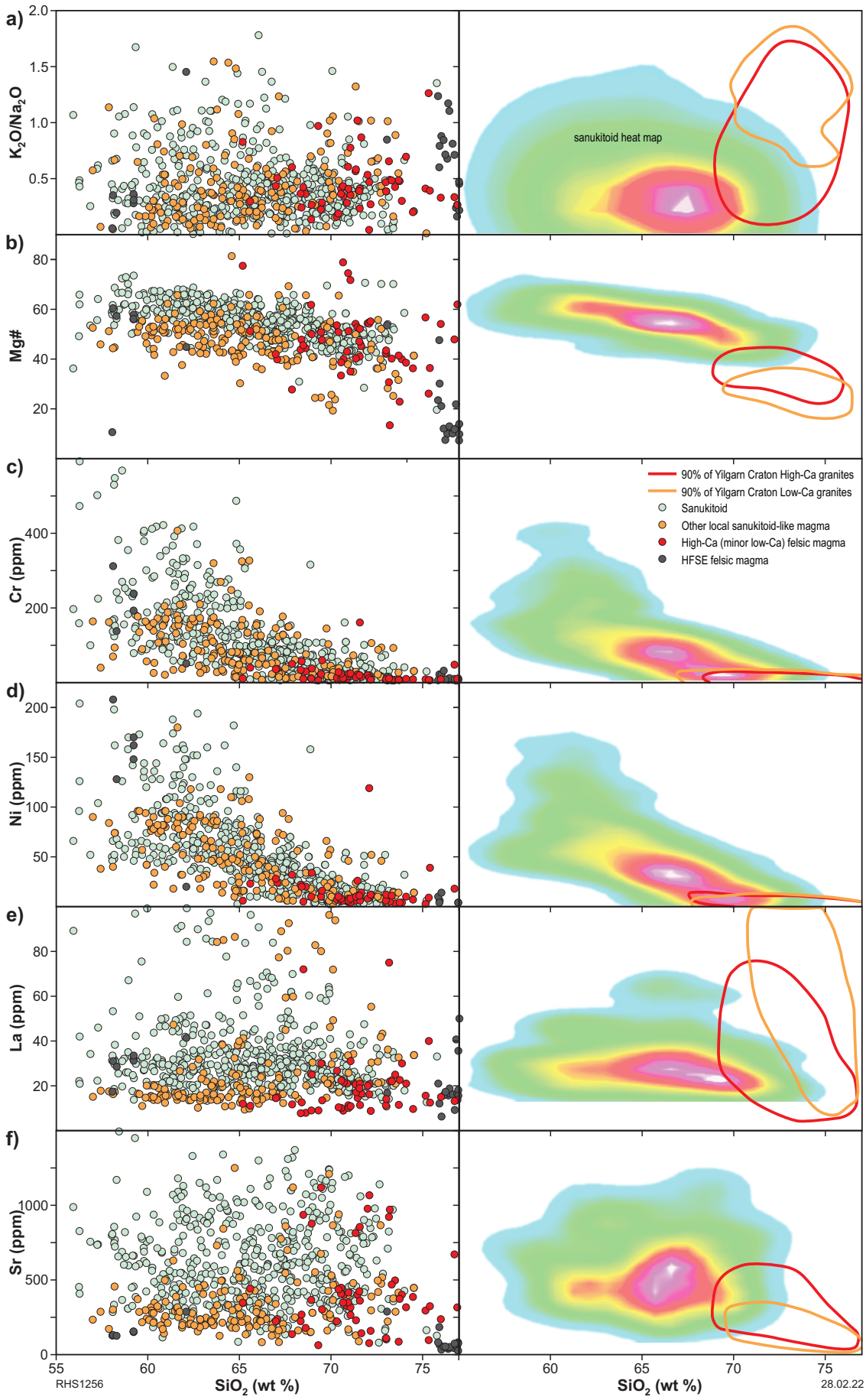

Figure 38. Variation with SiO_2 of various chemical parameters considered useful in the identification of sanukitoids, including K_2O/Na_2O, $Mg^{\#}$, Cr, Ni, La, and Sr. Right-hand column shows heat maps that outline the relative sample density for >95% of sanukitoid samples (hotter colours represent high density of samples) and compares them with the compositional range for High- and Low-Ca granites from the Yilgarn Craton

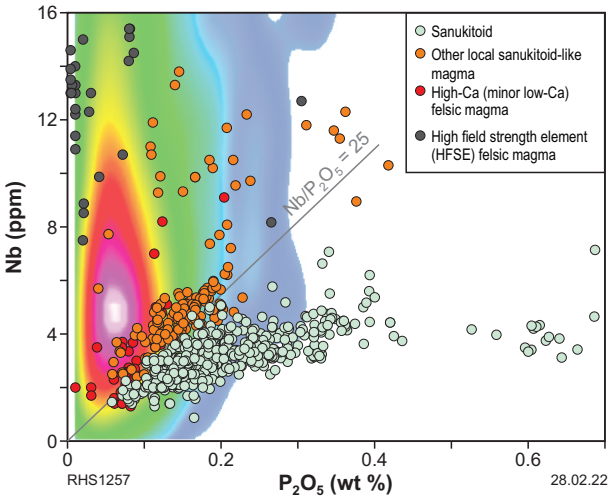

Figure 39. Variation of Nb with P_2O_5 highlighting the compositional contrast between sanukitoids and other felsic rock groups. The heat map shows a density distribution of >90% of granites (other than the Mafic granites) from the Yilgarn Craton

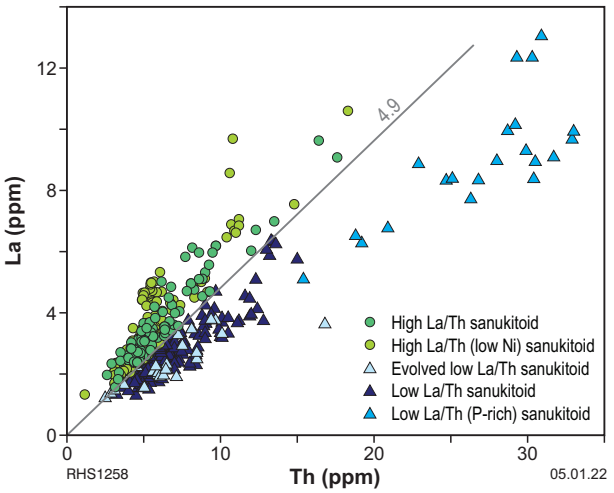

Figure 40. Variation of La with Th for rocks classified as sanukitoids

Nevertheless, the low-La dacites have slightly lower LILE concentrations than typical sanukitoids, and are enriched in HFSE (Ti, Nb, and Y) and HREE and depleted in LREE, with lower La/Nb ratios (Figs 43, 44). The possible explanations for these differences include derivation from a source that was more mafic (e.g. basaltic crust), rather than ultramafic, and less metasomatically enriched than the source for the sanukitoids. Alternatively, the differences might indicate mixing (diluting) of primitive sanukitoid magmas with contemporaneous basaltic magma. It is interesting to note that the high silica end of the compositional range for the low-La dacites merges with the range for local High-Ca granites and these two magma types share a similar geographical range. Hence, an additional hypothesis is that the low-La dacites reflect mixing of a mantle-derived mafic magma with high-Ca felsic crustal melts (or any average Archean felsic component). Barnes and Van Kranendonk (2014) constructed this model to explain the compositions of widespread low-La andesitic to dacitic rocks that formed within the main 2708–2690 Ma period of mafic magmatism in the Kurnalpi Terrane. However, in the case of the low-La dacites in the central Kalgoorlie Terrane, extrapolating the composition of available felsic components through the composition of the lowest-silica low-La dacites (at ~57 wt% SiO_2) to silica contents appropriate for a mafic end-member to any binary mix, identifies a putative mafic end-member with $Mg^{\#}$ >50, TiO_2 >1.0 wt%, P_2O_5 >0.2 wt % and a significant positive mantle-normalized Zr (Hf) anomaly. None of the mafic magmas studied here, except for mafic sanukitoid or the lamprophyres described by Smithies et al. (2018b) meet all these criteria.

Compared with the medium- and high-La dacites, the low-La dacites show a slightly narrower range in silica, but a significantly narrower range in incompatible trace element ratios (La/Sm, La/Yb, Th/Yb, Th/Zr, Dy/Yb) (Fig. 44) sensitive to fractionation of common igneous mafic minerals (e.g. hornblende and pyroxene). Visual descriptions of the low-La dacites indicate hornblende porphyritic intrusive and amygdaloidal (subvolcanic and volcanic) rocks with a very inhomogeneous distribution of mafic and felsic minerals resulting in mafic accumulations, and hornblende-rich layers, bands, and clots. Hence, it is possible that a significant proportion of the silica variation in the low-La dacites might reflect physical processes related to mixing and unmixing of mafic and felsic mineral components, perhaps during eruption from and/or recharge of high-level crystal-rich magma chambers. However, the relatively constant Nb and Th concentrations irrespective of silica content do not support this model. The prospect of an intermediate rather than mafic parental liquid permits the suggestion that these are lower crustal melts rather than mantle melts. However, most $Mg^{\#}$ values concentrate in the 50–55 range, 20% of the rocks have higher Mg#, with <10% of the population having Mg# >60. Such values appear inconsistent with experimental data that suggests that the $Mg^{\#}$ of intermediate melts of mafic crust are typically <40 (Lu et al., 2015). Hence, irrespective of the processes that have promoted compositional variation within the low-La dacites, it seems likely that their parental magmas included mafic melts of hydrated mantle. Our preferred petrogenetic model is that the low-La dacites represent hybrid magmas formed through early mixing of sanukitoid and basaltic magmas.

Medium-La and high-La dacites show many compositional similarities with low-La dacites but extend to more felsic compositions, have steeper (more fractionated) mantle-normalized trace element patterns with minimal or positive Zr anomalies, higher Na_2O+K_2O, and higher FeO and/or lower MgO (and correspondingly lower $Mg^{\#}$ <50) at a given silica content (Fig. 42). The high-La dacites also consistently have high concentrations of other incompatible trace elements including Th, Nb, MREE, and Zr, in some cases similar to (e.g. Th) or greater than (e.g. Nb) the enrichments seen in the sanukitoids (Fig. 43). The medium-La dacites show more scattered enrichments in these trace elements, although typically at higher concentrations than seen in the low-La dacites.

Champion and Cassidy (1998, 2002a,b) show that the Mafic granites of the Eastern Goldfields region can be divided into a series of geochemical populations based on minor variations in major and trace element compositions, probably reflecting similar ranges in the bulk source compositions. These authors recognized two broad end-members – low- and high-LILE – which they subdivided into a number of subgroups (clans). The medium-La dacites have compositions very similar to what Champion and Cassidy (2002a) called the Kanowna Belle clan. The enrichments in incompatible trace elements seen in the medium-La dacites make a petrogenesis through mixing basaltic and felsic (TTG) magmas very unlikely, as with the low-La dacites.

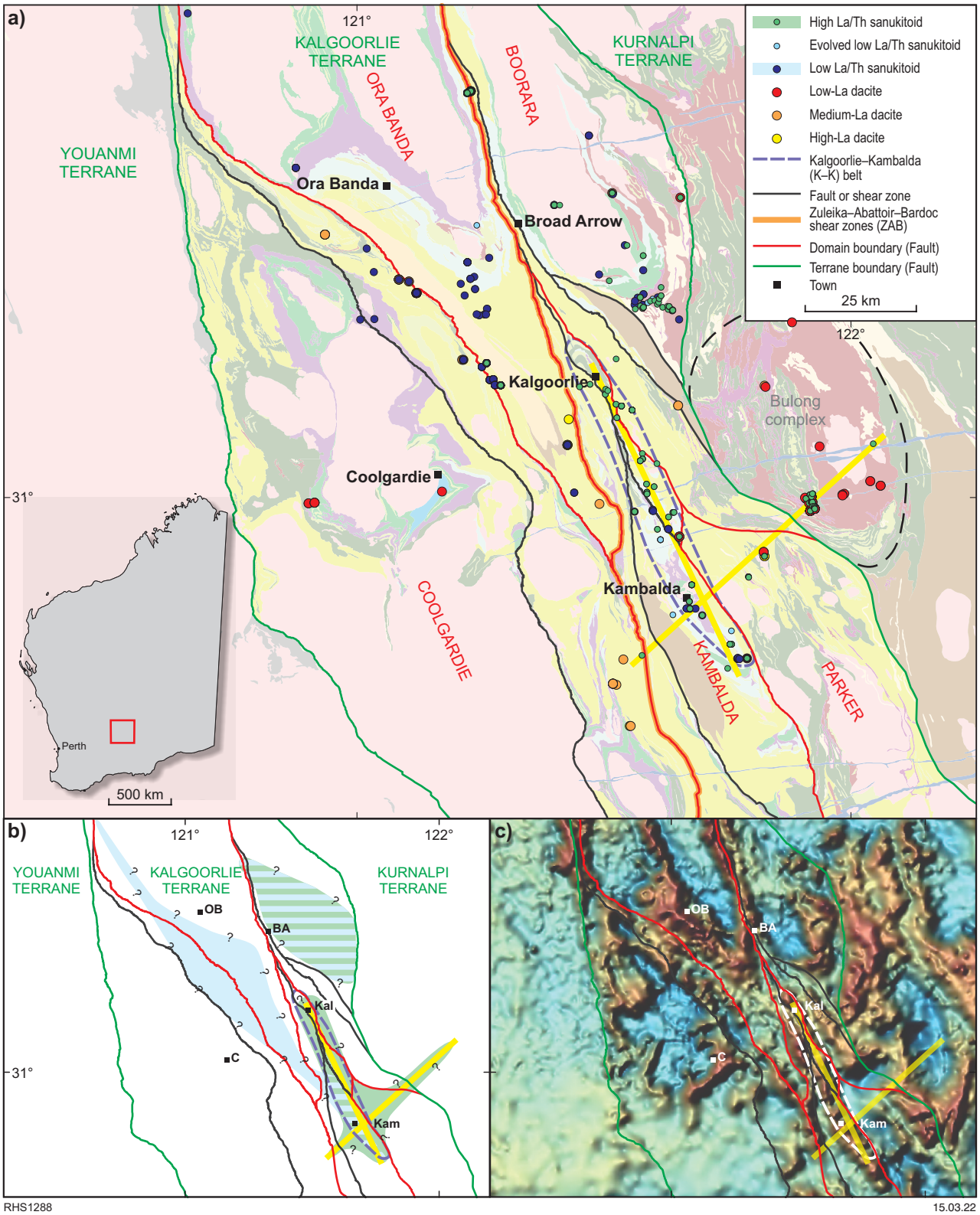

Figure 41. Geological map of the study area within the Kalgoorlie Terrane showing a) the distribution of samples of the various sanukitoid types as well as high-, medium-, and low-La dacites. Also shown is the Kalgoorlie–Kambalda belt (K-K belt: dashed line) and other apparent trends outlined by the sanukitoids (yellow). A summary of these trends and the broad outline of sanukitoid distribution is given in b) and c) compares this distribution with potential trends identified in regional geophysical datasets (in this case 0.5VD Bouguer gravity) (see Figure 34 for fault names)

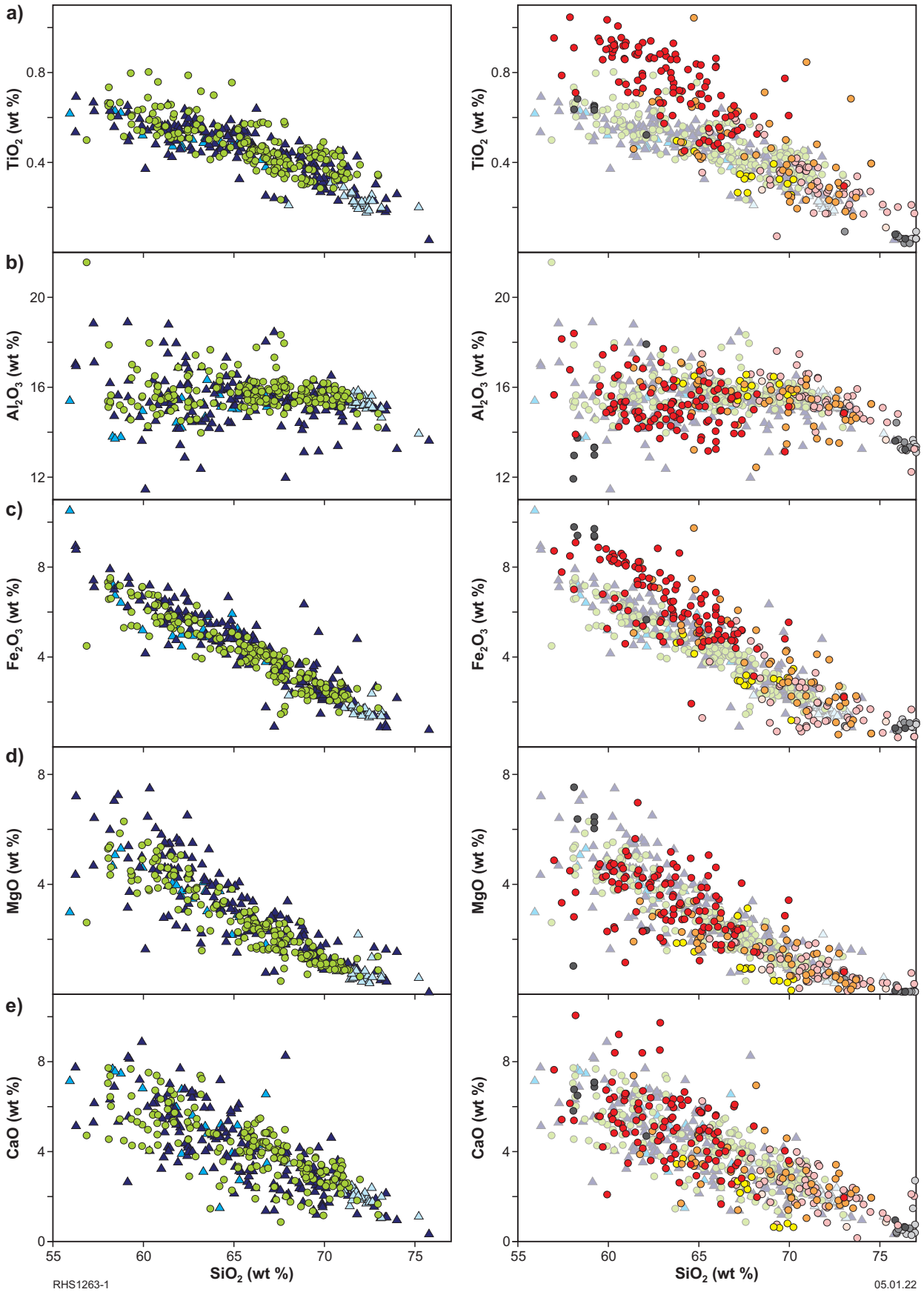

Figure 42. Variation in major elements and Mg# with SiO_2 for the various felsic rock types. The left-hand column shows sanukitoids. The right-hand column shows the sanukitoid-like rocks (low-, medium-, and high-La dacites) and other felsic units (bold symbols) and compares them with the sanukitoids (faded symbols)

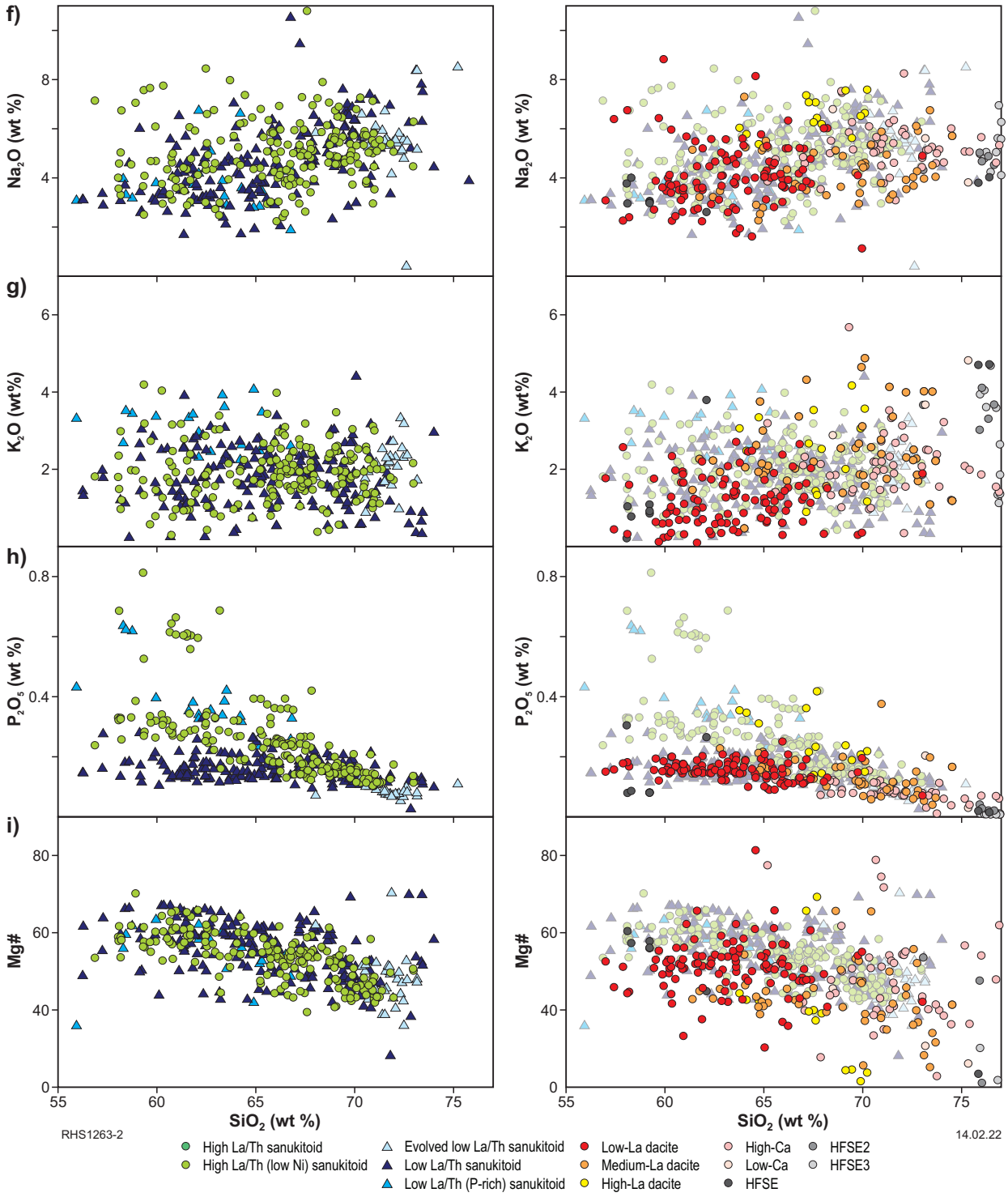

Figure 42. continued

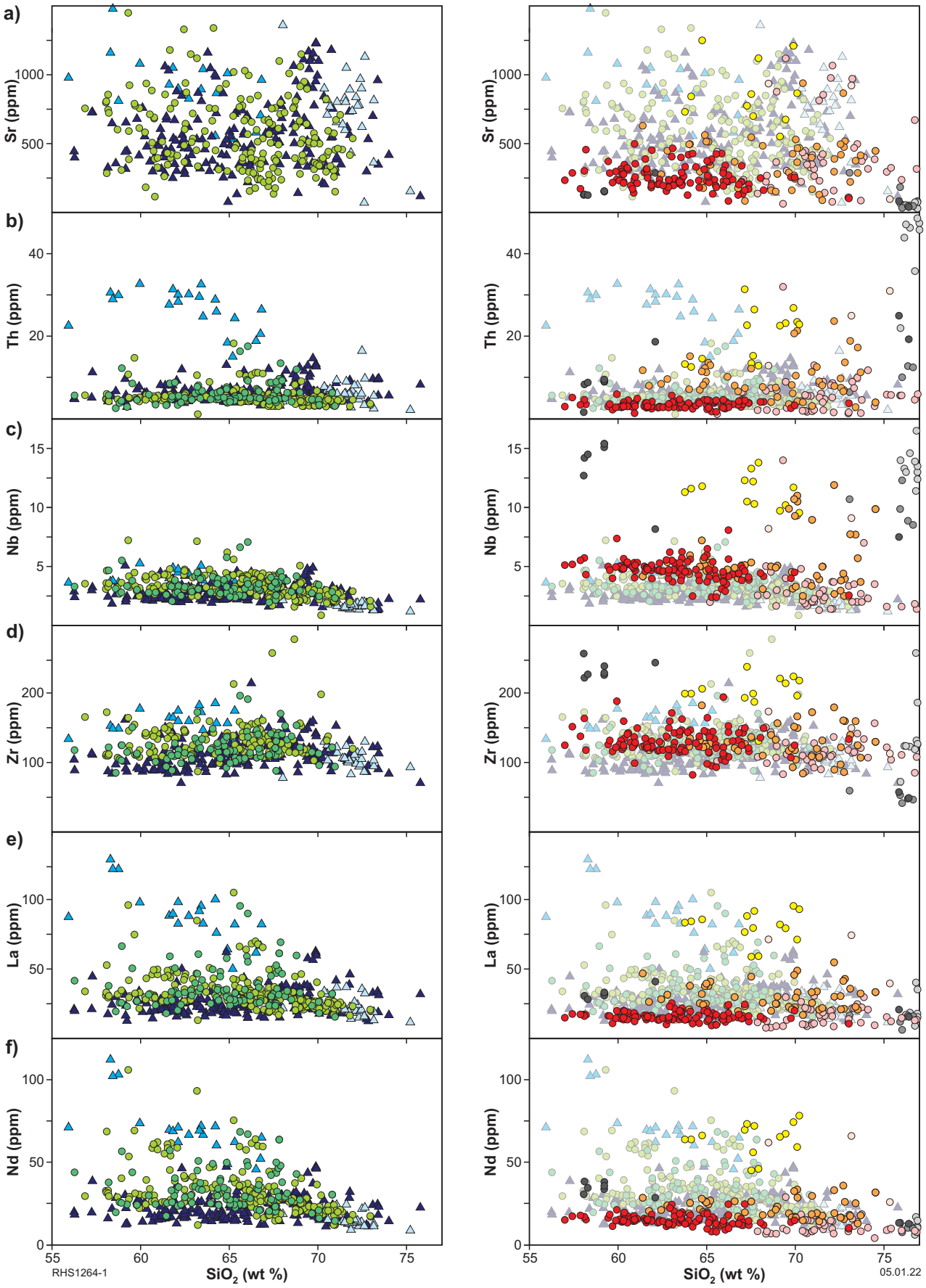

Figure 43. Variation in trace elements with SiO_2 for the various felsic rock types. The left-hand column shows sanukitoids. The right-hand column shows the sanukitoid-like rocks (low-, medium-, and high-La dacites) and other felsic units (bold symbols) and compares them with the sanukitoids (faded symbols)

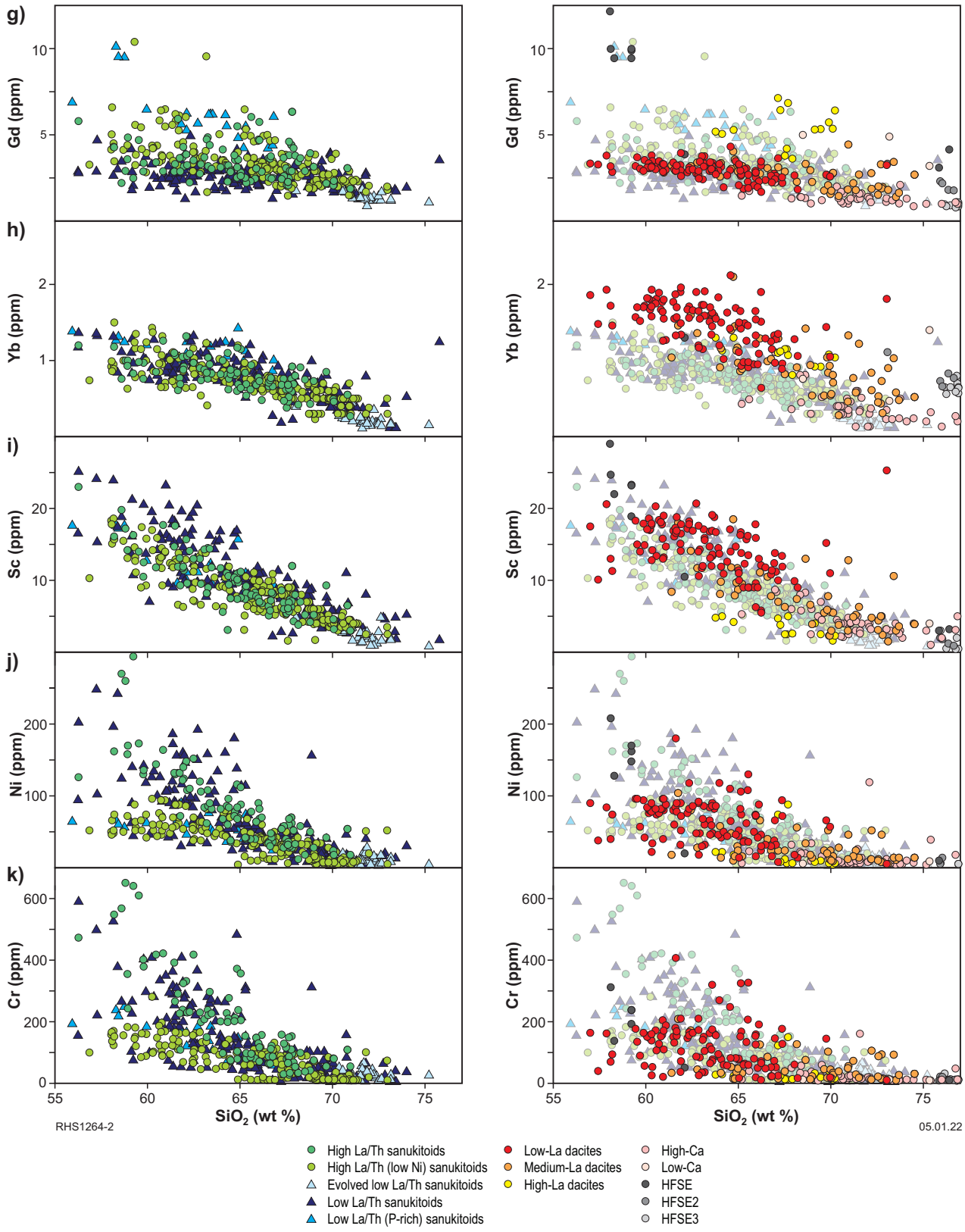

Figure 43. continued

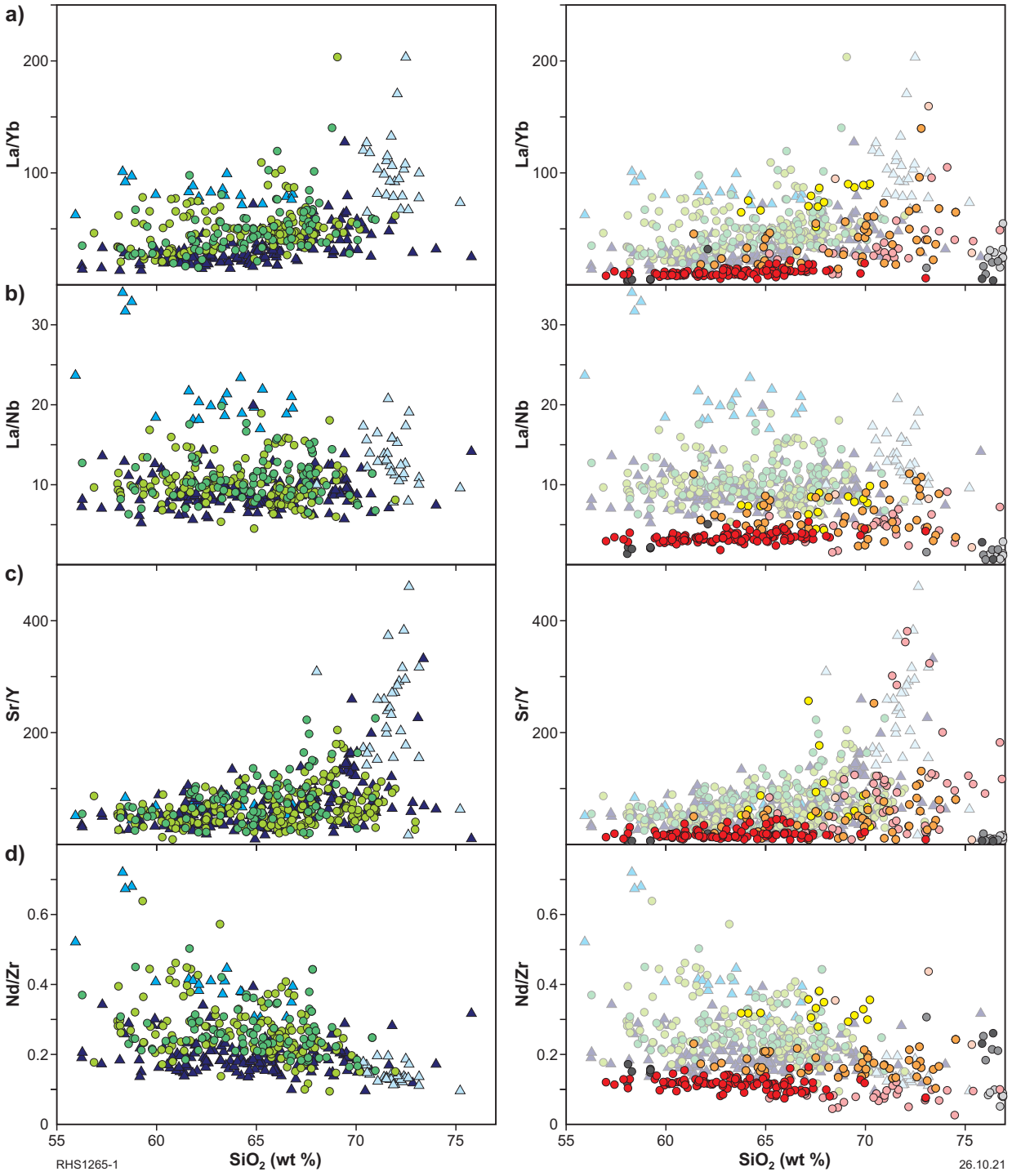

Figure 44. Variation in trace element ratios with SiO_2 for the various felsic rock types. The left-hand column shows sanukitoids. The right-hand column shows the sanukitoid-like rocks (low-, medium-, and high-La dacites) and other felsic units (bold symbols) and compares them with the sanukitoids (faded symbols)

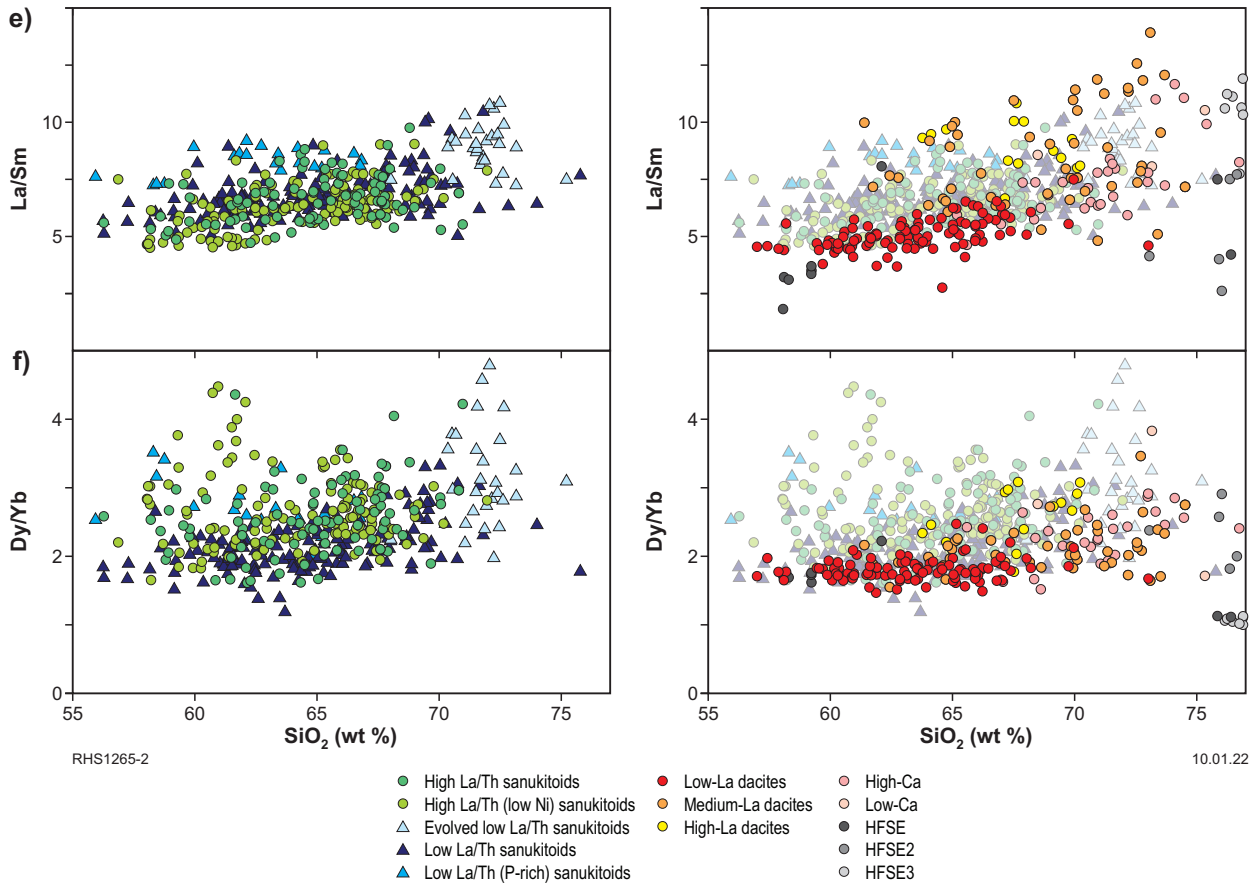

Figure 44. continued

Table 4. Nd isotope data for felsic rocks of the Black Flag Group (sample locations are provided in Appendix 1)

Sample	Classification	Source	Age (Ma)	Age source	Sm (ppm)	Nd (ppm)	$^{147}Sm/^{144}Nd$	$^{143}Nd/^{144}Nd$	1σ	ε_{Nd} (at T)	1σ	T_{DM}^{2} (Ga)
230261	Evolved Low La/Th sanukitoid	GSWA	2680	assumed	3.67	25.00	0.0878	0.510742	0.000012	0.49	0.24	2.97
233755	Evolved Low La/Th sanukitoid	GSWA	2680	assumed	2.25	13.70	0.0929	0.510837	0.000014	0.60	0.27	2.96
223074	High La/Th sanukitoid	GSWA	2690	assumed	3.97	21.30	0.0959	0.510953	0.000005	1.94	0.10	2.87
223138	High La/Th sanukitoid	GSWA	2700	assumed	5.27	29.90	0.0961	0.510979	0.000005	2.66	0.10	2.83
223141	High La/Th sanukitoid	GSWA	2700	assumed	10.40	57.30	0.0935	0.510918	0.000005	2.41	0.10	2.85
223153	High La/Th sanukitoid	GSWA	2700	assumed	5.91	33.70	0.0941	0.510957	0.000005	2.98	0.10	2.81
227865	High La/Th sanukitoid	GSWA	2680	assumed	4.06	24.30	0.1042	0.511083	0.000012	1.50	0.24	2.89
227954	High La/Th sanukitoid	GSWA	2690	assumed	11.10	67.10	0.1004	0.510766	0.000005	−3.28	0.10	3.26
229904	High La/Th sanukitoid	GSWA	2690	assumed	8.12	50.00	0.0939	0.510897	0.000005	1.56	0.10	2.90
229913	High La/Th sanukitoid	GSWA	2690	assumed	6.22	36.40	0.0956	0.510923	0.000005	1.47	0.10	2.91
2000969007	High La/Th sanukitoid	Barley et al. (2003)	2662	Champion (2013)	7.50	44.00	0.1034	0.511103	0.000020	1.80	0.39	2.85
211529	High La/Th (low Ni) sanukitoid	GSWA	2690	assumed	7.68	40.50	0.1022	0.511101	0.000005	2.67	0.10	2.81
211547	High La/Th (low Ni) sanukitoid	GSWA	2690	assumed	5.40	34.00	0.0921	0.510908	0.000005	2.41	0.10	2.83
227886	High La/Th (low Ni) sanukitoid	GSWA	2680	assumed	4.77	26.30	0.1067	0.511158	0.000011	2.10	0.21	2.85
227894	High La/Th (low Ni) sanukitoid	GSWA	2690	assumed	6.52	33.00	0.1083	0.511189	0.000005	2.28	0.10	2.84
227909	High La/Th (low Ni) sanukitoid	GSWA	2690	assumed	7.55	45.40	0.0912	0.510881	0.000005	2.17	0.10	2.85
230907	High La/Th (low Ni) sanukitoid	GSWA	2680	assumed	9.80	57.80	0.0986	0.511019	0.000012	2.18	0.24	2.84
204681	Low La/Th sanukitoid	GSWA	2690	assumed	4.96	30.10	0.0994	0.510969	0.000005	1.05	0.10	2.94
224513	Low La/Th sanukitoid	GSWA	2690	assumed	3.54	17.00	0.1022	0.510973	0.000005	0.17	0.10	3.00
233603	Low La/Th sanukitoid	GSWA	2680	assumed	4.22	25.90	0.0970	0.510923	0.000011	0.85	0.22	2.94
233640	Low La/Th sanukitoid	GSWA	2680	assumed	3.56	18.50	0.1078	0.511073	0.000011	0.03	0.22	3.00
230730	Low La/Th (P-rich) sanukitoid	GSWA	2680	assumed	6.39	40.50	0.0963	0.510878	0.000011	0.20	0.22	2.99
230799	Low La/Th (P-rich) sanukitoid	GSWA	2680	assumed	11.1	74.50	0.0894	0.510782	0.000009	0.72	0.17	2.95
224528	Low La/Th (P-rich) sanukitoid (altered)	GSWA	2690	assumed	9.00	47.50	0.0932	0.510842	0.000005	0.70	0.10	2.96
114144	UF Low-La dacite	GSWA	2690	assumed	2.34	12.10	0.1099	0.511208	0.000005	2.07	0.10	2.86
204687	UF Low-La dacite	GSWA	2680	assumed	2.28	11.80	0.1231	0.511354	0.000011	0.25	0.21	2.99
223086	UF Low-La dacite	GSWA	2690	assumed	2.32	10.10	0.1159	0.511283	0.000005	1.46	0.10	2.91
230883	UF Low-La dacite	GSWA	2680	assumed	3.14	15.50	0.1306	0.511528	0.000019	1.09	0.37	2.93
204146	UF Medium La dacite	GSWA	2690	assumed	4.69	33.60	0.0834	0.510715	0.000005	1.64	0.10	2.89
230040	UF Medium La dacite	GSWA	2680	assumed	4.27	26.60	0.1012	0.510719	0.000012	−4.60	0.24	3.35
2001969035	UF Medium La dacite	Barley et al. (2003)	2660	Champion (2013)	2.20	13.00	0.0926	0.510901	0.000020	1.53	0.39	2.86
240405	High-La dacite	GSWA	2680	assumed	7.41	56.10	0.0788	0.510629	0.000009	1.39	0.17	2.90
230996	High-Ca	GSWA	2680	assumed	2.62	13.20	0.1148	0.511245	0.000013	0.99	0.25	2.93
236483	High-Ca	GSWA	2680	assumed	1.53	8.24	0.1050	0.511136	0.000011	2.24	0.21	2.84
2001967017A	High-Ca	Barley et al. (2003)	2667	Champion (2013)	2.00	11.50	0.0917	0.510830	0.000020	0.54	0.39	2.94
2001967019A	High-Ca	Barley et al. (2003)	2675	Champion (2013)	1.80	10.50	0.0955	0.510884	0.000020	0.39	0.39	2.96
223068	High Ca (altered)	GSWA	2690	assumed	2.53	8.90	0.1153	0.511273	0.000005	1.46	0.10	2.91
2001969001	Low-Ca	Barley et al. (2003)	2632	Champion (2013)	3.80	26.00	0.0969	0.510926	0.000020	0.17	0.39	2.94
223194	HFSE	GSWA	2680	assumed	9.06	35.80	0.1478	0.511798	0.000012	0.38	0.24	2.98
2001969039	HFSE	Barley et al (2003)	2650	Champion (2013)	2.80	13.40	0.1224	0.511386	0.000020	0.69	0.39	2.92

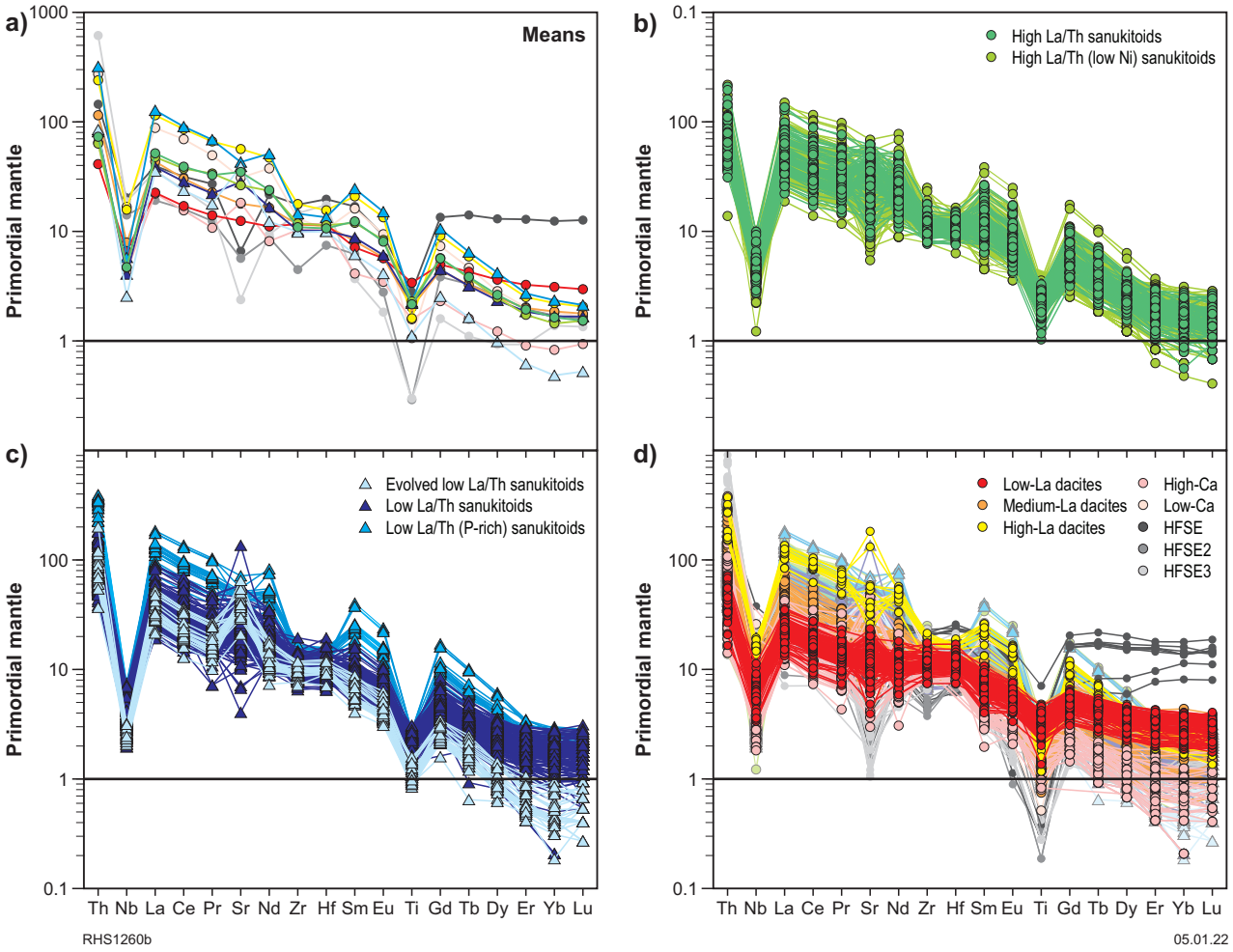

Figure 45. Mantle-normalized trace element patterns for various felsic geochemical groups and units (Normalizing values from Sun and McDonough, 1989)

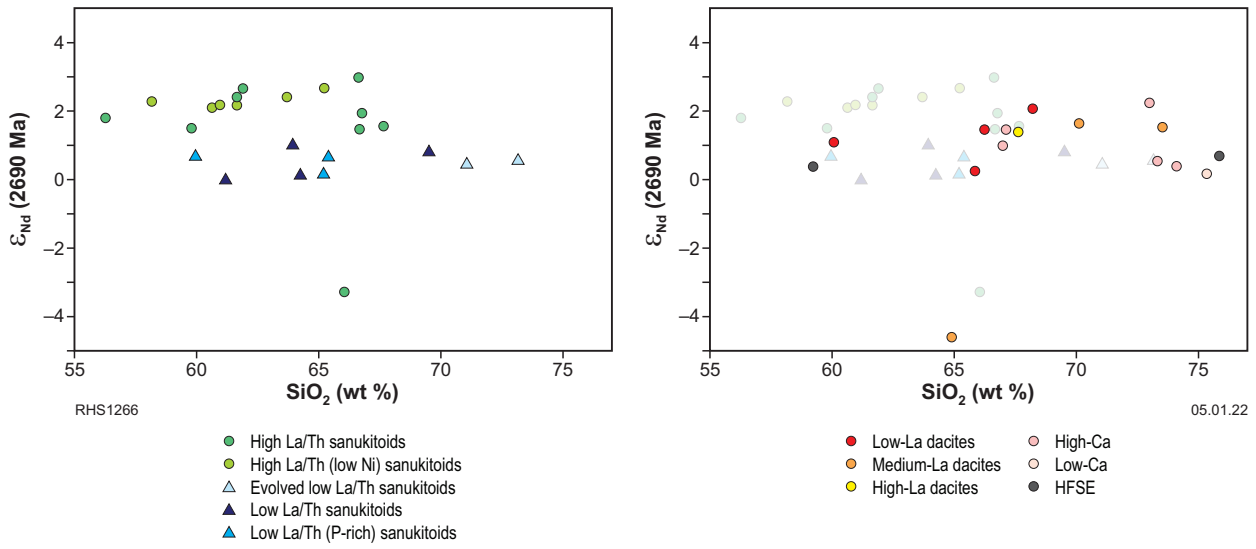

Figure 46. Variation in initial $\varepsilon_{Nd\ (2690\ Ma)}$ values with SiO_2 for the various felsic rock types. The left-hand column shows sanukitoids. The right-hand column shows the sanukitoid-like rocks (low-, medium-, and high-La dacites) and other felsic units (bold symbols) and compares them with the sanukitoids (faded symbols)

The $Mg^{\#}$ for the medium-La dacites is still as high as ~45 at minimum silica contents of ~63 wt% (hence, $Mg^{\#}$ should be even higher, if extrapolated to primitive compositions at ~60 wt% silica), which as with the low-La dacites, also appears to question simple crustal melting as the origin of the parental magmas. Many of the high-La dacites lie at the low silica end of the range for High-Ca granites but are otherwise compositionally very similar to High-Ca granites, particularly at higher silica contents. An exception is for P_2O_5 contents, which are higher in the high-La dacites than in High-Ca granites. For these reasons and the generally hydrated (hornblende-rich) nature of the medium-La dacites (and perhaps the high-La dacites), we suggest that these are also sanukitoid-like. Mixing between sanukitoid magmas and basaltic magmas at or near the source of sanukitoid formation remains our preferred model for producing low-La dacites and possibly most of the medium-La dacites. However, few regionally sampled basaltic melts, when hybridized with melts of sanukitoid composition, have the capacity to evolve to compositions as Nb-enriched as the high-La dacites and some members of the medium-La dacites. Two exceptions include the high-Mg andesitic volcanic rocks that are grouped as geochemical equivalents of HFSE granites (referred to below as HFSE1), and evolved tholeiitic magmas (e.g. L-U7) that otherwise form granophyres within fractionating mafic sills. Rocks with HFSE1 compositions are very rare, whereas tholeiitic sills fractionating to L-U7 compositions are known to intrude the Black Flag Group.

Rocks compositionally equivalent to High-Ca granites

These rocks typically have a restricted range of high silica values (SiO_2 mainly >67 wt%) and are amongst the most Al_2O_3-rich and K_2O-, HREE-, and Th-poor rocks when compared with most sanukitoids and sanukitoid-like rocks (i.e. rocks equivalent with Mafic granites). However, they are indistinguishable from evolved low La/Th sanukitoids in major element composition. Like the latter sanukitoids, the high-Ca rocks have steeply inclined (strongly fractionated) mantle-normalized trace element patterns, but in the case of samples within the study region, these can be distinguished from the evolved sanukitoids, which have slightly less prominent positive Zr (Hf) anomalies, higher Th and LREE concentrations, and lower HREE concentrations. Hence, they have slightly higher La/Yb and Th/Yb ratios as well as higher La/Nb and Sr/Y ratios (Figs 43, 44). The high-Ca rocks examined have La concentrations of ~10 ppm, which is within the lower range of La concentrations expected for High-Ca granites (or TTG), and is consistent with ~20% partial melting of mafic crust with compositions similar to the LTB that forms the main mafic magma composition sampled from the regional greenstones (assuming LTB La concentrations of ~2 ppm).

Rocks compositionally equivalent to high field strength element (HFSE) granites

Three minor groups have been tentatively equated with HFSE granite-like compositions (Figs 42–44). Although many of these samples are of high-level intrusive rocks, volcanic examples also occur (e.g. DDH PMLJH001). These are variably characterized by high Na_2O and/or K_2O concentrations and high total Fe, but they are specifically identified based on prominent enrichments in various incompatible trace elements. Strong enrichments in Nb, Zr and particularly, Yb, at silica contents <60 wt% are diagnostic of HFSE1. Enrichments in U, Y, and Yb and depletions in Zr at silica contents of 72–77 wt% characterize HFSE2 and enrichments in Th and Nb at silica contents of 76–77 wt% characterize HFSE3. The HFSE1 group, in particular, is extremely enriched and has the major element compositions of a high MgO andesite. HFSE1 is characterized at SiO_2 ~59 wt%, by MgO contents typically from 6 to 7.5 wt%, $Mg^{\#}$ >55 (but significantly more FeO rich than the sanukitoids at the same SiO_2 content), and flat mantle-normalized trace element patterns at unusually high concentrations (e.g. Nb >12 ppm, Zr >220 ppm, Yb >6 ppm). The extremely enriched tholeiitic magmas reflect potential parents to A-type granites.

Rocks compositionally equivalent to Low-Ca granites

Three samples have compositions equivalent to Low-Ca granites, these are silica-rich (SiO_2 >68 wt%) rocks, which compared to High-Ca granites are typically potassic (K_2O >3 and mostly >4 wt%), low in CaO and show enrichments in incompatible trace elements, with strong enrichments in LREE being particularly diagnostic. Not considering the magma series that extend to low silica values (i.e. rocks compositionally equivalent to the Mafic granites), a plot of Ce against K_2O proves particularly useful at distinguishing between the high- and low-Ca series (Champion and Cassidy, 2002a).

Spatial and temporal trends

Sanukitoids

Of the diamond drillcores examined, approximately 20 provided information (e.g. stratigraphic succession or intrusive contacts) that might be used to determine relative age differences between felsic rocks of different geochemical groups within segments of the Black Flag Group stratigraphy (Fig. 47). Within the study region, there are 31 samples that have both a published U–Pb zircon radiometric age determination, and have readily available whole-rock geochemical data; these provide absolute age constrains on magmatism (Table 5).

The most striking feature of the geographical distribution of the various felsic geochemical groups relates to the sanukitoids (Fig. 41). Of the two main compositions of sanukitoids, the high La/Th group is concentrated in the southern and eastern parts of the region, while the low La/Th group (excluding the evolved low La/Th subgroup) is mainly concentrated in the north. Sanukitoids in the northwestern part (Kundana region) are exclusively low La/Th types, although high La/Th and low La/Th sanukitoids occur to the northeast, and locally show mutually intrusive (subvolcanic) or interlayered (volcanic) relationships (Fig. 47). There appears to be a very strong structural control on the occurrence of the high La/Th sanukitoids, in a broad north-northwest trending band connecting Kalgoorlie and Kambalda (referred to as the 'K-K belt') within or proximal to the Boulder–Lefroy Fault. To some extent, the association with the fault (and hence the strong linearity of the trend) reflects a sample bias to drillcores sited on mineral exploration targets. Nevertheless, the distribution of the high La/Th sanukitoids in the K-K belt is clearly constrained to within specific fault-bound blocks of the Black Flag Group. In the northern (Kalgoorlie) portion of the K-K belt, the sanukitoids are exclusively of the high La/Th type but in the southern portion high and low La/Th types occur, showing locally mutually intrusive (subvolcanic) or interlayered (volcanic) relationships.

Table 5. U–Pb zircon geochronology of felsic rocks with readily available geochemical data

Sample No.	*Classification*	*Age*	*Sample material*	*Latitude*	*Longitude*	*Description/notes*	*Reference*
203736	Evolved low La/Th sanukitoid	2680 ± 8	Drillcore (CD20297-W1)	-31.3331	121.7804	Quartz-feldspar porphyry, Victory Flames, Saint Ives, Kambalda region, age of igneous crystallization	Wingate et al., 2022a
230328	Evolved low La/Th sanukitoid	2682 ± 14	Drillcore (LD81635)	-31.2391	121.6997	Feldspar porphyritic intrusion, Kambalda region	Lu et al., 2020a
2004967310	Evolved low La/Th sanukitoid	2693 ± 18	Drillcore	-30.5987	121.5991	Volcanic metasandstone, Kanowna Belle, Ballarat Grit, tentative age from 6 analyses- significant range of common-Pb and discordance	Sircombe et al., 2007
2004967316	Evolved low La/Th sanukitoid	2695 ± 6	Drillcore	-30.6062	121.5896	Volcanic metasandstone, Kanowna Belle, Ballarat Grit, poor quality zircon	Sircombe et al., 2007
2004967377	Evolved low La/Th sanukitoid	2655 ± 15	Outcrop	-30.4496	121.2432	Biotite monzogranite, Mt Ellis, Owen Monzogranite, age of igneous crystallization, low zircon yield	Sircombe et al., 2007
2001969039	HFSE granite	2650 ± 3	Outcrop	-29.8266	121.7281	Seriate to quartz-feldspar porphyritic granite, Donkey Rocks, age of igneous crystallization	Dunphy et al., 2003
2001967017A	High-Ca granite	2667 ± 3	Outcrop	-30.6703	121.0315	K-feldspar megacrystic biotite monzogranite, Camel Dam, Bali Monzogranite, age of igneous crystallization	Dunphy et al., 2003
2001967019A	High-Ca granite	2675 ± 3	Outcrop	-31.2650	121.0805	Biotite quartz-feldspar gneiss, Quairnie Rock, age of igneous crystallization	Dunphy et al., 2003
E75	High-Ca granite	2698 ± 6	Drillcore	-30.8010	121.6373	Dacite lava, Golden Ridge	Krapež et al., 2000
NIM011	High-Ca granite	2702 ± 4	Drillcore	-30.7883	121.6543	Dacite, Mimbus Mine site, age of igneous crystallization	Hollis et al, 2017
222662	High La/Th sanukitoid	2653 ± 9	Outcrop	-30.5753	121.6164	Porphyritic dacite, Four Mile Hill, 4 km north-northwest of Kanowna	Wingate et al., 2021a
229913	High La/Th sanukitoid	2666 ± 7	Drillcore (LD 7006)	-31.2978	121.7557	Diorite intrusion, Lake Lefroy, southeast of Kambalda	Lu et al., 2020b
245105	High La/Th sanukitoid	2664 ± 4	Drillcore (GDD534)	-30.6191	121.5639	Coarse-grained volcaniclastic or epiclastic (?) rock, Panglo Sandstone, Golden Valley Prospect	Wingate et al., 2021b
245115	High La/Th sanukitoid	2688 ± 6	Drillcore (RHDD18007)	-30.5956	121.6095	Sericitized plagioclase-porphyritic dacitic intrusion, Red Hill porphyry, Kanowna Consols	Wingate et al., 2021c
97967038G	High La/Th sanukitoid	2656 ± 3	Drillcore (WCVXD-73)	-30.4089	121.4111	Biotite-hornblende granodiorite (Golden Cities granodiorite), collar location Woodcutters prospect, age of igneous crystallization	Fletcher and McNaughton 2002
2000967006D	High La/Th sanukitoid	2661 ± 3	Drillcore (MAD2)	-30.7201	121.5253	Aphanitic feldspar-amphibole porphyry clast in polymictic conglomerate, collar ~2.5 km southeast of Parkeston, age of igneous crystallization and maximum depositional age	Fletcher et al., 2001
2000969007	High La/Th sanukitoid	2662 ± 3	Drillcore (SHD13)	-30.9117	121.5783	Massive equigranular to feldspar porphyritic hornblende quartz diorite/tonalite phase of Ellington granite, intrudes Black Flag Group. Collar location ~4 km southeast of Hannan South Mine, age of igneous crystallization	Fletcher et al., 2001
2004967308	High La/Th sanukitoid	2668 ± 7	Drillcore (GVD97)	-30.6105	121.5628	Volcanic metasandstone, Kanowna Belle, Golden Valley Conglomerate, age of igneous crystallization and maximum depositional age	Sircombe et al., 2007
2000967011D	Low-Ca granite	2667 ± 3	Drillcore (CD29)	-30.8372	121.4030	Intensely (sericite-carbonate-albite) altered fine-grained strongly feldspar-phyric porphyry, intrudes the Black Flag Group. Collar location in area now occupied by the Centurian Pit, age of igneous crystallization	Fletcher et al., 2001
2001969001	Low-Ca granite	2632 ± 4	Outcrop	-30.8542	121.9876	Medium-grained, equigranular biotite monzogranite (Juglah Monzogranite),~4.8 km from Boundary Dam, age of igneous crystallization	Dunphy et al., 2003
E179	Low-Ca granite	2676 ± 5	Outcrop	-30.8447	121.4302	Dacitic conglomerate clasts: Gibson Honman Rock, maximum depositional age	Krapež et al., 2000
211051	Low La/Th sanukitoid	2690 ± 7	Unknown	-30.6319	121.2619	Fragmental hornblende-phyric andesitic rock, west end of White Flag Lake, age of igneous crystallization/maximum depositional age.	Lu et al., 2017
240481	Low La/Th sanukitoid	2694 ± 8	Drillcore (18APD012)	-30.1816	121.2238	Felsic volcanic to volcaniclastic rock probably of dacitic composition, Aphrodite prospect, age of igneous crystallization/maximum depositional age	Wingate et al., 2022b
245127	Low La/Th sanukitoid	2682 ± 4	Drillcore (NGDD19021)	-30.9909	121.4403	Plagioclase porphyritic, volcaniclastic sandstone, Ellen Dam, age of igneous crystallization/maximum depositional age	Wingate et al., 2021d
2004967367	Low La/Th sanukitoid	2696 ± 2	Drillcore	-30.5788	121.2397	Volcanic metasandstone, Three-in-Hand prospect, age of igneous crystallization/maximum depositional age	Sircombe et al., 2007
2004967369	Low La/Th sanukitoid	2689 ± 2	Drillcore	-30.5787	121.2397	Porphyritic micro–diorite sill, Three-in-Hand prospect, age of igneous crystallization	Sircombe et al., 2007
236002	Low-La dacite	2702 ± 6	Drillcore (18EISD001)	-31.0278	121.9182	Metadacite-felsic volcanolithic breccia, Daisy Milano, age of igneous crystallization	Wingate et al., 2022c
E353	Low-La dacite	2708 ± 5	Outcrop	-30.7768	121.8276	Silicified feldspathic volcanogenic sandstone, Bulong, age of igneous crystallization/maximum depositional age	Kositcin et al., 2008
E357	Low-La dacite	2706 ± 5	Drillcore	-30.3934	121.6552	Volcanogenic conglomerate, Black Swan, age of igneous crystallization/maximum depositional age	Kositcin et al., 2008
E359	Low-La dacite	2708 ± 5	Outcrop	-30.9966	121.9835	Feldspathic volcanogenic sandstone; Mt Monger; age of igneous crystallization/maximum depositional age	Kositcin et al., 2008
245122	Medium-La dacite	2701 ± 5	Drillcore (PDDD18003)	-30.4683	120.9358	Plagioclase porphyritic volcaniclastic sandstone, Paradigm sandstone, Carbine Prospect, Mount Burges Station, age of igneous crystallization/ maximum depositional age	Wingate et al., 2021e

NOTE: Ages are quoted with 95% uncertainties

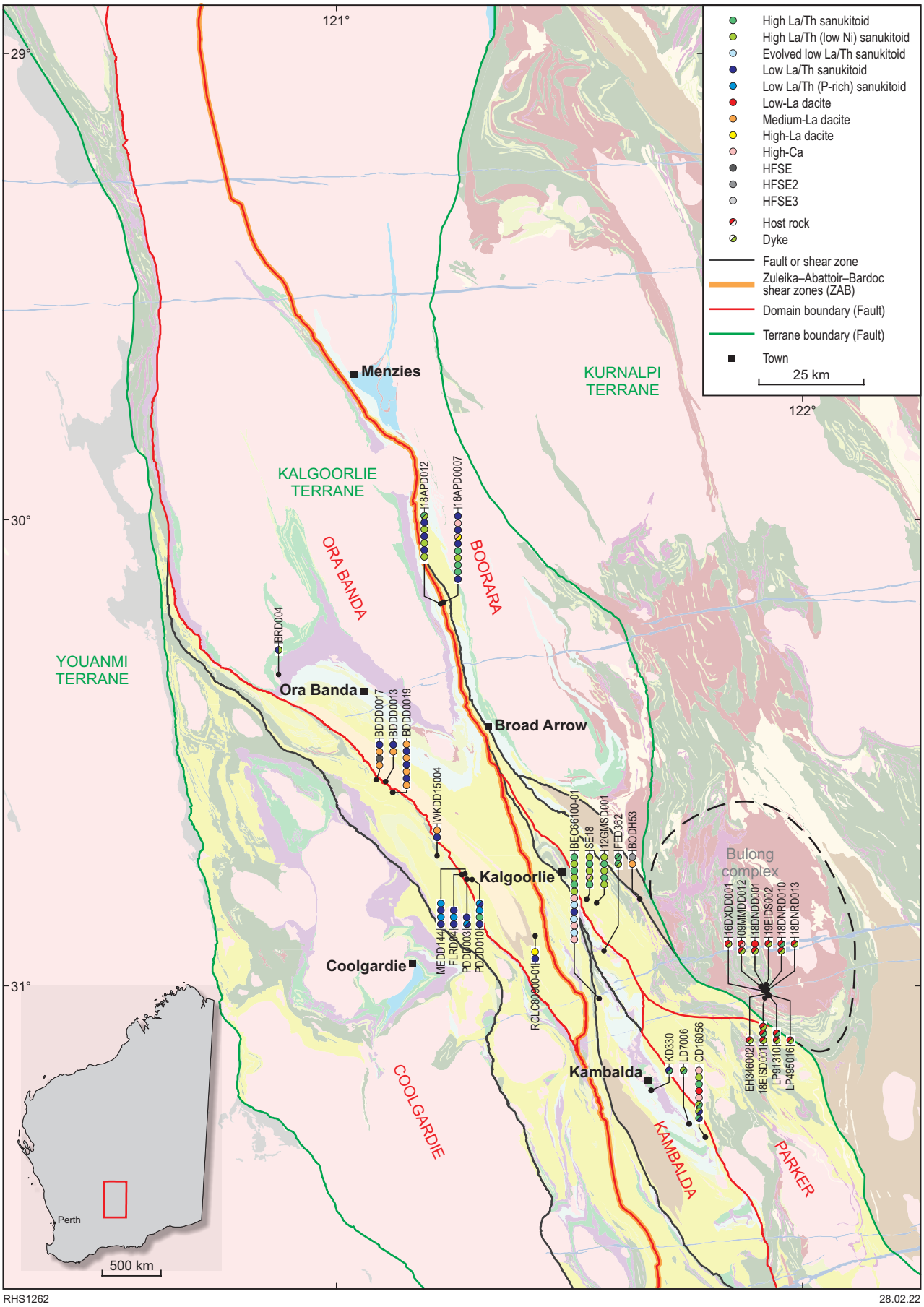

Figure 47. Geological map of the study area within the Kalgoorlie Terrane, showing the locations of sampled diamond drillcores where information on the relative stratigraphic positions of the volcanic or volcaniclastic rocks or intrusive relationships could be obtained

A smaller number of exclusively high La/Th sanukitoids form a prominent northeasterly trend, oblique to the main structural and stratigraphic trends of the greenstones, and intersect the K-K belt in the Kambalda – St Ives region. There is no clear offset in the surface geological features related to this trend, although it is broadly coincident with the southern margin of a regional geophysical anomaly (gravity low) and has the same orientation as cryptic geophysical, isotopic, and geochemical trends previously interpreted to reflect the boundaries of deep basement domains (Smithies et al., 2018c; Gessner et al., 2017). However, the interpretation of the high La/Th sanukitoid trend requires caution, as these samples are primarily from mineral exploration drill targets, themselves possibly investigating the geophysical anomaly itself. Much of the unsampled basement in the region on both sides of the trend is mapped as Black Flag Group volcanic and volcaniclastic rock (possibly high La/Th sanukitoid).

Magmatism relating to the Black Flag Group extends broadly from c. 2690 to c. 2660 Ma (e.g. Squire et al., 2010; Tripp, 2013) (Fig. 48; Table 5). However, sanukitoid magmatism in the form of high-level intrusions appears to extend to younger ages. Examples include the Kanowna Porphyry (a high La/Th sanukitoid according to our data) with ages as young as 2655 ± 6 Ma and 2649 ± 4 Ma (Ross et al., 2004) and other high La/Th sanukitoids within the Kanowna Belle area [e.g. 2653 ± 9 Ma (222662) and 2656 ± 3 Ma (97967038)], although many of these ages remain within uncertainty of 2660 Ma.

Eight U–Pb zircon dates are available for rocks that can be geochemically verified as high La/Th sanukitoids and indicate magmatism between at least 2688 ± 6 Ma and 2653 ± 9 Ma (Fig. 48). Six U–Pb zircon dates are available for rocks that can be geochemically verified as low La/Th sanukitoids (not including evolved low La/Th sanukitoids) and indicate magmatism between at least 2696 ± 2 Ma and 2682 ± 4 Ma. In many cases, the low quality and low yields of zircon and complex age populations are recognized as reasons for treating these data with caution (e.g. Sircombe et al., 2007). Relative age relationships between the evolved low La/Th sanukitoids and other magmatic phases can be determined from several drillhole intersections (Fig. 47). The evolved low La/Th and high La/Th sanukitoids are interlayered in DDH BEC66100-01, but in other intersections, evolved low La/Th sanukitoid volcanic layers typically form the oldest phase. Four out of five U–Pb zircon dates on geochemically verified evolved low La/Th sanukitoids give ages between 2695 ± 6 Ma and 2680 ± 8 Ma. The remaining sample gave a significantly younger age of 2655 ± 15 Ma. Ignoring the younger age, the group of old ages suggests that the evolved low La/Th sanukitoid volcanic rocks form a part of an early phase of sanukitoid magmatism, but only the contact relationships in drillcore provide any indication that these evolved rocks formed before the other low La/Th sanukitoids (Fig. 47).

Contact relationships (Fig. 47) clearly require that high and low La/Th magmatism was comagmatic for at least a portion of the depositional history of the Black Flag Group. However, evidence from the geochemically matched geochronological data (Fig. 48) suggests that this period of overlap may have been quite limited, with much of the high La/Th magmatism (seven of the eight dated samples) occurring after much of the low La/Th magmatism. In some regions, the igneous component of the entire preserved Black Flag Group stratigraphy reflects accumulation from only one of the main compositional types of sanukitoid magmatism. According to the stratigraphic interpretation of Tripp (2013, 2019) (Fig. 49), the northwestern Kundana – Ora Banda region exposes mainly the lower (White Flag Formation) and middle (Gibson–Honman Formation) parts of the Black Flag Group in a south-southeast plunging anticline.

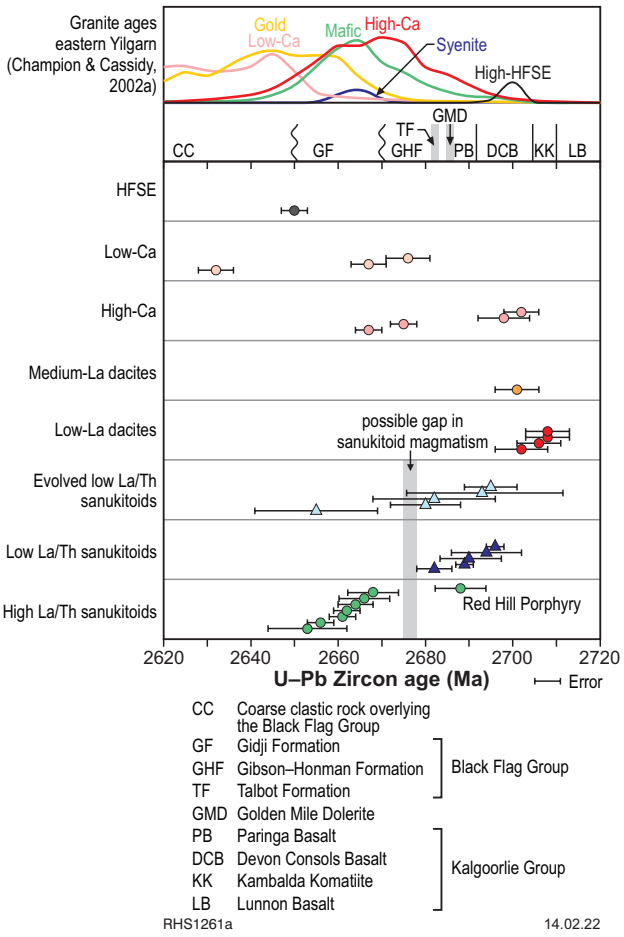

Figure 48. Summary of geochronological data and relationships for felsic units within the study region. See Table 5 for individual U–Pb zircon geochronology results and references. Black Flag Group stratigraphy was modified from Tripp (2013). Histograms showing the age distribution of granite types are from Czarnota et al. (2010), using data from Champion and Cassidy (2002a). Ages are shown with 95% uncertainties

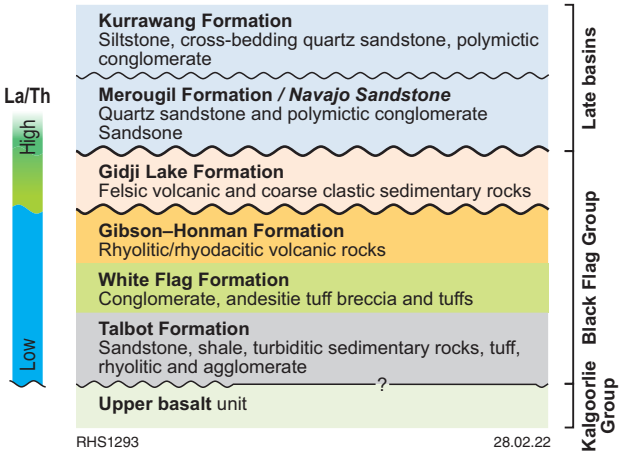

Figure 49. Stratigraphy of the Black Flag Group (modified from Tripp; 2013, 2019)

Two dated samples geochemically confirmed to be low La/Th sanukitoid lie in the region assigned to the White Flag Formation and have crystallization ages of 2696 ± 2 Ma (2004967367) and 2689 ± 2 Ma (2004967369), which is consistent with deposition in the lower stratigraphic levels of the Black Flag Group units (Tripp, 2013, 2019). To the south-southeast, a single dated sample from the Gibson–Honman Formation with available geochemistry (E179; from Gibson–Honman Rocks) has an age of 2678 ± 5 Ma, interpreted to represent the maximum depositional age of a dacite clast in a volcanolithic conglomerate (Krapež et al., 2000). This age is used to characterize the Gibson–Honman Formation (Tripp, 2013, 2019). Although this sample has a composition equivalent to Low-Ca granite, the age is clearly relevant to the low La/Th sanukitoid volcanic rocks that dominate the Black Flag Group of this area.

Although numerous geochronological data exist from the northern part of the K-K belt, geochemical data required to link the compositions of the samples are only readily available for two samples of high La/Th sanukitoids. These give ages of magmatic crystallization of 2661 ± 3 Ma (2000967006) and 2662 ± 3 Ma (2000969007). Our geochemical data indicate that all sanukitoids (intrusive or extrusive) in this region are of the high La/Th variety. These ages are characteristic of the Gidji Lake Formation, which unconformably overlies the Gibson–Honman Formation (Tripp, 2013, 2019) and forms the upper unit of the Black Flag Group.

In the southern part of the K-K belt where high-, low-, and evolved low La/Th sanukitoids occur, dates of geochemically verified samples are only available for high-La/Th sanukitoids and evolved low-La/Th sanukitoids and are from subvolcanic intrusions within greenstone. The single sample of high La/Th sanukitoid gave an age of 2667 ± 7 Ma (229913).

Hence, in broad terms, it seems that the northwestern Kundana – Ora Banda region records or preserves mainly the lower part (Gibson–Honman Formation and below) of the Black Flag Group, overwhelmingly dominated by low La/Th sanukitoids and the northern part of the K-K belt records only the uppermost part (Gidji Lake Formation), overwhelmingly dominated by high La/Th sanukitoids. In this regards, the La/Th ratio of Black Flag Group rocks might provide a first-order estimate of stratigraphic position. The geochemically matched geochronological data (Fig. 48) potentially identifies a small amagmatic gap from 2675–2678 Ma (taking analytical uncertainty into account; although with one notable exception, the high La/Th Red Hill Porphyry sample 245115 dated at 2688 ± 6 Ma). This gap potentially dates the unconformity between the Gidji Lake Formation and the Gibson–Honman Formation described by Tripp (2013, 2019).

Geochronological constrains in the other area of mixed high and low La/Th sanukitoids to the north-northeast of Kalgoorlie are mainly from samples from or near Kanowna Belle. Five of these can be geochemically classified into a specific magma type. Available geochemical data, mainly from intrusive phases, indicate that felsic magmatism in the Kanowna Belle region (i.e. within 5 km of Kanowna Belle mine itself) is dominated by high La/Th sanukitoids (71% high La/Th sanukitoid, 12% low La/Th sanukitoid, 11% high-Ca magmatism, 4% evolved low La/Th sanukitoid volcaniclastic rocks, 1% HFSE intrusion), although the ratio of high- to low-La/Th sanukitoid samples throughout the wider northeastern region is close to unity. Geochemically confirmed high La/Th sanukitoid from the Kanowna Belle region has been dated at 2653 ± 9 Ma (222662) and 2656 ± 3 Ma (97967038), which is consistent with forming subvolcanic equivalents of the Gidji Lake Formation. Geochemically confirmed high La/Th sanukitoid forms a clast within the Golden Valley Conglomerate, with an igneous crystallization age of 2668 ± 7 Ma (2004967308), within uncertainty of the age of both, the Gidji Lake and Gibson–Honman Formation. However, a recent date of the Red Hill Porphyry (245115: Table 5), also a geochemically confirmed high La/Th sanukitoid, gave an igneous crystallization age of 2688 ± 6 Ma, significantly older than the other high La/Th sanukitoids. Several other dated intrusive rocks, unaccompanied by readily available geochemistry, give older ages (e.g. 2674 ± 6 Ma; 2676 ± 4 Ma; 2677 ± 5 Ma; 2682 ± 5 Ma: Kositcin et al., 2008, Krapež et al., 2000, Ross et al., 2004) consistent with forming subvolcanic equivalents of the Gibson–Honman Formation, although not necessarily inferring they are of low La/Th sanukitoid. Two samples from a unit locally known as the Ballarat Grit and geochemically similar to be evolved low La/Th sanukitoid (assuming a relatively juvenile volcaniclastic origin and hence a relatively primary igneous composition) give igneous crystallization ages of 2693 ± 18 Ma (2004967310) and 2695 ± 6 Ma (2004967316) (Sircombe et al., 2007), consistent with forming part of the White Flag Formation.

It should be stressed that Tripp's geochronological compilations (2013, 2019) suggest that volcanism related to the Black Flag Group occurred broadly from <2690 Ma to >2665 Ma, with intrusive magmatism from <2691 Ma to <2650 Ma. We have mainly addressed compositional aspects of Black Flag Group magmatism here, but our data are broadly consistent with that of Tripp (2013, 2019) in that high La/Th compositions have a higher proportion of intrusive samples than the generally older low La/Th sanukitoids.

Geographical trends in Nd-isotope data

One of the most significant compositional distinctions between the high La/Th and low La/Th sanukitoids is the consistently more radiogenic Nd-isotope values of the former (Fig. 46). Hence, although most of the high La/Th sanukitoids appear to be equally or slightly more enriched in incompatible trace elements than the low La/Th sanukitoids at any given $Mg^{\#}$ or silica content (Fig. 43), they are isotopically more primitive (mantle-like). The Nd-isotope data also suggest that the bulk source for the low La/Th sanukitoids included a component that was significantly older (>2.9 Ga) (Fig. 50) than the model ages for the high La/Th sanukitoids (T_{DM}^2 ~2.85 Ga). Incorporating a larger proportion of a younger mantle component into the source for the high La/Th sanukitoids might satisfy the Nd-isotope constraints but not the observations that the bulk source for the high La/Th sanukitoid may have been slightly more enriched. A more plausible explanation is that the enriched component of the bulk source for high La/Th sanukitoids was compositionally different (relatively enriched in incompatible trace elements) and younger than that in the bulk source for low La/Th sanukitoids. From the spatial viewpoint, the same inferred crustal boundary (ZAB shear zone boundary) separating the western and eastern domains based on asymmetric regional-scale chemostratigraphy differences, also appears to approximate an isotopic boundary. To the west of this boundary, strongly radiogenic high La/Th sanukitoids are absent.

Other magma types

The sanukitoid-like low-La dacite occurs mainly in the southern part of the study region, on either side of the K-K belt (Fig. 41), but appears to be more common in the Mount Monger Station region in the western part of the Bulong complex. Unlike the sanukitoids, the low-La dacites show no relationship between La/Th ratio and geographical distribution. However, the only low-La sanukitoid to the west of the ZAB boundary with existing Nd-isotope data does have a significantly less radiogenic composition (initial $\varepsilon_{Nd\ (2690\ Ma)}$ = 0.25) than the three analysed samples to the east of that boundary (1.1 – 2.1), consistent with the relationships shown by the sanukitoids.

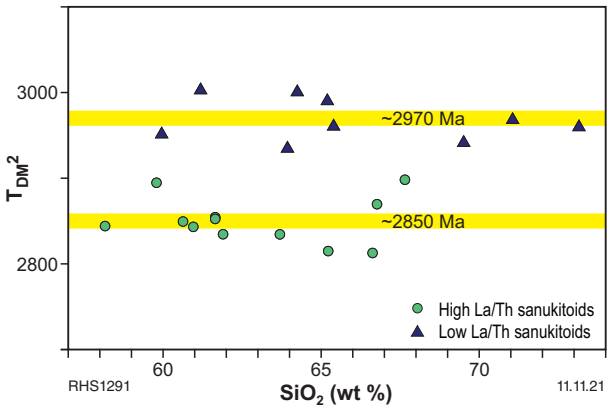

Figure 50. Variation in depleted mantle model ages (T_{DM}^2) with SiO_2 for the high- and low- La/Th sanukitoids

Four samples geochemically verifiable as low-La dacites have been dated, all to the east of the K-K belt, with three of these in the Mount Monger Station region. All dates fall within a narrow age range from 2708 to 2702 Ma. In all 10 drillcores to the east of the K-K belt that show contact relationships between low-La dacite and other units, the dacite was consistently intruded by subvolcanic dykes of high La/Th sanukitoid and was the oldest observed felsic component (Fig. 47). Of the samples collected to the west of the K-K belt (and ZAB), one is a felsic intrusion into rocks of the Brilliant Formation in the lower Coolgardie sequence and the other two are felsic volcanic rocks stratigraphically within or beneath the Lindsays Basalt, and subsequently at least as old as the lowest part of the upper Coolgardie sequence. The first sample possibly pre-dates the Black Flag Group, but the second two samples clearly pre-date the Black Flag Group. The two low-La dacites sampled within the K-K belt (DDH PFC43200-2 and CD16056) do not show clear stratigraphic relationships; neither sample GSWA 233792 from PFC43200-2 nor the units above and below it show clear evidence of a volcanic origin. Hence, based on available data, it is quite likely that the low-La dacite represents a c. 2706 Ma felsic volcanic event clearly older than the Black Flag Group. Thus, the low-La dacite compositions potentially provide a stratigraphic time marker. Along with the La/Th ratio of sanukitoids, these potential compositional age references might prove useful in elucidating field relationships, although they should be considered with caution.

Medium-La dacite was not found within the K-K belt but was sampled west and east of that belt and along the full north–south extent of the study region. It was also sampled in several drillcore intersections from the Kundana region (e.g. BDDD0019; Fig. 47) to the west-northwest of Kalgoorlie, where it is interlayered with low La/Th sanukitoid. These two compositional types are difficult to distinguish visually and include juvenile volcanolithic deposits, where the clasts and matrix are compositionally indistinguishable from each other. A single age determination from a geochemically verifiable medium-La dacite (245122, Table 5) from the Mount Burges Station (Carbine Prospect) area yielded an interpreted magmatic crystallization age of 2701 ± 5 Ma. This age is possibly slightly younger than low-La dacite magmatism and slightly older than low La/Th sanukitoid magmatism, but within uncertainty of both, although some depositional overlap with low La/Th sanukitoid is required, based on crosscutting relationships observed in drillcore BDDD0019.

Like the sanukitoids, the medium-La dacites can be divided into low- and high-La/Th subgroups, each with a distinctive spatial distribution. Medium-La dacites with high La/Th ratios occur mainly to the east of the K-K belt, like the high La/Th sanukitoid. Medium-La dacites with low La/Th occur along a distinct north-northwesterly trend that extends the full north–south extent of the study region.

High-La dacite is less common than the low- and medium-La dacite but forms part of the Black Flag Group to the west of the K-K belt. No radiometric ages exist for geochemically verifiable high-La dacite, although it is interlayered with low La/Th sanukitoid and must share at least part of the magmatic age range for those rocks.

Volcanic and subvolcanic rocks with compositions similar to High-Ca granites are widespread throughout the study region (Fig. 37). They also occur within the K-K belt, where they form volcanic interlayers with high La/Th sanukitoid and are likewise interlayered with low La/Th sanukitoid in the Kundana region (Fig. 47). Two samples of geochemically verifiable high-Ca volcanic rocks, give U–Pb ages of 2702 ± 4 Ma and 2698 ± 6 Ma (Table 5). However, composite granite plutons within the region, including the Bali Monzogranite, also have High-Ca granite components dated between 2675 Ma and 2667 Ma (Table 5).

Volcanic and subvolcanic rocks with compositions similar to Low-Ca granites are rare and seem restricted to the central part of the region (east and west of Kalgoorlie). Two closely spaced geochemically verifiable samples form components of the Black Flag Group, one with a U–Pb age of 2667 ± 3 Ma (Fletcher et al., 2001) and the other, from Gibson–Honman Rock (Krapež et al., 2000), with an age of 2676 ± 5 Ma. Low-Ca granite forming domal composite granite bodies within the region have crystallization ages as young as 2632 ± 4 Ma (Dunphy et al., 2003).

Volcanic and subvolcanic rocks with compositions similar to HFSE granites are mainly restricted to the northern part of the study region. They form volcanic interlayers with medium-La dacite within the Kundana (DDH BDDD0017) and Nimbus (DDH BODH53) regions, suggesting immediately pre-Black Flag Group ages around c. 2700Ma. However, a single U–Pb age determination from an intrusive HFSE magma (informally know as Donkey Rocks Monzogranite) gave an age of 2650 ± 3 Ma (Dunphy et al., 2003).

Regional tectonomagmatic evolution and implications

One outcome of constructing the greenstone geochemical barcode, apart from the chemostratigraphic functionality, is that it also provides data that permit the effective mapping of magmatic and lithospheric architectural evolution. Both these appear to ignore many of the boundaries previously used to construct domains and potentially even terranes. The new data also maps specific events of potential importance in magmatic evolution in the lead up to Au mineralization.

As discussed earlier, changes in compositional proxies for crustal contamination (e.g. Th/Ti, La/Nb, Th/Nb) and fractional crystallization (e.g. Al_2O_3/TiO_2, $Mg^{\#}$), particularly above lower crustal levels (e.g. low Al_2O_3/TiO_2), reveal systematic changes in magma ascent history throughout the evolution of the mafic sequences. Minimal evidence for either crustal contamination or fractional crystallization during emplacement of the oldest mafic units (L-U1, L-U2) is consistent with rapid magma transfer through dyke

intrusion, which is also the likely case for the ascent of the slightly later komatiitic magmas. This, along with high inferred magma volumes supports a general rifting environment for the early history of the Kalgoorlie Group. Clear evidence for contamination and fractional crystallization begins before komatiite magmatism (e.g. L-Ca) in the western domains (i.e. the Coolgardie and Ora Banda Domains), possibly as extension decreases in the thicker crust to the west (Fig. 32). Such evidence only occurs after komatiite magmatism in the eastern domains (i.e. Kambalda, Boorara, Parker Domains and Bulong complex). The subsequent increase in the degree of contamination (LTB→ITB→HTSB) with increasing stratigraphic height is likely a combined effect of the production of higher degree partial melts of the mantle, and of the progressive thermal weakening of the lower crust through ongoing mantle magma input (including komatiite magmatism at c. 2706 Ma), making assimilation progressively easier. The higher degree melts have significantly lower incompatible trace element concentrations and hence, even small additions of crustal material produce significant changes in trace element geochemistry (and particularly in ratios), often with little change in major element composition.

The formation of the upper basaltic unit, and the transition into and the early stages of Black Flag Group deposition, perhaps reflect the most magmatically dynamic period of the Eastern Goldfields greenstone evolution. Many units forming the upper basaltic stratigraphy clearly erupted from mid- to upper crustal chambers (many initially filled by L-U2 magmas) undergoing extensive fractional crystallization (e.g. L-U3–7). This change to a more magmatically dynamic upper crustal regime probably accompanies an overall decrease in extension, at least in the upper crust, and probably some magmatic thickening of the crust. The result was a tendency for magmas to pond, forming chambers large enough to undergo significant fractionation prior to eruption triggers. The HTSB lavas are also abundant in the upper mafic stratigraphy of the eastern domains. Their scarcity in the western domains presumably either reflects an eastward migration in the axis of magma flux or topographical controls (i.e. fault movement) after (i.e. erosion), before or during magmatism. Recharge by and mixing of HTSB into some of the mid- to upper crustal (L-U3–7) chambers locally produced extremely enriched L-S units (e.g. L-S3a, 3b, L-S4) and likely provided eruption triggers.

A dynamic lower crustal/upper mantle environment is also suggested by the formation of HTSB itself. These have ultramafic parental compositions (Barnes et al., 2021) like earlier komatiitic magmatism, represent a sudden change in magma composition with little, if any, compositional transition, and in the case of HTSB magmatism, include an unprecedented influx of crustal material. There is very little difference in major element compositions between the more primitive ITB (I-S1) and the more primitive HTSB (H-HMg#) magmas (Fig. 21). Both approximate the transition between komatiite and komatiitic basalt compositions in terms of MgO vs Mg#. The primary distinction is in the evidence in the HTSB, either for significantly more crustal contamination or contamination by a bulk crustal component with a higher Th/Nb ratio, or both. For both magma types, contamination of the very primitive parental compositions occurred at a very early stage and at very deep crustal levels, and no significant contamination accompanied further compositional evolution. Barnes et al., (2021) suggest that the high and constant Th/Nb ratio in HTSB probably reflects ultramafic parental magmas with very low initial incompatible trace element concentrations that have assimilated enough crust for the initial magmatic Th/Nb ratios to be overprinted by values reflecting the contaminant. Nevertheless, within the range of magmas with similar MgO, Mg#, and Al_2O_3/TiO_2 ratios as the HTSB, none have Th/Nb ratios as high as HTSB and only the rare KB3 and H-LTh magmas have Th/Nb ratios that partially bridge the compositional gap between the HTSB and all other magmas (Fig. 51). The H-LTh can be adequately explained in terms of mixing or contamination between komatiite and ITB at the emplacement scale. Similarly, KB3 is typically stratigraphically associated with komatiite and probably simply represents significantly, but only locally, contaminated komatiites.

Compositional similarities between L-U3–7 lavas (e.g. Victorious Basalt) and samples from layered sills (e.g. Golden Mile Dolerite) emplaced within and above the Kalgoorlie Group, as well as emplacement of HTSB into the Black Flag Group (e.g. Powder Gabbro), indicate that the latest stages of upper basalt deposition and the early stages of Black Flag Group deposition reflect a period of maximum magmatic diversity, which also included low La/Th sanukitoid magmatism. This magmatic stew was potentially initiated by a catastrophic lower crustal event that also initiated HTSB magmatism.

Sanukitoid-like low-La dacites (Fig. 36) formed as early as c. 2708 Ma to 2702 Ma, more or less synchronously with komatiite magmatism (Fig. 48). Evidence presented here suggests that the hydrated, hornblende-bearing, low-La dacites are unlikely to represent any form of hybridization between felsic crustal melts and mantle-derived mafic or ultramafic magmas.

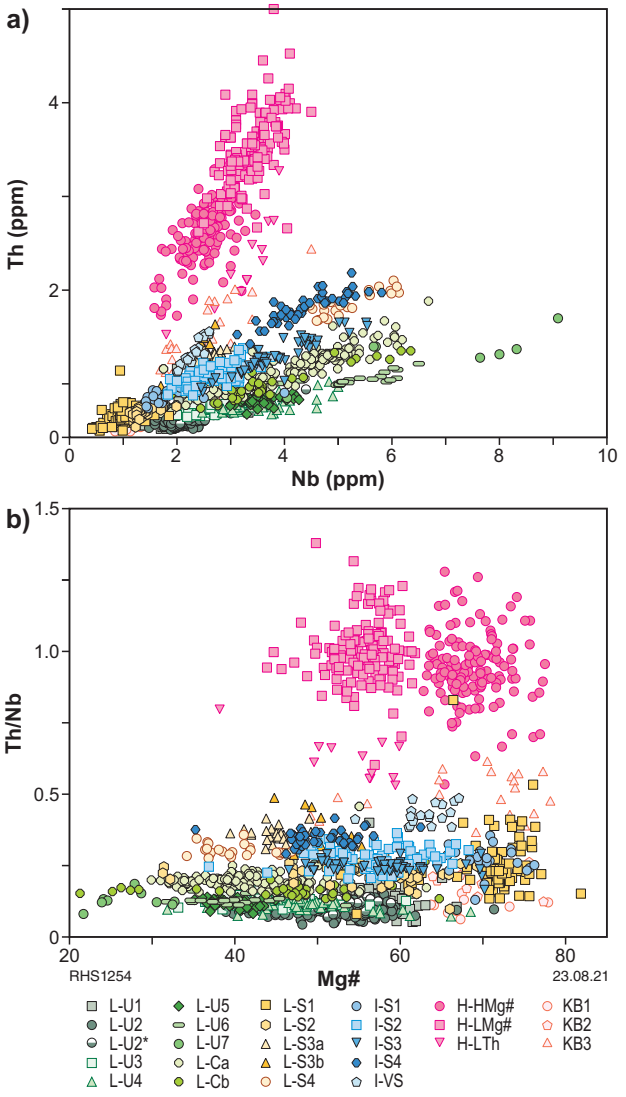

Figure 51. Variation in Th and Th/Nb with Mg# for individual LTB, ITB, HTSB and KB geochemical groups and units

In addition, in the absence of clear evidence that subduction processes directly influenced the evolution of the Kalgoorlie Terrane at this stage, the low-La dacites are unlikely to reflect melting of a recently established metasomatized mantle wedge. Nevertheless, they do reflect melting of hydrated ultramafic lower crust or mantle lithosphere. The hydrated and hornblende-bearing, medium-La dacites appear to have formed at a slightly later stage (c. 2701 Ma and younger) that overlaps with low La/Th sanukitoid magmatism at a stage when HTSB and L-U3–7 (and hence also remnant L-U2) magmatism was still active (Fig. 48). Thus, despite the dominance of voluminous and nominally dry, mafic, and ultramafic magmatism, hydrated lithospheric mantle source regions were still either preserved or being created and then partially melted throughout the period from c. 2708 Ma to c. 2660 Ma.

Recent work by Murphy et al., (2021) has provided clear evidence that varioles in basalt (i.e. in variolitic basalts), like the HTSB Paringa Basalt (but also the slightly older and immediately post-komatiite I-S2 Devon Consuls Basalt), can reflect flux melting of a hydrated mantle source. Processes that might hydrate a mantle source include subduction-like processes or lower crustal delamination or dripping events (e.g. Murphy et al., 2021). An issue posed by the abundance of HTSB magmatism, 5–10 Myr after komatiite magmatism, and by a proposed hydrated mantle source for voluminous variolitic ITB and HTSM magmas, is whether this represents an intractable anomaly within the plume paradigms commonly employed to explain komatiite. Irrespective of this issue, it is inviting to suggest that a significant post-komatiite (post-plume?) mantle disturbance event reinvigorated high-degree mantle melting more or less at the stage where evidence for primarily extension-related magma transfer was waning. Whatever the process, these ultramafic parental HTSB magmas underwent significantly greater interaction with or contamination by, lower crustal material than any preceding or subsequent mafic or felsic magma, including the sanukitoids and sanukitoid-like magmas, many of which are isotopically more primitive than the HTSB. One possibility is that the collapse of the mantle upwelling feeding komatiite magmatism resulted in a rapid and temporary transition to compression (e.g. Ueda et al., 2008; Gerya et al., 2015) that destabilized thermally weakened lower crust and remnant lithospheric mantle. The suggestion that variolitic basalt formation can reflect transfer of significant amounts of volatile components to the mantle (Murphy et al., 2021), also provides a mechanism of hydrating the lithospheric mantle sources for sanukitoids. Hence, HTSB-forming events might be crucial steps in sanukitoid petrogenesis and in providing a source of fluids that eventually might feed mineral systems.

The greenstone geochemical barcode presents a very asymmetric picture of the distribution of various characteristic mafic and felsic lithologies across the study area. The observed lithogeochemical variations, on their own, provide no basis for separating the Coolgardie Domain (upper sequence) from the Ora Banda Domain or the Kambalda Domain from either the Boorara and Parker Domains or the Bulong complex. These variations do, however, suggest that the bulk lithospheric source component contributing throughout mafic magmatic evolution in the western domains was either compositionally distinct or architecturally distinct, and most likely both, from that contributing to the magmatic evolution of the eastern domains. The surface expression of the boundary between these two bulk mantle source regions is now separated along a combined ZAB shear zone, as previously hinted by Hayman et al. (2015), based on the distribution of their enriched lower basalt unit.

Hence, prior to komatiite magmatism, early L-U1 and L-U2 magmatism in the western domains was replaced by L-Ca magmas, with compositions not seen in the east. At higher stratigraphic levels, L-S1 and L-S2 magmas followed komatiite magmatism in the west but not the east. In L-S1 and L-S2 magmas, the combination of unusually high Al_2O_3/TiO_2 (>>20), slightly higher SiO_2, and lower Ni concentrations suggests an already refractory (melt depleted), and probably more harzburgitic lithospheric mantle source contributed to magmatism in this region. The absence of this magmatism to the east of the ZAB suggests either that the refractory harzburgitic source was already removed (? delaminated, thermally eroded) as the focus of rifting migrated eastwards or that the ZAB is the upper crustal expression of the boundary between two already distinct lithospheric domains.

Compositional differences in lithospheric source components across the ZAB are reflected in the geochemical and Nd-isotope data for the sanukitoids and also reflected in the Nd isotopes data from the low-La dacite. Virtually all high La/Th sanukitoid magmatism is restricted to the east and is characterized by radiogenic $\varepsilon_{Nd\ (2690\ Ma)}$ values >1.5. The slightly older low La/Th sanukitoid occurs east and west of the ZAB. Nd-isotope data are available for two samples within the K-K belt and seven samples to the west of the ZAB and all give $\varepsilon_{Nd\ (2690\ Ma)}$ values <1.05 (Fig. 45). The model ages (T_{DM}^2) for the two groups are clearly distinct (Fig. 50), with average values for low La/Th sanukitoids of c. 2970 Ma (n=9) and c. 2850 Ma (n=12) for high La/Th sanukitoids. Thus, the ZAB is not only the surface expression of the boundary separating the bulk source regions for mafic magmatism, but also of the zone where fundamental changes occurred in the sources of sanukitoid magmatism.

The available data provide no clear indication whether the differences in $\varepsilon_{Nd\ (2690\ Ma)}$ or T_{DM}^2 values between high- and low-La/Th sanukitoids reflect distinct source compositions or different mixing proportions between low ε_{Nd} lithospheric mantle (and crust) and high ε_{Nd} juvenile asthenospheric mantle. For example, although the high La/Th sanukitoids appear to be slightly more enriched in incompatible trace elements than the low La/Th sanukitoids, there is no clear correlation between La/Th ratios and either $\varepsilon_{Nd\ (2690\ Ma)}$ or (T_{DM}^2) values within or between the sanukitoid groups (Fig. 52), which would support a separate source. Conversely, both La/Sm and Th/Nb ratios appear to broadly decrease with increasing $\varepsilon_{Nd\ (2690\ Ma)}$ or decreasing T_{DM}^2, suggesting lithosphere–asthenosphere mixing. Irrespective, these data indicate that crustal material at least as old as c. 2970 Ma forms a major component of the bulk source for the low La/Th sanukitoids and material at least as old as c. 2850 Ma forms a component of the bulk source for the high La/Th sanukitoids.

Pawley et al., (2012), Mole et al., (2015, 2019), and Smithies et al., (2018a) have suggested that the Eastern Goldfields Superterrane developed as a rift over a basement of Youanmi and/or Burtville Terrane crust. There is no clear requirement that this suggested rift ever evolved to the extent that new oceanic crust and micro-continental ribbons were created, and subsequently reassembled (e.g. Smithies et al., 2018a), although models involving subduction and arc accretion during the c. 2730–2660 Ma period (e.g. Morris and Kirkland, 2013; Witt et al., 2018) cannot be discounted. Nevertheless, the enriched signatures interpreted to reflect subduction-like processes, seen in some mafic and felsic magmas associated with formation of the Superterrane, are more easily accounted for in terms of melting lithospheric mantle that was metasomatized during subduction events related to the evolution of the Youanmi Terrain, rather than the Eastern Goldfields Superterrane (Smithies et al., 2018a).

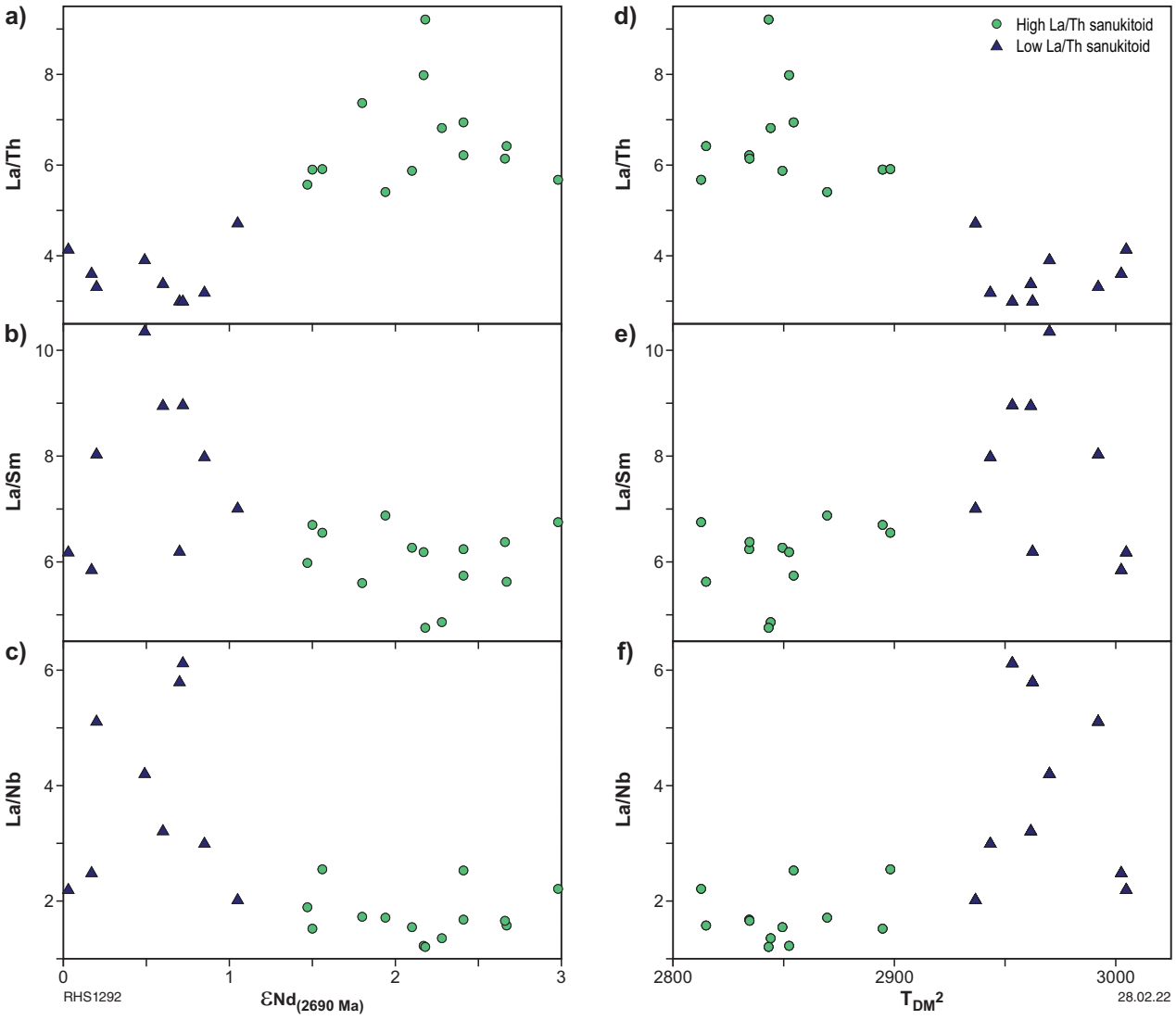

Figure 52. Variation in La/Th, La/Sm, and La/Nb ratios with initial $\varepsilon_{Nd\ (2690\ Ma)}$ values and depleted mantle model ages (T_{DM}^2) for the high- and low- La/Th sanukitoids

Such events correspond with the c. 2970 and c. 2850 Ma T_{DM}^2 ages for the low- and high- La/Th sanukitoids, respectively (e.g. Lowrey et al., 2020). The simplest explanation is that hydrated and enriched c. 2970 Ma and c. 2850 Ma Youanmi lithospheric mantle, perhaps additionally hydrated as a result of events leading to HTSB formation, was the main source for these sanukitoids.

The broadly north–south ZAB segment defines the local contours in the Nd-isotope compilation map of the Yilgarn Craton (Lu et al., 2021) (Fig. 53), separating felsic magma sources with T_{DM}^2 = 2920–3000 Ma in the west from those with T_{DM}^2 = 2800–2920 Ma to the east. From the isotopic data perspective, this contour indicates some form of lithospheric structure or gradient considerably more clearly than any data or region of data corresponding with the Ida Fault. If the distinct $\varepsilon_{Nd\ (2690\ Ma)}$ values shown by the available data for the high and low La/Th sanukitoids reflect two compositionally distinct lithospheric mantle sources, then the ZAB is the surface expression of a lower lithospheric boundary. Alternatively, and probably less likely, if the distinct $\varepsilon_{Nd\ (2690\ Ma)}$ values shown for the high and low La/Th sanukitoids reflect a significant change in the mix of asthenosphere mantle melt with melts derived from a single, homogeneous, lithospheric mantle source, then T_{DM}^2 gradients in this region might define a significant change in the extent of lower crustal extension (rifting).

Irrespective of these alternatives, it seems clear that the highly Au-endowed region examined here, directly overlies a region where geochemical and isotopic gradients define a significant feature in the regional lithosphere architecture. The arguments presented by Hayman et al. (2015) further suggest that the same or similar feature is observed in the Agnew area in the far north of the Ora Banda Domain, and it is possible that its trace will be effectively defined northwards and southwards by detailed mapping of the Nd-isotopic gradients and more integrated geochemical-stratigraphic work.

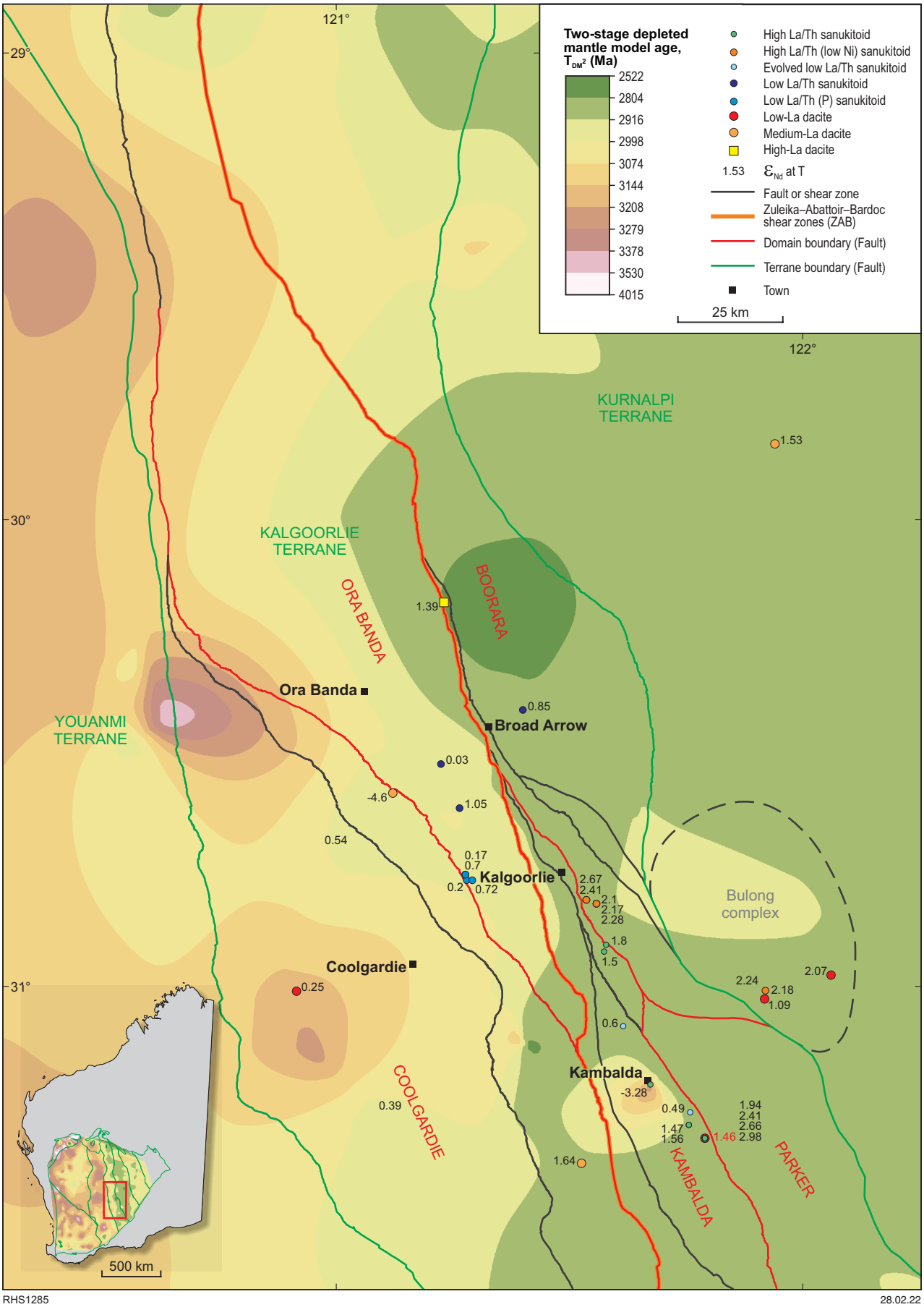

Figure 53. Part of the Yilgarn Craton Nd-isotope map (Lu et al., 2021) covering the study area and contoured for two-stage depleted mantle model ages (T_{DM}^2). The location and initial $\varepsilon_{Nd\ (2690\ Ma)}$ values of samples taken for the present study (Table 4) are also indicated and show the close correspondence of the ZAB shear zones with maximum T_{DM}^2 contour. This correspondence breaks down to the north and the relationships in that area are constrained by very few Nd-isotope data

Conclusions

The interpretations of data presented here have been significantly influenced by a wealth of field and laboratory experience and expertise from government, industry and university investigators. The interpretations, nevertheless, remain heavily based on geochemical trends and their validity or applicability needs to be carefully considered on a case-by-case basis in light of local geological context. However, the data do show clear, persistent and systematic composition variations that should be highly informative on a number of levels.

This new dataset of ~2800 high-quality whole-rock geochemical analyses of subvolcanic, volcanic, and volcaniclastic rocks from the greenstone sections of the Kalgoorlie Group are used to construct chemostratigraphic barcodes within the broader Ora Banda – Kambalda region, encompassing most of the previously defined domains of the Kalgoorlie Terrane as well as the Bulong complex area of the Kurnalpi Terrane. Probably the most functional aspect of this geochemical dataset is in the augmentation of current lithostratigraphy with clear geochemical constraints that uniquely identify a large number (26) of distinct geochemical groupings in commonly generic basalt. These distinctions highlight the controls that various fundamental igneous processes and source compositional variations exerted on evolving magma compositions.

These geochemical barcodes are based on the currently better-known and sampled stratigraphic sections and provide templates for lithogeochemical data sourced from other parts of a specific greenstone belt to be evaluated for possible lithostratigraphic or chemostratigraphic equivalence. We emphasize that in many cases, a single or low number of analyses will not be sufficient to uniquely identify a lithostratigraphic position, but more comprehensive sampling, particularly if it incorporates the underlying and overlying stratigraphic units, almost certainly will. It is hoped that the geochemical barcodes provide an accurate and useful stratigraphic tool from the mine site to the regional scale.

The applicability of the barcodes to greenstone stratigraphy outside of the study area has not been tested yet, although it is clearly expected to decrease. This is because legitimate geochemical units not considered within this study will be expected and the lithospheric sources causing contamination in various common mantle-derived parental magmas (e.g. primitive L-U units) will vary regionally.

According to the new barcode data, individual established lithostratigraphic units (typically at formation level) seldom comprise a single geochemical unit. Most formations comprise at least two distinct geochemical units, most of these distinct units occur at multiple stratigraphic levels and in most other regional stratigraphic columns. Thus, individual greenstone formations combine overlapping flow fields, each representing the products of a discrete eruptive event and/or eruptive centres supplied by genetically unrelated magma sources. This potentially makes some formation boundaries arbitrary reflections of changing source eruptions. Although complex, this diversity ensures that, in most cases, the position of stratigraphically unknown geochemical samples can be uniquely established as long as samples are taken over a continuous stratigraphic interval that incorporates the overlying and underlying units.

The application of chemostratigraphic barcoding is more reliable or appropriate for the Kalgoorlie Group than for the overlying Black Flag Group because of the greater continuity of the low-viscosity flows that characterize its basalt-dominated stratigraphy. Geochemical characteristics and relationships within the felsic-dominated Black Flag Group, nevertheless provide broad stratigraphic information and significant insight into crustal architecture and regional geological evolution. The subvolcanic, volcanic, and volcaniclastic rocks of the Black Flag Group have the composition of sanukitoids, likely derived from a metasomatically enriched lithospheric mantle source. Within the magmatic history of the Black Flag Group, a change from relatively low to high La/Th ratio sanukitoids correlates quite strongly with the spatial and temporal distribution of sanukitoid magmas. The low La/Th sanukitoid is typically older (>c. 2678 Ma) and more common in the region's west, while the high La/Th sanukitoid is typically younger (<c. 2675 Ma) and virtually restricted to the east. We also identify a compositionally specific, sanukitoid-like, low-La dacite group possibly forming a regionally relevant time marker at c. 2706 Ma.

The subdivision of the regional mafic stratigraphy into three levels (lower, middle and upper basalts; e.g. Swager et al., 1990) broadly reflects changes in magma compositions and provides useful markers of relative level within a particular stratigraphy. These changes reflect a range of conditions and processes operating at various crustal levels and at various stages and continue to influence a systematic compositional change in the felsic rocks of the Black Flag Group, overlying the basalt-dominated stratigraphy. They include a change from a crustal deformation regime that allowed rapid transfer from source to deposition site, through dykes, of weakly fractionated and uncontaminated magmas (L-U1 and L-U2) – to an environment favouring ponding in mid- to upper crustal chambers prior to eruption of variable fractionated L-U3–7 magmas. We can also see a broad, and non-systematic increase in the extent that mafic magmas became contaminated by crust, despite the occurrence in the upper stratigraphy of L-U3–7 magmas. An additional consequence of these changes is an increase in the compositional diversity of magmatism with decreasing age, reaching a climax broadly at the transition between the Kalgoorlie and Black Flag Groups, where evidence suggests comagmatic intrusion and/or extrusion of the L-U magmas, L-S magmas, HTSB magmas, low- and medium-La dacite group magmas, and sanukitoid magmas. At this time, the resurgence of locally voluminous ultramafic magmas parental to the HTSB might reflect a catastrophic event at the crust–mantle boundary, at a stage when the hydrated mantle source of sanukitoids was either created, tapped or both.

The regional distribution of the mafic chemostratigraphic associations is distinctly asymmetric, in many cases, ignoring previously established domain boundaries. However, a broadly north-trending structure incorporating segments of (from south to north) the ZAB does appear to separate the western domains (Coolgardie and Ora Banda) from the eastern domains (Kambalda, Boorara, Parker, and the Bulong complex). These domains have distinctive chemostratigraphic variations that probably reflect a fundamental crustal architectural control and potentially provide some basis for reassessing the present domain boundaries. In particular, the mafic units in the western domains probably reflect melting of a more depleted source beneath thicker lithosphere. The Ora Banda Domain is clearly part of the western domains throughout evolution of the lower and middle greenstone stratigraphic evolution, but also appears transitional to the eastern domains, in terms of its diversity of fractionated, layered sill-derived magmatism in its upper stratigraphy. The chemostratigraphic differences between the western and eastern domains extend to the felsic units of the Black Flag Group. The subvolcanic, volcanic, and volcaniclastic rocks of the Black Flag Group show a wide range in La/Th ratios, which broadly correlates with the crystallization age and the geochemical and isotopic compositions of their source. In particular, the low La/Th sanukitoids, which are more common west of the ZAB have less radiogenic Nd (i.e. is more 'crustal'), whereas the high La/Th sanukitoids, virtually restricted to east of the ZAB, have

more mantle-like isotopic compositions. The simplest explanation for the regional compositional variations in the mafic and felsic rocks is that the ZAB is the exposed trace of a structure separating compositionally contrasting lithospheric domains. Based on the geochemical and isotopic data, the northern and southern extensions of that trace should be entirely traceable.

Acknowledgements

The authors thank Paul Morris and Scott Halley for their reviews of the manuscript and for several conversations covering the barcoding project in general. We also thank the numerous mining and exploration companies that have openly shared information and allowed, and in many cases actively encouraged, access to drillcore for the purpose of sampling.

References

Arndt, HT and Jenner, GA 1986, Crustally contaminated komatiites and basalts from Kambalda, Western Australia: Chemical Geology, v. 56, p. 229–255.

Barley, ME, Brown, SJ, Krapěz, B and Cas, RAF 2002, Tectono-stratigraphic analysis of the Eastern Yilgarn Craton: an improved geological framework for exploration in Archaean terranes: Australian Minerals Industry Association Report, 437A.

Barley, ME, Brown, SJA, Cas, RAF, Cassidy, KF, Champion, DC, Gardoll, SJ and Krapež, B 2003, AMIRA Project P624. An integrated geological and metallogenic framework for the eastern Yilgarn Craton: Developing geodynamic models of highly mineralised Archean granite-greenstone terranes Final Report April 2003. AMIRA Project P624 Report.

Barnes, SJ and Arndt, NT 2018, Distribution and Geochemistry of Komatiites and Basalts Through the Archean: Earth's Oldest Rocks. Elsevier B.V., doi:10.1016/b978-0-444-63901-1.00006-x.

Barnes, SJ and Van Kranendonk, MJ 2014, Archean andesites in the east Yilgarn Craton, Australia: Products of plume-crust interaction?: Lithosphere, v. 6, p. 80–92.

Barnes, SJ, Van Kranendonk, MJ and Sonntag, I 2012, Geochemistry and tectonic setting of basalts from the Eastern Goldfields Superterrane: Australian Journal of Earth Sciences, v. 59, p. 707–735.

Barnes, SJ, Williams, M, Smithies, RH, Hanski, E and Lowrey, JR 2021, Trace Element Contents of Mantle-Derived Magmas Through Time: Journal of Petrology, v. 62, p. 1–38.

Begg, GC, Hronsky, JMA, Arndt, NT, Griffin, WL, O'Reilly, SY and Hayward, N 2010, Lithospheric, cratonic and geodynamic setting of Ni-Cu-PGE sulfide deposits: Economic Geology, v. 105, p. 1057–1070.

Blewett, RS, Czarnota, K and Henson, PA 2010, Structural-event framework for the eastern Yilgarn Craton, Western Australia, and its implications for orogenic gold: Precambrian Research, v. 183, p. 203–229, doi.org/10.1016/j.precamres.2010.04.004.

Campbell, IH, Griffiths, RW and Hill, RI 1989, Melting in an Archaean mantle plume: heads it's basalts, tails it's komatiites: Nature, v. 339, p. 697–699.

Carey, ML 1994, Petrography and geochemistry of selected sills from the Kambalda-Kalgoorlie region, WA: Honours thesis, Australian National University, Canberra, Australia, 80p.

Cas, R, McMann, R, Olin, P, Hayman, P, Squire, R, Campbell, I, Smithies, H, Sapkota, J and Wyche, S 2019, Distinguishing thick dolerite sills from ponded lavas: new emplacement origin for the gold-rich, Archean Golden Mile Dolerite, Kalgoorlie, Western Australia: IAVCEi Conference, Montreal.

Cassidy, KF, Champion, DC, McNaughton, NJ, Fletcher, IR, Whitaker, AJ, Bastrakova, IV and Budd, A (editors) 2002, The characterisation and Metallogenic Significance of Archaean Granitoids of the Yilgarn Craton, Western Australia: Minerals and Energy Research Institute of Western Australia (MERIWA), Project no. M281/AMIRA Project no. 482 (unpublished Report No. 222).

Cassidy, KF, Champion, DC, Krapěz, B, Barley, ME, Brown, SJA, Blewett, RS, Groenewald, PB and Tyler, IM 2006, A revised geological framework for the Yilgarn Craton, Western Australia: Geological Survey of Western Australia, Record 2006/8.

Champion, DC 2013, Neodymium depleted mantle model age map of Australia: explanatory notes and user guide: Record 2013/44. Geoscience Australia: Canberra, doi:10.11636/Record.2013.044.

Champion, DC and Sheraton, JW 1997, Geochemistry and Nd-isotope systematics of Archaean granites of the Eastern Goldfields, Yilgarn Craton, Australia: implications for crustal growth processes: Precambrian Research, v. 83, p. 109–132.

Champion, DC and Cassidy, KF 1998, Metallogenic potential of granitoids: Kanowna Belle and Granny Smith regions: Final report to Golden Valley Joint Venture and Placer Pacific Ltd., Australian Geological Survey Organisation (unpublished).

Champion, DC and Cassidy, KF 2002a, Granites of the northern Eastern Goldfields: their distribution, age, geochemistry, petrogenesis, relationship with mineralisation, and implications for tectonic environment (including a simplified key for discriminating granite groups in the northern Eastern Goldfields). In: Cassidy, KF, Champion, DC, McNaughton, NJ, Fletcher, IR, Whitaker, AJ, Bastrakova, IV and Budd, AR 2002, Characterization and metallogenic significance of Archaean granitoids of the Yilgarn Craton, Western Australia: Aust. Miner. Ind. Res. Assoc. Project P482/MERIWA Project M281, Final Report, 514p.

Champion, DC and Cassidy, KF 2002b, Granites in the Leonora-Laverton transect area, north eastern Yilgarn, in Cassidy, KF, editor, Geology, geochronology and geophysics of the north eastern Yilgarn Craton, with an emphasis on the Leonora-Laverton transect area: Geoscience Australia, Record 2002/18, p. 13–35.

Champion, DC, Huston, D, Main, P, Jarrett, AJM, Thorne, J, Gilmore, S, Webber, S, Webster, T, Byass, J, DiBugnara, D, Williamson, A, Long, I and Peljo, N 2021, Exploring for the Future – Baseline whole rock geochemistry of Northern Australia Data Release — Geochemistry of drill core samples from the McArthur Basin, Lawn Hill platform and Tomkinson Province, Northern Territory and Queensland, Record 2020/041, Geoscience Australia, Canberra, doi:10.11636/Record.2020.041.

Czarnota, K, Champion, DC, Cassidy, KF, Goscombe, B, Blewett, R, Henson, PA and Groenewald, PB 2010, Geodynamics of the eastern Yilgarn Craton: Precambrian Research, v. 183, p. 175–202.

Drummond, BJ, Goleby, BR and Swager, CP 2000, Crustal signature of Late Archaean tectonic episodes in the Yilgarn craton, Western Australia: evidence from deep seismic sounding: Tectonophysics, v. 329, p. 193–221.

Dunphy, JM, Fletcher, IR, Cassidy, KF and Champion, DC 2003, Compilation of SHRIMP U–Pb geochronological data, Yilgarn Craton, Western Australia, 2001–2002: Geoscience Australia, Geoscience Australia Record 2003/15, p. 139.

Fayol, N and Jébrak, M 2017, Archean Sanukitoid Gold Porphyry Deposits: A New Understanding and Genetic Model from the Lac Bachelor Gold Deposit, Abitibi, Canada: Economic Geology, v. 112, p. 1913–1936.

Fletcher, IR and McNaughton, NJ 2002, Granitoid geochronology: SHRIMP zircon and titanite data. In: Cassidy, KF, Champion, DC, McNaughton, NJ, Fletcher, IR, Whitaker, AJ, Bastrakova, IV and Budd, AR 2002. Characterization and metallogenic significance of Archaean granitoids of the Yilgarn Craton: Project P482/MERIWA Project M281, Final Report. Australian Mineral and Industry Research Association, Western Australia, p. 514.

Fletcher, IR, Dunphy, JM, Cassidy, KF and Champion, DC 2001, Compilation of SHRIMP U–Pb geochronological data, Yilgarn Craton, Western Australia, 2000–2001: Geoscience Australia, Record 2001/47, 111p.

Gerya, TV, Stern, RJ, Baes, M, Sobolev, SV and Whattam, SA 2015, Plate tectonics on the Earth triggered by plume–indiced subduction initiation: Nature, v. 527, p. 221–225.

Gessner, K, Smithies, RH, Kirkland CL and Lu, Y 2017, Mapping the Yilgarn Craton's deep crustal structure by integrating time constrained geochemical data with geophysics, *in* W Gorczyk and K Gessner 2018, 3rd Lithosphere Dynamics Workshop, 5–6 November 2017, The University of Western Australia: Geological Survey of Western Australia, Record 2018/7, p. 3.

Goleby, BR, Blewett, RS, Formin, T, Fishwick, S, Reading, AM, Henson, PA, Kennett, BLN, Champion, DC, Jones, L, Drummond, BJ and Nicoll, M 2006, An integrated multi-scale 3D seismic model of the Archaean Yilgarn Craton, Australia: Tectonophysics, v. 420, p. 75–90, doi:10.1016/j.tecto.2006.01.028.

Gresham, JJ and Loftus-Hills, GD 1981, The geology of the Kambalda nickel field, Western Australia: Economic Geology, v. 76, p. 1373–1416.

Halley, S 2021, Geochemistry Workshop in ioGAS based on the Eastern Goldfields Greenstone Geochemical Barcoding Project, 34p.

Hayman, PC, Thébaud, N, Pawley, MJ, Barnes, SJ, Cas, RAF, Amelin, Y, Sapkota, J, Squire, RJ, Campbell, IH and Pegg, I 2015, Evolution of a ~2.7Ga large igneous province: A volcanological, geochemical and geochronological study of the Agnew Greenstone Belt, and new regional correlations for the Kalgoorlie Terrane (Yilgarn Craton, Western Australia): Precambrian Research, v. 270, p. 334–368.

Hayman, PC, Campbell, IH, Cas, RAF, Squire, RJ, Doutch, D and Outhwaite, M 2021, Differentiated Archean Dolerites: Igneous and Emplacement Processes that Enhance Prospectivity for Orogenic Gold: Economic Geology, v. 116, p. 1949–1980.

Hill, RI, Chappell, BW and Campbell, IH 1992, Late Archaean granites of the southeastern Yilgarn Block, Western Australia: age, geochemistry, and origin: Transactions Royal Society Edinburgh. Earth and Environmental Sciences, v. 83, p. 211–226, doi:10.1017/S0263593300007902.

Hollis, SP, Mole, DR, Gillespie, P, Barnes, SJ, Tessalina, S, Cas, RAF, Hildrew, C, Pumphrey, A, Goodz, MD, Caruso, S, Yeats, CJ, Verbeeten, A, Belford, SM, Wyche, S and Martin, LAJ 2017, 2.7 Ga plume associated VHMS mineralization in the Eastern Goldfields Superterrane, Yilgarn Craton: insights from the low temperature and shallow water, Ag-Zn-(Au) Nimbus deposit: Precambrian Research, v. 291, p. 119–142.

Jones, SA, Cassidy, KF and Davis, BK 2020, Unravelling the D1 event: evidence for early granite-up, greenstone-down tectonics in the Eastern Goldfields, Western Australia: Australian Journal of Earth Sciences, doi:10.1080/08120099.2020.1755364.

Kositcin, N, Brown, SJA, Barley, ME, Krapež, B, Cassidy, KF and Champion, DC 2008, SHRIMP U-Pb zircon age constraints on the Late Archaean tectonostratigraphic architecture of the Eastern Goldfields Superterrane, Yilgarn Craton, Western Australia: Precambrian Research, v. 161, p. 5–33.

Krapež, B, Brown, SJA, Hand, J, Barley, M and Cas, RAF 2000, Age constraints on recycled crustal and supracrustal sources of Archaean metasedimentary sequences, Eastern Goldfields Province, Western Australia: evidence from SHRIMP zircon dating: Tectonophysics, v. 322, p. 89–133.

Lowrey, JR, Wyman, DA, Ivanic, TJ, Smithies, RH and Maas R 2020, Archean Boninite-like Rocks of the Northwestern Youanmi Terrane, Yilgarn Craton: Geochemistry and Genesis: Journal of Petrology, v. 60, p. 2131–2168.

Lu, Y-J, Loucks, RR, Fiorentini, ML, Yang, Z-M and Hou, Z-Q 2015, Fluid flux melting generated postcollisional high Sr/Y copper ore–forming water-rich magmas in Tibet: Geology, v. 43, no. 7, p. 583–586.

Lu, Y, Wingate, MTD, Sapkota, JK and De Paoli, M 2017, 211051: porphyritic andesite, White Flag Lake: Geochronology Record 1426: Geological Survey of Western Australia, 4p.

Lu, Y, Wingate, MTD and Smithies, RH 2020a, 230328: porphyritic microgranite, Lake Lefroy; Geochronology Record 1654: Geological Survey of Western Australia, 4p.

Lu, Y, Wingate, MTD and Smithies, RH 2020b, 229913: hornblende metagranodiorite, Lake Lefroy; Geochronology Record 1653: Geological Survey of Western Australia, 4p.

Lu, Y, Wingate, MTD, Champion, DC, Smithies, RH, Johnson, SP, Mole, DR, Poujol, M, Zhao, J, Maas, R and Creaser, RA 2021, Samarium–neodymium isotope map of Western Australia: Geological Survey of Western Australia, digital data layer, <www.dmirs.wa.gov.au/geoview>.

McMann, RM 2018, A syn-depositional sill intrusive model for the Golden Mile Dolerite, Kalgoorlie, Western Australia: Honours thesis, Geology. University of Tasmania, Hobart, 93p.

Mole, DR, Fiorentini, ML, Cassidy, KF, Kirkland, CL, Thébaud, N, McCuaig, TC, Doublier, MP, Duuring, P, Romano, SS, Maas, R, Belousova, EA, Barnes, SJ and Miller, J 2015, Crustal evolution, intra-cratonic architecture and the metallogeny of an Archaean craton: Geological Society, London, Special Publications, v. 393, p. 23–80.

Mole, DR, Kirkland, CL, Fiorentini, ML, Barnes, SJ, Cassidy, KF, Isaac, C, Belousova, EA, Hartnady, M and Thébaud, N 2019, Time-space evolution of an Archean craton: A Hf-isotope window into continent formation: Earth-Science Reviews, v. 196, 46p, doi:10.1016/j.earscirev.2019.04.003.

Morris, PA 1993, Archaean mafic and ultramafic volcanic rocks, Menzies to Norseman, Western Australia: Geological Survey of Western Australia, Report 36, 107p.

Morris, PA and Kirkland, CL 2013, Melting of a subduction-modified mantle source: A case study from the Archean Marda Volcanic Complex, central Yilgarn Craton, Western Australia: Lithos, v. 190, p. doi:10.1016/j.lithos.2013.11.016.

Murphy, DT, Wiemer, D, Bennett, VC, Spring, T, Trofimovs, and Cathey, HE 2021, Paleoarchean variole-bearing metabasalts from the East Pilbara Terrane formed by hydrous fluid phase exsolution and implications for Archean greenstone belt magmatic processes: Precambrian Research, v. 357.

Nelson, DR 1995a, 112159: porphyritic dacite, Royal Arthur: Geochronology Record 488: Geological Survey of Western Australia, 5p.

Nelson, DR 1995b, 112110: felsic volcanic rock, Nelson's Fleet: Geochronology Record 526: Geological Survey of Western Australia, 4p.

Nelson, DR 1997, Evolution of the Archaean granite-greenstone terranes of the Eastern Goldfields, Western Australia: SHRIMP U-Pb zircon constraints: Precambrian Research, v. 83, p. 57–81.

Pawley, MJ, Wingate, MTD, Kirkland, CL, Wyche, S, Hall, CE, Romano, SS and Doublier, MP 2012, Adding pieces to the puzzle: Episodic crustal growth and a new terrane in the northeast Yilgarn Craton, Western Australia: Australian Journal of Earth Sciences, v. 59, p. 603–623.

Pearce, JA 2014, Immobile Element Fingerprinting of Ophiolites: Elements, v. 10, p. 101–108.

Roberts, D 1988, Kambalda – St Ives area nickel sulphide and gold deposits, *in* Excursion guidebook: Boddington and Eastern Goldfields, Western Australia *edited by* BH Smith, CA Stoakes, AL Govey, and CJ Oates: The second international conference on prospecting in arid terrain, Perth, Western Australia, 26 April 1988, The University of Western Australia: Department of Geology and University Extension, Publication no. 18, p. 68–76.

Ross, AA, Barley, ME, Brown, SJA, McNaughton, NJ, Ridley, JR and Fletcher, IR 2004, Young porphyries, old zircons: new constraints on the timing of deformation and gold mineralisation in the Eastern Goldfields from SHRIMP U–Pb zircon dating at the Kanowna Belle Gold Mine, Western Australia: Precambrian Research, v. 128, p. 105–142.

Sapkota, J 2020, GSOD20 Eastern Goldfields Stratigraphy (Poster): Geological Survey of Western Australia, GSWA Open Day 2020, Fremantle, Western Australia, 20 February 2020, <www.dmirs.wa.gov.au/gswaopenday>.

Shirey, SB and Hanson, GN 1984, Mantle-derived Archaean monozodiorites and trachyandesites: Nature, v. 310, p. 222–224.

Sircombe, KN, Cassidy, KFC, Champion, DC and Tripp, G 2007, Compilation of SHRIMP U-Pb geochronological data, Yilgarn Craton, Western Australia, 2004–2006: Geoscience Australia, Geoscience Australia Record 2007/01, 182p.

Smithies, RH 2019, A new look at lamprophyres and sanukitoids, and their relationship to the Black Flag Group and gold prospectivity (PowerPoint): Geological Survey of Western Australia, GSWA Open Day 2019, Fremantle, Western Australia, 22 February 2019, <www.dmirs.wa.gov.au/gswaopenday>.

Smithies, RH and Champion, DC 1999, Late Archaean felsic alkaline igneous rocks in the Eastern Goldfields, Yilgarn Craton, Western Australia: a result of lower crustal delamination?: Journal of the Geological Society of London, v. 156, p. 561–576.

Smithies, RH and Champion, DC 2000, The Archaean high-Mg diorite suite: Links to tonalite-trondhjemite-granodiorite magmatism and implication for early Archaean crustal growth: Journal of Petrology, v. 41, p. 1653–1671.

Smithies, RH, Ivanic, TJ, Lowrey, JR, Morris, PA, Barnes, SJ, Wyche, S, Lu, Y-J 2018a, Two distinct origins for Archean greenstone belts: Earth and Planetary Science Letters, v. 487, p. 106–116, doi:10.1016/j.epsl.2018.01.0342018a.

Smithies, RH, Lu, Y, Kirkland, CL, Cassidy, KF, Champion, DC, Sapkota, J, de Paoli, M and Burley, L 2018b, A new look at lamprophyres and sanukitoids, and their relationship to the Black Flag Group and gold prospectivity: Geological Survey of Western Australia, Record 2018/15, 23p.

Smithies, RH, Lu, Y, Gessner, K, Wingate, MTD and Champion, DC 2018c, Geochemistry of Archean granitic rocks in the South West Terrane of the Yilgarn Craton: Geological Survey of Western Australia, Record 2018/10, 13p.

Smithies, RH, Lu, Y, Johnson, TE, Kirkland, CL, Cassidy, KF, Champion, DC, Mole, DR, Zibra, I, Gessner, K, Sapkota, J, De Paoli, MC and Poujol, M 2019, No evidence for high-pressure melting of Earth's crust in the Archean: Nature Communications, 10:5559 doi:10.1038/s41467-019-13547-x.

Squire, RJ, Allen, CM, Cas, RAF, Campbell, IH, Blewett, RS and Nemchin, AA 2010, Two cycles of voluminous pyroclastic volcanism and sedimentation related to episodic granite emplacement during the late Archean: Eastern Yilgarn Craton, Western Australia: Precambrian Research, v. 183, p. 251–274.

Stanley, CR and Lawie, D 2007, Average relative error in geochemical determination: clarification, calculation, and a plea for constituency: Exploration and Mining Geology, v. 16, p. 267–275.

Sugiono, D, Thébaud, N, LaFlamme, C, Fiorentini, M, Martin, L, Rogers, J, Lorusso, G and McFarlane, C 2021, Integration of multiple sulfur isotopes with structural analysis unveils the evolution of ore fluids and source of sulfur at the Kanowna Belle Archean orogenic gold deposit, Yilgarn Craton, Western Australia: Mineralium Deposita, doi:10.1007/s00126-020-01032-1.

Sun, SS and McDonough, WF 1989, Chemical and isotopic systematics of oceanic basalts: implication for mantle composition and processes: Geological Society of London, Special Publications, v. 42, p. 313–345.

Swager, CP, Goleby, BR, Drummond, BJ, Rattenbury, MS and Williams, PR 1997, Crustal structure of granite-greenstone terranes in the Eastern Goldfields, Yilgarn Craton, as revealed by seismic reflection profiling: Precambrian Research, v. 83, p. 43–56.

Swager, CP, Griffin, TJ, Witt, WK, Wyche, S, Ahmat, AL, Hunter, WM and Mcgoldrick, PJ 1990, Geology of the Archaean Kalgoorlie Terrane – an explanatory note: Western Australia Geological Survey, Report 48, 26p.

Thébaud, N, Sugiono, D, LaFlamme, C, Miller, J, Fisher, L, Voute, F, Tessalina, S, Sonntag, I and Fiorentini, M 2018, Protracted and polyphased gold mineralisation in the Agnew District (Yilgarn Craton, Western Australia): Precambrian Research, v. 310, p. 291–304.

Tripp, GI 2013, Stratigraphy and structure in the Neoarchaean of the Kalgoorlie district, Australia: critical controls on greenstone-hosted gold deposits: Ph.D thesis, School of Earth and Environmental Science, Townsville, Queensland: James Cook University.

Tripp, GI 2019, Stratigraphy and Structure in the Neoarchaean of the Kalgoorlie district, Australia: Critical Controls on Greenstone-hosted Gold Deposits: Geological Survey of Western Australia, Report 199, 967p.

Ueda, K, Gerya, T and Sobolev, SV 2008, Subduction initiation by thermal–chemical plumes: numerical studies: Physics of the Earth and Planetary Interiors, v. 171, p. 296–312.

Wingate, MTD, Fielding, IOH, Lu, Y and Sapkota, J 2021a, 222662: porphyritic dacite, Four Mile Hill: Geochronology Record 1759: Geological Survey of Western Australia, 4p.

Wingate, MTD, Fielding, IOH, Lu, Y and Smithies, RH 2021b, 245105: volcaniclastic sandstone, Kanowna Belle mine: Geochronology Record 1835: Geological Survey of Western Australia, 4p.

Wingate, MTD, Fielding, IOH, Lu, Y and Smithies, RH 2021c, 245115: porphyritic microgranite, Kanowna Consols mine: Geochronology Record 1836: Geological Survey of Western Australia, 4p.

Wingate, MTD, Fielding, IOH, Lu, Y and Smithies, RH 2021d, 245127: porphyritic metadacite, Ellen Dam: Geochronology Record 1838: Geological Survey of Western Australia, 4p.

Wingate, MTD, Fielding, IOH, Lu, Y and Smithies, RH 2021e, 245122: volcaniclastic sandstone, Carbine mine: Geochronology Record 1837: Geological Survey of Western Australia, 5p.

Wingate, MTD, Lu, Y, Fielding, IOH, Cassidy, KF and Smithies, RH 2022a, 203736: porphyritic metagranitic rock, Victory deposit; Geochronology Record 1852: Geological Survey of Western Australia, 5p.

Wingate, MTD, Lu, Y, Fielding, IOH and De Paoli, M 2022b, 240481: porphyritic metadacite, Aphrodite prospect; Geochronology Record 1859: Geological Survey of Western Australia, 5p.

Wingate, MTD, Lu, Y, Fielding, IOH and Smithies, RH 2022c, 236002: metadacite, Daisy Milano mine; Geochronology Record 1857: Geological Survey of Western Australia, 4p.

Witt, WK, Ford, A, Hanrahan, B and Mamuse, A 2013, Regional-scale targeting for gold in the Yilgarn Craton: Part 1 of the Yilgarn Gold Exploration Targeting Atlas: Geological Survey of Western Australia, Report 125, 130p.

Witt, WK, Ford, A and Hanrahan, B 2015, District-scale targeting for gold in the Yilgarn Craton: Part 2 of the Yilgarn Gold Exploration Targeting Atlas: Geological Survey of Western Australia, Report 132, 276p.

Witt, W, Cassidy, KF, Lu, Y and Hagemann, S 2018, The tectonic setting and evolution of the 2.7 Ga Kalgoorlie–Kurnalpi Rift, a world-class Archean gold province, Mineralium Deposita, doi:10.1007/s00126-017-0778-9.

Woodall, RW 1965, Structure of the Kalgoorlie goldfield, *in* Geology of Australian ore deposits, v. I , Commonwealth Mining & Metallurgical Congress, (8th: Australia and New Zealand) *edited by* J McAndrew (2nd edition): Australasian Institute of Mining and Metallurgy, p. 71–79.

Appendices

Appendix 1

Whole-rock major and trace element data for samples used in the Report

Available with the PDF online as an accompanying digital resource

Appendix 2

Diamond drillcores used for geochemical sampling

Available with the PDF online as an accompanying digital resource

Appendix 3

Layered PDF versions of all geochemical variation diagrams

Available with the PDF online as an accompanying digital resource

Appendix 4

Summary statistics relating to the geochemistry of mafic units

Available with the PDF online as an accompanying digital resource

Appendix 5

Workflow for classifying geochemical samples

The following workflow provides a method of visually or graphically reproducing the specific compositional features that uniquely identify the individual units or groups described here. It does not reproduce the process originally used to identify the units or groups. Users should be aware that this workflow will not identify, or will erroneously assign, data from any legitimate new geochemical groups not encountered within our dataset and it will not allow for significant legitimate expansion of specific compositional fields. For these reasons, it may not be appropriate to apply this workflow to areas outside the study region. Preliminary applications to data from the Agnew region, for example, clearly identify significant migration in specific fields, likely relating to slight changes in magma bulk compositions (i.e. including melt source and any subsequent contaminant) as expected. Nevertheless, the procedure employs sufficient critical compositional variation diagrams that any completely new units or significant expansions to the fields of old units, should be apparent to the user.

The importance of spatial, stratigraphic, and more broadly geological context cannot be over emphasized. In a core intersection or in a specific geographical region, if all samples are L-U2, except for a single (or a few) sample that is L-U1 on some but not most plots, common sense would suggest that it too is probably L-U2 and that either analytical errors or weak alteration (for example) might account for any discrepancies.

It is also important to note that fields isolated using the following workflow, typically encompass 90–95% of the data (i.e. up to 10% outliers excluded). Using the following method, we have reclassified our data for mafic rocks, with a 95% success rate. Most of the 5% of samples given alternative classifications relate to examples where we originally (and arguably correctly) exercised geological discretion in classification.

Workflow

If major element oxide data does not exist, recalculate:

Al (ppm) to Al_2O_3 wt% (Al/10000*1.8895)

Ti (ppm) to TiO_2 wt% (Ti/10000*1.6681)

Mg (ppm) to MgO wt% (Mg /10000*1.6579)

Fe (ppm) to FeO wt% (Fe/10000*1.2865)

Fe (ppm) to Fe_2O_3 wt% (Fe/10000*1.4297)

Ca (ppm) to CaO wt% (Ca/10000*1.3992)

Na (ppm) to Na_2O wt% (Na/10000*1.3480)

K (ppm) to K_2O wt% (K/10000*1.2046)

P (ppm) to P_2O_5 wt% (P/10000*2.2914)

Calculate:

Total Fe as Fe_2O_3 (Fe_2O_3T) [i.e. Fe2O3 + (FeO/1.1113)]

Total Fe as FeO (FeOT) [i.e. FeO + (Fe_2O_3*1.1113)]

$Mg^{\#}$ [=100*(MgO/40.3)/((MgO/40.3)+(FeOT/71.85))]

ASI (if Na data present) =[(Al_2O_3/101.96)/((CaO/56.1)+(Na_2O/61.98)+(K_2O/94.2))]

Quarantine ultramafic data (not used further in barcoding):

Set aside all data with MgO >21 wt%

Set aside all data with Ti/Zr >70 AND MgO >18 wt%

Group the remaining data as:

Mafic (basic), if Ti/Zr >48

Felsic (intermediate and acid), if Ti/Zr <48

For mafic samples

Unless clear evidence for anomalism in the major or trace elements was detected, mafic samples have not been filtered for alteration. Most of the plots we used for discrimination and interpretation are based on elements typically regarded as moderately or strongly fluid immobile. No measures of compositional evolution or crustal contamination (e.g. La/Sm, La/Yb, Th/Nb etc., or even U/Th) show a clear correlation with concentrations of CaO, Na_2O, or K_2O and these element oxides did not vary systematically with loss on ignition (LOI). Throughout the entire basalt dataset, we could identify 81 analyses that show some form of anomalism on a mantle-normalized trace element diagram, but removal of these analyses had no perceptible effect on compositional trends or fields; all analyses were retained.

Isolate all samples with Th/TiO_2 >2 (plot of Th vs TiO_2) as HTSB and KB3:

- Classify all samples with Th/TiO_2 >3.33 (plot of Th vs TiO_2) as either H-HM$g^{\#}$ ($Mg^{\#}$ >62) or H-LM$g^{\#}$ ($Mg^{\#}$ <62) (set aside)
- Classify all remaining HTSB+KB3 samples with Ni <150 ppm AND Th/Nb >0.5 as H-LTh (set aside)
- Classify remaining samples as KB3, if a relationship to komatiite can be reasonably inferred (set aside).

Classify samples with Al_2O_3/TiO_2 between 25 and 28.5 AND with TiO_2 >0.54 wt% as L-S2 (set aside).

Classify samples with Al_2O_3/TiO_2 between 24.5 and 32.5 AND with Al_2O_3 <15.5 wt% as L-S1.

Also classify remaining samples with Zr <30 ppm AND TiO_2 <0.54 wt% as L-S1 (set aside).

Classify samples with Th >0.2 ppm AND TiO_2 <0.6 wt% as KB1 (set aside).

Classify samples with TiO_2 >2.0 wt% as L-U7 (set aside).

Isolate all samples with Th/Zr ratio >0.0143 (this group includes I-S4, I-VS, L-S3a, and L-S3b):

- Classify samples with Al_2O_3/TiO_2 >19 as I-VS (set aside)
- Classify samples with Zr >70 ppm as I-S4 (set aside)
- Group all remaining samples as L-S3
- Classify all L-S3 samples within the western domains as L-S3a (set aside)
- Classify all remaining samples as L-S3b (set aside).

Isolate, using a plot of Th (ppm) (y-axis) against TiO_2 wt% (x-axis), all samples above a line, y = 1.366x−0.55 (this groups the I-S trend):

- Classify samples with TiO_2 <0.6 wt% as I-S1 (set aside)
- Of the remainder, classify samples with Al_2O_3/TiO_2 <15 as I-S3 (set aside)
- Classify all remaining samples as I-S2 (set aside).

Return to a plot of Th vs Zr and isolate samples with a Th/Zr ratio >0.01 AND Th <0.55 ppm and add to L-S3 (L-S3b) (set aside).

Classify, using a plot of Th (ppm) against TiO_2 wt%, samples with TiO_2 >1.75 wt% AND Th <0.9 ppm as L-U6 (set aside).

Classify, using a plot of Zr (ppm) against TiO_2 wt%, samples with Zr <48 ppm AND TiO_2 <0.8 wt% as L-U1 (set aside).

Using a plot of Th (ppm) against TiO_2 wt%:

- Isolate all samples with a Th/TiO_2 ratio <0.41 [this includes L-U2 and most of the L-U3–7 trend (L-U6 and L-U7 already set aside)]. Of these samples (Th/TiO_2 ratio <0.41):
  - Classify all samples with Al_2O_3 >17 AND TiO_2 <1.17 as L-U3 (set aside)
  - Classify all samples with Al_2O_3/TiO_2 >15.3 as L-U2 (set aside)
  - Classify all samples with Nb <2.7 ppm as L-U2* (set aside)
  - Classify all samples with Al_2O_3 >15.6 wt% as L-U5 (set aside)
  - View remaining samples on plots of Th, Nb, Zr vs TiO_2, isolate significant trend outliers and classify remaining samples as L-U4 (set aside)
  - If trend outliers represent a rational geochemical trend, classify them as a new group.

  Samples of L-U2 (L-U2*) and L-U3 that fall in the area where these units almost merge, should be further considered from a geographical perspective, and using any additional geological context, allocated to the most likely group.

  The samples of L-U3, LU-4, and L-U5 that fall in the area where these units almost merge, should be further considered from a geographical perspective, and using any additional geological context, allocated to the most likely group.

- Isolate all samples with a Th/TiO_2 ratio >0.41 (this includes L-Ca and L-Cb as well as L-S4). Of these samples (Th/TiO_2 ratio >0.41):
  - Classify all samples with Th/Nb >0.27 as L-S4 (set aside)
  - Classify remaining samples as L-C. If L-Ca and L-Cb require discriminating, this can be achieved effectively using Na_2O concentration (L-Cb >3.5 wt% > L-Ca) or a plot of Fe_2O_3 (wt%) (y-axis) against Sc (ppm) (x-axis), where most L-Ca and L-Cb lie above and below, a line y = −0.1818x+20, respectively.

  Samples of L-C lying in regions merging with L-S3, L-U3, and L-U4 should be further considered from a geographical perspective, and using any additional geological context, allocated to the most likely group.

For felsic rocks

Unless there is reason to indicate the following conditions are not related to alteration, remove all data with:

Ti/Zr <48 AND CaO >8 wt%

Ti/Zr <48 AND Na_2O <0.5 wt%

Ti/Zr <48 AND K_2O >4.5 wt%

Ti/Zr <48 AND Na_2O+K_2O <3.5 wt%

Ti/Zr <48 AND ASI >1.2

Although it appears that felsic volcanic and subvolcanic magmatism in greenstone belts is seldom compositionally equivalent with the felsic magmas forming the main granitic regions separating greenstones, particularly in the case of the High-Ca and Low-Ca granites, this is not always the case. Therefore, the potential equivalents of High-Ca and Low-Ca granites (for example) need to be identified. This is typically not easy because of the extent to which established geochemical populations of felsic magmas overlap. Consideration of mineralogy and field descriptions is very important. Most syenites (feldspar rich, quartz poor) and sanukitoids (hornblende rich) are mineralogically distinctive and many High-Ca granites can be distinguished from many Low-Ca granites based on feldspar mineralogy and proportions.

Identifying the compositional affiliation of a single sample can be impossible. Identifying trends in geologically plausible suites of samples is more productive. One of the biggest challenges is the identification of Mafic granites or sanukitoids from High-Ca granites. Without the benefit of accompanying genetically related mafic (low silica) samples, isolated samples of sanukitoids with SiO_2 >66 wt% are very difficult to distinguish from High-Ca granites (and almost impossible at SiO_2 >72 wt%), although $Mg^{\#}$ >45 and Cr >35 ppm should distinguish most sanukitoids at these SiO_2 levels.

Based on a craton-wide compilation of granite compositions, Champion and Sheraton (1997) and Champion and Cassidy (2002a) present numerous geochemical variation diagrams that can be used to identify or discriminate analyses of High-Ca, Low-Ca, HFSE-rich, and Mafic granites (mainly sanukitoids), and syenites. No single diagram is without considerable overlap, particularly between the fields for High-Ca and Low-Ca granites, but when most or all diagrams are considered collectively, effective discrimination is possible in most cases. We have found the following plots to be most useful:

- Ce vs K_2O: discriminating High-Ca and Low-Ca granites (Fig. 54)
- K_2O vs Ce/K_2O: discriminating High-Ca and Low-Ca granites (Fig. 55)
- Al_2O_3 vs Ce/K_2O: discriminating High-Ca and Low-Ca granites (Fig. 56).

- SiO_2 vs Ce/K_2O: discriminating Mafic granites and syenites from High-Ca and Low-Ca granites (Fig. 57)
- Fe_2O_3(total) vs SiO_2: discriminating HFSE-rich granites from High-Ca and Low-Ca granites (Fig. 58)
- Yb vs SiO_2: discriminating HFSE-rich granites (Fig. 59)
- Fe_2O_3(total) vs SiO_2: discriminating syenites, Mafic granites, and HFSE-rich granites from each other (Fig. 60)
- K_2O+Na_2O vs SiO_2: discriminating syenites (Fig. 61)
- $Mg^{\#}$ vs SiO_2: discriminating Mafic granites from High-Ca and Low-Ca granites (Fig. 62)
- Ni vs SiO_2: discriminating Mafic granites from High-Ca granites (Fig. 63).

After identifying samples equivalent to High-Ca, Low-Ca, HFSE-rich granites, and syenites, the procedure for subdividing and classifying the remaining Mafic granites (including sanukitoids and sanukitoid-like rocks) is described below (Fig. 36). As discussed above, a degree of overlap in all compositional fields is expected. This means that, for example, a few samples from an otherwise compositionally coherent suite of sanukitoids might fail the first test used here to identify sanukitoids (i.e. Nb/P_2O_5 <25) and be classified as 'others', and then plot apparently anonymously as sanukitoids within all subsequent classification plots. Common sense suggests these are sanukitoids and in an iterative approach to classification, such discrepancies can be rectified.

Classifying Mafic granites:

- After applying the filters (above), view samples with Ti/Zr <48 on a plot of Nb vs P_2O_5.
  - Group all samples with Nb/P_2O_5 <25 as sanukitoids
  - Group all samples with Nb/P_2O_5 >25 as potential sanukitoid-like rocks.
- For sanukitoids: verify that all ***geologically related*** suites (e.g. hornblende-bearing rocks of broadly andesitic to dacitic composition from one specific area or stratigraphic position) form trends or fields where at 60 wt% SiO_2, most (not necessarily all) samples have $Mg^{\#}$ >60, MgO >5 wt%, Ba and Sr each >500 ppm, La >20 ppm, and Ni and Cr each >100 ppm.
  - For samples within the region covered in this Report, using a plot of La vs Th, classify all samples with La/Th ≥4.9 as high La/Th sanukitoid and all samples with La/Th <4.9 as low La/Th sanukitoid.
- At this stage, particularly if filtering samples taken from outside of the area considered in this Report (where Nb/P_2O_5 might not be a suitable discriminator of sanukitoid), it would be advisable to also examine potential sanukitoid-like rocks on plots of $Mg^{\#}$, MgO, Ba, Sr, La, Ni, and Cr. The suites that otherwise meet all requirements of sanukitoids should be classified as such.
- For remaining potential sanukitoid-like rocks sampled within the region covered in this Report:
  - Classify any sample or suite with anomalously high concentrations of La (>60 ppm) AND other LREE, AND Zr (>175 ppm), AND Nb (>9 ppm), AND Sr (>500 ppm), and compared with other potential sanukitoid-like rocks, relatively high Na_2O, P_2O_5, and low total Fe (as either Fe_2O_3T or FeOT), MgO and $Mg^{\#}$, and Sc concentration (extrapolated to 60 wt% SiO_2) <8 ppm as high-La dacite (includes dacites and rhyolites)
  - Classify as low-La dacite (includes andesites and dacites), any sample or suite that (at 60 wt% SiO_2) satisfies most of the following: $Mg^{\#}$ ~50, Fe_2O_3T >8 wt%, MgO >4 wt%, Ba and Sr each <500 ppm, La <20 ppm, and Ni and Cr each >70 ppm, Sc >15 ppm, and Th <5 ppm
  - Most or all remaining samples should be medium-La dacites (includes dacites and rhyolites). When trends are extrapolated to 60 wt% SiO_2, most (not necessarily all) samples should have $Mg^{\#}$ ~45, Fe_2O_3 (total Fe) ~8 wt%, MgO ~3.5 wt%, Ba between 500 ppm and 1000 ppm and Sr ~500 ppm, La between 20 ppm and 40 ppm, and Ni and Cr each <50 ppm, Sc ~15 ppm, and Th ~10 ppm.

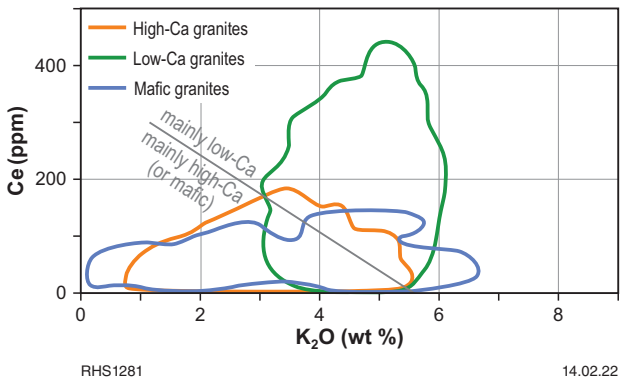

Figure 54. Variation of Ce with K_2O for granites of the Yilgarn Craton, distinguishing High-Ca, Low-Ca, and Mafic granites (data associated with Champion and Sheraton, 1997 and Champion and Cassidy, 2002a)

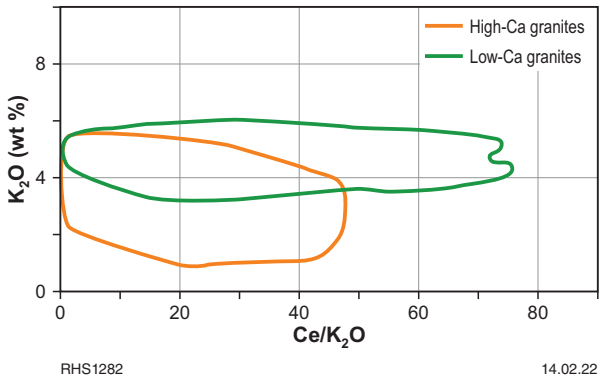

Figure 55. Variation of K_2O with Ce/K_2O for granites of the Yilgarn Craton, distinguishing High-Ca and Low-Ca granites (data associated with Champion and Sheraton, 1997 and Champion and Cassidy, 2002a)

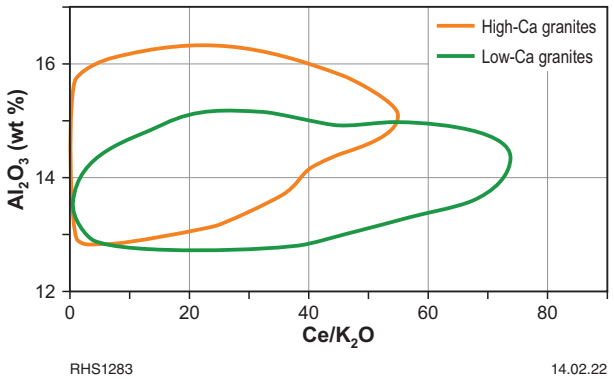

Figure 56. Variation of Al_2O_3 with Ce/K_2O for granites of the Yilgarn Craton, distinguishing High-Ca and Low-Ca granites (data associated with Champion and Sheraton, 1997 and Champion and Cassidy, 2002a)

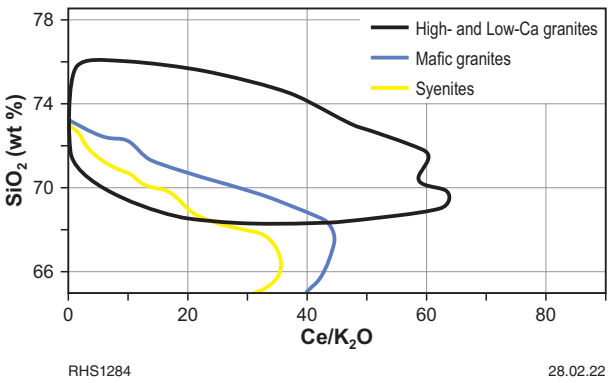

Figure 57. Variation of SiO_2 with Ce/K_2O for granites of the Yilgarn Craton, distinguishing High-Ca and Low-Ca granites, and syenites (data associated with Champion and Sheraton, 1997 and Champion and Cassidy, 2002a)

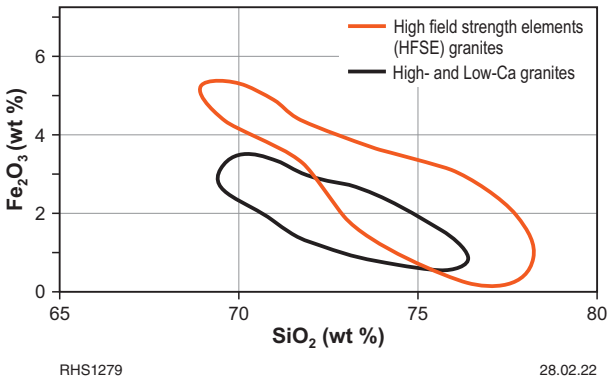

Figure 58. Variation of Fe_2O_3 with SiO_2 for granites of the Yilgarn Craton, distinguishing High-Ca, Low-Ca, and HFSE-rich granites (data associated with Champion and Sheraton, 1997 and Champion and Cassidy, 2002a)

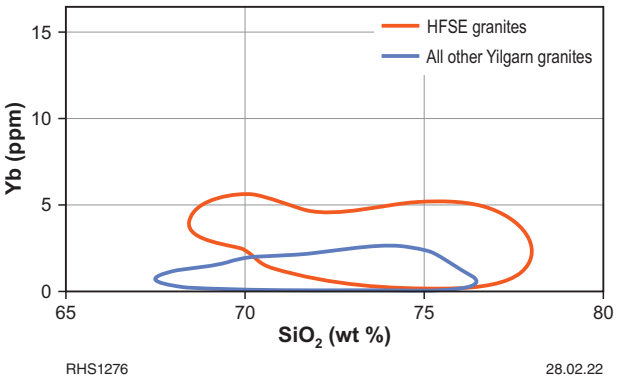

Figure 59. Variation of Yb with SiO_2 for granites of the Yilgarn Craton, distinguishing HFSE-rich granites from other granites (data associated with Champion and Sheraton, 1997 and Champion and Cassidy, 2002a)

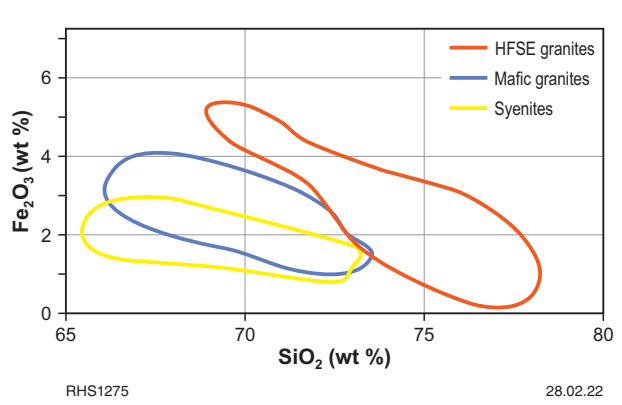

Figure 60. Variation of Fe_2O_3 with SiO_2 for granites of the Yilgarn Craton, distinguishing HFSE-rich granites, syenites, and Mafic granites (data associated with Champion and Sheraton, 1997 and Champion and Cassidy, 2002a)

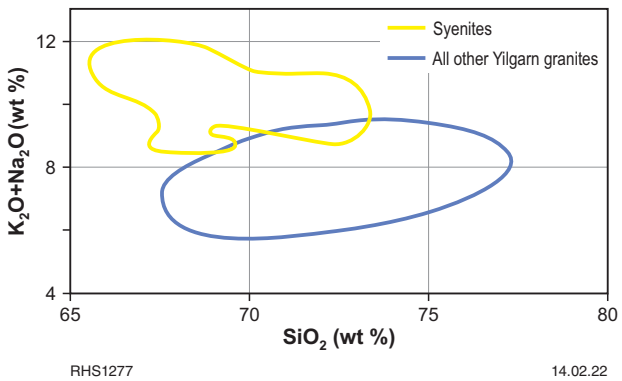

Figure 61. Variation of K_2O+Na_2O with SiO_2 for granites of the Yilgarn Craton, distinguishing syenites from other granites (data associated with Champion and Sheraton, 1997 and Champion and Cassidy, 2002a)

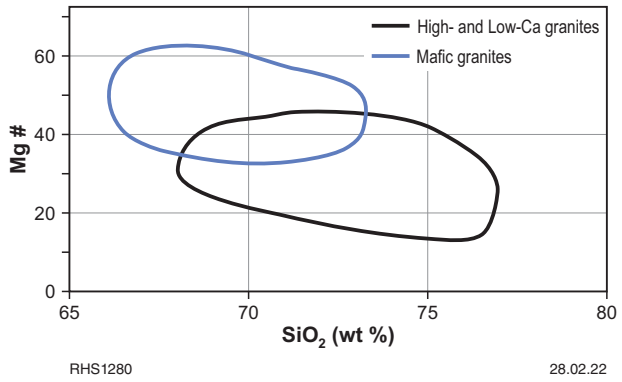

Figure 62. Variation of $Mg^{\#}$ with SiO_2 for granites of the Yilgarn Craton, distinguishing High-Ca, Low-Ca, and Mafic granites (data associated with Champion and Sheraton, 1997 and Champion and Cassidy, 2002a)

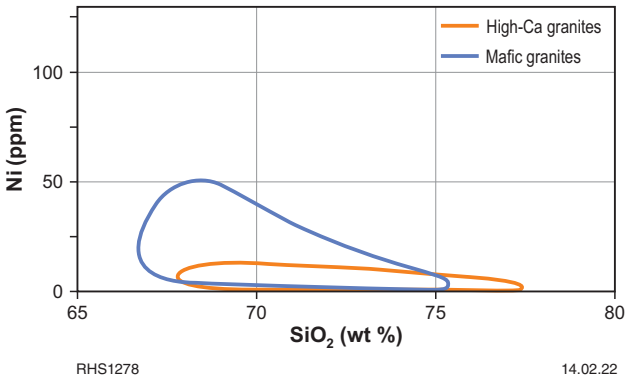

Figure 63. Variation of Ni with SiO_2 for granites of the Yilgarn Craton, distinguishing High-Ca and Mafic granites (data associated with Champion and Sheraton, 1997 and Champion and Cassidy, 2002a)

Appendix 6

Summary of the chemostratigraphy of the Ora Banda – Kambalda region and its practical field applications

Also available with the PDF online as an accompanying digital resource

This Appendix is designed as an independent practical guide to the potential field applications of the barcoding chemostratigraphy for mafic volcanic rocks of the Kalgoorlie Group and the felsic volcanic, volcaniclastic, and subvolcanic intrusive rocks of the Black Flag Group. The data are directly relevant to the region broadly between Ora Banda and Kambalda (Fig. 64). For more detailed geochemical, petrological, and geodynamic descriptions, interpretations and implications see the main text of Report 226.

Using a database of ~2800 high-quality whole-rock geochemical data and available stratigraphic information, we have attempted to identify the various geochemical components comprising the basaltic and felsic stratigraphy for parts of the domains lying within the region, broadly between Ora Banda and Kambalda. These domains include the Coolgardie, Kambalda, Ora Banda, Boorara, and Parker Domains of the Kalgoorlie Terrane and the western part of the Bulong Domain (Bulong complex) in the Kurnalpi Terrane. The mafic stratigraphy is shown in Figure 65. The mafic stratigraphy in each area is divided into three levels (lower, middle, and upper) according to previous lithostratigraphic interpretations and is based on the classic Kalgoorlie–Kambalda stratigraphy (e.g. Woodall, 1965; Gresham and Loftus-Hills, 1981; Roberts, 1988, Swager et al., 1990; Morris, 1993). Komatiite provides a convenient marker at the base of the middle level. We provide no information on the relative stratigraphic thicknesses of the levels within each column. The dashed line shown in the upper part of the Coolgardie and Ora Banda columns (Fig. 65) indicates that either an upper stratigraphic level does not appear to have been developed or preserved (Coolgardie, e.g. Swager et al., 1990) or that the boundary between the middle and upper levels is unclear (Ora Banda). Relatively low sample numbers mean that the chemostratigraphy for some parts of the Boorara and Parker Domains and for the Bulong complex is less robust than for the regions to the west. For units where this might be of concern, the number of samples collected is indicated in Figure 65. Otherwise, for each stratigraphic formation, the volume of each specific geochemical unit is proportional to the number of samples analysed. Whilst the relative number of samples of each specific geochemical unit might be broadly representative of true relative abundances in most cases, it is clearly open to sample bias. The geochemical units are organized vertically where the relative stratigraphic position of geochemical units within a formation is known or reasonably inferred. Otherwise, the geochemical units within formations are organized horizontally.

All samples collected as part of the greenstone geochemical barcoding project represent the visually least-altered examples of lithologically, texturally, and mineralogically homogeneous core intervals. We largely restricted our analysis to data from volcanic rocks covering the mafic and felsic (intermediate and acid) compositional range, i.e. SiO_2 from ~45 to 77 wt%, and MgO up to 18 wt% (except in the case of some partial cumulate layers). Komatiites and samples from mafic dykes and sills are not discussed in detail. All major element concentrations are quoted on a volatile-free basis (i.e. anhydrous).

For the classification and screening of rocks with broadly mafic compositions, we slightly modified the approach used by Barnes et al., (2012). In particular, the maximum SiO_2 content used to identify rocks of broadly basaltic composition was raised from 56 wt% to 57 wt%. The approach used by Barnes et al. (2012) uses variations in ratios of incompatible trace elements (e.g. Ti, Th, La, Nb, Zr) that are relatively immobile during hydrothermal alteration and low- to medium-grade metamorphism and insensitive to small variations in major elements related to common igneous processes.

Unless clear evidence for anomalism in the major or trace elements was detected, mafic samples have not been filtered for alteration. No measures of compositional evolution or crustal contamination (e.g. La/Sm, La/Yb, Th/Nb etc. or even U/Th) show a clear correlation with concentrations of CaO, Na_2O, or K_2O. Nor do these element oxides vary systematically with measures of alteration such as LOI, which in our dataset has values below 5 wt% for >80% of samples. Throughout the entire basalt dataset, we could identify 81 analyses that show some form of anomalism on a mantle-normalized trace element diagram but removal of these analyses had no perceptible effect on compositional trends or fields; most of these mafic analyses were retained.

The following screens and caveats were applied to the data:

- Intrusive rocks with SiO_2 <57 wt% and MgO <18 wt% were classified as dolerite or gabbro, depending upon grain size. Those samples with MgO >18 wt% were classified as peridotite
- Non-intrusive rocks with SiO_2 <57 wt% were classified as basaltic, if MgO <18 wt% and >3 wt% or komatiite, where MgO >18 wt%
- Many samples with MgO between 16 wt% and 18 wt% (and a few with MgO <16 wt%) have Al_2O_3/TiO_2 ratios ~20 (Al/Ti of ~1.0), a criteria Barnes et al. (2012) used to identify komatiitic basalts (KB). In nearly every case, these were directly associated with true komatiites (olivine spinifex-textured rocks or rocks intimately associated with olivine spinifex-textured rocks) and have been classified as KB. In some cases, these formed a compositionally distinct series that extended to much lower MgO contents
- Intrusive rocks with SiO_2 >57 wt% were almost invariably plagioclase-porphyritic and were classified as felsic dykes [andesitic (SiO_2 up to 63 wt%), dacitic (SiO_2 63–68 wt%) or rhyolitic (SiO_2 68–77 wt%)]
- Rocks with SiO_2 >57 wt% and evidence for a volcanic and volcaniclastic origin were classified as felsic volcanic or volcaniclastic (andesitic, dacitic or rhyolitic)
- Rocks with SiO_2 >57 wt% but with no clear evidence for a volcanic and volcaniclastic origin were classified as felsic (andesitic, dacitic or rhyolitic).

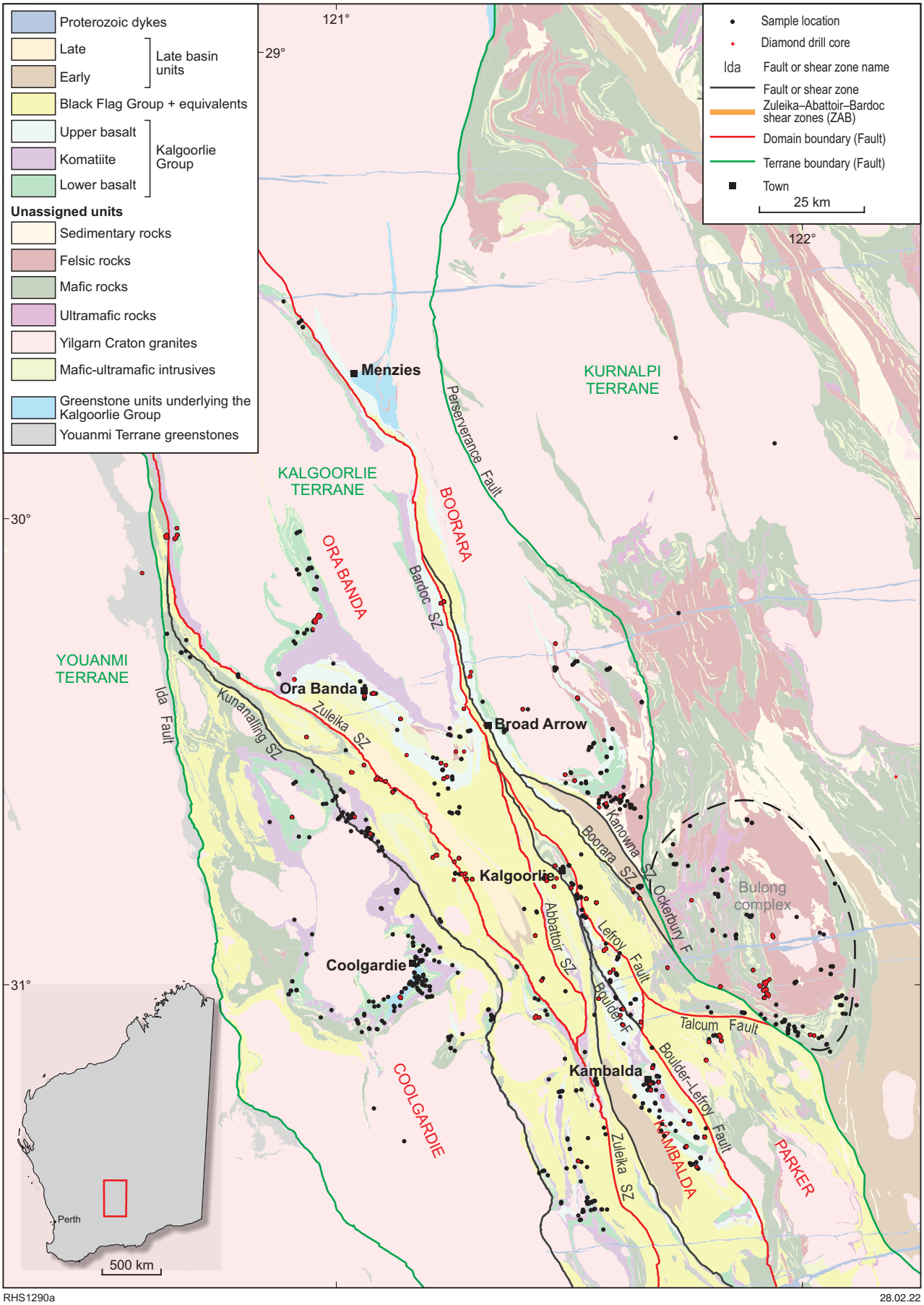

Figure 64. Geological map of the study area within the Kalgoorlie Terrane, showing a simplified version of the current interpreted bedrock geology, including the major faults and shear zones. Also shown is the distribution of sites of greenstone lithologies sampled for whole-rock geochemical data, including the locations where diamond drillcore has been sampled. Diamond drillcore locations are typically the sites of multiple (up to 55) individual samples

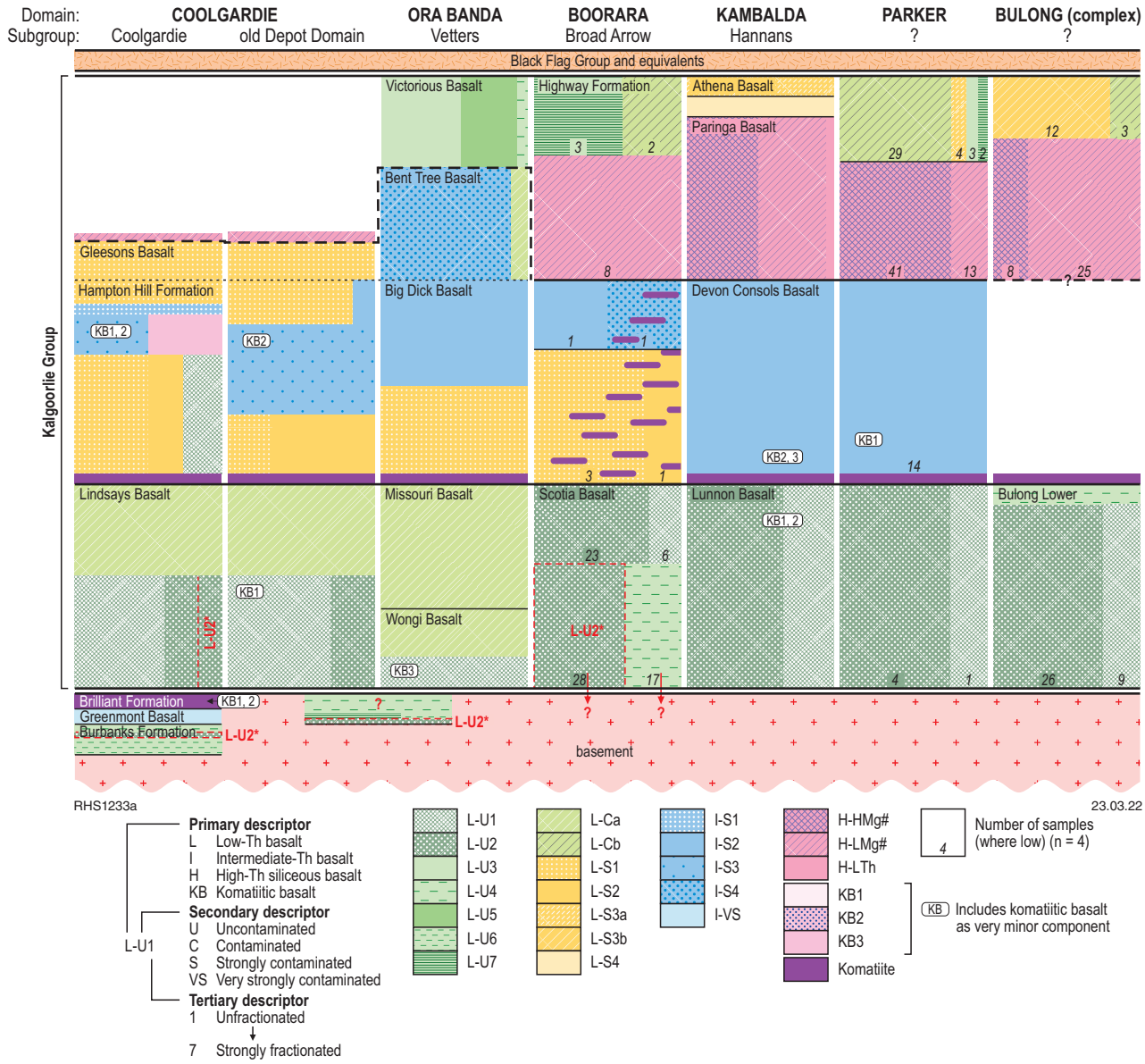

Figure 65. Chemostratigraphic columns representing each of the domain regions within the study area. Also included is a brief graphical explanation of the coding system used here (see text for further details and explanation)

- Rocks with SiO_2 >57 wt% were initially excluded from the dataset if:
  - The aluminium saturation index [ASI = molar Al_2O_3/($CaO+Na_2O+K_2O$)] exceeded 1.1 (i.e. the sample was peraluminous, in many cases indicative of feldspar-destructive alteration)
  - SiO_2 exceeded 77.5 wt% (i.e. silica concentrations higher than values achievable through normal igneous processes, i.e. silicified)
  - Na_2O was <1 wt% or Na_2O+K_2O <3.5 wt% (values suggestive of alkali loss).

Subdividing mafic rocks

Having applied the screens described above, mafic samples were further divided into primary lithochemical groups, including low-Th basalt (LTB, a proxy for any LREE-HFSE-Th-poor basalts), intermediate-Th basalt (ITB), and high-Th siliceous basalt (HTSB) groups as defined by Barnes et al. (2012) (Fig. 66). The geochemical range, in terms of Th (Nb, Zr, La) vs TiO_2 for each of these geochemical groups is tightly constrained and within each group, several discrete subgroups can be identified. These typically have a range of unique compositional features.

LTB, ITB, and HTSB groups, by definition, are commonly but not invariably distinguished on a plot of Th vs TiO_2 alone (see note below on precision limitations on low concentration Th data). Although Th concentrations are generally more sensitive to contamination and fractionation, the fluid immobile and only slightly less incompatible elements, Zr, Nb, and La should ideally also be used to discriminate broadly similar low, intermediate, and high groups. Instances where variation in one or more of these elements is slightly decoupled from the others, provide potential means of further subdivision. Hence, some LTB samples identified because of their low Th, Nb, and La concentrations might have slightly high Zr concentrations that result in Zr/TiO_2 ratios within the range typical of ITB, rather than LTB. In this case, a Zr-enriched LTB sample might be identified.

Similarly, if anomalism is identified with Th, the result might be a Th-enriched LTB. If this is a persistent characteristic within a specific geographical region and/or at a specific stratigraphic level, then we define an LTB group with high-Th (or Zr). Similar arguments apply for the identification of ITB. HTSB should be identified based only on Th and La vs TiO_2. We have used all four trace elements (each plotted against TiO_2) to identify our primary mafic groups. In cases where a sample plots in one field based on two elements (e.g. Th and Zr vs TiO_2) and in another based on the other two elements (La, Nb vs TiO_2), geological judgement is required to classify the sample. For example, you may need to consider whether this is an unusual or a persistent feature within a spatially or stratigraphically related series of samples. Although it is clearly feasible that a group of related samples might truly have perfectly transitional characteristics between LTB and ITB or ITB and HTSB, we have not yet identified any such cases.

Some basalts with MgO generally between 10 wt% and 18 wt% and $Mg^{\#}$ [molar ratio of Mg/(Mg+Fe), where Fe is total iron calculated as Fe^{2+}] from 60–78 (higher than typical LTB), have Al_2O_3/TiO_2 ratios ~20 but concentrations of Th, Zr, Nb, and La considerably lower than that of HTSB (and mostly lower than LTB). These are typically directly associated with komatiites and are classified as KB.

Primary mafic geochemical groups were further manually subdivided into smaller geologically plausible geochemical groups. This was an iterative process undertaken by simultaneously viewing the position of data points with respect to natural data clusters on plots of:

- TiO_2 vs Th, Nb, Zr, and La
- Th vs Nb and Zr
- Nb/Yb vs Th/Yb
- Al_2O_3/TiO_2 vs Al_2O_3 or Th/Nb
- Mantle-normalized incompatible trace element diagrams
- $Mg^{\#}$ vs all major elements, Cr, Ni, and Al_2O_3/TiO_2
- Longitude vs latitude vs position in drillcore (i.e. a map).

All these elements are strongly incompatible in mafic systems (until a TiFe oxide is stabilized in the case of Ti) and should increase in concentration with increased fractionation or decreased partial melting. Ratios between these elements will mainly reflect variations in bulk source compositions or mineralogy and provide an opportunity to subdivide magmas.

The Al_2O_3/TiO_2 ratio of a mantle-derived magma should not change significantly (from ~20) until plagioclase crystallizes and fractionates at low-pressure.

Compositional variations in the plots listed above, highlight the controls that various fundamental igneous processes and source compositional variations might have exerted on an evolving magma, and at least in the case of TiO_2, P_2O_5 and most of the selected trace elements are not strongly influenced by postmagmatic alteration.

A total of 26 minor units were identified and most of these were either LTB or ITB. These groups or units commonly show a moderate degree of compositional overlap with other groups or units in one or many of the compositional variation diagrams. However, each has either a compositional feature or a geographical distribution (or both) that allows it to be uniquely distinguished. Plots of TiO_2 vs Th and Zr and Al_2O_3/TiO_2 vs Al_2O_3 appear to be particularly useful in distinguishing these geochemical populations. These geochemical units cannot be given stratigraphic names because in most cases they occur at several stratigraphic positions, even within a single subgroup stratigraphy, and commonly form one of several distinct compositional units that together form an established stratigraphic unit. For example, the Big Dick Basalt in the Vetters Subgroup comprises at least two distinct geochemical units and the Lindsays Basalt in the upper Coolgardie succession comprises at least three units.

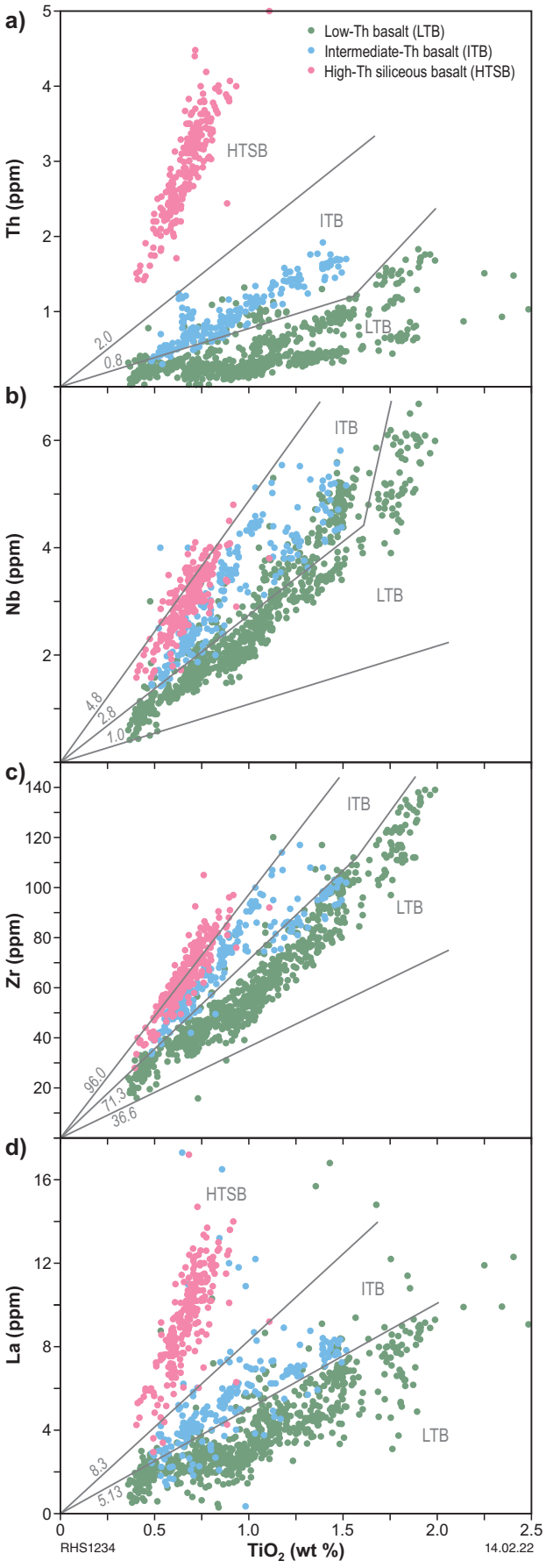

Figure 66. Variation in Th, Nb, Zr, and La with TiO_2 used for primary classification of basalts into LTB, ITB, and HTSB (after Barnes et al., 2012). Numbers indicate the x/TiO_2 ratio of the lines chosen to separate the various groups

Note on precision limitations on low concentration Th data

A degree of caution needs to be exercised regarding discrimination procedures such as the one outlined above, which utilizes trace elements typically present at concentrations approaching analytical detection limits. This is particularly the case for Th. Under such circumstances, it can be difficult to be certain that some of the typically more incompatible trace element-depleted groups are not simply an artefact of variation within the limits of analytical precision. In Figure 67, we show the estimated precision of analyses for Th, Nb, Zr, and La at very low concentrations, based on historical analytical results from BV Minerals (Champion et al., 2021). These uncertainties are generally small, but clearly, at least in the case of Th, potentially provide a plausible explanation for some of the compositional groups. However, we are confident that these groups are geologically meaningful for several reasons. Firstly, the precision estimates are indicative values based on analysis of a wide range of rock types and standards, most with significantly higher concentrations of Th and Nb (for example), and almost certainly would be improved, if calculated based only on samples and standards with very low concentrations. Secondly, mantle-normalized incompatible trace element patterns are typically smooth between Th, with a relatively high analytical uncertainty, and La and other LREE with a significantly lower analytical uncertainty, strongly suggesting the analytical precision for Th is much better than the indicated values. Thirdly, the same groups are often well-defined and are consistently identified on a wide range of compositional variation diagrams, including those using major element data at concentrations not subject to the same limitation in precision. Fourthly, most of the groups make geological sense in terms of their geographic and/or stratigraphic distribution. In addition, these compositional groups typically comprise samples analysed within more than one analytical batch.

Most of the basalt units were grouped and named primarily using plots of Th against TiO_2 and Th against Zr. The naming convention was constructed to emphasize the magmatic or petrogenetic history of the unit without any necessary implications in terms of direct genetic relationships to other units. It is clear from the systematic data spread in bivariate plots utilizing incompatible trace elements that varying degrees of crustal contamination reflects the greatest control over compositional differences between the units identified here. The primary classification itself is based on increasing amounts of crustal contamination from LTB to ITB to HTSB. However, we have added a secondary code that reflects the relative degrees of contamination of a specific unit within a given primary classification (Fig. 68). An additional code is added to indicate the relative extent of fractionation of a specific unit. Thus:

- For the primary classification descriptor,
  - LTB is denoted as 'L'
  - ITB is denoted as 'I'
  - HTSB is denoted as 'H'.
- The secondary measure of the amount of crustal material incorporated by a mafic parental magma was based broadly on the position of a unit in plots of Th against TiO_2 and Th against Zr (with Th/TiO_2 and Th/Zr ratios increasing with increasing contamination), relative to the other units of the same primary classification, such that:
  - U = uncontaminated or nearly so
  - C = contaminated
  - S = strongly contaminated
  - VS = very strongly contaminated.
- The degree of fractionation was a qualitative measure within each primary classification group for each specific secondary measure of contamination (e.g. L-S for strongly contaminated LTB). It was based on the concentration range of Th and Nb in each unit such that (for example) L-S1 had lower Th concentrations (was less fractionated) than L-S2, which in turn was less fractionated than L-S3, and so on.

Hence, L-U5 would be an uncontaminated but strongly fractionated LTB, whereas I-S2 would be a strongly contaminated but only weakly fractionated ITB.

Mafic units identified so far (GSWA Report 226) include:

- LTB
  - L-U1 and L-U2: two units of uncontaminated (or nearly so) and relatively unfractionated primitive LTB, including one local variant (L-U2*)
  - L-U3–7: five units of uncontaminated (or nearly so) but moderately to strongly fractionated LTB
  - L-Ca: a coherent unit of contaminated LTB showing a continuous fractionation trend, that [except for a possibly Zr-enriched variant (L-Cb)] cannot plausibly be divided into discrete units
  - L-S1 and L-S2: two units of strongly contaminated but relatively unfractionated LTB
  - L-S3a, L-S3b, and L-S4: three groups of strongly contaminated and strongly fractionated LTB.
- ITB
  - I-S1–3: three units of strongly contaminated and weakly to moderately fractionated ITB
  - I-S4: a strongly contaminated and strongly fractionated ITB
  - I-VS: a very strongly contaminated and relatively weakly fractionated ITB.
- HTSB: all HTSB by definition, are strongly contaminated with crustal material. The three groups recognized are:
  - H-HMg#: HTSB with high Mg#
  - H-LMg#: HTSB with lower Mg#
  - H-LTh: HTSB with lower Th concentration compared with other HTSB.
- KB: Three units (KB1 to 3).

Appendix 5 (**Workflow for classifying geochemical samples**) provides a method for visually or graphically reproducing specific compositional features that uniquely identify the individual units or groups described here. It does not reproduce the process used to identify the units or groups in the first place. Users need to be aware that it will either not identify, or erroneously assign, data from any legitimate new geochemical groups not encountered within our dataset and it will not allow for significant legitimate expansion of specific compositional fields. For these reasons, it may not be appropriate to apply this workflow to areas outside the study region. Nevertheless, the procedure employs sufficient critical compositional variation diagrams that any completely new units should become apparent.

It should be recognized that industry exploration assay datasets, typically collected over much more specific regions and in many cases, containing an order of magnitude more data than the dataset we use here, inevitably show a considerably greater scatter of data that hides much of the detail shown in our data (Fig. 67). Although these larger datasets might include discrete basalt geochemical populations not sampled in this study, it is highly likely that most of the scatter can be attributed to factors including:

- analytical techniques less accurate and precise than those used here
- less homogeneous sample material (i.e. mixed lithologies particularly in the case of rock chip samples or samples taken at or over pre-specified intervals)

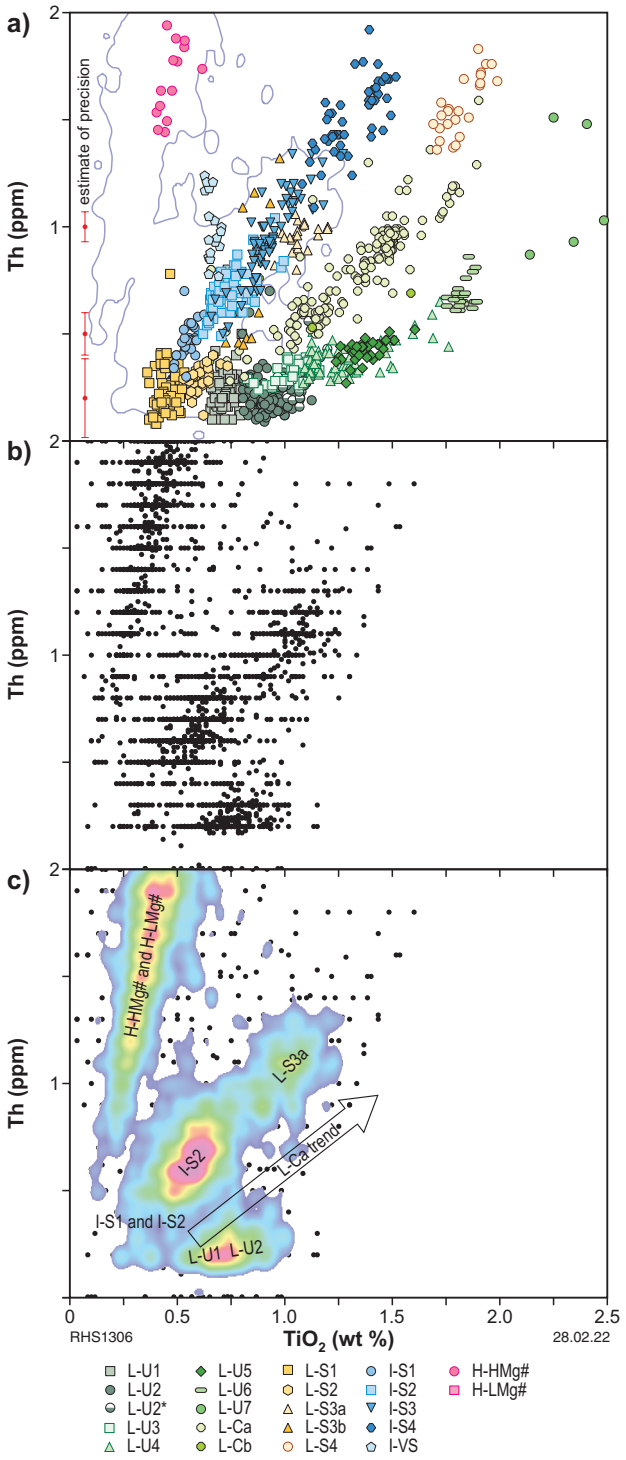

Figure 67. Variation in Th with TiO_2 showing: a) all basaltic data (this study) from within the study region (purple line outlines the extent of the data heat map shown in c below). The estimates of precision (error bars) for Th are based on historical analytical results from BV Minerals (from Champion et al., 2021) and relate only to data presented in part a; b) a subset of ~10 000 data points from a mineral exploration dataset collected from a specific area within the study region; c) a heat map of the data presented in b) showing specific data hotspots reflecting the range of basalt compositional groups expected for the Hannans Subgroup in the Kambalda Domain

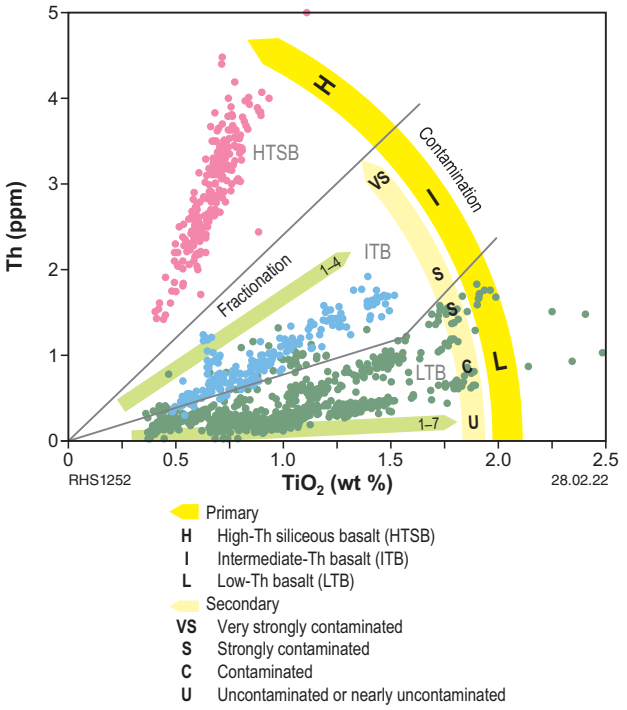

Figure 68. Variation in Th with TiO_2 used for the classification of basalts (after Barnes et al., 2012), showing the rationale behind the system used to give unique codes to each specific mafic geochemical unit (see text for details)

- sampling protocols that do not specifically target the least-altered material or specifically do target altered and/or mineralized material.

When using large assay datasets, employing heat maps can help reduce the impact of scatter related to these factors. Figure 67 provides a simple example of this. When we apply a simple heat map to the industry data, discrete compositional populations become apparent. In this case, it becomes clear that the overall compositional diversity strongly suggests the data are probably from the Kambalda Domain (see below) with compositional hotspots indicating the dominance of L-U1, L-U2, I-S3a, and H-HMg$^{\#}$– H-LMg$^{\#}$ basalts. Although limited scatter occurs into the regions of L-S1, L-S2, and L-Ca basalts, the heat map clearly indicates that these compositional populations are at best, very insignificant, and certainly require verification, for example in this case, by looking at a corresponding heat map on a plot of Al_2O_3/TiO_2 vs Al_2O_3.

Using selected major and trace elements, we employ a selection of the compositional variation diagrams that together offer effective identification of most or all of the specific compositional groups. These include plots of TiO_2 vs Th and Zr and Al_2O_3/TiO_2 vs Al_2O_3. On each of these plots and for each of the domains or regions discussed in GSWA Report 226, we show where each compositional unit of the chemostratigraphic column lies within the wider population, comprising all analyses of mafic volcanic rocks within the study area (Figs 69–74). The digital versions of these figures (Appendix 3 of GSWA Report 226) are in layered PDF format so that users can toggle between the specific compositional fields of interest.

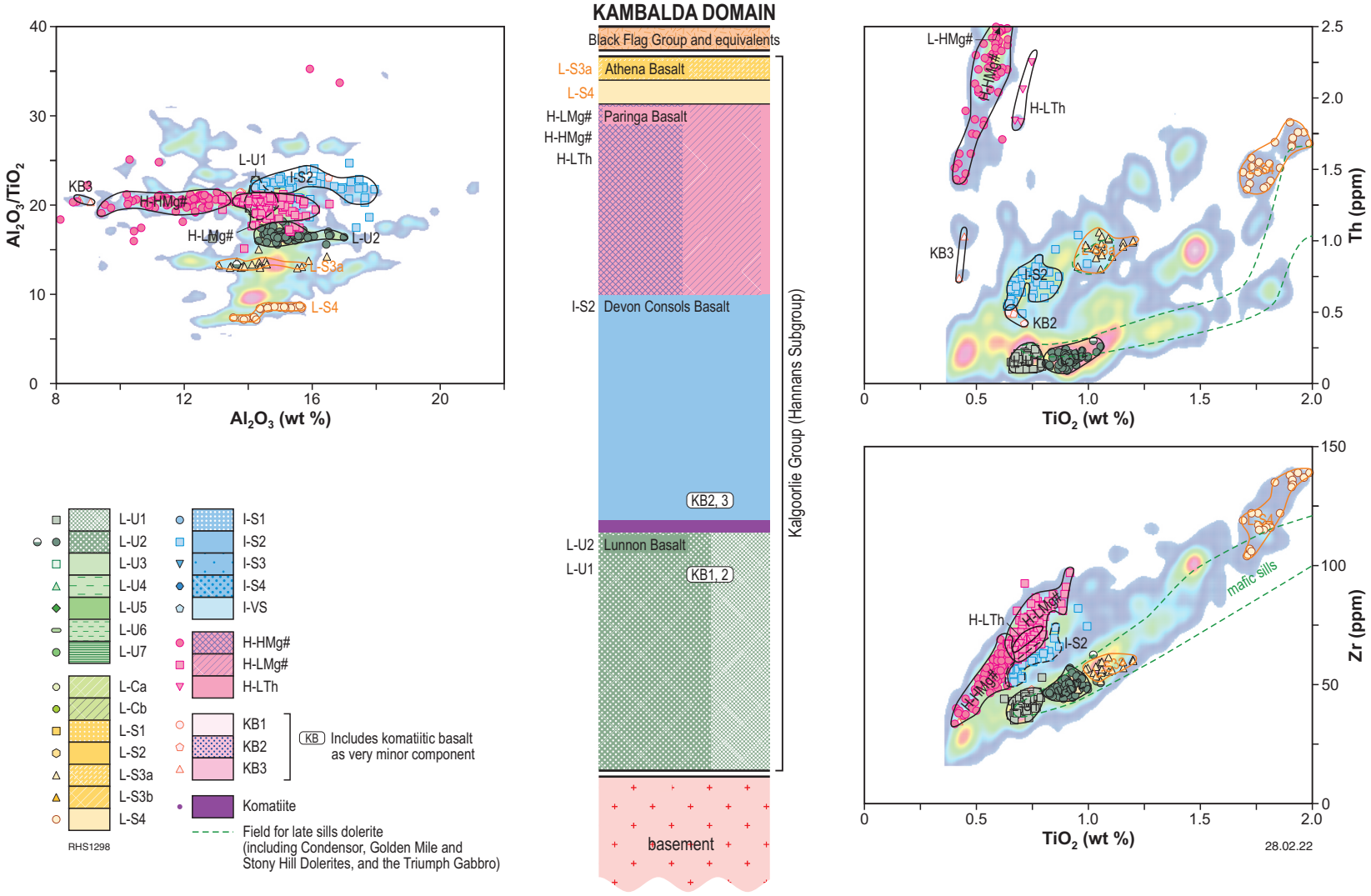

Figure 69. Stratigraphic column and selected geochemical variation diagrams identifying mafic units of the Kambalda Domain

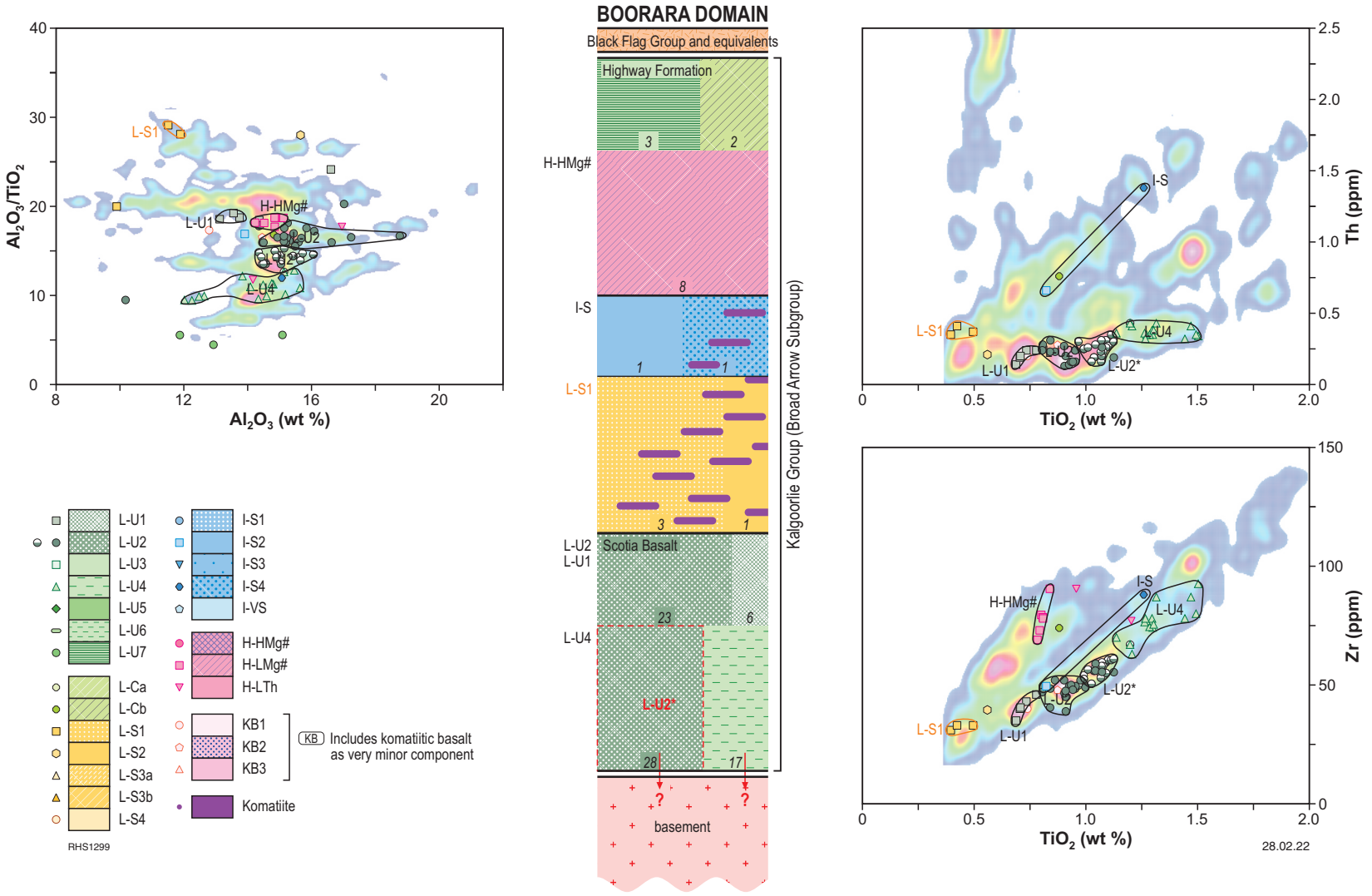

Figure 70. Stratigraphic column and selected geochemical variation diagrams identifying mafic units of the Boorara Domain

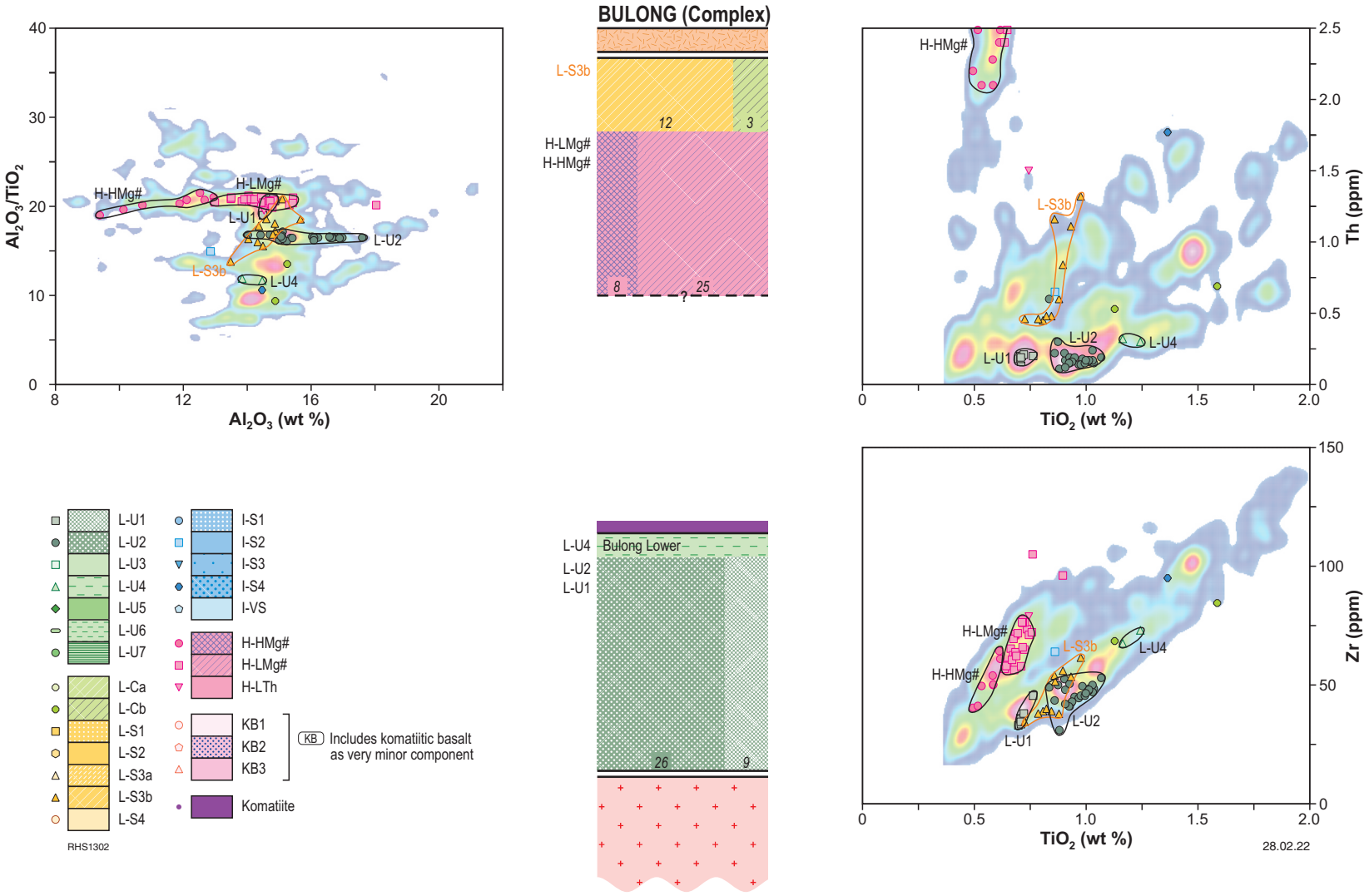

Figure 71. Stratigraphic column and selected geochemical variation diagrams identifying mafic units of the Bulong complex

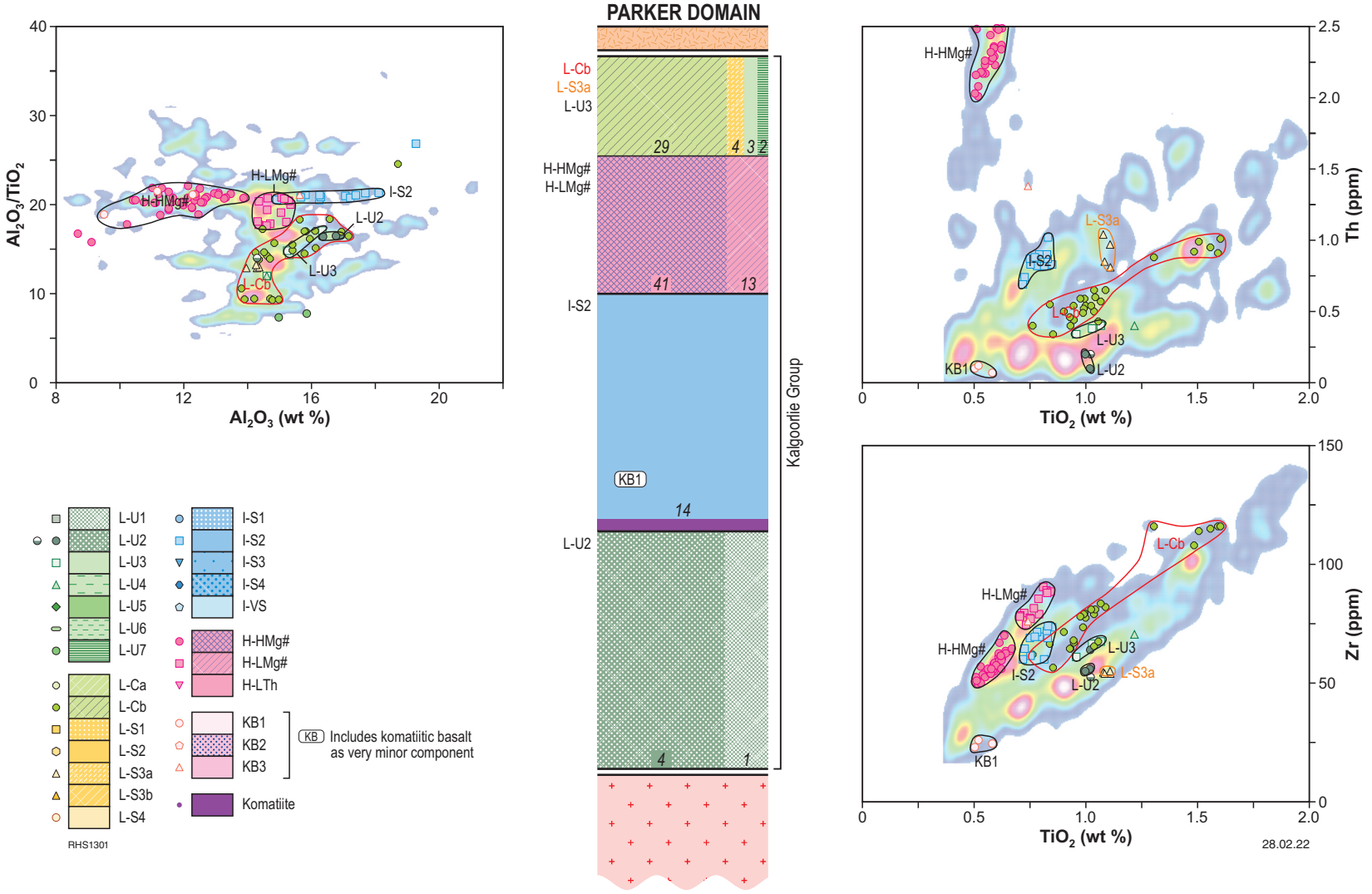

Figure 72. Stratigraphic column and selected geochemical variation diagrams identifying mafic units of the Parker Domain

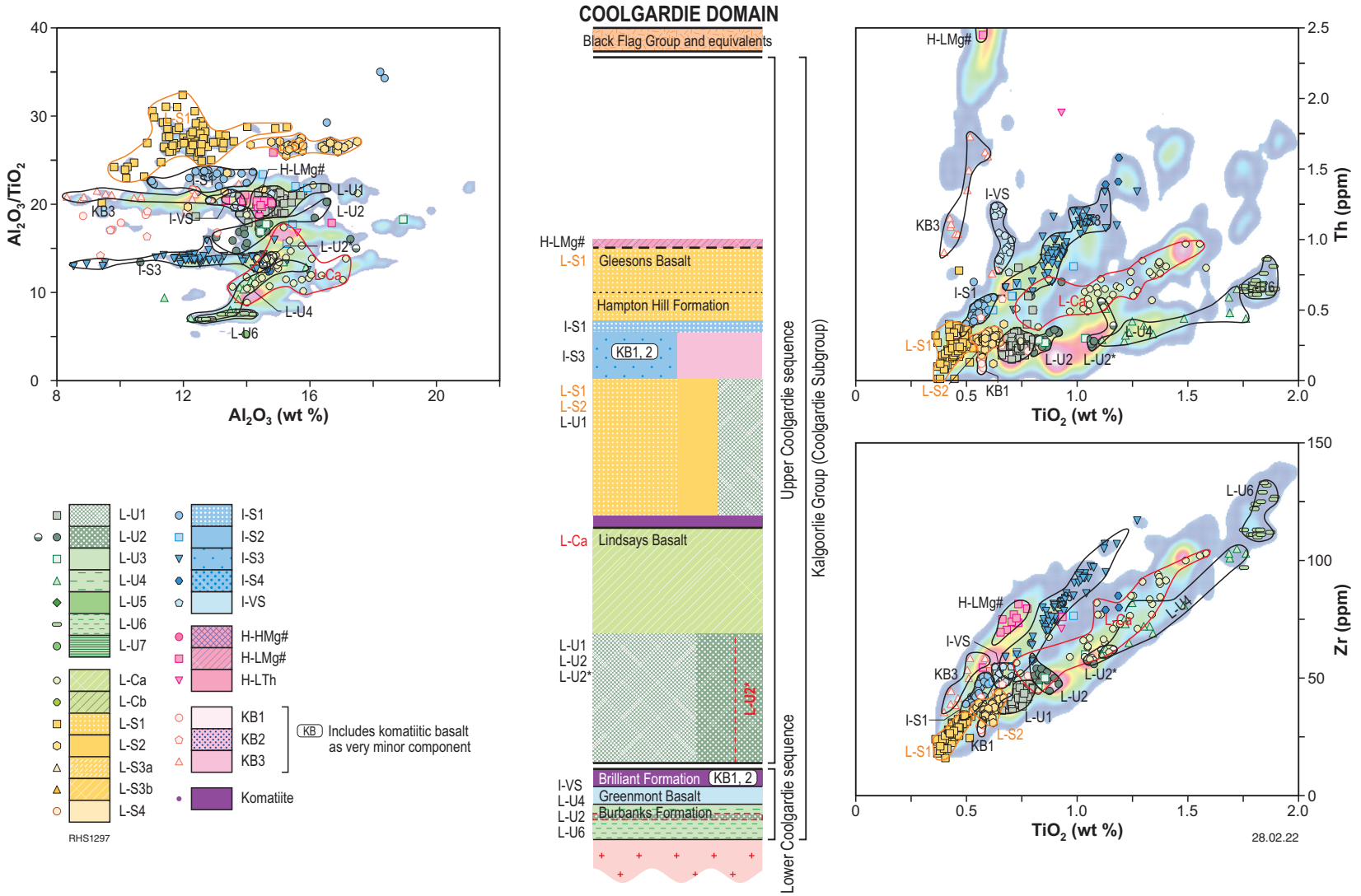

Figure 73. Stratigraphic column and selected geochemical variation diagrams identifying mafic units of the Coolgardie Domain

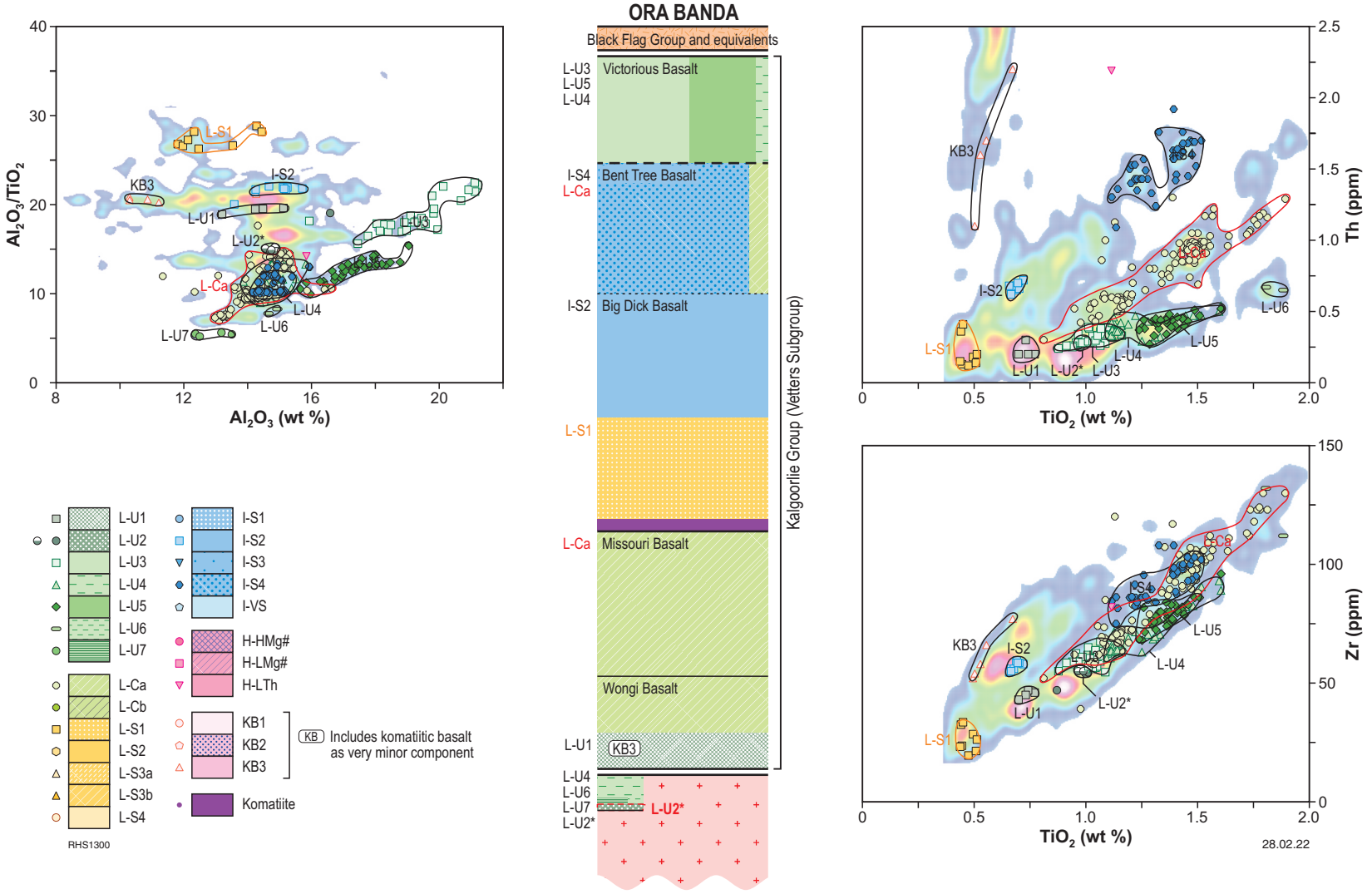

Figure 74. Stratigraphic column and selected geochemical variation diagrams identifying mafic units of the Ora Banda Domain

Subdividing felsic rocks

The geochemical barcoding approach is particularly applicable to basalt-dominated stratigraphy, since low-viscosity mafic (and ultramafic) lavas can travel long distances and blanket the underlying surface. However, the approach is less effective in the case of felsic volcanic and volcaniclastic accumulations, although broad but significant compositional variations can still be observed and utilized.

Felsic (andesite to rhyolite, or intermediate and acid) rock samples taken during this study are mainly from plagioclase (±hornblende or quartz) porphyritic dykes or sills representing subvolcanic intrusions and from volcanic or volcaniclastic deposits, including very immature proximal turbidite units (i.e. typically quartz-poor, poorly sorted, not conspicuously graded deposits). The majority of these samples are from the Black Flag Group, which is interpreted to have been deposited between 2690–2665 Ma across all of the domains of the Kalgoorlie Terrain within the study area. However, the presence of older felsic volcanic rocks is speculated within the lower Coolgardie sequence and demonstrated at numerous localities within the study area, with >2700 Ma felsic volcanic units occurring in (for example) the Bulong complex (e.g. Nelson, 1995a; Barley et al., 2002).

From the original set of 845 felsic samples, filtering for alteration removed a total of 213 (~25%) samples, 50% of which were excluded based on high ASI (up to 2.2), reflecting secondary alteration or significant sedimentary reworking or both. It is important to note that, once filtered, there is no clear difference in the composition or compositional range of the intrusive, volcanic or volcaniclastic rock populations; i.e. no clear evidence that a specific depositional process has significantly modified the primary magmatic compositions.

The majority of subvolcanic intrusions and associated volcanic or volcaniclastic deposits forming the Black Flag Group have the composition of sanukitoids and comprise one of the first recognized examples of Archean sanukitoid volcanic rocks, and one of the most voluminous intrusive/extrusive sanukitoid systems anywhere in global Archean terrains (Smithies et al., 2018). Sanukitoids are relatively rare hornblende-bearing rocks, typically in the monzonitic to dioritic and granodioritic (andesitic to dacitic but reaching rhyolitic) compositional range. They have been attributed to direct extraction as low-degree felsic partial melts from a hydrated mantle source (Shirey and Hanson, 1984; Smithies and Champion, 2000). However, more recently they were interpreted to be (or include examples that are) fractionated from mafic to ultramafic parental magmas (including calc-alkaline lamprophyres), themselves partial melts of metasomatically hydrated and enriched mantle lithosphere (Smithies et al., 2018, 2019). Sanukitoids are amongst the most hydrated and oxidized magmas known from the Archean and their presence implicitly defines a translithospheric plumbing system that transferred fertile mantle material to upper crustal levels (Smithies, 2019; Smithies et al., 2019). In the Yilgarn Craton, and in other Archean regions, sanukitoids have a clear spatial and temporal association with gold mineralization (Champion and Cassidy, 1998; Witt et al., 2013, 2015; Fayol and Jébrak 2017). In the Eastern Goldfields, many of the structures used as magma pathways by sanukitoids are faults that also played a primary role in the structural evolution of the 2664–2657 Ma sedimentary basins (Late Basins) that overlie the Black Flag Group.

Classification of the felsic rocks

A workflow for classifying felsic rocks is provided in Appendix 5. Figure 75 attempts to graphically show aspects of this workflow. Although this classification is based primarily on geochemical

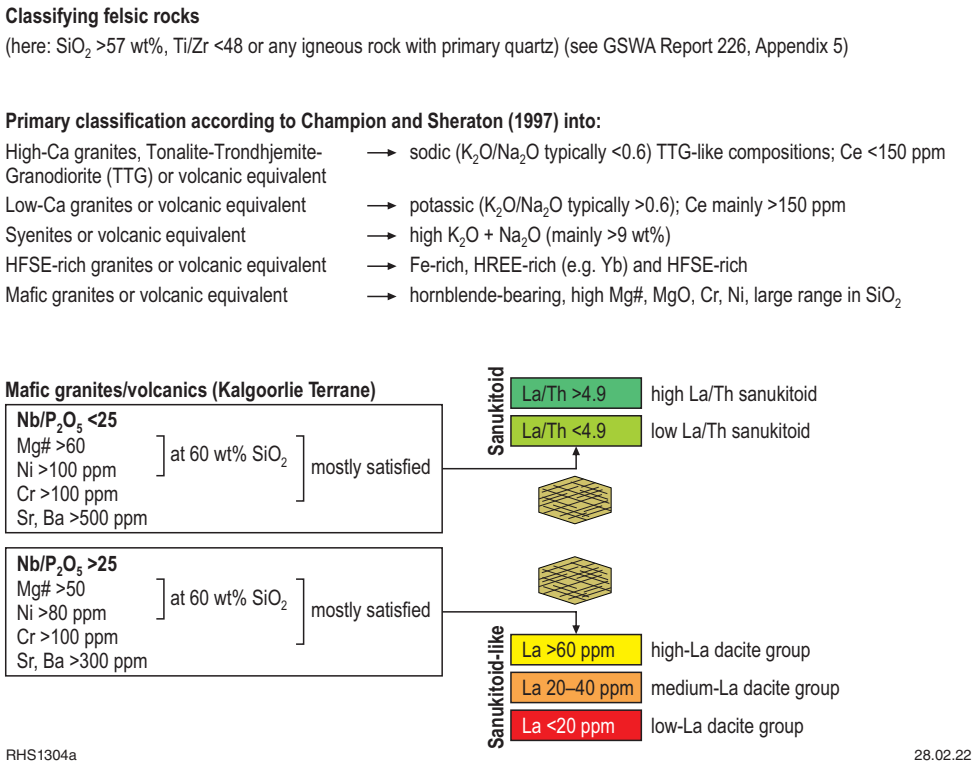

Figure 75. Flow sheet explaining the methodology used here to classify felsic units

data, the geographical and lithological association of samples and mineralogy remain extremely important considerations. For example, sanukitoids typically have quite specific field appearances and mineralogy, particularly at the lower silica end of their compositional range, where they are invariably hornblende-rich and often contain cognate (hornblende-plagioclase±pyroxene) xenoliths. However, whereas lower-silica sanukitoid is also typically distinctive geochemically, at the higher silica end of their range, sanukitoid can be virtually indistinguishable from High-Ca granite. Similarly, High-Ca granites are typically plagioclase rich and K-feldspar poor, but can fractionate to K-feldspar-bearing examples that geochemically resemble Low-Ca granites. In both cases, the spatial and temporal associations may help in classification.

The granite classification scheme of Champion and Sheraton (1997) and Champion and Cassidy (2002) was initially applied to the felsic rocks within the study area. This classification divides Archean granites into five broad groups including:

- High-Ca granites, typically with SiO_2 >68 wt% and a compositional range broadly consistent with that of Archean tonalite–trondhjemite–granodiorite (TTG) suites, reflecting deep crustal melting of dominantly mafic source regions
- Low-Ca granites, typically with SiO_2 >68 wt% but generally more potassic compositions (broadly equivalent to Archean K-rich granite series), and generally more enriched in incompatible trace elements, reflecting higher temperature melting of dryer, more heterogeneous and slightly more refractory sources, including mafic crust and earlier formed TTG crust
- HFSE granites, generally highly silica rich (SiO_2 >70 wt%), Fe rich and strongly enriched in (e.g.) Nb, Zr, and REE, usually with characteristics consistent with the involvement of tholeiitic parental magmas or sources
- Syenites, very alkali rich and typically quartz poor, but also Fe rich and enriched in (e.g.) Nb, Zr, and REE, and additionally in large ion lithophile elements (LILE; e.g. Sr and Ba), thought to be derived through melting of a metasomatically enriched deep lithospheric source (Smithies and Champion, 1999)
- Mafic granites, typically hornblende-bearing rocks showing a wide range of silica concentrations upwards of ~57 wt% with a significant proportion of samples with SiO_2 <68 wt%. Sanukitoids form a large component (>50%) of this group. The remainder includes suites that have $Mg^{\#}$, and/or Cr, Ni, and/or Sr or Ba concentrations lower than expected for sanukitoids, but generally slightly higher than is typical of modern calc-alkaline magmas (e.g. Barnes and Van Kranendonk, 2014), possibly as a result of a hotter Archean mantle.

The entire felsic dataset was divided between samples with compositions equivalent to:

- Mafic granites 87%, of which 66% are true sanukitoid and 34% are sanukitoid-like (see below)
- High-Ca granites (10%)
- HFSE granites (3%)
- Low-Ca granites (<<1%).

Rocks compositionally equivalent to Mafic granites

Sanukitoids

Geochemical identification of sanukitoids is not always straightforward and is particularly problematic in populations that contain few samples with silica contents below ~65 wt%. Felsic rocks with such low silica contents are relatively uncommon in Archean terrains. However, they are unusually common in the Kalgoorlie–Kambalda region, particularly in the Black Flag Group. A sanukitoid suite should be a geochemically coherent (genetically related) group of relatively sodic (K_2O/Na_2O <1.0) rocks, which at low silica values (at 60 wt% SiO_2 or reasonably extrapolated to that value) are dominated by members with $Mg^{\#}$ ≥60, Cr and Ni concentrations ≥100 ppm, Sr and Ba concentrations ≥500 ppm, and La concentrations ≥25 ppm. At silica contents >65 wt% sanukitoid is difficult to geochemically distinguish from High-Ca granites or rocks of TTG suites. Smithies et al. (2019) suggest that some High-Ca granites or TTGs, particularly those showing flat mantle-normalized HREE patterns that reflect hornblende fractionation might be fractionated sanukitoids. Nevertheless, at silica contents >65 wt%, most sanukitoid suites (and Mafic granites, and volcanic equivalents, in general) should range to higher Mg# and higher Ni and Cr concentrations and might show flat or reversely fractionated (spoon-shaped) mantle-normalized HREE patterns.

From a practical point of view, the important aspects of a sanukitoid petrogenesis emphasize derivation from a highly MgO-rich hydrated source. Therefore, any magmatic series that ranges to low silica (<~65 wt%) members containing abundant primary hornblende and having high $Mg^{\#}$ and Cr and Ni concentrations, might also be considered sanukitoid-like (see below).

Most felsic magma series in the Kalgoorlie–Kambalda region that satisfy all or most aspects of the sanukitoid definition (Fig. 76) have a Nb/P_2O_5 ratio <25, whereas most other felsic magma types have higher ratios (Fig. 77). Whilst this discrimination appears to be useful for the Kalgoorlie–Kambalda region, it fails to identify all significantly hydrated sanukitoid-like magmas (see low-La dacites below). The concentrations of both Nb and P are likely to be strongly related to lithospheric mantle-enrichment processes – the concentration of Nb in sanukitoids, for example, has been linked to variations in the relative proportions of fluid- and melt-mediated metasomatism (Smithies and Champion, 2000). We do not recommend the application of this discrimination plot to other regions without further testing.

Two main groups, high La/Th sanukitoids (La/Th = 4.9 and greater) and low La/Th sanukitoids (La/Th <4.9) can be distinguished using a plot of La vs Th (Fig. 78). These groups are broadly equivalent to the high- and low-LILE subgroups of Mafic granites described by Champion and Cassidy (1998). Both groups span the full silica range from <58 wt% to >75 wt%. A third, smaller group has La/Th <4.9, but is restricted to high silica values between 70 wt% and 74 wt%. It has incompatible trace element patterns similar to high La/Th sanukitoids, but is also transitional to silica-rich examples of low La/Th sanukitoids. We referred to this third group as evolved low La/Th sanukitoids. It shows an extensive overlap with rocks that have compositions equivalent to High-Ca granites, but typically has higher Th and LREE concentrations and lower HREE concentrations.

The low La/Th sanukitoid group includes a small P-rich low La/ Th sanukitoid subgroup with a distinctly higher P, Th, LREE trend. The high La/Th sanukitoid group includes a small population with distinctly lower Ni concentrations.

High La/Th sanukitoids also have distinctly more radiogenic Nd-isotope compositions with initial $\varepsilon_{Nd\ (2690\ Ma)}$ values lying between 1.5 and 2.7 compared with a range for all types of low La/Th sanukitoids between 0 and 0.8.

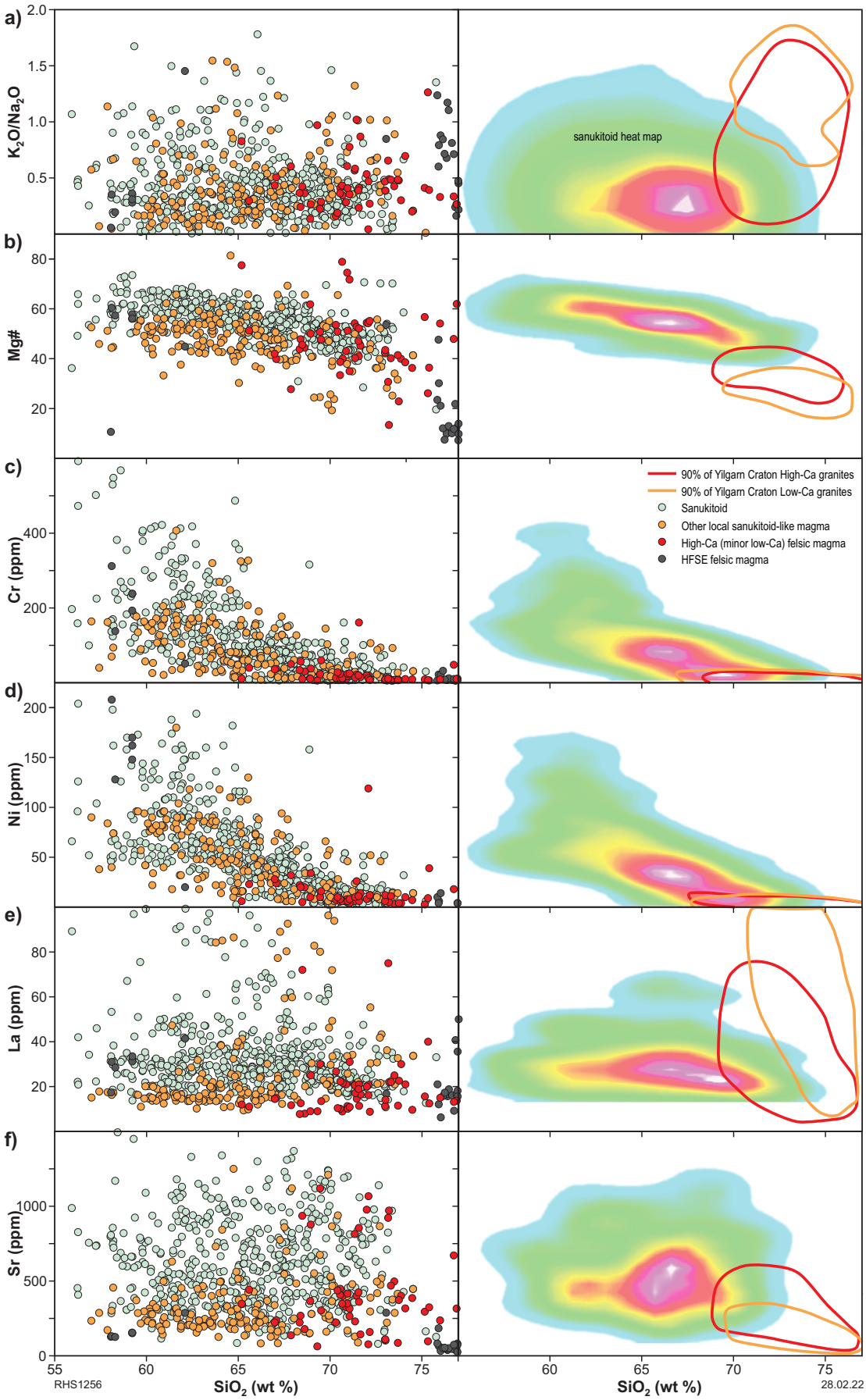

Figure 76. Variation with SiO_2 of various chemical parameters considered useful in the identification of sanukitoids, including K_2O/Na_2O, Mg#, Cr, Ni, La, and Sr. Right-hand column shows heat maps that outline the relative sample density for >95% of sanukitoid samples (hotter colours represent high density of samples) and compares this with the compositional range for High- and Low-Ca granites from the Yilgarn Craton

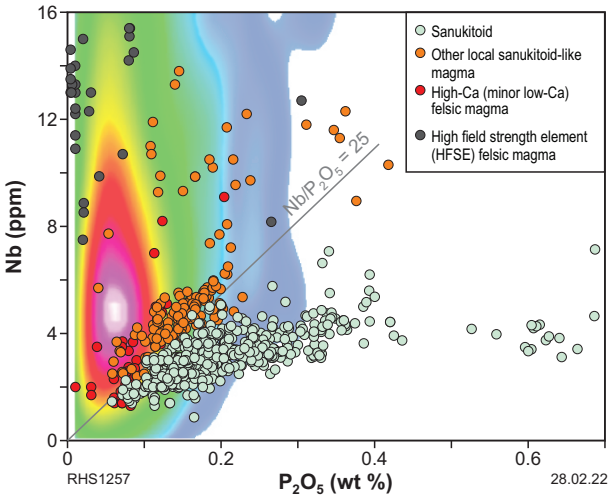

Figure 77. Variation of Nb with P_2O_5 highlighting the compositional contrast between sanukitoids and other felsic rock groups. The heat map shows the density distribution of >90% of granites from the Yilgarn Craton other than the Mafic granites of Champion and Sheraton, 1997

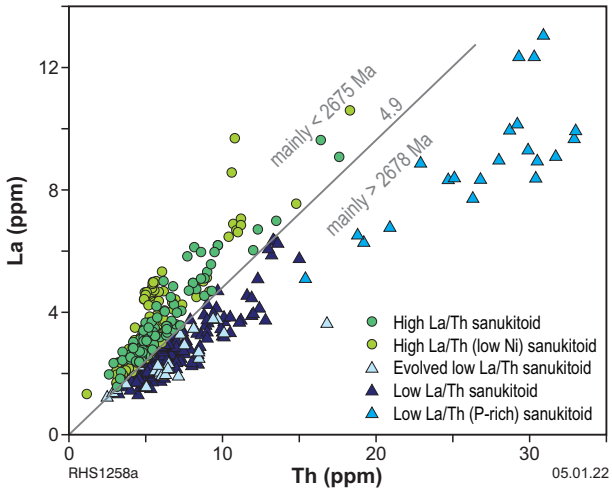

Figure 78. Variation of La with Th for rocks classified as sanukitoids. Available U–Pb (in zircon) dating on Black Flag Group sanukitoids that can be geochemically confirmed to be high La/Th or low La/Th suggest that the age of igneous crystallization of low-La/Th sanukitoids was older than c. 2678 Ma, whereas that of the high-La/Th sanukitoids was younger than c. 2675 Ma

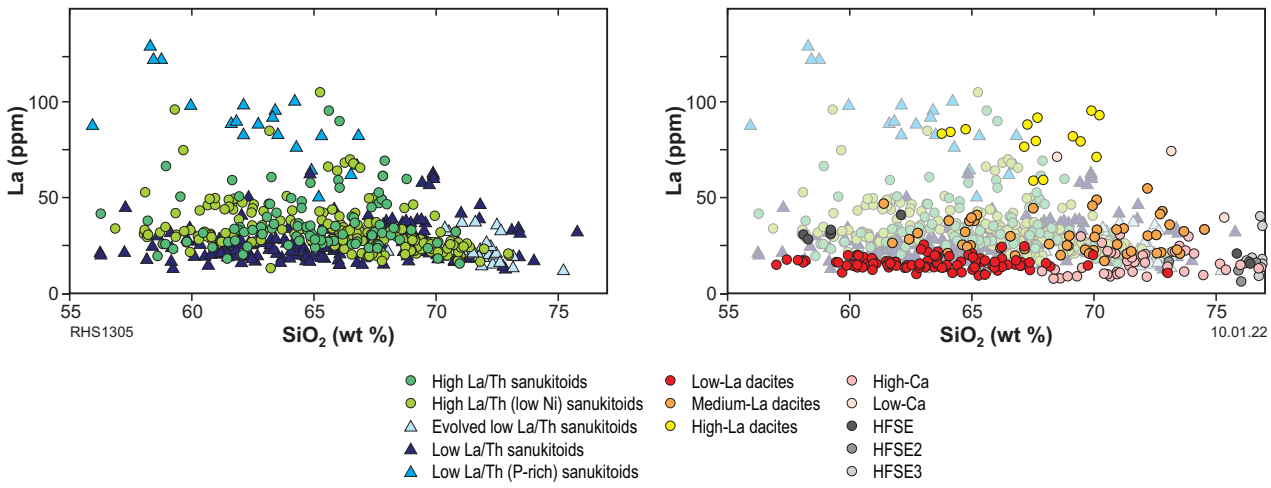

Figure 79. Variation in La with SiO_2 for the various felsic rock types. The left-hand column shows sanukitoids. The right-hand column shows the sanukitoid-like rocks (low-, medium-, and high-La dacites) and other felsic units (bold symbols) and compares these with the sanukitoids (faded symbols)

Non-sanukitoid samples compositionally equivalent to Mafic granites

A large population of subvolcanic, volcanic, and volcaniclastic rocks with Mafic granite compositions has La/Th ratios overlapping those of the high- and low-La/Th sanukitoid groups, but has Nb/P_2O_5 ratios >25. Three groups can be recognized based on distinctive mantle-normalized trace element patterns (see GSWA Report 226) and are reasonably well distinguished based on La concentrations (Fig. 79). These will simply be referred to as low-La (La <20 ppm), medium-La (La 20–60 ppm), and high-La (La >70 ppm) dacites, noting that the low-La dacite group also includes abundant andesite and the medium- and high-La dacite groups include rhyolite.

Apart from generally lower LREE concentrations, the low-La dacites have compositions that closely approach those of sanukitoids, with relatively high $Mg^{\#}$ (mainly 50–55 at 60 wt% SiO_2), Ni (mainly 75–100 ppm at 60 wt% SiO_2), Sr and Ba (both mainly ~300 ppm at 60 wt% SiO_2) concentrations. Indeed, concentrations of Cr (at 60 wt% SiO_2) are typical of sanukitoids. We consider these rocks to be sanukitoid-like.

Medium-La and high-La dacites show many compositional similarities with the low-La dacites but extend to more felsic compositions, have steeper (more fractionated) mantle-normalized trace element patterns with minimal or positive Zr anomalies, higher Na_2O+K_2O, higher FeO and/or lower MgO (and correspondingly lower $Mg^{\#}$, mostly below 50) at a given silica content (see main text).

Distribution and age

Sanukitoids

Of the two main compositional types of sanukitoids, the high La/Th group is concentrated in the southern and eastern parts of the region, while the low La/Th group (excluding the evolved low La/Th subgroup) is mainly concentrated in the north and west (Fig. 80). Sanukitoids in the northwestern part (Kundana region) are exclusively low La/Th types, but to the northeast, high La/Th and low La/Th sanukitoids occur, and locally show mutually intrusive (subvolcanic) or interlayered (volcanic) relationships.

Geochronological data (see GSWA Report 226) for high La/Th sanukitoids indicate magmatism between at least c. 2688 and c. 2653 Ma (Fig. 81), and between c. 2696 and c. 2682 Ma for low La/Th sanukitoids (not including evolved low La/Th sanukitoid).

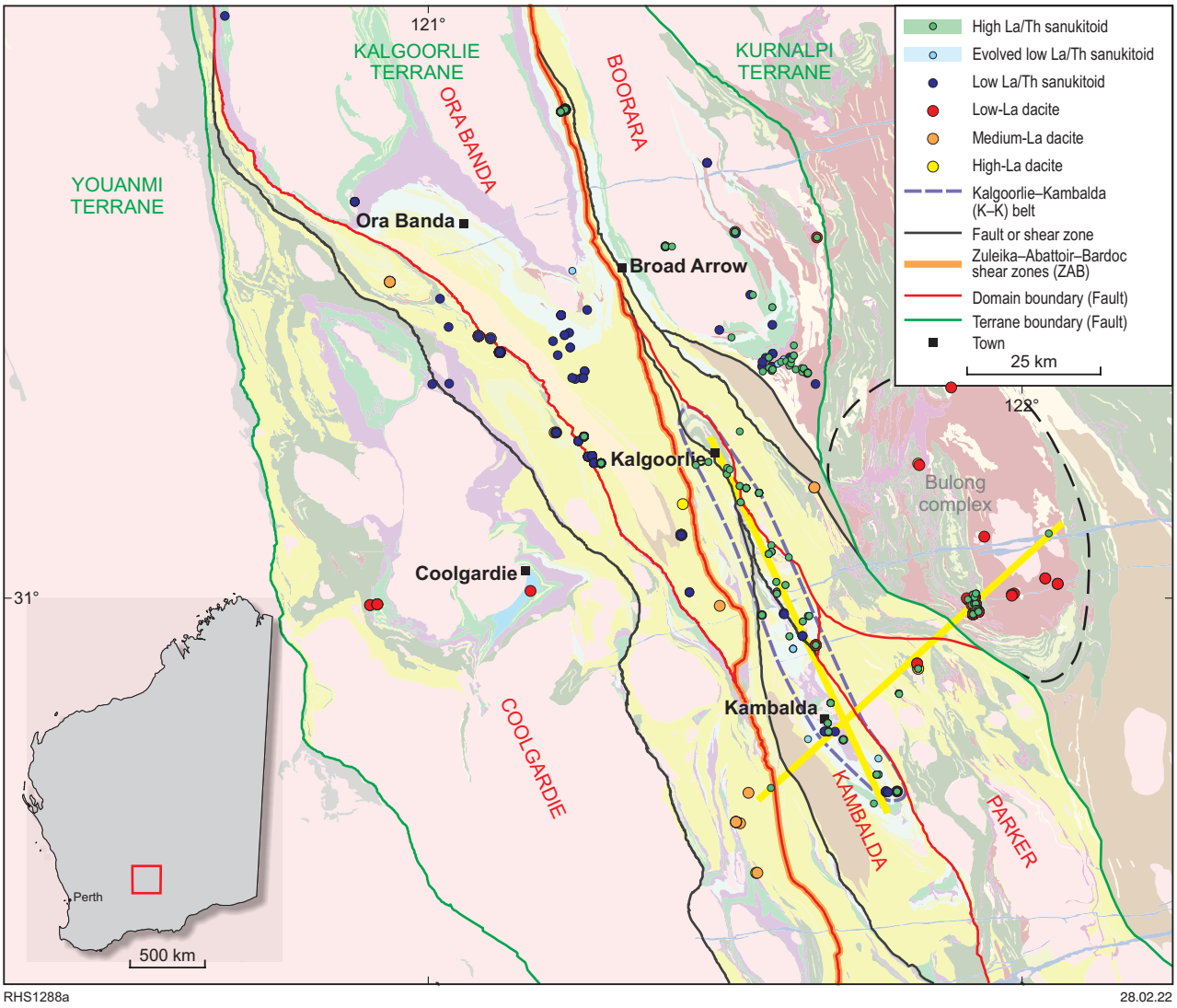

Figure 80. Geological map of the study area within the Kalgoorlie Terrane, showing the distribution of samples of the various sanukitoid types as well as high-, medium-, and low-La dacites. Also shown is the Kalgoorlie–Kambalda belt (dashed line) and other apparent trends outlined by the sanukitoids (yellow)

Evolved low La/Th sanukitoids have ages between c. 2695 and c. 2680 Ma.

Contact relationships clearly require that high- and low-La/Th magmatism was comagmatic although available dating suggests that this period of overlap may have been quite limited, with much of the high La/Th magmatism occurring after much of the low La/Th magmatism. In some regions, the igneous component of the entire preserved Black Flag Group stratigraphy reflects accumulation only from one of the main compositional types of sanukitoid magmatism. The spatial and temporal distribution of the sanukitoid groups is broadly consistent with Tripp's (2013, 2019) stratigraphic interpretations. Thus, at least in broad terms, it seems that the northwestern Kundana – Ora Banda region records or preserves mainly the lower part (Gibson–Honman Formation and below) of the Black Flag Group, overwhelmingly dominated by low La/Th sanukitoids, whereas the northern part of the Kambalda Domain records only the uppermost part (Gidji Lake Formation) overwhelmingly dominated by high La/Th sanukitoids. In this regard, the La/Th ratio of Black Flag Group rocks might provide a first-order estimate of age and stratigraphic position (Fig. 78).

It should be stressed that geochronological compilations by Tripp (2013, 2019) suggest that volcanism related to the Black Flag Group occurred broadly from <2690 Ma to >2665 Ma, with intrusive magmatism from <2691 Ma to <2650 Ma. We have addressed mainly the compositional aspects of Black Flag Group magmatism but our data are broadly consistent with that of Tripp (2013, 2019), in that high La/Th compositions have a higher proportion of intrusive samples than the older low La/Th sanukitoids.

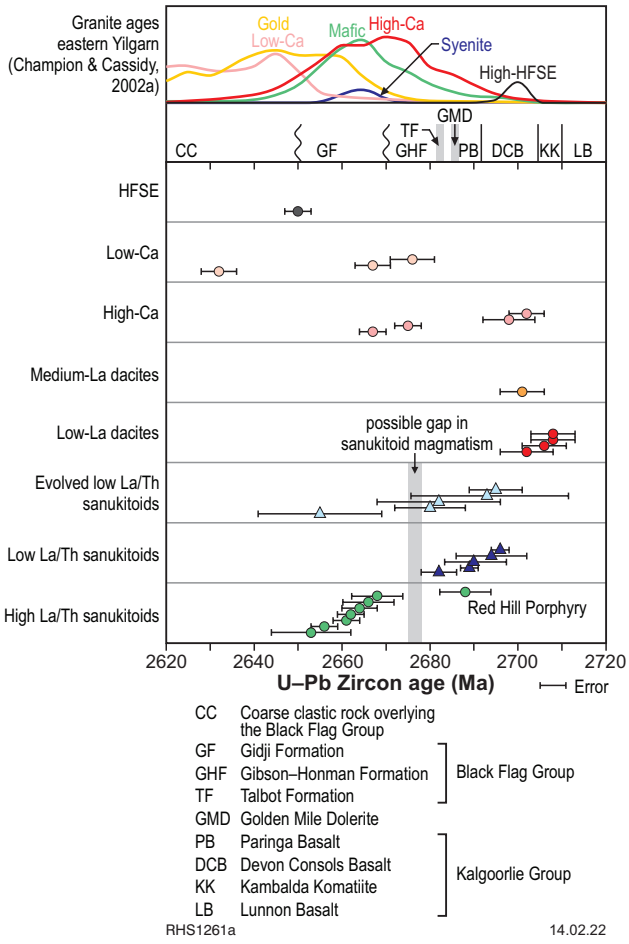

Figure 81. Summary of geochronological data and relationships for felsic units within the study region. See GSWA Report 226, Table 5 for individual U-Pb (zircon) geochronology samples and references. Black Flag Group stratigraphy modified from Tripp (2013). Histograms showing age distribution of granite types are from Czarnota et al. (2010), using data from Champion and Cassidy (2002a)

Other magma types

The sanukitoid-like low-La dacite occurs mainly in the southern part of the study throughout the Kambalda Domain, but appears to be more common in the Mount Monger Station region in the western part of the Bulong complex. Four samples have been dated (see GSWA Report 226) and all dates fall within a narrow age range from 2708–2702 Ma. In all drillcores that show contact relationships between low-La dacite and other units, the dacite was consistently intruded by subvolcanic dykes of high La/Th sanukitoids and was the oldest felsic component observed. Thus, low-La dacite compositions potentially provide a stratigraphic time marker. Along with the La/Th ratio of sanukitoids, these potential compositional age references might prove useful in elucidating field relationships, although they need to be considered with caution.

Some points from this Report with potentially significant implications in local to regional geological interpretation

- There are at least 12 major geochemically discrete units within the study area that have LTB-like compositions. This represents a significant problem or source of serious misinterpretation when LTB compositions are erroneously regarded as synonymous with Lunnon Basalt (i.e. the stratigraphic unit) or are even more broadly referred to as Lunnon-like. Similar problems arise regarding the Devon Consols Basalt and the ITB groups. Of the 12 LTB units, seven are L-U units and only two of these (L-U1 and L-U2) occur within the Lunnon Basalt.

  Hence, **LTB is not synonymous with Lunnon Basalt**. Only a basalt pile within the region between Kalgoorlie and Kambalda, comprising combinations of primitive L-U1 <L-U2 alone, overlain by komatiite and then by I-S2 (i.e. Devon Consols Basalt) is Lunnon Basalt. Likewise, ITB is not synonymous with Devon Consols Basalt.

- Individual lithostratigraphic units within the area, typically of formation level, seldom comprise a single geochemical unit. Those that do, include the Greenmont Basalt (I-VS, lower Coolgardie succession), the Gleesons Basalt (L-S1, upper Coolgardie succession), the Paringa Basalt (HTSB, upper Hannans Subgroup), and the Athena Basalt (L-S3a, upper Hannans Subgroup). Most formations comprise at least two or more distinct geochemical units, and in most cases these units cannot be related back to a common parental magma composition. Thus, individual greenstone formations combine overlapping deposits or flows from fissures or vents supplied by several genetically unrelated magma sources. This potentially makes some stratigraphic formation boundaries arbitrary reflections of changing source eruptions. Nevertheless, the subdivision of the regional (domain) stratigraphies into three levels (lower, middle, and upper basalts), does in most cases reflect broader changes in magma compositions and provides useful markers of relative level within a particular stratigraphy.

- In many cases, the mafic chemostratigraphic columns appear to ignore previously established domain boundaries. However, a broadly north-trending structure incorporating segments of (from south to north) the Zuleika Shear Zone, Abattoir Fault and the Bardoc Shear Zone (ZAB) does appear to separate the western domains (Coolgardie and Ora Banda) from the eastern domains (Kambalda, Boorara, Parker and the Bulong complex), having distinctive chemostratigraphic variations, which in the western domains, probably reflects melting beneath thicker lithosphere and possibly a slightly more melt-depleted source. The chemostratigraphic differences between the western and eastern domains extends to the felsic units of the Black Flag Group.
- Because textural or mineralogical features often cannot effectively discriminate between compositionally distinct basaltic units, mapping the discrete units at a stratigraphic member level might not be possible without a level of geochemical sampling density even greater than employed here. In any case, this would almost certainly not add any clarity to the potential ambiguities involved in identifying higher order lithostratigraphic boundaries. This also has implications for using geochemistry to infer stratigraphic position because, except in very rare cases, a single or low number of analyses will not be sufficient to uniquely identify a lithostratigraphic position, but more comprehensive sampling, particularly if it incorporates the underlying and overlying stratigraphic units almost certainly will.
- There are significant geochemical differences between the lower and upper stratigraphic successions of the Coolgardie Domain. Here, the lithogeochemistry provides a clear indication that the upper (Lindsays Basalt and above) and lower (below Lindsays Basalt) successions do not represent a structural repetition (although it remains plausible that they might be in thrust contact). The lower Coolgardie succession almost certainly should not be considered as part of the Coolgardie Subgroup, as is presently the case.
- A lack of significant chemostratigraphic difference strongly supports the re-incorporation of the Depot Domain into the Coolgardie Domain. However, there are a few anomalies. For example (see main text):
  - I-S2 overlies I-S1 in drillcore (BDDD0017), immediately west of the Zuleika Shear Zone (approximately 10 km to the north of the Powder Gabbro)
  - In the Kundana region near Bullock Hole, immediately west of the Zuleika Shear Zone that marks the boundary between the Coolgardie Domain and the Ora Banda Domain (in the north) or the Kambalda Domain (in the south), stratigraphy identical to the upper part of the Vetters Subgroup is intersected in drillcore (PGDD15001, MEDD148, MEDD144, and FLRD04) and in outcrop
  - Between the Connolly Gneiss and the Maloneys Dam Granite, approximately 13 km southeast of Londonderry Siding, the greenstone stratigraphy is dominated by a I-S4–L-Ca association very reminiscent of the upper part of the Vetters Subgroup and otherwise unique within the upper Coolgardie succession. However, this observation is based on limited data (7 analyses).
- The Black Flag Group is overwhelmingly dominated by volcanic, volcaniclastic, and subvolcanic rocks with compositions typical of sanukitoids. Slightly older felsic volcanic and subvolcanic rocks are also sanukitoid-like.
- Sanukitoid-like, low-La dacite group rocks possibly form a regional magmatic time marker at c. 2706 Ma.
- Sanukitoids of the Black Flag Group can be subdivided into:
  - an older (mainly pre-c. 2680 Ma) low La/Th group, which mainly occurs in the northwestern part of the region
  - a younger (mainly post c. 2670 Ma) high La/Th group, which dominates the eastern part of the area.
- Based on Nd-isotopic variations, the translithospheric ZAB structure, identified based on variations in the geochemistry of the underlying greenstone basalts, also separates the more radiogenic (mantle-like) source of the high La/Th sanukitoids to the east from the less radiogenic source of the low La/Th sanukitoids to the west.

References

Barley, ME, Brown, SJ, Krapez, B and Cas, RAF 2002, Tectono-stratigraphic analysis of the Eastern Yilgarn Craton: an improved geological framework for exploration in Archaean terranes: Australian Minerals Industry Association Report, 437A.

Barnes, SJ, and Van Kranendonk, MJ 2014, Archean andesites in the east Yilgarn Craton, Australia: Products of plume-crust interaction?: Lithosphere, v. 6, p. 80–92.

Barnes, SJ, Van Kranendonk, MJ and Sonntag, I 2012, Geochemistry and tectonic setting of basalts from the Eastern Goldfields Superterrane: Australian Journal of Earth Sciences, v. 59, p. 707–735.

Cassidy, KF, Champion, DC, McNaughton, NJ, Fletcher, IR, Whitaker, AJ, Bastrakova, IV and Budd, A (editors) 2002, The characterisation and Metallogenic Significance of Archaean Granitoids of the Yilgarn Craton, Western Australia: Minerals and Energy Research Institute of Western Australia (MERIWA), Project no. M281/AMIRA Project no. 482 (unpublished Report No. 222).

Champion, DC, and Sheraton, JW, 1997, Geochemistry and Nd isotope systematics of Archaean granites of the Eastern Goldfields, Yilgarn Craton, Australia: implications for crustal growth processes: Precambrian Research, vol. 83, p. 109–132.

Champion, DC and Cassidy, KF 1998, Metallogenic potential of granitoids: Kanowna Belle and Granny Smith regions: Final report to Golden Valley Joint Venture and Placer Pacific Ltd., Australian Geological Survey Organisation (unpublished).

Champion, DC and Cassidy, KF 2002a, Granites of the northern Eastern Goldfields: their distribution, age, geochemistry, petrogenesis, relationship with mineralisation, and implications for tectonic environment (including a simplified key for discriminating granite groups in the northern Eastern Goldfields), *in* Cassidy, KF, Champion, DC, McNaughton, NJ, Fletcher, IR, Whitaker, AJ, Bastrakova, IV and Budd, AR 2002, Characterization and metallogenic significance of Archaean granitoids of the Yilgarn Craton, Western Australia: Aust. Miner. Ind. Res. Assoc. Project P482/MERIWA Project M281, Final Report, 514p.

Champion, DC, Huston, D, Main, P, Jarrett, AJM, Thorne, J, Gilmore, S, Webber, S, Webster, T, Byass, J, DiBugnara, D, Williamson, A, Long, I and Peljo, N 2021, Exploring for the Future – Baseline whole rock geochemistry of Northern Australia Data Release — Geochemistry of drill core samples from the McArthur Basin, Lawn Hill platform and Tomkinson Province, Northern Territory and Queensland, Record 2020/041, Geoscience Australia, Canberra, doi:10.11636/Record.2020.041.

Czarnota, K, Champion, DC, Cassidy, KF, Goscombe, B, Blewett, R, Henson, PA and Groenewald, PB 2010, Geodynamics of the eastern Yilgarn Craton: Precambrian Research, v. 183, p. 175–202.

Fayol, N and Jébrak, M 2017, Archean Sanukitoid Gold Porphyry Deposits: A New Understanding and Genetic Model from the Lac Bachelor Gold Deposit, Abitibi, Canada: Economic Geology, v. 112, p. 1913–1936.

Gresham, JJ and Loftus-Hills, GD 1981, The geology of the Kambalda nickel field, Western Australia: Economic Geology, v. 76, p. 1373–1416.

Morris, PA 1993, Archaean mafic and ultramafic volcanic rocks, Menzies to Norseman, Western Australia: Geological Survey of Western Australia, Report 36, 107p.

Nelson, DR 1995a, 112159: porphyritic dacite, Royal Arthur: Geochronology Record 488: Geological Survey of Western Australia, 5p.

Nelson, DR 1995b, 112110: felsic volcanic rock, Nelson's Fleet: Geochronology Record 526: Geological Survey of Western Australia, 4p.

Roberts, D 1988, Kambalda – St Ives area nickel sulphide and gold deposits, *in* Excursion guidebook: Boddington and Eastern Goldfields, Western Australia *edited by* BH Smith, CA Stoakes, AL Govey, and CJ Oates: The second international conference on prospecting in arid terrain, Perth, Western Australia, 26 April 1988, The University of Western Australia: Department of Geology and University Extension, Publication no. 18, p. 68–76.

Shirey, SB and Hanson, GN 1984, Mantle-derived Archaean monozodiorites and trachyandesites: Nature, v. 310, p. 222–224.

Smithies, RH 2019, A new look at lamprophyres and sanukitoids, and their relationship to the Black Flag Group and gold prospectivity (PowerPoint): Geological Survey of Western Australia, GSWA Open Day 2019, Fremantle, Western Australia, 22 February 2019, <www.dmirs.wa.gov.au/gswaopenday>.

Smithies, RH and Champion, DC 1999, Late Archaean felsic alkaline igneous rocks in the Eastern Goldfields, Yilgarn Craton, Western Australia: a result of lower crustal delamination?: Journal of the Geological Society of London, v. 156, p. 561–576.

Smithies, RH and Champion, DC 2000, The Archaean high-Mg diorite suite: Links to tonalite-trondhjemite-granodiorite magmatism and implication for early Archaean crustal growth: Journal of Petrology, v. 41, no. 12, p. 1653–1671.

Smithies, RH, Lu, Y, Kirkland, CL, Cassidy, KF, Champion, DC, Sapkota, J, de Paoli, M and Burley, L 2018, A new look at lamprophyres and sanukitoids, and their relationship to the Black Flag Group and gold prospectivity: Geological Survey of Western Australia, Record 2018/15, 23p.

Smithies, RH, Lu, Y, Johnson, TE, Kirkland, CL, Cassidy, KF, Champion, DC, Mole, DR, Zibra, I, Gessner, K, Sapkota, J, De Paoli, MC and Poujol, M 2019, No evidence for high-pressure melting of Earth's crust in the Archean: Nature Communications, 10:5559, doi:10.1038/s41467-019-13547-x.

Swager, CP, Griffin, TJ, Witt, WK, Wyche, S, Ahmat, AL, Hunter, WM and Mcgoldrick, PJ 1990, Geology of the Archaean Kalgoorlie Terrane – an explanatory note: Geological Survey of Western Australia, Report 48, 26p.

Tripp, GI 2013, Stratigraphy and structure in the Neoarchaean of the Kalgoorlie district, Australia: critical controls on greenstone-hosted gold deposits: Ph.D thesis, School of Earth and Environmental Science. Townsville, Queensland: James Cook University.

Tripp, GI 2019, Stratigraphy and Structure in the Neoarchaean of the Kalgoorlie district, Australia: Critical Controls on Greenstone-hosted Gold Deposits: Geological Survey of Western Australia, Report 199, 967p.

Witt, WK, Ford, A, Hanrahan, B and Mamuse, A 2013, Regional-scale targeting for gold in the Yilgarn Craton: Part 1 of the Yilgarn Gold Exploration Targeting Atlas: Geological Survey of Western Australia, Report 125, 130p.

Witt, WK, Ford, A and Hanrahan, B 2015, District-scale targeting for gold in the Yilgarn Craton: Part 2 of the Yilgarn Gold Exploration Targeting Atlas: Geological Survey of Western Australia, Report 132, 276p.

Woodall, RW 1965, Structure of the Kalgoorlie goldfield, *in* Geology of Australian ore deposits, v. I, Commonwealth Mining & Metallurgical Congress, 8th, Australia and New Zealand *edited by* J McAndrew (2nd edition): Australasian Institute of Mining and Metallurgy, p. 71–79.

REPORT
226

GEOCHEMICAL CHARACTERIZATION OF THE MAGMATIC STRATIGRAPHY OF THE KALGOORLIE AND BLACK FLAG GROUPS – ORA BANDA TO KAMBALDA REGION

RH Smithies, JR Lowrey, J Sapkota, MC De Paoli, P Hayman, SJ Barnes, DC Champion, Q Masurel, N Thébaud, LL Grech, M Drummond and R Maas

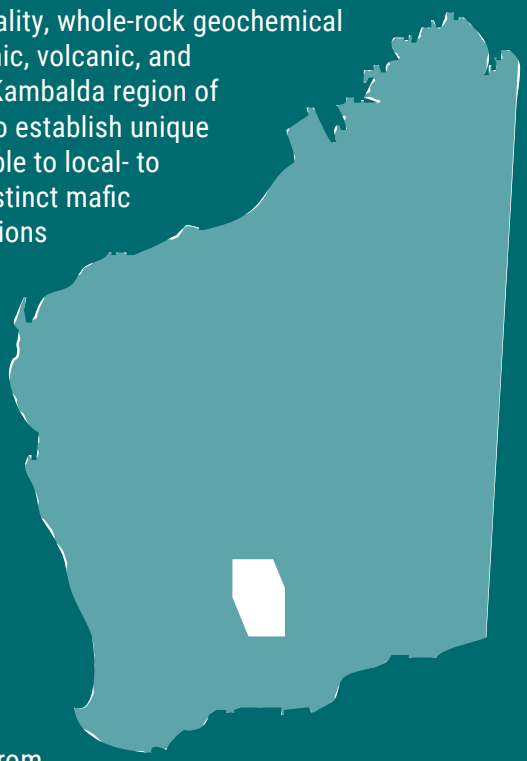

This Report discusses the use of ~2800 new, high-quality, whole-rock geochemical data from drillcore and outcrop samples of subvolcanic, volcanic, and volcaniclastic rocks collected from the Ora Banda – Kambalda region of the Eastern Goldfields Superterrane. The purpose is to establish unique lithogeochemical characteristics (bar codes) applicable to local- to regional-scale greenstone stratigraphy. Twenty-six distinct mafic compositional units are identified based on combinations of major and trace element variations and are used to erect chemostratigraphic columns that highlight trends in compositional changes in evolving magma compositions throughout the region. Although complex, this chemostratigraphic diversity ensures that, in most cases, the position of stratigraphically unknown geochemical samples can be uniquely established as long as enough samples are taken over a continuous stratigraphic interval that also incorporates the overlying and underlying units. The regional distribution of the mafic chemostratigraphic associations is distinctly asymmetric, in many cases ignoring previously established domain boundaries. However, a broadly north-trending structure incorporating segments of (from south to north) the Zuleika Shear Zone, Abattoir Fault, and the Bardoc Shear Zone does appear to separate western domains from eastern domains. These domain groups have distinctive chemostratigraphic variations that probably reflect a fundamental crustal architectural control and potentially provide some basis for reassessing the present domain boundaries. The chemostratigraphic differences between the western and eastern domains extend to the felsic units of the Black Flag Group.

Further details of geoscience products are available from:

First Floor Counter
Department of Mines, Industry Regulation and Safety
100 Plain Street
EAST PERTH WESTERN AUSTRALIA 6004
Phone: +61 8 9222 3459 Email: publications@dmirs.wa.gov.au
www.dmirs.wa.gov.au/GSWApublications